SPECTROSCOPY OF ULTRACOLD LITHIUM-RUBIDIUM MOLECULES

A Dissertation

Submitted to the Faculty

of

Purdue University

by

Ian Stevenson

In Partial Fulfillment of the

Requirements for the Degree

of

Doctor of Philosophy

May 2018

Purdue University

West Lafayette, Indiana

THE PURDUE UNIVERSITY GRADUATE SCHOOL
STATEMENT OF DISSERTATION APPROVAL

Dr. Dan Elliot, Chair

School of Electrical and Computer Engineering

Dr. Yong Chen

School of Electrical and Computer Engineering

Dr. Chris Greene

Department of Physics and Astronomy

Dr. Francis Robicheaux

Department of Physics and Astronomy

Approved by:

Dr. Venkataramanan Balakrishnan

Head of the School of Electrical and Computer Engineering

TABLE OF CONTENTS

Page

Page

ABSTRACT

Ian Stevenson Ph.D., Purdue University, May 2018. Spectroscopy of Ultracold Lithium-Rubidium Molecules. Major Professor: Dan Elliott.

I present spectroscopic data on ultracold lithium-rubidium molecules in a dual species magneto-optical-trap in order to find suitable intermediate states to transfer population to the rotational, vibrational and electronic ground state via a stimulated Raman process. First, I improved the accuracy of the energetic location of the ground state by two orders of magnitude using photoassociation as a spectroscopic tool to measure the energy of bound states relative to the scattering continuum. Second, we studied the $d\,^3\Pi$ - $D\,^1\Pi$ and $A\,^1\Sigma^+$ - $b\,^3\Pi_{0^+}$ excited electronic manifolds with a combination of resonantly-enhanced-multi-photon-ionization and depletion spectroscopy finding suitable singlet-triplet mixed states to use in the Raman transfer scheme. Finally, I demonstrate robust optical phase locked loops to maintain the coherence between the two lasers required for the Raman process.

1. INTRODUCTION

Laser cooling of atoms has been an active area of research since it was conceived. Researchers have continued in the never ending search for colder, denser atomic clouds starting from optical molasses, then magneto-optical-traps (MOT) [1] and finally Bose-Einstein condensates (BEC) [2]. The track for molecules has been much less smooth. Direct laser cooling of molecules is impossible for all but a select few, like SrF [3], and other techniques like buffer gas cooling [4] or electrostatic traps [5] struggle to reach even fairly modest temperatures like 10 mK. For a select, but very useful class of diatomic molecules, researchers discovered that they can cool the individual atoms that make the molecule and then form the molecule at an ultracold temperature. These molecules are of the form XY, where X,Y$\in$[Li,Na,K,Rb,Cs], called bi-alkali's. Homo-nuclear bi-alkali's were first studied because it is simpler to only trap one species. There are two main techniques to form these molecules: photoassociation (PA) and magneto-association (MA). The earliest experiments in bi-alkali's consisted of using PA to study Na_2 [6], Cs_2 [7] and Rb_2 [8]. Since then, researchers have discovered that MA is often superior to PA because MA creates all molecules in one quantum state whereas PA populates a spread of states in all degrees of freedom, including rotation, vibration and hyperfine. In the past ten years, interest shifted to hetero-nuclear molecules like KRb [9, 10], LiCs [11], RbCs [12, 13], NaCs [14] and LiRb (studied here).

The advantage hetero-nuclear molecules offer is that they have a non-zero electric dipole moment in their lowest electronic state. The electric dipole moment is a fundamental difference between hetero-nuclear bi-alkali's and atoms, which provides a long range interaction between trapped hetero-nuclear molecules and opens the door for new physics [15–18]. There are strategies to induce long range interactions in trapped atomic systems like atom-in-cavity experiments and through the use of magnetic atoms. Magnetic atom experiments like those in Dysprosium [19], Erbium and Chromium [20, 21] have had success in creating dipolar BECs and realizing exotic states of matter [22].

However, the magnetic interaction in these atoms is weak compared to the electric dipole interaction in molecules.

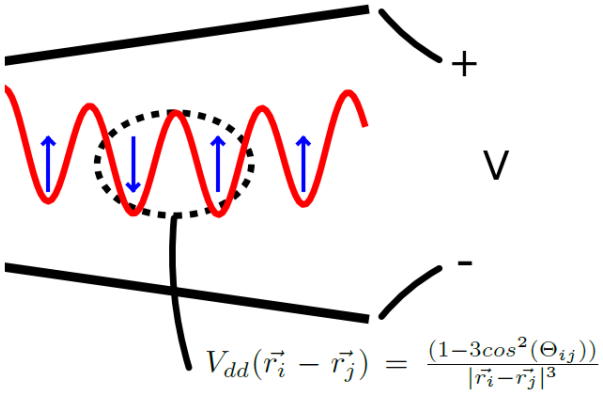

Fig. 1.1. Using trapped electric dipoles as qubits, borrowed from Ref. [23]. The blue arrows represent the dipoles, physically a diatomic polar molecule (like LiRb) in the ground state. The black bars are the electrodes ~ 1 cm apart. The red trace represents the 1-D optical lattice potential.

1.1 Quantum computing

Much of the interest in hetero-nuclear bi-alkali's was kicked off by a proposal from DeMille in 2002 that provided a method to use a system of trapped electric dipoles as a quantum computer [23]. This is shown graphically in Fig. 1.1 and the simplicity of DeMille's scheme is to be appreciated. His idea is to trap a large number of electric dipoles (hetero-nuclear bi-alkali's) in a one-dimensional (1-D) optical lattice. These dipoles form his qubits with $|0\rangle$ being dipole aligned with the DC field and $|1\rangle$ being dipole anti-aligned. A qubit is a two-state quantum system to be used for quantum computing. The electric field provided by his plates has a few functions. First it induces the dipole moment, second it provides the lab frame to distinguish $|0\rangle$ and $|1\rangle$ and finally, it has a gradient along the trap direction which DC Stark-shifts the electric dipoles so that the transition energy $E_{|0\rangle\rightarrow|1\rangle}$ is unique for each position in the trap. The Hamiltonian of a molecule at x_a is

$$H_a = H_{int} - \vec{d_a} \cdot \vec{E_a} \text{ where } \vec{E_a} = \vec{E}_{ext}(x_a) + \vec{E}_{int}(x_a). \tag{1.1}$$

The two electric field components are $\vec{E}_{ext} = [E_0 + x_a \frac{\partial E}{\partial x}]\hat{z}$ and $\vec{E}_{int} = \sum_{b \neq a} \frac{-\vec{d_b}}{|x_a - x_b|^3}$ ($\vec{d_a}$ is the dipole moment of qubit a). Selecting $E_0\hat{z}$ so that $\vec{E}_{ext} \gg \vec{E}_{int}$ causes DC Stark shifts by the field plates to dominate over shifts by nearby dipoles. This choice protects the transition energy at each lattice site from being shifted too significantly by neighboring dipole-dipole interactions. The array of qubits can then be set to an arbitrary internal state by concocting a series of RF pulses. Further, the small modification of the exact transition energy at each site by the dipole-dipole interaction with its neighbors modifies the Rabi frequency leading to entanglement. From here a combination of long, cNOT operation pulses and short, single bit changing pulses can turn this system into a quantum computer. Of course, this proposal looks very good on paper, but in practice it has been very difficult to implement. At almost every step, the difficulty is in producing the long-lived 1-D optical lattice of polar molecules.

1.2 Quantum simulator

As demonstrated by the KRb experiment at JILA [24], dipolar molecules can be used to simulate Hamiltonians. In this example, they simulated the spin 1/2 lattice model with rovibronic ground state KRb molecules in a 3D optical lattice. The interaction Hamiltonian is

$$H = \frac{J_\perp}{2} \sum_{i>j} V_{dd}(\vec{r_i} - \vec{r_j})(S_i^+ S_j^- + S_i^- S_j^+) \tag{1.2}$$

where $V_{dd}(\vec{r_i} - \vec{r_j}) = \frac{(1-3cos^2(\Theta_{ij}))}{|\vec{r_i} - \vec{r_j}|^3}$ is the dipole-dipole interaction energy, $J_\perp = -\frac{d_{\uparrow\downarrow}^2}{4\pi\epsilon_0 a^3}$ is the tunneling energy cost, $d_{\uparrow\downarrow} = \langle\downarrow |\vec{d}| \uparrow\rangle$ is the spin-exchange dipole moment, a is the lattice constant, and Θ_{ij} is the angle between position vectors of the two dipoles. The spin 1/2 system will interact through spin-spin interactions leading to physics like spin exchange. In the JILA model, the dipole moment acts as the spin and the molecules interact through the dipole-dipole interaction. This leads to dipole exchange interactions which are very similar to spin-exchange mathematically. This is shown graphically in Fig. 1.2. The JILA team was able to see basic exchange interactions, and as the filling factors increase, so do the range of possible model systems [25]. Quantum simulators are a quantum computer that only solve one class of problems and in this case, Hubbard models. As work on more classical realizations of quantum computing involving qubits

have stalled because of their complexity, quantum simulators have received increased attention across the ultracold community [26].

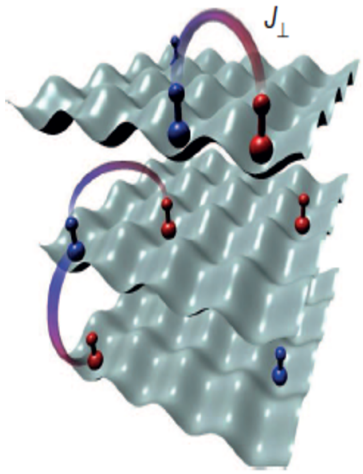

Fig. 1.2. Polar molecules are loaded into a deep 3D lattice, borrowed from Ref. [24]. Blue and red represent different rotational states, and $J_\perp$ is the spin - exchange interaction energy. The JILA KRb team realized this model in 2013 and observed spin oscillations around 50 Hz.

1.3 Coherent imaging

One final experiment that can be done with hetero-nuclear molecules is coherent imaging of rotational wavefunctions. Specifically, if we put the molecule in a state like

$$|\Psi\rangle = c_1(t)|0\rangle + c_2(t)|1\rangle, \tag{1.3}$$

we can take a time resolved picture of the wavefunction where $|0\rangle$ is some molecular state with vibrational quantum number v, hyperfine quantum number F, projection onto the lab axis m_F and rotational quantum number J=0 while state $|1\rangle$ has the same v, F, and m_F but J=1. $c_1(t)$ and $c_2(t)$ are the time evolving constants for this superposition which will have angular frequency $\omega = \frac{E_1 - E_0}{\hbar}$. To coherently image the wavefunctions, an intense laser pulse needs to arrive at $t_0 + \frac{2\pi n}{\omega}$ for each repetition of the experiment and over a large number of repetitions the probability distribution of the electronic wavefunction at t_0 can be recovered. This type of experiment could also be done for vibrational superposition states though the experimental feasibility will be determined by ω, which will be several orders of magnitude larger.

Species	Dipole Moment (Debye)	Reactive	Species	Dipole Moment (Debye)	Reactive
LiNa [28]	0.6	Y	NaRb [29]	3.3	N
LiK	3.6	Y	NaCs	4.6	N
LiRb	4.1	Y	KRb [9]	0.6	Y
LiCs	5.5	Y	KCs	1.9	N
NaK [30]	2.8	N	RbCs [31]	1.2	N

Table 1.1.
Summary of ultracold bi-alkali experiments following the JILA path. The dipole moments were calculated by Ref. [32], and chemical stability was calculated by Ref. [33].

1.4 JILA's path to ultracold molecules

The most successful method for producing dense ultracold molecules comes out of Jun Ye's group at JILA [9, 27]. Their experimental sequence is as follows. First, load a dual species magneto-optical trap. Sacrifices on each specie's density and temperature will be made to ensure both species can be trapped. Next, load an optical dipole from the MOTs. In the dipole trap the atoms are evaporatively cooled until they both reach degeneracy. To form the molecules, they use a fast ramp of the interspecies scattering length through a Feshbach resonance which forms molecules in the least bound triplet state. Finally, a pair of laser pulses transfers the loosely bound molecules to the ground state through a stimulated Raman process called STIRAP.

As seen in Table 1.1, a number of bi-alkali teams have implemented the JILA approach to ultracold molecule production. Additionally, all of these experiments seek to solve the biggest problem with the JILA KRb experiment. As discovered in 2008 [9], the KRb molecules only lived in the dipole trap for a fraction of a second before being consumed by chemical reactions of the form

$$AB + AB \rightarrow A_2 + B_2, \tag{1.4}$$

where A and B are the two atomic species. For KRb and all bi-alkali's containing Li, the reaction in Eq. (1.4) is exothermic [33] and will rapidly proceed at ultracold temperatures.

For all other bi-alkali's, the reaction is endothermic [33] and they are said to be chemically stable. JILA's solution to this problem is to isolate the molecules from one-another in a deep three dimensional optical lattice. Interestingly, reactive molecules versus non-reactive molecules maybe a distinction without reason as evidenced by recent work in NaRb [34] (at least for bosons).

1.5 DeMille's approach to ultracold molecules

The latest approach to ultracold molecules comes out of David DeMille's lab at Yale. His idea is that, although most hetero-nuclear diatomic molecules cannot be laser cooled, a few can be. The condition for laser cooling is that the molecule needs an excited state that mostly decays back to the ground state, which is called a (nearly) closed transition. A closed or cycling transition occurs when spontaneous decay from the excited state is exclusively to the initial state. Compared to atoms, molecules have two additional degrees of freedom, nuclear vibration and rotation, which makes finding truly closed transitions impossible (as there are no selection rules for vibration) and finding nearly closed transitions tricky. However, if the first excited state potential is close enough in shape to the ground potential, nearly closed transitions can happen. DeMille has since discovered that SrF fits into this class. However, the transition is only closed to something like 10^5 scattering events [35] before the molecules are lost, and this isn't enough to trap the molecules starting from room temperature. To remedy this problem, he cools the molecules with a He buffer gas first, getting the temperature down to about 3 K. The molecules are shot out of the buffer gas cell in a molecular beam. The beam is slowed and trapped in a magneto-optical-trap. Currently, his team is able to trap around 10^4 molecules at roughly 1 mK [36]. While impressive, the cost in this approach is the fantastic complexity of this experiment. It takes 12 lasers to return population to the main cooling transition [3]. The buffer gas cell is extraordinarily tricky. To prevent dark state formation, large magnetic fields and laser polarizations need to oscillate at 1 MHz [3]. And his next step, to sympathetically cool molecules with atoms [37], is untested and fraught with peril from chemical reactions. Nevertheless, DeMille's success has inspired a host of competitors in CaF [38, 39], BaF [40], and YO [41].

	Our LiRb experiment	Data exists
Dual species MOT	✓	✓
Conservative trap and cool		✓
Interspecies Feshbach resonance		✓
Transfer to ground state with STIRAP		

Table 1.2.
Summary of prior work in LiRb on implementing the JILA approach to ultracold molecule formation. Data on LiRb interspecies Feshbach resonances can be found in Ref. [42].

1.6 Our Challenge

Our long term goal for the lithium-rubidium (LiRb) experiment is to create a dense cloud of ultracold molecules in the ground state. The cloud could then be used to realize exotic states of matter or be used as the qubits in a quantum computer. As seen in Table 1.2, there exists data [42] or examples [43] for all of the steps in the JILA approach for LiRb except for the stimulated Raman transfer. We need a measurement of the ground state well depth and data on mixed states to provide a path for an adiabatic transfer of weakly bound molecules into the ground state. Our spectroscopic work on establishing the depth of the LiRb ground state can be found in Chapter 4, and our work on finding suitable pathways for the stimulated Raman transfer can be found in Chapter 5 and Chapter 6. Additionally, phase coherence is required between the two lasers used in the STIRAP sequence and our work on phase locking lasers can be found in Chapter 7

2. DUAL SPECIES MOT

Magneto-optical-traps (MOTs) are a staple of ultracold atom experiments because they are easy to implement and incredibly useful. They reliably trap 10^8 atoms at under 500 μK. In this thesis, most of the work has been done on LiRb molecules formed out of a pair of spatially overlapped MOTs, one for each species. This chapter outlines the operating principles of these MOTs; how we generate the laser light for each trap; and the details of the vacuum system in which the MOTs live.

The students before me put together the original dual species MOT. I have left in place the vacuum system (as changing that is difficult and time consuming), but I have modified the MOT setup. The most important change is that I replaced a traveling wave electro-optic-modulator (EOM) that produced the Li repump with a resonant EOM. The original EOM was driven by nearly 10 W of RF power which caused thermal drifts in the beam alignment. Additionally, I changed how we generate the RF drives for the Rb acousto-optic-modulators (AOMs). Previously, we had a monolithic printed-circuit-board (PCB) that produced all 8 RF drives for the experiment. Unfortunately, some of the components failed and were impossible to replace. The smaller board I designed both solves this issue (as replacing it only replaces one or two RF drive chains) and it helps reduce lab clutter which is a real problem for experiments of this size.

2.1 MOTs

MOTs work off the exchange of momentum between atoms and photons. They bring atoms from a temperature of tens of K down to around 1 mK which requires millions of atom-photon scattering events inside a closed transition. Luckily, all alkali atoms have closed $J \rightarrow J+1$ transitions on their D_2 lines (where J is the total angular momenta of the atom). We will need to add a repump laser because the trapping lasers are not perfect and can accidentally excite into hyperfine states outside of the cycling transition. The atoms will gain or lose momentum when interacting with the laser because the momentum

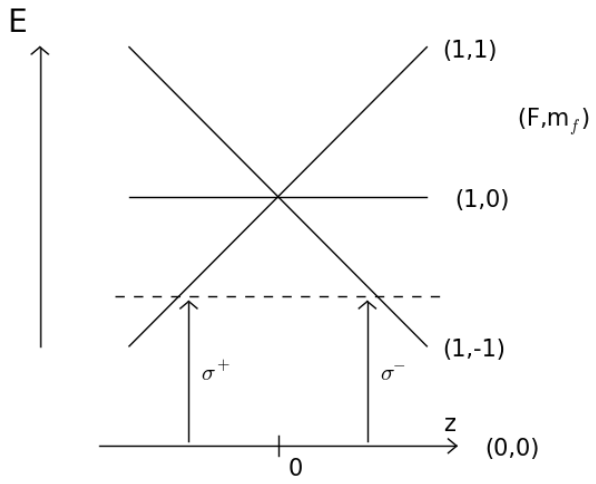

Fig. 2.1. Conceptual model of a 1D MOT. Drift out of the center brings the atom into resonance with the σ^+ or σ^- polarized light which applies radiation pressure forcing the atom back to the MOT center, adapted from Ref. [44].

kick from each laser photon will be in the direction of laser propagation while spontaneous emission back to the initial state will, on average, net a zero momentum change. In this scenario, the atoms will gain momentum in the direction of laser propagation on average. By picking lasers red detuned from the atomic lines in a counter-propagating geometry, the atoms will interact more strongly with the laser against which they are moving because of the Doppler effect and always slow down. We form an optical molasses by picking the lasers to have circular polarization, thereby driving the $m_F \rightarrow m_F + 1$ transition which dodges Zeeman dark states. The molasses cools the atoms, but does not trap them.

To get trapping it is necessary to introduce a magnetic field gradient $\frac{d\vec{B}}{dz}$. This creates a position dependent Zeeman splitting in sub-levels of the atom, shown in Fig. 2.1. Now the atoms will always be pushed back to the magnetic field zero-crossing, in addition to being slow moving because of the molasses. Experimentally it is very easy to realize a $\vec{B}$ field that has a linear gradient with a pair of anti-Helmhotz coils. True atom cooling involves a 3-D picture with six trapping beams counter propagating in each independent direction.

As MOTs and flourescence work on atoms scattering photons, it is very useful to be able to estimate the photon scattering rate. Ref. [45] provides a method to calculate the scattering rate of laser photons by an atom as

$$R_{sc} = \frac{\Gamma}{2}\frac{(I/I_{sat})}{1+4(\Delta/\Gamma)^2+(I/I_{sat})}, \tag{2.1}$$

where Γ is the natural linewidth of the transition, I is the laser intensity, I_{sat} is the saturation intensity of the atomic transition and Δ is the detuning.

2.2 Extended Cavity Diode Laser

To create the laser light for our MOTs, we use three extended cavity diode lasers (ECDLs). An ECDL is formed by carefully isolating a Fabry-Perot diode laser and applying optical feedback. An ECDL schematic is shown in Fig. 2.2 (a). These semiconductor Fabry-Perot laser diodes are very susceptible to optical feedback and will try to follow the frequency of any light sent to them. We exploit this fact to stabilize and

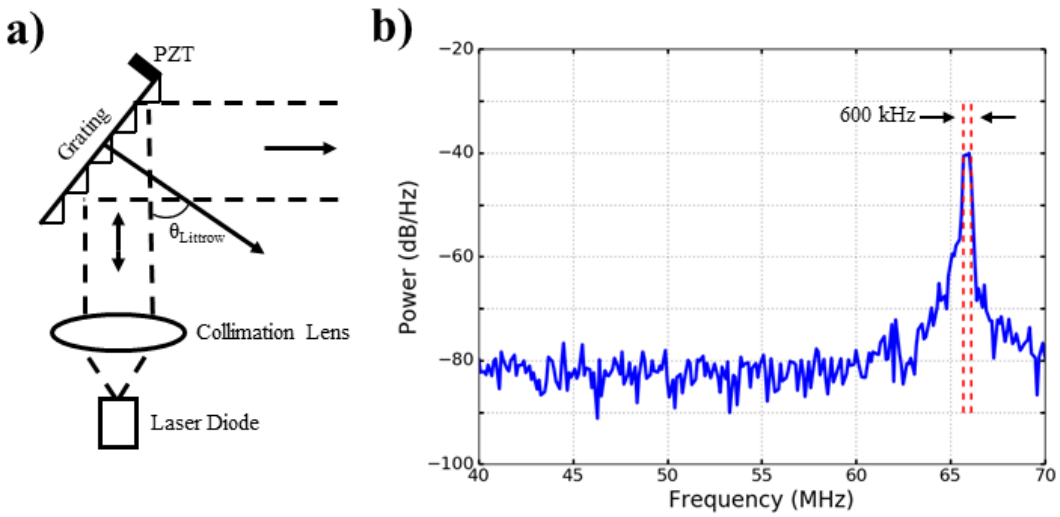

Fig. 2.2. **(a)** An extended cavity diode laser. Optical feedback from the grating forces the laser into single mode operation controlled by the distance between the grating and diode. The grating is chosen for Littrow angle close to 45^o and first order diffraction of around 20%. **(b)** Beat-note between an ECDL and one tooth of a frequency comb. Because the frequency comb can be treated as an infinitely narrow frequency source, the FWHM of the beat-note reveals the linewidth of the ECDL to be around 1 MHz (details on beat-note production can be found in Chapter 7).

control their wavelength. The extended cavity is formed between the diode back face and a grating which sends back a small amount of light, and sets the wavelength of the laser. We mount the laser diode in a collimation tube (Thorlabs model LT230P-B) and set the adjustable lens to form a collimated beam on the output. We diffract the collimation tube output off a holographic grating (Thorlabs model GH13-18V) (The grating needs to be chosen for the laser at hand. This grating works well for lasers near 780 nm wavelength, as it reflects back about 20% of the light at nearly a 45° angle.), and send the first order diffraction back to the laser diode. The Littrow angle for a grating can be approximated by

$$2a\sin(\theta_L) = m\lambda_D, \tag{2.2}$$

where a is the grating period, θ_L is the Littrow angle, m is the diffraction order (usually 1), and λ_D is the laser wavelength. Usually, the grating is set 2 - 3 cm away from the diode and mounted with a PZT (MMech model AE0203D04) in its kinematic-adjuster (Thorlabs model KS05) for fine cavity length adjustment. The zeroth order diffraction is used as the ECDL output.

To maintain single mode operation, we also carefully control the diode temperature and current. We use commercial temperature controllers (Thorlabs model TED200C or TED8020) with a temperature sensor (AD590) mounted near the collimation tube and a thermo-electric-cooler (CUI Inc. model CP85438 or Thorlabs TECD25) to control the temperature of the diode to 1 mK accuracy. We use a variety of different current controllers; the best of these are home built Libbrecht - Hall designs [46], the schematics for which can be found in Ref. [47]. Our homebuilt controllers can source up to 200 mA of current, they offer better than 200 nA root-mean-squared noise performance and they have a modulation input that works up to 100 MHz. Additionally our lasers are mounted on vibration absorbing foam and in an aluminum metal enclosure, both of which help isolate the diode from environmental perturbations. I recommend the one piece enclosure design in Ref. [48] for future lasers. In the end, our ECDLs produce a laser output with a linewidth around a MHz, as shown in Fig. 2.2 (b), and can maintain single mode operation for several hours at a time.

2.3 Saturated Absorption

To maintain the frequency of the ECDLs near atomic lines for a long time, we lock our lasers to atomic saturated absorption resonances. The basic setup for saturated absorption is shown in Fig. 2.3. We send counter-propagating lasers beams, one strong and one weak, through vapor cells. The weak beam is sent to a photodiode which measures the absorption by the atomic vapor. Without the strong pump laser, the weak probe laser sees the Doppler broadened background several GHz in width. With the pump laser present though, the probe laser sees the atoms moving perpendicular to the pump beam are already saturated and these atoms absorb less light. Thus, saturated absorption produces sub-Doppler lineshapes, limited only by the natural linewidth of the transition. However, there are two additional problems. First, the sub-Doppler features are much weaker than the Doppler background. To resolve these small features, we electronically subtract the Doppler background by measuring the absorption of a second probe beam sent through the cell. Second, saturated absorption produces crossover resonances. These resonances occur when the Doppler velocity of the atoms spans the frequency difference of the two lasers and occur halfway between each possible pair of excited states. The crossover resonances can be stronger than the true resonances, depending on the intensity of the pump and probe lasers. This can be a useful feature instead of a bug, as it gives us twice as many resonances to which to lock.

With saturated absorption, we use the atomic vapor cells as the frequency discriminator, but to lock to these resonances we have to generate an error signal. To do this we slowly dither the laser frequency by applying a small amplitude sinusoid at 10 kHz to the laser current. As the laser sweeps through an atomic resonance, the photodiodes will see a phase shift on the modulation signal. Conceptually, this phase shift occurs because the sign of the first derivative changes around the resonance. By phase shifting the photodiode signal and mixing with the modulation source, we can recover the phase information, forming our error signal.

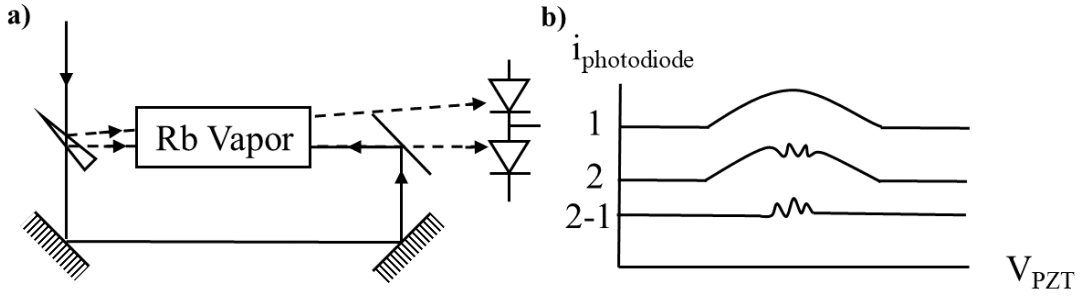

Fig. 2.3. **(a)** Table setup for saturated absorption. A vapor cell has two weak laser beams propagate through it and sent to photodiodes. One weak beam counter-propagates with a much stronger laser. **(b)** Signal seen by photodiodes as we ramp the laser frequency. Both photodiodes see the Doppler broadened absorption profile several GHz in width. However, the bottom photodiode also sees the effect of the strong counter-propagating laser. Background-free, Doppler-free spectrum can be recovered by taking the difference of the two signals electronically.

2.4 Loop Filter

The loop filter we used to apply feedback to the ECDL is shown in Fig. 2.4. ECDLs have two electronic control paths. The diode current has a modulation input, which has a frequency response out to about 10 MHz and a π phase shift near 1 MHz. Second, the PZT in the grating mount fine-tunes the cavity length and has a frequency response out to about a few kHz. Like other loop filter designs [49], we utilize both paths. Our current feedback path, pictured on top in Fig. 2.4, has the standard feature: it has a phase advance filter tuned to a few MHz (we tried a more traditional filter tuned for slightly under a MHz, but found ours to work better), it provides a maximum gain of 12, it has a variable resistor to provide fine control over the gain, and it allows us to add a bias voltage for fine control over the laser frequency via the current modulation. On the bottom path in Fig. 2.4, is our PZT feedback. We have an op-amp that is either an integrator or a high-gain low-pass filter. A switch chooses between the two functions. This is followed by a variable resistor that sets the PZT gain and a summing op-amp to add a bias voltage to fine tune the laser frequency via the PZT voltage. As shown in Fig. 2.4, our two bias voltages are controlled by a pair of potentiometers. These are tuned following the advice of Ref. [50] to allow wide mode-hop free tuning of the laser.

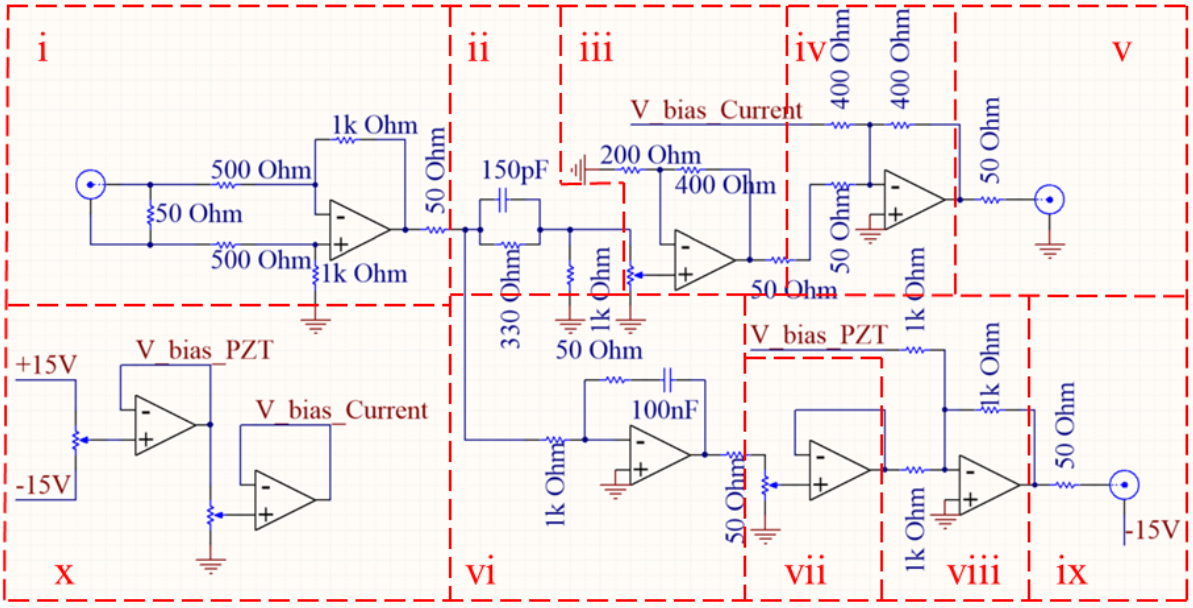

Fig. 2.4. Loop filter used for both phase detectors. **i** Edge launch input, impedance match and buffer op-amp with a gain of two. **ii** Phase-advance filter for current feedback. Zero is set at 3 MHz and pole set at 5 MHz. **iii** Current feedback amplitude control and buffer op-amp with gain of three, to prevent stage loading effects. **iv** Summing op-amp, adds current bias voltage to current error signal, provides gain of two to error signal. **v** Current feedback output, impedance match and edge launch. **vi** Integrator in PZT path. Provides a low-pass filter with gain of 10 and cutoff at $f_c = 160$ Hz when switch is closed. Integrates when switch is open. **vii** PZT gain control and buffer op-amp. **viii** Summing op-amp, adds PZT bias voltage to PZT error signal. **ix** PZT feedback output, impedance match and edge launch connector, shield biased at -15V. **x** Bias generation.

Omitted from Fig. 2.4, are an inverting om-amp and a pair of switches to control the sign of both feedback paths.

2.5 Acousto-Optic-Modulator

An acousto-optic-modulator (AOM) adds an acoustic phonon to the laser photon, as shown in Fig. 2.5 (a), thus allowing precise control over the laser frequency. By tuning the AOM alignment, either the acoustic phonon is added to the laser or subtracted from it. The AOM needs to be driven by an RF field and common AOMs require 80 MHz, 110 MHz or 200 MHz RF drives. It takes around 1 W of RF power to efficiently transfer

power into the first order diffracted beam. For a well aligned AOM 80 % diffraction into the first order beam is not uncommon. Additionally, AOMs can function as a fast optical switch with turn on and off times around 25 ns.

Fig. 2.5 (b) shows our electronics to control the Rb AOMs. It consists of a voltage-controlled-oscillator (VCO, Minicircuits ROS-100+ or ROS-300+) driving an RF switch (HMC221B) and a voltage-controlled-attenuator (VCA, RVA-800+ or RVA-2500+). Not shown is an off-board RF amplifier (Minicircuits ZHL-2-S+ or ZHL-1-2W-S+) to boost the modest power out of the oscillator to around 1 W. The oscillator and attenuator are controlled by a precision digital-to-analog-converter (DAC8812) which is programmed by a PIC24 micro-controller. The micro-controller also controls the RF switch. Previously, the VCOs were controlled by LabVIEW, via its analog output board. The advantage to using the micro-controller is both in speed and lab compactness. The micro-controller has enough memory for basically any algorithm we would want and can sit waiting for a digital trigger to execute its code. Our AOM board has two output channels, one digital input, one digital output and two analog inputs. We have used this circuit for a variety of tasks, like controlling the output laser power after the AOM to better than 0.1%, and rapidly cycling the MOT lasers. Code for all applications may be found in Appendix D and the full circuit diagrams are in Appendix C.

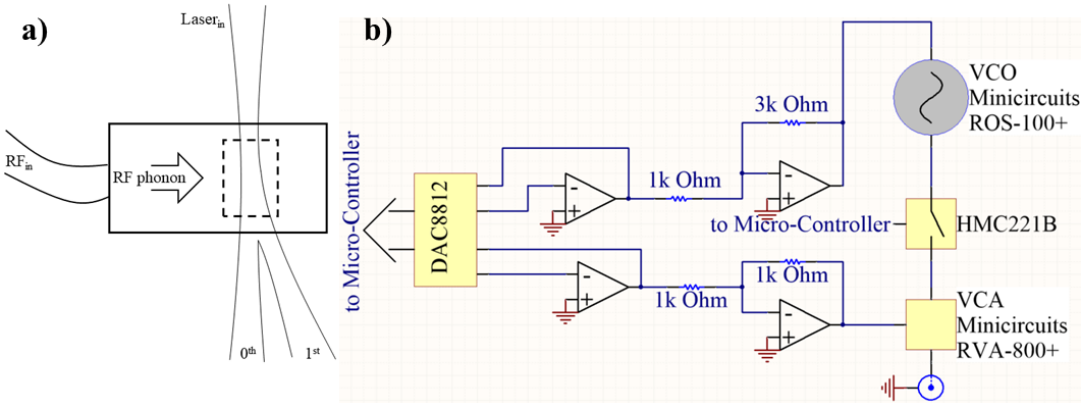

Fig. 2.5. **(a)** Acousto-Optic-Modulator. Alignment of the AOM needs to be fine tuned to meet the phase matching condition, either $\vec{k}_{\text{laser}} + \vec{k}_{\text{phonon}} = \vec{k}_{1^{\text{st}}\text{order}}$ or $\vec{k}_{\text{laser}} - \vec{k}_{\text{phonon}} = \vec{k}_{1^{\text{st}}\text{order}}$. **(b)** AOM control circuit.

2.6 Rb MOT

To form our Rb MOT, we have two EDCLs locked to two different atomic resonances. As shown in Fig. 2.6 (a), we have the main cooling laser that addresses the $5S_{1/2}$ F=3 $\rightarrow$ $5P_{3/2}$ F=4 closed transition. Because the laser is not perfect and has a broad, weak pedestal in frequency, there is a very small probability for an atom to end up in the $5P_{3/2}$ F=3 state. The atom can then decay to the F=2 ground state falling out of the cooling transition. To remedy this, we have a second laser tuned to the $5S_{1/2}$ F=2 $\rightarrow$ $5P_{3/2}$ F=3 transition which will return atoms to the main cycling transition. The Rb cooling laser is a 1 W Tiger laser from Sacher LaserTechnik. The repump laser is a homemade ECDL with a QPhotonics QLD-780-80s diode.

The preparation of these lasers is shown in Fig. 2.7. Both lasers are sent through optical isolators, to reduce back reflections that will destabilize the lasers, and then a small amount of light is picked off for saturated absorption locking. The saturated absorption locking signal is shown in Fig. 2.6 (b), and the resonances that we lock to

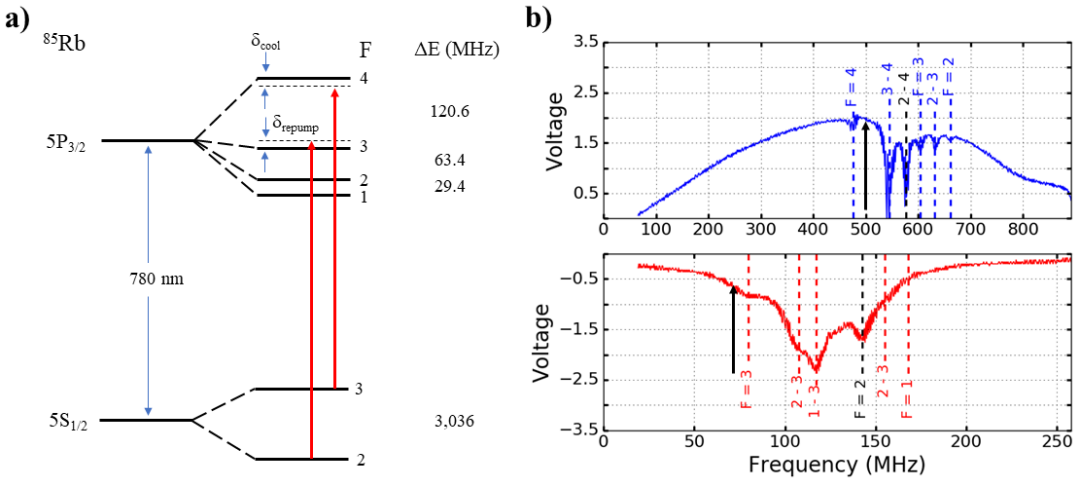

Fig. 2.6. **(a)** Energy level diagram for ^{85}Rb showing the cooling transition. Two lasers are identified by red arrows. **(b)** Saturated absorption spectroscopy of ^{85}Rb. Top trace is from the Rb cooling laser, starting from $F = 3$ in the ground state, bottom trace is from the Rb re-pump laser, starting from $F = 2$ in the ground state. Transitions are identified by the excited state quantum number, with hyphened labels denoting crossover resonances. The black-dashed lines identify the transition each laser is locked to, and the bold, black arrows show the laser frequency after up-shifting in the AOM.

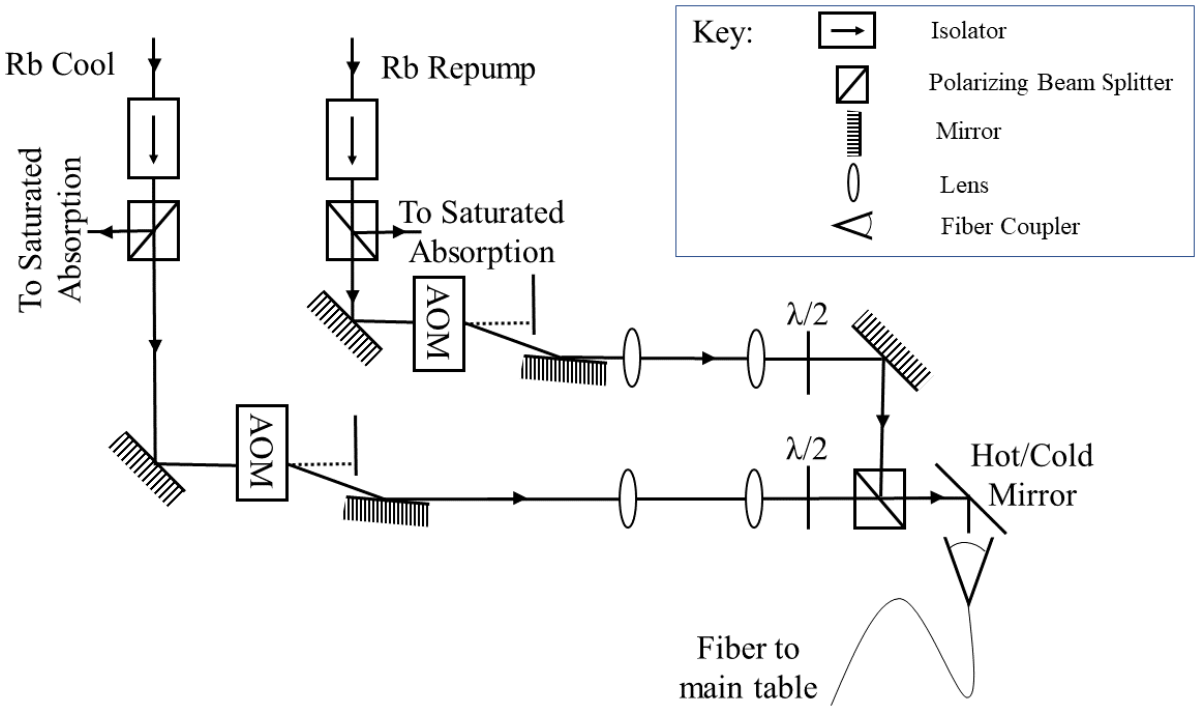

Fig. 2.7. Preparation of Rb trapping lasers. Both lasers are sent through isolators and a small amount of light is sent off to the saturated absorption locking setup. Both lasers are frequency up-shifted in AOMs, and sent through beam shaping lenses before being combined at orthogonal polarizations on a polarizing beam splitter. The hot-cold mirror combines the Rb light with Li light (not shown here) and is coupled into an angle-cut, PM fiber which sends the light to the experiment table.

are highlighted. These don't line up exactly with the desired atomic transitions for two reasons. First, there needs to be a detuning of a few natural lifetimes to make a MOT work. The temperature and size of the MOT can be loosely controlled by changing this detuning. Second, we up-shift the frequency of both lasers in a pair of AOM's and the frequency of the lasers as seen by the MOT atoms is highlighted in Fig. 2.6 (b) by the thick black arrows. Up-shifting in the AOM's allows us fine control over the laser frequency, and more importantly, they provide a fast optical switch to turn on and off the MOT beams in under a μs. After the lasers are up-shifted, they are sent through a telescope, combined at orthogonal polarizations on a beam splitter and then coupled into an angle-cut, polarization maintaining fiber. The telescope helps mode match the fiber to increase coupling efficiency, and the fiber allows us to transport the laser light to the experiment on a different optical table. The fiber needs to be angle cut to reduce back-

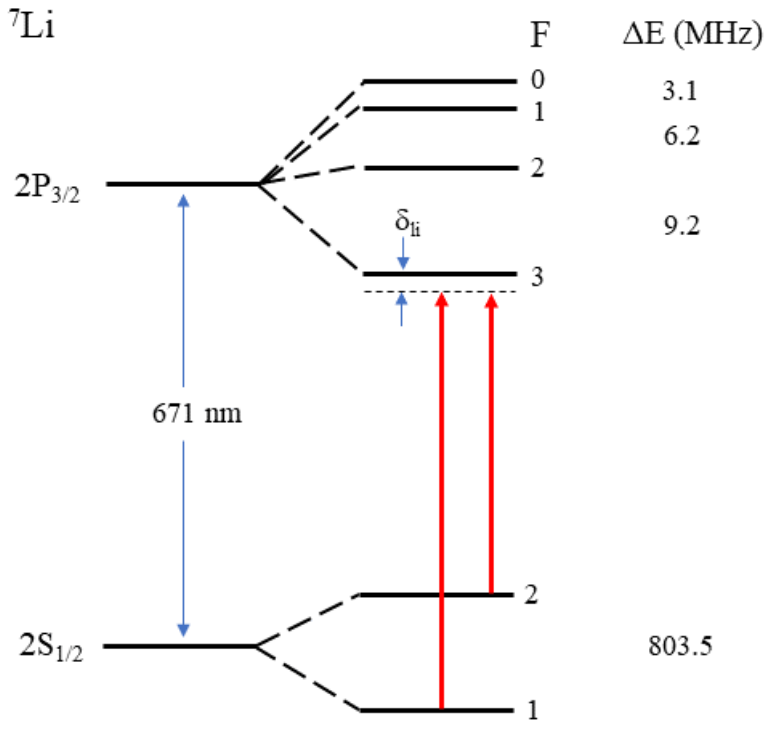

Fig. 2.8. Energy level diagram for ^{7}Li showing the cooling transition. One laser with sidebands is used for both transitions, shown as red arrows. As we do not resolve the excited state hyperfine structure, the saturated absorption spectrum is quite simple for the Li MOT and is omitted. Consult Ref. [51] for an example spectra.

reflections and because the fiber is polarization maintaining, we can split the beams based on their polarizations on the experiment table to form the Rb dark MOT. A summary of the Rb MOT laser powers post fiber and detunings is provided in Table 2.1, and the typical MOT size is given in Table 2.2.

2.7 Li MOT

Our Li MOT follows the same prescription as the Rb MOT, as shown in Fig. 2.8. Again, we have the main cooling laser addressing the $2S_{1/2}$ F=2 $\rightarrow$ $2P_{3/2}$ transition and there is a repump laser on the $2S_{1/2}$ F=1 $\rightarrow$ $2P_{3/2}$ transition. However, the astute reader will note that the hyperfine splitting in the $2P_{3/2}$ state is on the same order as the natural linewidth ($\Gamma = 2\pi \times 5.89$ MHz). This prevents us from resolving the hyperfine structure of the excited state and addressing individual excited hyperfine states. As a result, the

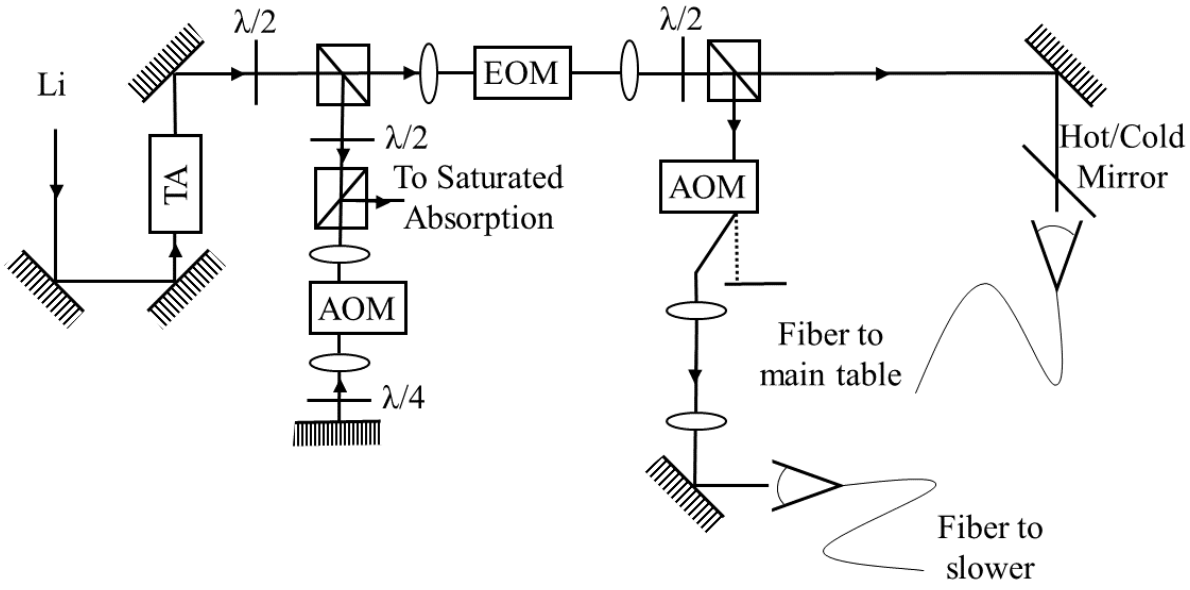

Fig. 2.9. Preparation of the Li trapping laser. The ECDL output is sent through a tapered-amplifier (TA), boosting its power from 25 mW to 250 mW. A small amount of light is picked off and double passed through an AOM before being sent to the saturated absorption setup. The main beam is sent through an EOM, which imposes sidebands at 815 MHz. Finally, the beam is split between a Zeeman slower beam, which is red shifted 80 MHz and the main beam which is combined with the Rb trap beams on a hot-cold mirror and fiber coupled.

Li MOT behaves more like a two species MOT with nearly an equal mixture of F=2 and F=1 and the temperature is much hotter than the Rb MOT.

The preparation of our Li trapping laser is shown in Fig. 2.9. Our Li laser is a commercial ECDL, Toptica DL Pro, and we use it to seed a Toptica BoosTA tapered amplifier. The tapered amplifier boosts the power from 25 mW to over 250 mW while maintaining frequency coherence. After the tapered amplifier, we pick off a small amount of the light for saturated absorption locking, shown in Ref. [51]. Unlike our Rb MOT, the 200 MHz AOM is in the locking path for Li, in a double pass configuration. This shifts the laser frequency by twice the drive frequency and we lock to the 1-2 crossover resonance. Unfortunately, we lose the ability to turn on and off the Li laser fast but we do not need an additional AOM for the Li system. To generate our repump light, we use a 815 MHz resonant EOM, Qubig model EO-Li7, to shift a third of the laser power into sidebands. After applying sidebands, we pick off a third of the laser power to use for a Zeeman slower, as explained in the next section. The slower beam is down-shifted in an

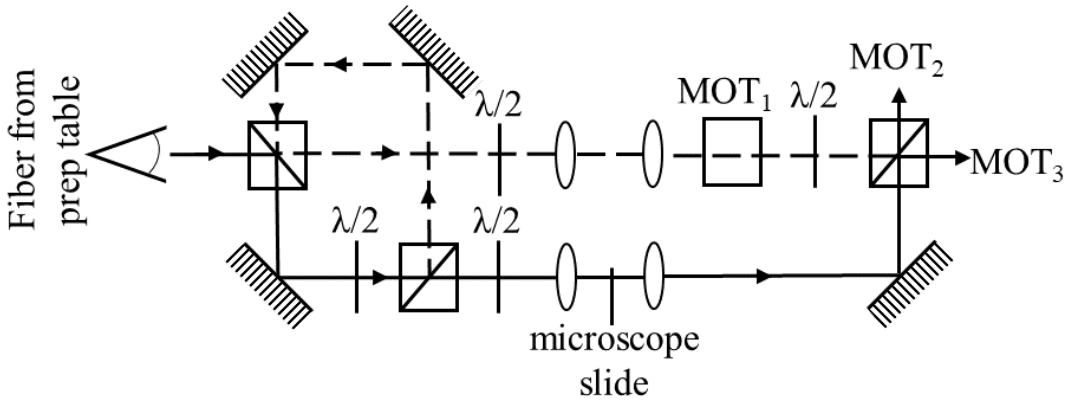

Fig. 2.10. Creation of the Rb darkSPOT MOT. The repump light is split from the other two lasers by its orthogonal polarization and its main path is shown by the solid black line. Removing the beam block allows recirculation of the repump light, path shown in dashed-black line, for easy switching between dark and light MOTs. In the dark MOT path, there is a small circular beam block on a microscope slide that images a hole onto the MOT region in the horizontal plane (formed by MOT beams MOT_2 and MOT_3). There is no repump light in the vertical MOT beam (labeled MOT_1) in the dark MOT.

AOM before being coupled into a fiber. The main trapping laser is combined with the Rb lasers on a hot-cold mirror and coupled into a joint fiber to be sent to the experiment table. A summary of the Li MOT laser powers post fiber and detunings is provided in Table 2.1, and the typical MOT size is given in Table 2.2.

2.8 Cohabitation

Methods have been developed for implementing MOTs and are quite reliable at this point. More difficult are dual species MOTs. Rarely do both species need the same magnetic field gradient. We operate at a 11 G/cm field gradient which is in between the optimum for Rb and Li. Additionally, there are problems with interspecies collisions, and for our pair of species, the collisions almost always result in Li atoms being ejected from the trap because of the mass difference. To help alleviate this problem, we use a Rb darkSPOT MOT [52]. In this trap, the repump laser is blocked in the center of the MOTs. Fig. 2.10, shows how we accomplish this. We split the repump laser off with a PBS, expand it, and then pass it through a pair of microscope slides with small beam

	$\Gamma/(2\pi)$ (MHz)	I_{sat} (mW/cm^2)	Laser	Detuning (MHz)	Power (mW)
^{85}Rb	6.06	1.7	Cool	-19	100
			Repump	+13	12
^{7}Li	5.89	2.5	Cool	-24	38
			Repump	-9	7
			Slower	-80	25

Table 2.1.
Details of trapping lasers. More complete atomic data for Rb may be found in Ref. [45]. The $1/e^2$ radius of all the MOT trapping lasers is 22 mm and the radius of the Zeeman Slower laser is similar.

blocks on them. Finally, the repump is recombined with the two horizontal trapping beams. As a result, in the center of the MOT, there is no repump light and the atoms are quickly pumped into the F=2 dark state. Once in the F=2 state, the atoms no longer interact with the trapping laser and drift until they hit the repump shell. As a result, they spend much less time in the excited 5P state and on average have much lower energy when colliding with the Li atoms. The difference between the dark Rb MOT and the light Rb MOT produces nearly an order of magnitude change in the size of the Li MOT.

To measure and observe the MOTs, we have two tools at our disposal. The simplest tool is a CCD camera outside the vacuum chamber pointed at the MOTs. In the MOT, the atoms continually fluoresce on their D_2 lines. Thus, the camera can observe the spatial shape of the MOTs and get a rough estimate of the size. However, the camera cannot differentiate between the Rb and Li MOT. Our more sensitive detection method uses a pair of photodiodes. A 2 inch diameter, 5 cm focal length lens in front of the photodiodes, 13 inch from the MOTs, focuses the MOT fluorescence onto the photodiodes and a hot-cold mirror separates the light by species. The photodiodes allow us to measure the number of atoms in the MOTs to within a factor of two and we can combine the photodiode measurements with the camera measurements to estimate the MOT density. Our typical MOT sizes are listed in Table 2.2.

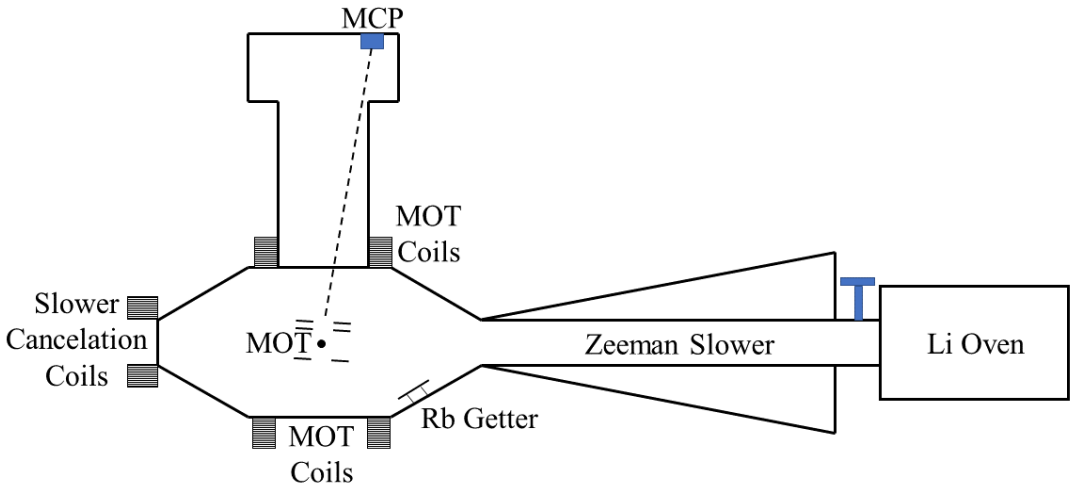

Fig. 2.11. Vacuum system cross-section.

2.9 Vacuum System

Our vacuum system is shown in Fig. 2.11. We have a 8 inch Kimble octagon with two 8 inch ports on top and bottom, six 2.75 inch windows and sixteen 1.33 inch windows. The windows are broad-band AR coated between 650-1100 nm by Abrisa technologies. There are two Varian starcell ion pumps that pump at 40 L/s to maintain a vacuum pressure of 10^{-10} Torr in the main chamber and 10^{-9} Torr in the Li oven.

On the main horizontal axis we have the Zeeman slower. We load the Li MOT from an atomic beam. The beam originates from an oven loaded with 10 g Li that is heated to over 400 C. The beam is formed by a pile of 0.8 mm diameter hypodermic needles and a valve separates the oven from the main chamber allowing us to turn on and off the atomic beam. We use the Zeeman slower to decelerate the atoms coming out of the oven which are too hot to be directly captured by the MOT. The slower is a half meter long cylinder, along which the Zeeman slower laser counter-propagates with the

	Number	Density (cm^{-3})	Temperature (μK)
^{85}Rb	10^6 - 10^8	5×10^9	100
^{7}Li	5×10^7	10^{10}	500

Table 2.2.
Typical MOT parameters.

atoms. Powerful spatially-varying magnets Zeeman shift the atomic levels into resonance with the laser as the atoms simultaneously propagate and slow down. The full details of the slower may be found in Ref. [53]. The Rb MOT is loaded from background vapor, provided by one of several Rb Getters from SAES, that boil off Rb atoms when a current is applied.

On the vertical axis of the vacuum chamber, we have a field free region for a time-of-flight spectrometer. As discussed in Chapter 3, our method for detecting molecules is to ionize them and count the ions. Around the MOT in Fig. 2.11, are the electric field plates that temporally focus the ions onto the micro-channel plate detector (MCP) which detects them. The bottom plate is biased at 400 V, the middle plate at 340 V and the top plate is grounded. The MCPs are at the top of the time-of-flight chamber off to the side to allow MOT beam access. In front of the MCP is a grounded screen to block unwanted ions. A -1900 V bias accelerates ions into the first MCP stack and then a -100 V bias accelerates the electrons off the first stack into the second stack. We record the signal off the back screen which is grounded and connected to a fast oscilloscope. Full details of the ion counting procedure may be found in Ref. [51].

3. SPECTROSCOPIC METHODS

Table 3.1 summarizes the spectroscopy that has been done on LiRb before this thesis. The work has been done primarily by two groups, ours and Tiemann's group at the University of Hannover. Under the direction of Dr. Tiemann, Ivanova *et al.* studied LiRb with Fourier transform spectroscopy in a heat pipe [54,58]. They mapped out most of the ground state, a few levels of the first triplet state and a small fraction of excited states. In our group, Dutta *et al.* studied low rotational states of the $B\ ^1\Pi$ [55]; Altaf *et al.* studied the top half of the $a\ ^3\Sigma^+$ potential and mapped out resonantly-enhanced-multi-photon-ionization (REMPI) transitions to the $f\ ^3\Pi$ state [56]; finally, Lorenz *et*

Electronic state	Vib. levels observed	Refs.	Atomic asymptote
$X\ ^1\Sigma^+$	0-45	[54, 55]	Li $2s\ ^2S+$
$a\ ^3\Sigma^+$	2-13*	[54, 56, 57]	Rb $5s\ ^2S$
$b\ ^3\Pi$	9-19	Chapter 6	
$A\ ^1\Sigma^+$	0-29	Chapter 6	Li $2s\ ^2S+$
$c\ ^3\Sigma^+$	-	-	Rb $5p\ ^2P$
$B\ ^1\Pi$	0-22	[55, 58, 59]	
$C\ ^1\Sigma^+$	7-13*, 26-44	Chapter 6	
$D\ ^1\Pi$	0-15	[58–60]	Li $2p\ ^2P+$
$d\ ^3\Pi$	0-22	Chapter 5	Rb $5s\ ^2S$
$f\ ^3\Pi$	0-10	[56]	Li $2s\ ^2S+$
$g\ ^3\Sigma^+$	0-5	[56]	Rb $4d\ ^2D$

Table 3.1.
List of low-lying states of LiRb that have been observed experimentally. Ranges of vibrational quantum numbers marked with an asterisk are not inclusive. Weakly-bound vibrational levels of many of these potentials used for photoassociation of ultracold LiRb molecules are not included.

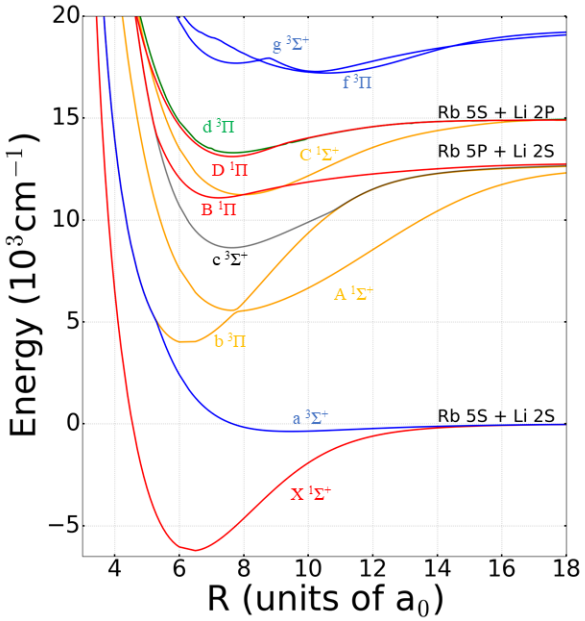

Fig. 3.1. Spectroscopy of LiRb. Curves in red ($X\ ^1\Sigma^+$, $B\ ^1\Pi$, and $D\ ^1\Pi$) are studied by Refs. [54, 58]; curves in blue ($a\ ^3\Sigma^+$, $f\ ^3\Pi$ and $g\ ^3\Sigma^+$) are studied by Ref. [56]; the curve in green ($d\ ^3\Pi$) is studied in Chapter 5; curves in orange ($b\ ^3\Pi$, $A\ ^1\Sigma^+$, and $C\ ^1\Sigma^+$) are studied in Chapter 6; finally, the curve in gray ($c\ ^3\Sigma^+$) has not been thoroughly studied.

al. discovered that we were unable to detect loosely bound singlet states with REMPI and confirmed assignments from Ivanova [59]. Fig. 3.1 shows a molecular energy level diagram highlighting these states.

When I inherited the LiRb experiment, we were producing LiRb molecules through photoassociation and detecting them through REMPI. We had detected 7 PA progressions below the Rb D_1 and D_2 atomic asymptotes and detected molecular formation in 3 of the progressions with REMPI. We saw that the molecules were produced in $X\ ^1\Sigma^+$ $v = 2 - 25$ [59] and in $a\ ^3\Sigma^+ v = 7 - 13$ [56]. For a primer on molecular notation and selection rules, see Appendix A. However, we had two primary problems: 1) we did not know the precise depth of the $X\ ^1\Sigma^+$ potential and 2) we did not have a method to detect weakly bound molecules in the $X\ ^1\Sigma^+$ potential. Additionally, as we started to solve some of these problems, we turned our attention to finding suitable intermediate states for STIRAP. These goals will guide our spectroscopic studies in the next couple of chapters.

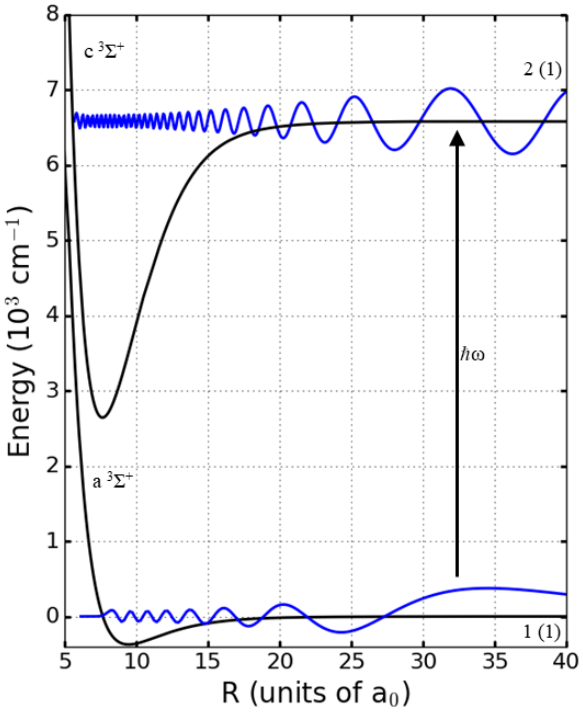

Fig. 3.2. Photoassociation in LiRb. y-axis is not to scale for better clarity. Blue traces are vibrational wavefunctions for the scattering state (bottom), and the least bound vibrational state (top).

Our method for spectroscopy is as follows. First, we load Li and Rb into a dual species MOT. Second, we make molecules with photoassociation followed by spontaneous decay. Third, we ionize the molecules with REMPI and count the ions. Finally, use PA, REMPI and depletion to study molecular transitions. In this chapter, I will review the steps in our spectroscopy, talk about how they work, discuss the driving lasers, explain the value of each method, and finally, present a quick PA experiment.

3.1 Photoassociation

PA is a purely quantum process by which the formation of a molecule is mediated by a photon. As shown in Fig. 3.2, PA happens when the scattering nuclear wavefunction, shown for the triplet ground potential well, has sufficient overlap with an excited state vibrational wavefunction and then, absorption of a photon resonant with the energy difference between the states can induce a transition to the excited state (provided this is allowed by the electronic selection rules). The excited state has a very short lifetime,

and will quickly decay, governed by its Franck-Condon factors (FCFs) and its overlap with scattering states, forming a spread of ground state molecules. The strength of a PA line is governed by a number of factors [61]:

$$R_{\mathrm{PA}} = \left(\frac{3\lambda_{\mathrm{th}}^2}{2\pi}\right)^{\frac{3}{2}} \frac{h}{2} n_A n_B A_\Omega |\langle \Psi_s | \vec{d} | \Psi_{\mathrm{PA}} \rangle|^2, \tag{3.1}$$

where λ_{th} is the thermal deBroglie wavelength, n_A and n_B are the density of the two atomic species, A_Ω is the angular factors and $|\langle \Psi_s | \vec{d} | \Psi_{\mathrm{PA}} \rangle|^2$ is the transition dipole moment between the states which can be separated into an electronic part and the FCF like overlap of the nuclear scattering wavefunction and the nuclear bound vibrational wavefunction. For a fixed density and excited state, the PA rate can be improved by increasing the overlap between the scattering wavefunction and the vibrational wavefunction (usually by picking a better excited state). However, the molecule production rate is

$$R_{v''} = \mathrm{FCF} \cdot R_{\mathrm{PA}}, \tag{3.2}$$

where FCF is the Franck - Condon Factors for decay to the desired state, v''. Usually states with better overlap with scattering wavefunctions have worse overlap with bound states leading to a trade off between PA rate and molecular production rate.

To drive PA, we primarily used a CW Ti:Sapphire laser. This laser produces up to 300 mW at 795 nm and is tunable between 735 - 905 nm, although its power decreases as we tune away from 795 nm. Based on Ref. [51], in which a previous student created a beat-note between the Ti:Sapphire and the frequency comb, we estimate the linewidth of the Ti:Sapphire to be 2-3 MHz, although it slowly drifts on the scale of a few MHz per minute. For some of our studies, we used a 795 nm ECDL for PA. This laser produced up to 100 mW of light and was much harder to tune compared to the Ti:Sapphire.

To use photoassociation as a spectroscopic tool is simple. PA measures excited state binding energies relative to the scattering continuum. Additionally, this can be combined with data linking those excited states to deeply bound ground states to measure the absolute binding energies of the ground states with high precision.

3.2 REMPI

To detect molecules formed by PA followed spontaneous decay to bound states, we turn to REMPI. REMPI is driven by a Nd:YAG-pumped pulsed dye laser. It is tunable between 550 - 583 nm (18150 - 17150 cm^{-1}) when loaded with the R590 dye, between 660 - 715 nm (15150 - 14000 cm^{-1}) when loaded with the LDS698, and between 710 - 750 nm (14100 - 13333 cm^{-1}) when loaded with the LDS750 dye. The repetition rate of this laser is 10 Hz, and it delivers $\sim$3 mJ/pulse to the MOT region in a 4 mm diameter beam (the LDS698 dye produces closer to 1 mJ/pulse and the LDS750 dye produces less). When one photon of this laser is resonant with a transition from an initial state (populated by spontaneous decay from the PA state) to an intermediate bound state (usually one of the vibrational levels of the $B\ ^1\Pi$, $D\ ^1\Pi$, $f\ ^3\Pi$, or $g\ ^3\Sigma^+$ electronic potentials), then the molecule may absorb two photons and ionize. We detect and count $LiRb^+$ ions using a time-of-flight spectrometer and a microchannel plate detector. To observe ions from deeply bound states or when using the redder dyes, we use a two-color variant of REMPI called RE2PI. In RE2PI we reduced the power of the dye laser pulse, and used the energetically higher photon from the 532 nm second-harmonic output of the Nd:YAG as the second photon.

Our detection method for all spectroscopy presented in this thesis is some form of REMPI. We use REMPI in large part because it is so sensitive. The number of molecules we detect is roughly

$$N = \tau \epsilon_d P_{\text{ion}} R_{v''}, \tag{3.3}$$

where τ = 14 (5) ms is the calculated transit time for the molecules after PA in the REMPI beam, $\epsilon_d = 0.5$ (0.3) is our estimate of the detector efficiency, P_{ion} is the measured probability of ionizing a given initial state. P_{ion} is a weak function of the REMPI pulse energy and gets as large as 0.5. Finally, $R_{v''}$ is the production rate of molecules in an initial state. For our set up, I estimate that we come close to detecting a quarter of the molecules we produce. In addition to being sensitive, the noise in our REMPI detection is very small. Our time-of-flight spectrometer separates $LiRb^+$ ions from Rb^+ ions by about 1 μs which results in a very small amount of Rb^+ ions in the $LiRb^+$ window. Additionally, I discovered that by keeping the Rb MOT small and the dye pulse energy low, I could get the $LiRb^+$ ions to outnumber the Rb^+ ions by more than a factor of ten.

My suspicion is that the primary cause of Rb^+ production is photo-dissociation of LiRb into Li and Rb^+, under these circumstances. But the end result is that our background ion count rate is less than 0.01 ions/shot while our on-resonance ion count can approach 10 ions/shot.

Because REMPI requires the first photon to be resonant with the transition between two bound states, it can be used to map out bound-to-bound transitions in the molecule. Additionally, because the pulsed dye laser is very tunable, we can quickly map out a large number of transitions by scanning the REMPI laser frequency.

3.3 Depletion Spectroscopy

We use a form of depletion spectroscopy to augment our REMPI studies. In this technique, we add a CW narrow-band depletion laser to the configuration. As previously demonstrated in Refs. [62, 63], the depletion laser reduces the REMPI ion count by resonantly transferring population from the initial state active in REMPI to other bound states. Our depletion laser is the CW Ti:Sapphire laser while the 795 ECDL takes over the PA role. We co-propagate the PA and depletion lasers, and then focus them to a spot size of about 200 μm in diameter at the center of the MOTs. Depletion spectroscopy has a high spectral resolution, limited primarily by the uncertainty of our wavemeter, 0.02 cm^{-1}.

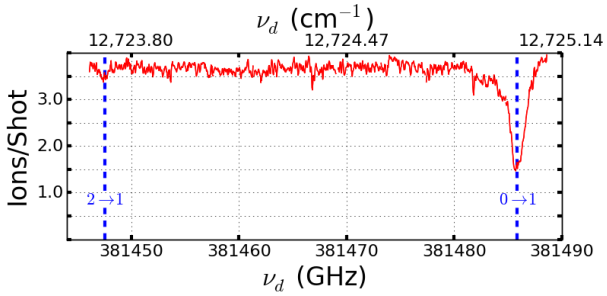

Fig. 3.3. Example of a depletion spectrum on the $v'' = 2$ state. For this spectrum, the REMPI laser was tuned to the $B\ ^1\Pi\ v' = 14 \leftarrow v'' = 2$ transition, the PA laser was locked to the 4(1) $v = -16\ J = 1$ line, and ν_d, the frequency of the depletion laser, was scanned. Labeling is $J'' \rightarrow J'$. Our observed $v'' = 2$ rotational constant, $B_{v''} = 6.38$ GHz, matches the previous measurement [55].

Besides shot noise in the ion count, two sources of uncertainty in depletion peak positions deserve mention: frequency drifts of both the PA laser and the REMPI laser. The PA laser frequency was maintained with an electronic lock. Our primary PA laser (for depletion) was a 795 nm ECDL locked to a low finese cavity. The cavity controlled for laser drifts on a time scale, but the cavity drifts slowly on the minute time scale because of thermal drifts in the lab. To compensate for this effect, we dithered the cavity at a few Hz with LabVIEW. Thus if the cavity drifted slightly above or below the PA frequency, LabVIEW could now see this effect in the ion count it was also monitoring, notice the direction to tune to get back on resonance thereby counteracting the slow drifts in the PA frequency. This homemade lock-in detection enabled us to stay on a PA resonance for hours at a time. Drift in the REMPI laser frequency was small, slow and nearly linear, so we were able to compensate in post-processing. Therefore, the primary limitation to the precision of these measurements was the shot noise in the signal.

Our goals for depletion spectroscopy are to help solve the weaknesses of REMPI spectroscopy. REMPI tends to produce dense spectra whereas depletion spectra can produce very clean spectra, as seen in Fig. 3.3. Additionally, REMPI is limited by the linewidth of the pulsed dye laser, which is fairly broad at 0.5 cm^{-1} whereas depletion spectra is limited by the linewidth of our wavemeter, 0.02 cm^{-1}. Because of the better resolution, we are able to get rotationally resolved spectra aiding in our understanding of the decay path after PA. Finally, the colors for the REMPI laser and the depletion laser are quite different, allowing us to study a different set of excited states.

3.4 Notation

As there will be many states and lasers involved in our spectroscopy, it is worth reviewing our state labeling scheme in this thesis. Our notation is as follows: v'' and J'' denote the vibrational and rotational levels of the $X\ ^1\Sigma^+$ and $a\ ^3\Sigma^+$ states, v and J denote the vibrational and rotational levels of the electronically excited states driven by PA resonances (and for these vibrational numbers, we count down from the asymptote using negative integers), and v' and J' denote vibrational and rotational labeling of other excited electronic states. Additionally, we use Hund's case (c) labeling for PA states and Hund's case (a) labeling for deeply bound states. The correspondence between the two

Hund's case (a)	Hund's case (c)	Atomic asymptote
$A\,^1\Sigma^+$	$2(0^+)$	Rb $5P_{1/2}$ + Li 2S
$c\,^3\Sigma^+$	$2(0^-)$	
	$2(1)$	
$b\,^3\Pi$	$3(0^+)$	Rb $5P_{3/2}$ + Li 2S
	$3(0^-)$	
	$3(1)$	
	$1(2)$	
$B\,^1\Pi$	$4(1)$	

Table 3.2.
Correspondence between Hund's cases (a) and (c) in LiRb. We use Hund's case (c) labeling for our PA states and Hund's case (a) for deeply bound state. Note that $B\,^1\Pi$ $v' = 20$ and $4(1)$ $v = -16$ denote the same state.

labeling schemes is shown in Table 3.2. The PA state that is central to much of this work has two equivalent notations: $4(1)$ $v = -16$ in Hund's case (c) notation and $B\,^1\Pi$ $v' = 20$ in Hund's case (a) notation. We will label this state using Hund's case (c) notation for consistency with the usual practice for long-range PA states although the state lives somewhere between the two Hund's cases.

3.5 Short Range PA

Our first project in photoassociation (though, the second chronologically), was aimed at exploring short-range photoassociation in LiRb. Normal, long-range PA works as indicated by Fig. 3.2, where wavefunction overlap of the excited state anti-node at the largest internuclear separation provides the transition strength. In short-range PA, the wavefunction overlap is provided by the ground state anti-node at the classical inner-turning point, as shown by the red arrow in Fig. 3.4. The downside to this approach is that the PA resonances will be an order of magnitude or two weaker, but the molecule production rate, especially in more deeply bound states can be equivalent to traditional PA resonances. This happens because molecule formation by PA is a two step process,

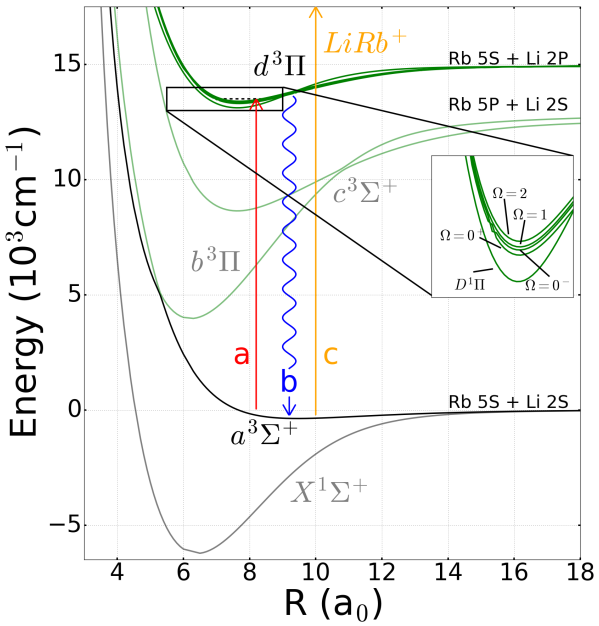

Fig. 3.4. LiRb potential energy curves for the lowest several bound states as calculated by Ref. [64]. **(a)** Short-range PA from the inner turning point of the $a\ ^3\Sigma^+$ potential to the bottom of the $d\ ^3\Pi$ potential. **(b)** Decay from excited state to $a\ ^3\Sigma^+$ bound states. **(c)** Molecule detection by REMPI through the $f\ ^3\Pi$ potential. **inset** Close up of the $d\ ^3\Pi$-$D\ ^1\Pi$ complex, revealing the different spin-orbit components as identified by Ref. [64].

PA to an excited state and then spontaneous decay to a deeply bound state, and while short-range PA pays a price in excited state formation rate, the excited states are much more likely to decay to bound states than to free atom pairs. Additionally, it is my operating theory that more deeply bound states are easier to detect with REMPI which further helps detect states populated by short-range PA.

The potential energy diagram for this experiment is shown in Fig. 3.4, and a sketch of the experiment is as follows. We fixed our REMPI laser to a known resonance, from Ref. [56], denoted in Fig. 3.4 by arrow **c** at frequency ν_c. Then we would scan the PA laser, denoted by arrow **a** at frequency ν_a, while recording the ion count. Shown in Fig. 3.5, is an example of a PA scan across a short-range PA resonance. In Fig. 3.5, we see the excitation of $d\ ^3\Pi_{0^\pm}\ v=0$ detected via the $f\ ^3\Pi\ v'=4\ \leftarrow a\ ^3\Sigma^+\ v''=7$ REMPI resonance [56]. There are several things of interest. First, because our MOTs have a minority population in Li F=1 and Rb F=3, we see an army of extra resonances, called hyperfine echos and denoted by an asterisk, that use the same excited state but different

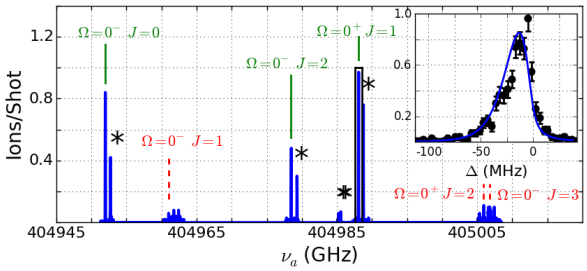

Fig. 3.5. PA scan across $d\ ^3\Pi$, $v = 0$, $\Omega = 0^{\pm}$, revealing rotational structure and a strong alternation of PA line strength, as detected by ionization. The REMPI laser was tuned to the $f\ ^3\Pi\ v'' = 4 \leftarrow a\ ^3\Sigma^+\ v'' =$ transition. ν_a is the frequency of the PA laser; $*$ denotes a hyperfine echo, from residual population originating in either Li $F = 1$ or Rb $F = 3$. Green solid lines and labels denote the strong PA resonances, along with our assignments; red dashed lines and labels identify the weak PA resonances. **inset** A closeup of the strongest PA resonance. Δ is the PA frequency relative to assigned line center; black dots are the raw data; blue solid line is the fit to Eq. (3.4).

scattering channels. Second, we see a very obvious alternation of the strength of the PA resonances by an order of magnitude as the excited J state changes. As can be seen in the literature, like Ref. [8,14,65], such a strong alternation of PA strength with changing rotational quantum number is uncommon.

After discovering that LiRb was a bit unusual, we sought to understand why. Our first step was to determine the dominant partial scattering waves (i.e. s-wave, or p-wave, or higher order partial waves). With help from our theory collaborator, Jesús Pérez-Ríos, we were able to turn a measurement of the collisional temperature into information about what partial waves contribute. We can measure the collisional temperature by fitting our PA lineshape [6] to

$$\sum_l \int_0^\infty e^{-\frac{h\nu}{k_B T}} \nu^{l+\frac{1}{2}} L_\Gamma(f, f_0 - \nu) d\nu, \tag{3.4}$$

where $L_\Gamma(f, f_0 - \nu)$ is a Lorentzian function centered at $f_0 - \nu$ and with linewidth Γ, and l is the angular momentum in the scattering channel. A careful scan across a PA resonance, along with the fit to Eq. (3.4), is shown in the inset to Fig. 3.5. We fit to Eq. (3.4) assuming s-wave scattering (a similar temperature was returned assuming p-wave scattering). The result is we extract $T_{LiRb} = 440(70)\ \mu$K, and Jesús's theory

predicts that at this temperature s-wave collisions dominate by a factor of 10 over p-wave collisions and even more significantly over higher-order partial waves.

At this point, we were left with a bit of a conundrum. The available theory on the $d\ ^3\Pi$ state from Ref. [64] predicts that the $\Omega = 0^+$ state will be lower in energy than the $\Omega = 0^-$ state. Consulting Fig. 3.6, which shows the parity of a $^3\Pi$ state, we see that the parity of the excited state alternates with rotational number. This matches what we see, except that the parities do not line up. If $\Omega = 0^+$ is the lower energy state, then for even parity $J = 0$ and $J = 2$ to be strong, it would require an odd parity scattering state, such as p-wave.

We are confident that our assignments of the J quantum number for these PA resonances are correct. Our assignment of the J quantum number allows us to extract a rotational constant, B_v, which matches the prediction from Ref. [64]. However, our other

v	Ω	$J = 0$	$J = 1$	$J = 2$	$J = 3$	B_v
0	0^-	404952.0	404961.0	404978.5	405006.8	4.5
0	0^+		404988.1	405005.9		4.5
0	1	–	406062.7	406080.6	406108.4	4.5
0	2	–	–	407067		
1	0^-	407918.6		407944.9		4.4
1	0^+		407952.0			
1	1	–	409037.4	409054.9		4.4

Table 3.3.
The frequencies for the observed $d\ ^3\Pi$ PA resonances in GHz. Uncertainties are ± 2 in the last digit recorded. Blank entries denote allowed transitions that did not appear in our spectra; solid horizontal lines denote forbidden transitions. The $v = 0$ splitting of the spin-orbit levels are 27.7, 1074.2, and 986.4, (all ± 0.3) GHz for $\Omega = 0^-/0^+$, $1/0^-$, and $2/1$, respectively, which differ significantly from their predicted values [64]. The J-dependent inversion symmetry for $\Omega \neq 0$ states was not resolved since the Λ doubling for the low lying rotational states accessed is small. The additional uncertainty for the $d\ ^3\Pi_2$ $J = 2$ line position is due to its significantly lower PA strength and its more complicated structure. The spin-orbit splittings and rotational constants are in agreement with our measurements using depletion spectroscopy, seen in Chapter. 5.

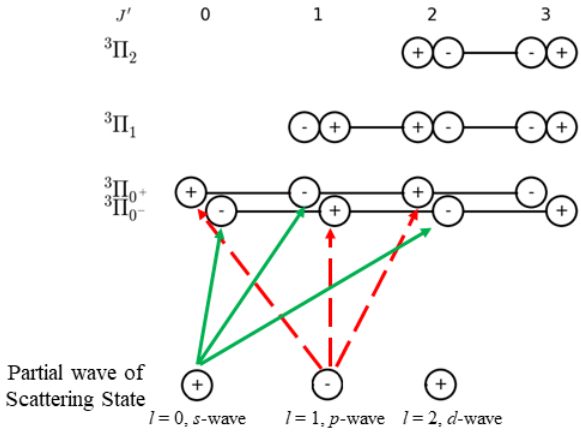

Fig. 3.6. Inversion parities for the partial waves of the scattering state and final d $^3\Pi_\Omega$ states, adapted and modified from Ref. [66]. The solid green and dashed red arrows correspond respectively to the alternating strong and weak dipole-allowed PA transitions to the d $^3\Pi_0$ manifold, shown in Fig. 3.5. The parity of every state or wave is shown as a plus or minus sign inside the circles. The transitions to $\Omega = 1$ or 2 states and the small energy splitting of the J states are not shown for clarity. Note that we can resolve the energy splitting between different parities for the $\Omega = 0^\pm$ states, but not for $\Omega = 1$ or 2 states.

spectroscopic data, like in Ref. [67, 68], do not support the conclusion that p-wave scattering is dominant, instead, like Jesús's theory, it supports s-wave scattering. At the end of the day, our conclusion, illustrated in Fig. 3.6, is that the prediction from Ref. [64] on Ω ordering is wrong: our data supports the conclusion that $\Omega = 0^-$ is lower energy than $\Omega = 0^+$.

In total, we found 15 new PA resonances, tabulated in Table 3.3, and contributed to evidence that short-range PA is fairly common for bi-alkali molecules. Additionally, we explored short-range PA as a method for producing ground state molecules. This work can be found in the thesis of David Blasing [69], who helped take the PA spectra shown here. At the start of this section we noted that PA in LiRb is a bit unique, and it is worth briefly discussing why. The collisional temperature for LiRb is quite a bit higher than other in other bi-alkalis, because Li MOTs are hotter than most other alkali MOTs. However, a quick comparison between the reduced mass of LiRb compared to other species like RbCs, quickly reveals that although LiRb is 5 times hotter, its reduced mass is 12 times lighter. The centrifugal barrier, which sets the dominant scattering

wave, is proportional to $\frac{1}{\mu}$, where μ is the reduced mass of the molecule. This makes LiRb effectively colder than its competitors. Thus, LiRb only has s-wave collisions contributing to PA, while in other seemingly colder species like RbCs, higher partial waves contribute to scattering.

4. 2(1) - 4(1) PHOTOASSOCIATION

For our second PA project, I worked on studying resonantly coupled PA states. Resonant coupling refers to the scenario where two states are mixed by an interaction internal to the molecular Hamiltonian, usually by the spin-orbit interaction in the heavier bialkalis. Although resonant-coupling is fairly common, mostly driven by the high density of states in molecules, exploiting it for PA is much harder. In other bi-alkali's, namely NaCs [14] and KRb [10], people have found that resonant coupling can be used to create high PA rates and to form deeply bound states after spontaneous decay. The simple picture of

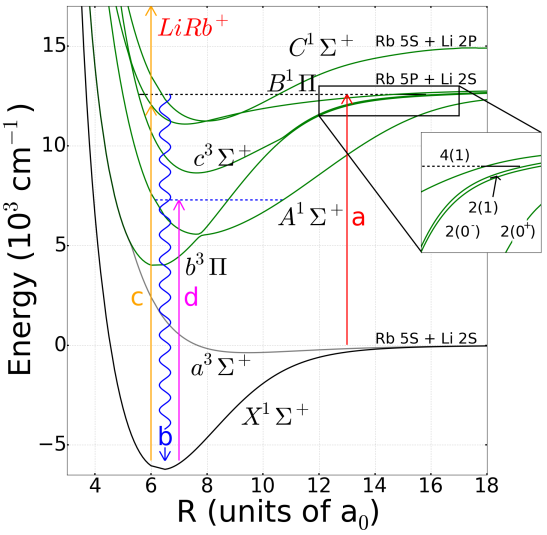

Fig. 4.1. Low-lying PEC diagram for the LiRb molecule from Ref. [64]. Vertical lines show various optical transitions, including **(a)** photoassociation of molecules below the Rb D_1 asymptote, at frequency ν_a; **(b)** spontaneous decay of excited state molecules leading to $X\ ^1\Sigma^+$ (and $a\ ^3\Sigma^+$); **(c)** REMPI or RE2PI to ionize LiRb molecules, at frequency ν_c; and **(d)** state-selective excitation to deplete the REMPI signal, at frequency ν_d. The black and blue dashed lines respectively represents our 2(1) - 4(1) mixed states and our depletion state. The inset shows an expanded view of the long-range potentials near the asymptote. Table 3.2 shows the correlation between long-range and short-range labeling.

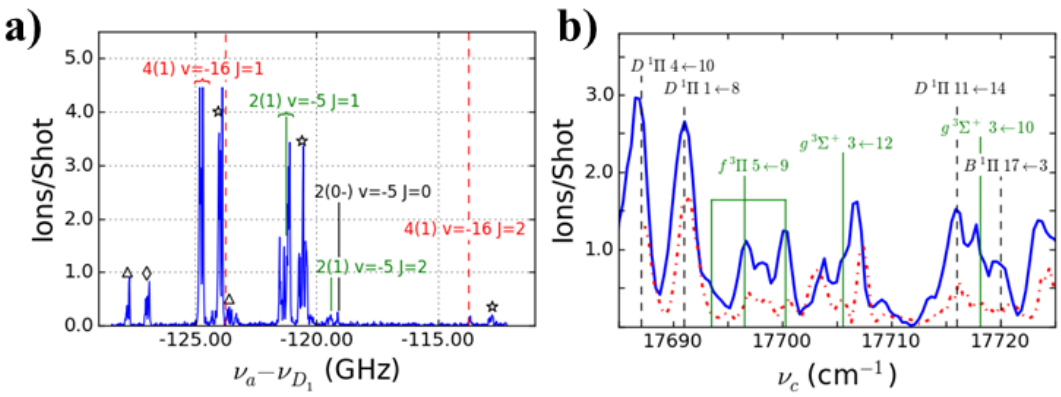

Fig. 4.2. Evidence of $2(1) - 4(1)$ mixing. **(a)** PA spectrum of the $2(1) - 4(1)$ mixed states. The REMPI laser frequency was held fixed at 17,686.8 cm^{-1} on the $D\ ^1\Pi\ v' = 4 \leftarrow v'' = 10$ transition. Hyperfine echoes are labeled by $\star$ for Li F=1, Rb F=2; $\triangle$ for Li F=2, Rb F=3; and $\diamond$ for Li F=1, Rb F=3. New 4(1) resonances as well as previously observed 2(1) and $2(0^-)$ are labeled [56]. Dashed lines show the expected rotational spacing of the 4(1) lines based on previous work [55]. **(b)** REMPI spectra from photoassociation through the 4(1) and 2(1) states; (blue solid) 4(1) $v = -16$ $J = 1$, (red dot-dashed) 2(1) $v = -5$ $J = 1$. The black dashed vertical lines represent transitions out of $X\ ^1\Sigma^+$ and the green solid vertical lines are transitions out of $a\ ^3\Sigma^+$; labeling is (excited state) $v' \leftarrow v''$.

how this works is as follows. There is a weakly bound excited state that is good for PA. This state is mixed by the spin-orbit interaction with an energetically close state that is deeply bound. The deeply bound excited state has good coupling to deeply bound ground states. Thus, we can get the best of both worlds, strong PA rate and strong decay to bound states all from one state, dodging the PA rate versus production rate trade-off most PA states suffer from.

4.1 Resonant Coupling

Pictured in Fig. 4.1 is a potential energy diagram for this study. We tune our PA laser, at frequency ν_a, below the Rb D_1 asymptote where the 2(1) PA progression will interact with the 4(1) progression. After decay to bound states, we fix our REMPI laser, at frequency ν_c, to detect PA, or we fix the PA laser and tune the REMPI laser to study

the decay products. Finally, our depletion laser, at frequency ν_d, helps probe rotational quantum numbers and detect weak REMPI lines.

In Fig. 4.2(a) we show the PA spectrum of the $2(1) - 4(1)$ mixed states near 122 GHz below the D_1 asymptote. For this spectrum the REMPI laser frequency, ν_c, was fixed on the $D\ ^1\Pi\ v' = 4 \leftarrow X\ ^1\Sigma^+\ v'' = 10$ transition [59] and the PA laser frequency, ν_a, was scanned. The $4(1)$ $v = -16$ $J = 1$ and $2(1)$ $v = -5$ $J = 1$ states in this spectrum are coupled, forming mixed states that possess characteristics of each, namely, the good photoassociation strength of a $2(1)$ state and the deep decay path of a $4(1)$ state. Coupling and mixing between vibrational levels of different electronic states can occur when states with the same rotational number J and angular momentum Ω lie close energetically [10,66]. Ω is the projection of the total angular momentum (excluding nuclear spin) onto the internuclear axis. Fig. 4.2(a) contains several hyperfine echoes, labeled with $\star$ for Li F=1, Rb F=2; $\triangle$ for Li F=2, Rb F=3; and $\diamond$ for Li F=1, Rb F=3. These are weaker PA lines that originate from population in our MOTs not in our main hyperfine component.

There are three features in Fig. 4.2 that provide evidence of resonant coupling of the $2(1)$ and $4(1)$ states.

(a) A $2(1)$ component is indicated by the large photoassociation amplitude of the $4(1)$ $v = -16$ state. We previously explored the $v = -3$, -4, and -5 lines of the $4(1)$ state [59], and found that the photoassociation amplitude for any vibrational levels more deeply bound than $v = -6$ had vanished. The enhanced photoassociation amplitude for $4(1)$ $v = -16$, with no visible photoassociation at $v = -15$ and $v = -17$, is an indication of mixing with a $2(1)$ state.

(b) The frequency spacing between the $J = 1$ and $J = 2$ lines of the $4(1)$ $v = -16$ state in Fig. 4.2(a) is increased by $\sim$1 GHz from the spacing expected based on earlier spectroscopy of LiRb [55] that studied highly excited rotational states of the $4(1)$ $v = -16$ manifold. We have marked the expected spacing between the $J = 1$ and 2 lines with vertical dashed red lines using $B_v = 2.503$ (0.001) GHz [55]. We expect the $J = 2$ state to be relatively unperturbed because it is much farther from the perturbing $2(1)$ state.

(c) Further evidence of $2(1) - 4(1)$ mixing is given in the REMPI spectra shown in Fig. 4.2(b). These provide an indirect measure of the relative spontaneous decay paths after photoassociation. We recorded these spectra by tuning the PA laser to the

4(1) $v = -16$ $J = 1$ line (blue solid spectrum) or the 2(1) $v = -5$ $J = 1$ (red dot-dashed spectrum). We have identified and labeled the lines in these spectra, and found population in vibrational levels of the $X\ ^1\Sigma^+$ and $a\ ^3\Sigma^+$ electronic potentials. Previously we observed that other 2(1) states decay only to $a\ ^3\Sigma^+$ states, while other 4(1) states decay solely to $X\ ^1\Sigma^+$ states [56, 59]. However, the 4(1) $v = -16$ $J = 1$ and the 2(1) $v = -5$ $J = 1$ states decay to both $X\ ^1\Sigma^+$ and $a\ ^3\Sigma^+$, providing further evidence of their coupling.

Our current and previous spectroscopy on 4(1) $v = -16$ state allows us to analyze two interesting spectroscopic quantities of LiRb. First, this leads us to a new, higher precision determination of the dissociation energy, D_e, of the $X\ ^1\Sigma^+$ potential. We use the transition frequency of the $B\ ^1\Pi\ v' = 20 \leftarrow X\ ^1\Sigma^+\ v'' = 0$ transition from Ref. [55], the PA frequency of the 4(1) $v = -16$ $J = 2$ peak in Fig. 4.2(a), measured to be 12575.21 (0.02) cm^{-1}, the rotational constant of the $B\ ^1\Pi\ v' = 20$ state also from Ref. [55], and the ground state molecular constants from Ref. [54]. This allows us to report a $X\ ^1\Sigma^+$ dissociation energy of 5928.08 (0.03) cm^{-1} relative to the ^{85}Rb 5s ^{2}S$_{1/2}$ F=2 + ^{7}Li 2s ^{2}S$_{1/2}$ F=1 asymptote. This determination agrees with, but is of much greater precision than, the previous value of 5927.9 (4.0) cm^{-1} [54].

We can also use this PA spectrum to estimate the admixture coefficients of the 2(1) − 4(1) $J = 1$ states. We write the mixed states $|\Psi_-\rangle$ (primarily 4(1) $J = 1$) and $|\Psi_+\rangle$ (primarily 2(1) $J = 1$) as

$$|\Psi_-\rangle = c|\Psi_{4(1)}\rangle - d|\Psi_{2(1)}\rangle, \text{ with energy } E_-, \tag{4.1}$$

and

$$|\Psi_+\rangle = d|\Psi_{4(1)}\rangle + c|\Psi_{2(1)}\rangle, \text{ with energy } E_+, \tag{4.2}$$

where $|\Psi_{4(1)}\rangle$ and $|\Psi_{2(1)}\rangle$ are the bare (unmixed) states with energies $E_{4(1)}$ and $E_{2(1)}$, respectively. We refer the reader to the treatment of resonantly coupled rotational states in Ref. [66]. We measure the frequency difference of the perturbed states to be $(E_+ - E_-)/h = 3.5$ (0.1) GHz, as shown in the PA spectra of Fig. 4.2(a). As discussed earlier, we know the size of the perturbation on the 4(1) state based on the deviation from the rotational constant for this state measured by Ref. [55]. Assuming an equal but opposite shift in the 2(1) energy, we find the energy difference of the unperturbed states to be $\delta = (E_{2(1)} - E_{4(1)})/h = 1.5$ (0.2) GHz. Following the treatment of Ref. [66], we can

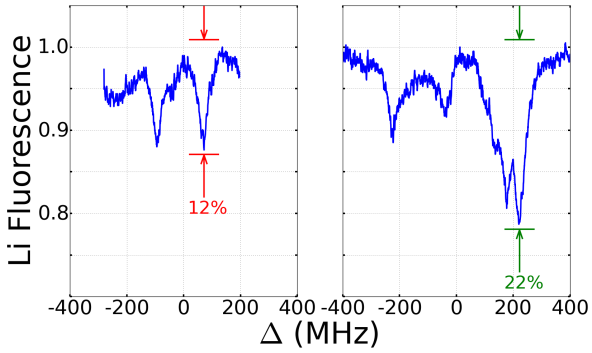

Fig. 4.3. Trap loss spectroscopy of 4(1) $v = -16$ $J = 1$ (left) and 2(1) $v = -5$ $J = 1$ (right) PA resonances. Detuning is relative to the assigned PA line center. Notice the relative strength favoring the 2(1) resonance, in contrast to the REMPI data in Fig. 4.2(a). More details on our trap loss experiments can be found in Ref. [70]. The structure in these spectra is caused by the hyperfine structure of the 4(1) and 2(1) states.

use the perturbed and unperturbed energy spacings to derive the coupling between the states, $V_{\rm int}$, by diagonalizing a simple 2x2 matrix,

$$\begin{vmatrix} E_{2(1)} - E & V_{\rm int} \\ V_{\rm int} & E_{4(1)} - E \end{vmatrix} = 0.$$

This will have solutions

$$E_{\pm} = \frac{1}{2}(E_{2(1)} + E_{4(1)}) \pm \frac{1}{2}\sqrt{4|V_{\rm int}|^2 + \delta^2}. \tag{4.3}$$

Re-solving this for the state coupling yields $V_{\rm int} = \frac{1}{2}\sqrt{(E_+ - E_-)^2 - \delta^2} = 1.6$ (0.2) GHz. Additionally we can find the eigenstates of our diagonalized matrix to find the admixture coefficients $|c| = 0.84$ (0.09) and $|d| = 0.53$ (0.05), consistent with our earlier assertion of strong mixing between the states.

4.2 Relative Decay Paths

To supplement the PA spectra discussed above, we have also observed the 4(1) − 2(1) $J = 1$ mixed resonance through trap loss measurements. We show these spectra in Fig. 4.3. In contrast to the REMPI signal, which indicates formation of a stable molecule in a specific vibrational level of the $X^1\Sigma^+$ or $a^3\Sigma^+$ state, a dip in the trap fluorescence signal results when the PA laser associates a molecule, regardless of whether

	$\frac{R_{CM}^-}{R_{CM}^+}$	$\frac{B^+(v'')}{B^-(v'')}$	$c^2\ \mathcal{R}^2(v'')$	$2cd\mathcal{R}(v'')$	$B^+(v'')$	$-2cd\mathcal{R}(v'')$	$B^-(v'')$
$X\ ^1\Sigma^+$ $v''=2$	2.5	4.6	-0.12	0.29	0.18	0.12	0.83
$a\ ^3\Sigma^+$ $v''=7$	1.5	2.8	-0.02	0.29	0.27	0.02	0.73
$X\ ^1\Sigma^+$ $v''=43$	2.2	4.0	-0.09	0.29	0.20	0.09	0.80

Table 4.1.
Enhancement of decay of $|\Psi_-\rangle$ across several vibrational levels. Note that $d^2\mathcal{R}(v'')$ is always negligible.

that molecule decays to a stable state or to a pair of free atoms. An interesting feature of these spectra is that the $|\psi_+\rangle$ PA resonance, whose primary constituent is the bare 2(1) $v=-5$ $J=1$ state, is stronger in trap loss (22% trap loss) than the $|\psi_-\rangle$ line (12% trap loss), while the $|\psi_-\rangle$ resonance is stronger than $|\psi_+\rangle$ in the REMPI spectra. In the following, we apply a simple model to characterize this.

Using the fractional losses of 22%, 12% and the lead of Ref. [70], we calculate that the PA rate to the 2(1) $v=-5$ $J=1$ state, $|\Psi_+\rangle$, is $R_{PA}^+ = 1.9\ (0.8)\times 10^6$ molecules/second and the PA rate to the 4(1) $v=-16$ $J=1$ state, $|\Psi_-\rangle$, is $R_{PA}^- = 1.1\ (0.5)\times 10^6$ molecules/second. The ratio of PA strengths, R_{PA}^+/R_{PA}^-, is 1.83 (0.15). (Most of the error in the individual PA rates is correlated, so the uncertainty in this relative measurement is much less than the quadrature sum of the individual uncertainties.)

We can calculate the PA rate using a quantum perturbative framework [61]

$$R_{PA} = \left(\frac{3\lambda_{th}^2}{2\pi}\right)^{\frac{3}{2}} \frac{h}{2} n_{Li} n_{Rb} A_\Omega |\langle \Psi_S | \vec{d} | \Psi_{PA}\rangle|^2. \tag{4.4}$$

In Eq. (4.4), $|\Psi_S\rangle$ is the scattering wavefunction, λ_{th} is the thermal de Broglie wavelength, n_{Li} and n_{Rb} are the atom densities and A_Ω are the radial factors for the two states and laser polarization. $|\Psi_{PA}\rangle$ is either $|\Psi_-\rangle$ or $|\Psi_+\rangle$, as given by Eqs. (4.1) or (4.2). Since none of the other nearby 4(1) vibrational levels have been observed in PA spectra, we assert that the cross section for PA to the deeply bound unperturbed $|\Psi_{4(1)}\rangle$ state is very

small. The other various factors in Eq. (4.4) are the same for $|\Psi_+\rangle$ and $|\Psi_-\rangle$, so the relative PA rates are related approximately through

$$\frac{R_{PA}^{+}}{R_{PA}^{-}} = \frac{|\langle\Psi_S|\vec{d}|\Psi_+\rangle|^2}{|\langle\Psi_S|\vec{d}|\Psi_-\rangle|^2} \simeq \frac{c^2|\langle\Psi_S|\vec{d}|\Psi_{2(1)}\rangle|^2}{d^2|\langle\Psi_S|\vec{d}|\Psi_{2(1)}\rangle|^2} \simeq \frac{c^2}{d^2} \tag{4.5}$$

Using $|c| = 0.84$ and $|d| = 0.53$ that we determined in Sec. 4.1, we estimate that the ratio of the trap loss peaks should be $\frac{c^2}{d^2} = 2.5$ (0.6), which is indeed consistent with our trap loss data.

We next examine the decay of excited state molecules to stable molecules, whose wavefunctions we designate $|\Psi_{v''}\rangle$. We write the decay strength as

$$\begin{aligned} B^+(v'') = |\langle\Psi_{v''}|\vec{d}|\Psi_+\rangle|^2 &= c^2|\langle\Psi_{v''}|\vec{d}|\Psi_{2(1)}\rangle|^2 \\ &+ 2cd|\langle\Psi_{2(1)}|\vec{d}|\Psi_{v''}\rangle\langle\Psi_{v''}|\vec{d}|\Psi_{4(1)}\rangle| + d^2|\langle\Psi_{v''}|\vec{d}|\Psi_{4(1)}\rangle|^2, \end{aligned} \tag{4.6}$$

and

$$\begin{aligned} B^-(v'') = |\langle\Psi_{v''}|\vec{d}|\Psi_-\rangle|^2 &= d^2|\langle\Psi_{v''}|\vec{d}|\Psi_{2(1)}\rangle|^2 \\ &- 2cd|\langle\Psi_{2(1)}|\vec{d}|\Psi_{v''}\rangle\langle\Psi_{v''}|\vec{d}|\Psi_{4(1)}\rangle| + c^2|\langle\Psi_{v''}|\vec{d}|\Psi_{4(1)}\rangle|^2, \end{aligned} \tag{4.7}$$

where $\langle\Psi_{v''}|\vec{d}|\Psi_{2(1)}\rangle$ and $\langle\Psi_{v''}|\vec{d}|\Psi_{4(1)}\rangle$ are the dipole transition matrix elements connecting the v'' vibrational state of $X\ ^1\Sigma^+$ or $a\ ^3\Sigma^+$ to the bare 2(1) $v = -5$ and 4(1) $v = -16$ states. Not shown in these equations are (1) an overall normalization factor, or (2) Hönl-London factors. The Hönl-London factors are based on the angular momenta of the excited and final states which are identical for the decay from the 2(1) state and the 4(1) state and will cancel in the ratio. The ratio of these decay strengths becomes

$$\frac{B^+(v'')}{B^-(v'')} \simeq \frac{c^2\ \mathcal{R}^2(v'') + 2cd\mathcal{R}(v'') + d^2}{d^2\ \mathcal{R}^2(v'') - 2cd\mathcal{R}(v'') + c^2}, \tag{4.8}$$

where $\mathcal{R}(v'') = \langle\Psi_{v''}|\vec{d}|\Psi_{2(1)}\rangle/\langle\Psi_{v''}|\vec{d}|\Psi_{4(1)}\rangle$ is the ratio of the dipole transition matrix elements.

We determine this ratio $B^+(v'')/B^-(v'')$ for individual final states from the REMPI and trap loss spectra, and give three examples in Table 4.1. R_{CM}^{-} and R_{CM}^{+} (column 2) are the cold molecule formation rates observed in REMPI in Fig. 4.2(a) when the PA laser is tuned to the $|\Psi^-\rangle$ or $|\Psi^+\rangle$ peak. There we observed that approximately twice as many molecules were formed in deeply bound singlet states when photoassociating

to $|\Psi_-\rangle$ compared to $|\Psi_+\rangle$ (this is difficult to see in Fig. 4.2(a) because of saturation effects). The cold molecule formation rate R_{CM} is related to the PA rate R_{PA} through $R_{CM} = R_{PA} \times B(v'')$. Using $R_{PA}^+/R_{PA}^- = 1.83$, as discussed above, we determined the relative decay strength $B^+(v'')/B^-(v'')$ for spontaneous decay to one of the vibrational states of $X\ ^1\Sigma^+$ or $a\ ^3\Sigma^+$ (column 3 in this table). We solve Eq. (4.8) for the ratio of transition moments $\mathcal{R}(v'')$, using $|c/d|^2 = 2.5$, and list these values in Table 4.1 as well. We show here only one of the solutions for $\mathcal{R}(v'')$. The other root is a value of order 2, which seems unreasonable since other unmixed 2(1) resonances lead to relatively small numbers of stable molecules.

Finally, we examine the decay strength $B^+(v'')$ and $B^-(v'')$, as computed using Eqs. (4.6) and (4.7). We show each of the terms within these equations individually in Table 4.1. Recall that we have omitted an overall normalization in these terms, as we are only examining their relative sizes. There are some notable features to these results. First, in any of the examples shown, for either of the PA resonances, the $|\langle\Psi_{v''}|\vec{d}|\Psi_{4(1)}\rangle|^2$ contribution is the most significant, while the $|\langle\Psi_{v''}|\vec{d}|\Psi_{2(1)}\rangle|^2$ contribution is insignificantly small. Second, the cross term $2cd\mathcal{R}(v'')$ makes a strong (secondary) contribution to each term. This cross term contribution is of opposite sign for the two PA resonances. That is, if it adds to the decay strength of the Ψ_- resonance, it diminishes the decay strength of the Ψ_+ resonance. Finally, observing the relative magnitudes of these terms, we note that the cross term is approximately half the magnitude of the strong $|\langle\Psi_{v''}|\vec{d}|\Psi_{4(1)}\rangle|^2$ contribution for the Ψ_+ resonance, strongly reducing this decay path. This is consistent with our observations, in which we note very low generation of $X\ ^1\Sigma^+$ or $a\ ^3\Sigma^+$ molecules when tuned to the $|\Psi_+\rangle$ PA peak.

A simple conceptual model that summarizes this analysis is thus. There is a fixed relative phase between the 4(1) and 2(1) vibrational wavefunctions that leads to constructive interference in the $|\Psi_-\rangle$ decay path and destructive interference in the $|\Psi_+\rangle$ decay path. A similar scenario was observed in NaK in coupled (3) $^3\Pi$ and (3) $^1\Pi$ states [71].

4.3 Decay from 4(1) PA resonance

At this point, we had accomplished one of our two large scale spectroscopic goals, by fixing the well depth of the $X\ ^1\Sigma^+$ potential to about 1 GHz uncertainty. Reviewing other

bi-alkali experiments that have observed 2(1) - 4(1) mixing in PA [10, 14], we discover that they were able to populate the ro-vibronic ground state directly via PA. We will make a brief diversion in the rest of this chapter to see if we populate and can detect ground state molecules as well.

We show in Fig. 4.4 the calculated Franck Condon factors for the spontaneous decay of the 4(1) $v = -16$ state to the various v'' levels of the $X^1\Sigma^+$ state. We calculated these FCFs using PECs from Ref. [54] and LEVEL 8.0 [72]. This plot suggests that the $v'' = 43$ level is the most highly populated, with a FCF of 0.35, and shows a secondary but still significant FCF of 0.13 for the $v'' = 42$ level. A broad pedestal of vibrational levels down to $v'' = 2$ is also populated to a lesser degree. Our observations here are in agreement with the calculated FCFs. We used a second dye, LDS 698 which lases from $14050-15050$ cm^{-1}, to study population in $v'' = 38-45$. We observed very strong population of $v'' = 43$ and to a lesser extent $v'' = 42$. Our RE2PI data on $v'' = 42$ and 43 will be presented in Chapter 6. Unfortunately, direct comparison of that data to the REMPI data presented in this chapter on deeply bound vibrational levels is difficult. The two different dyes have different powers and modeling RE2PI is very difficult (modeling REMPI isn't any easier). At this point in time, our best estimate for the production rate of $v'' = 43$ is $R_{v''=43} = R_{PA}^{-} FCF_{43}(1.15c^2) = 3 \times 10^5$ molecules/second. The factor 1.15 represents the enhancement factor for bound state decay discussed in Sec. 4.2. This production rate is

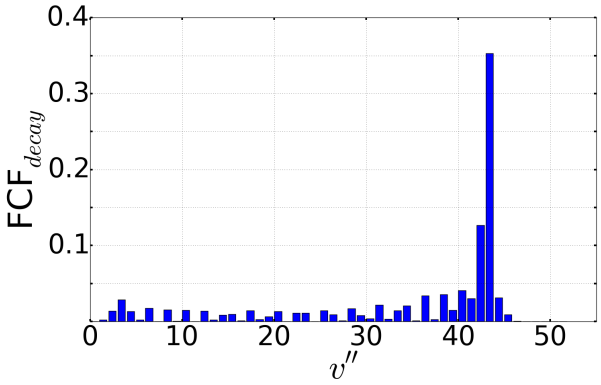

Fig. 4.4. Calculated Franck - Condon factors using PECs from Ref. [54] with assistance from LEVEL 8.0 [72] for the decay path from the PA state, 4(1) $v = -16$, to $X\ ^1\Sigma^+$ v''. Notice the maximum, $v'' = 43$.

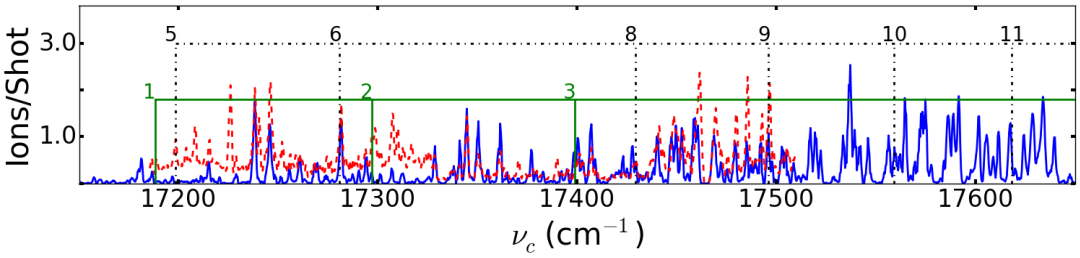

Fig. 4.5. REMPI (blue solid) and RE2PI (red dashed) scan, the PA laser was locked to the 4(1) $v = -16$ $J = 1$ line. Black numbers and dot-dashed lines label $B\ ^1\Pi$ $v' \leftarrow v'' = 2$ transitions while green numbers and solid lines label $B\ ^1\Pi$ $v' \leftarrow v'' = 0$ transitions. No transitions from $v'' = 43$ show up in our REMPI (or RE2PI) data taken with the R590 dye. All transitions observed can be assigned to $X\ ^1\Sigma^+$ $v'' = 0$ - 20 and $a\ ^3\Sigma^+$ $v'' = 6$ - 13. The RE2PI data is necessary because for deeply bound initial states ionization by REMPI is out of range energetically. For example, $v' = 1,\ 2,\ 3 \leftarrow v'' = 0$ and $v' = 5 \leftarrow v'' = 2$ on this plot would not be observable without RE2PI (even though there are nearby visible peaks in REMPI).

quite large and we expect that it could be increased further by increasing the PA power or MOT sizes.

To explore the deeply bound vibrational levels populated after PA through the 2(1) - 4(1) mixed states, we used REMPI and RE2PI with the R590 dye which lases from $17050 - 18150$ cm^{-1}. We show a typical REMPI scan in Fig. 4.5. In this spectrum, we scan ν_c, the REMPI or RE2PI laser frequency, with the PA laser locked to the 4(1) $v = -16$ $J = 1$ line. We have observed most of these REMPI lines previously in our studies of photoassociation through other vibrational lines of the 2(1) and 4(1) series [56, 59]. Our current focus is finding population of low-lying vibrational levels. For example, we have marked the series $B\ ^1\Pi$ $v' \leftarrow v'' = 2$ transitions with black dashed vertical lines in Fig. 4.5. The global maximum occurs at $v' = 14 \leftarrow v'' = 2$ (not shown). The progression provides strong evidence of population of the $v'' = 2$ vibrational state.

In contrast, population of the $v'' = 0$ vibrational state is difficult to observe in the RE2PI spectra of Fig. 4.5. The 4(1) $v = -16$ $J = 1$ state decays weakly to the ground vibrational state, predicted to be around 100 molecules/second, compared to other vibration levels such as $v'' = 2$, predicted to be around 2×10^4 molecules/second. Furthermore, the candidate lines in Fig. 4.5 that might originate from the $v'' = 0$ vibrational state,

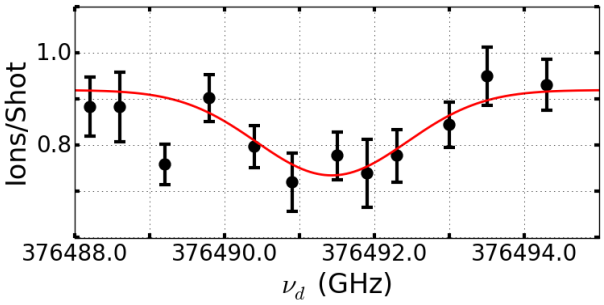

Fig. 4.6. Evidence of $X\ ^1\Sigma^+\ v''=0\ J''=0$ population. Depletion spectra of the $A\ ^1\Sigma^+\ v'=10\ J'=1 \leftarrow v''=0\ J''=0$ transition. The PA laser is locked to the 4(1) $v=-16\ J=1$ peak, the RE2PI laser was tuned to the $B\ ^1\Pi\ v'=3 \leftarrow v''=0$ transition shown in Fig. 4.5. Here we extract a depletion of 0.19 (0.04) ions/shot.

labeled by green solid lines, are obscured by nearby stronger lines. For example, the $B\ ^1\Pi\ v'=2 \leftarrow v''=0$ transition is much weaker than it looks on Fig. 4.5 because it is right next to a much stronger $v''=4$ RE2PI transition.

In order to identify these weak lines we have employed a form of depletion spectroscopy [63], in which we introduce a CW laser beam tuned to a $A\ ^1\Sigma^+\ v' \leftarrow X\ ^1\Sigma^+\ v''$ transition [73]. For these measurements, we use the 150 mW ECDL to photoassociate the molecules, and the more tunable Ti:Sapphire laser to drive the depletion transition. The PA and depletion beams copropagate, and are focused to a 200 μm diameter spot size in the MOT region. In Fig. 4.6, we show depletion of a $v''=0$ line. For this depletion spectrum, we tuned the RE2PI laser to the $B\ ^1\Pi\ v'=3 \leftarrow v''=0$ transition, and varied ν_d, the depletion laser frequency, through the $A\ ^1\Sigma^+\ v'=10,\ J'=1 \leftarrow v''=0,\ J''=0$ transition. Each data point is the average of 10 measurements of the total ion count accumulated over 100 laser pulses, and error bars show the 1σ standard deviation. We fitted our depletion data to a Lorentzian line shape with a commercial fitting program, extracting the height of the Lorenztian to be -0.19 (0.04) ions/shot. The data in Fig. 4.6 clearly shows population in the ground state $v''=0$ vibrational level.

We have two ways to estimate the $v''=0,\ J''=0$ production rate. First, we measured the PA rate and calculated the branching ratio. This gives us a $v''=0,\ J''=0$ production rate of 70 (50) molecules/second. Second, we measured the cold ion production rate in REMPI. To get the cold molecule production rate: $R_{CM}=\frac{N}{\tau\epsilon_d P_{ion}}$, we estimate τ, the

transit time in the REMPI beam, to be 14 (5) ms, ϵ_d, the detector efficiency, to be about 50 (20) % and P_{ion}, the ionization probability, to be about 5^{+45}_{-4} % which gives us a generation rate of 600 molecules/second. Due to the large uncertainties in τ, ϵ_d, and P_{ion}, the uncertainty of R_{CM} is comparable to its magnitude. While none of the quantities in this estimate are very exact, the uncertainty in P_{ion} dominates and could fall anywhere between 1 % and 50 %. Within the uncertainties, these two estimates of the production rate agree and we report the average, rounded to the nearest digit, 300 molecules/second.

5. SPECTROSCOPY OF THE $D\ ^3\Pi$ STATE

Now we will turn our attention to our second spectroscopy goal, to find suitable intermediate states for a stimulated Raman transfer (STIRAP) to $X\ ^1\Sigma^+\ v = 0,\ J = 0$ from $a\ ^3\Sigma^+\ v = 14,\ K = 0$ (the least bound triplet state). For efficient STIRAP, we need an excited state with three properties. First, it needs both singlet and triplet spin character. Second, the state needs to have a reasonable FC overlap with weakly bound triplet states and third, it needs reasonable overlap with deeply bound singlet states.

Before delving into our experiments, let us review how other teams have executed STIRAP in their bi-alkali experiments, as shown in Table 5.1. By far the most common singlet-triplet mixed state pair is $B\ ^1\Pi$ - $c\ ^3\Sigma^+$, which is the Hund's (a) labeling of the 2(1) - 4(1) interaction. However, as also seen in Table 5.1, this state pair would have a second photon around 550 nm. We would like to use two diode lasers for STIRAP and there are no diode lasers around 550 nm. Looking at the other possibilities, we have the $d\ ^3\Pi$ - $D\ ^1\Pi$ and $A\ ^1\Sigma^+$ - $b\ ^3\Pi_{0^+}$ state pairs. We will investigate the $d\ ^3\Pi$ - $D\ ^1\Pi$ state pair in this chapter and the $A\ ^1\Sigma^+$ - $b\ ^3\Pi_{0^+}$ state pair in Chapter 6.

State Pair	Previous Uses	Laser 1 (Diode?)	Laser 2 (Diode?)
$B\ ^1\Pi - c\ ^3\Sigma^+$	KRb [9], LiNa [28], NaRb [29], NaK [30]	543 - 585 nm (N)	795 - 850 nm (Y)
$A\ ^1\Sigma^+ - b\ ^3\Pi$	RbCs [31]	750 - 860 nm (Y)	1330 - 1720 nm (Y)
$d\ ^3\Pi - D\ ^1\Pi$		500 - 520 nm (Y)	700 - 740 nm (Y)

Table 5.1.
Summary of STIRAP pathways used in other molecules, along with the laser wavelength ranges required in LiRb and availability of laser diodes.

5.1 Spectroscopy details

We used two techniques, RE2PI and depletion spectroscopy, to measure the $d\ ^3\Pi$ bound states relative to $a\ ^3\Sigma^+$ $v = 13$ or $v = 11$. Ultimately, we combined the depletion data in this chapter, with the PA data from Chapter 3 to reference all of the states measured in this chapter to the scattering continuum. In RE2PI spectroscopy, we tune the PA laser to either the $v = -11$ or $v = -8$ lines of the $2(0^-)$ long range state, from which spontaneous decay leads primarily to the vibrational levels of the $a\ ^3\Sigma^+$ state [56]. We count the number of ions detected over the course of 100 laser pulses, and tune the laser frequency ν_c of the PDL in 0.35 cm^{-1} increments. We record the number of ions detected, normalized by the number of laser pulses, as a function of the PDL frequency ν_c.

In order to reach the full range of vibrational levels of the $d\ ^3\Pi$ states, we used two different laser dyes in the PDL. An LDS 698 dye covered the 13950 - 14950 cm^{-1} range, and an LDS 750 dye covered from 13300 to 13950 cm^{-1}. These dyes are difficult to work with because of short lifetimes and low power output. The LDS 750 dye in particular was very troublesome: it has a lifetime $\leq$8 hours, produces low power ($\leq$0.5 mJ/pulse for much of its range) and because it has a very broad pulse width (i.e. lots of spontaneous emission) the baseline noise of our RE2PI spectra is enhanced over what we have observed with other dyes.

The $2(0^-)$ $v = -11$ PA line at $\nu_a = 12516.89$ cm^{-1} is relatively weak, but it decays almost exclusively to a single vibrational level ($v'' = 11$) of the $a\ ^3\Sigma^+$ state. This facilitates straight-forward identification of the vibrational levels of the intermediate state. Unfortunately, several vibrational levels of the $d\ ^3\Pi$ state do not appear in this spectrum, presumably due to poor Franck-Condon overlap with the $v'' = 11$ state. This problem was even more evident when using the LDS 750 dye in the PDL. For this reason, we collected several RE2PI spectra using the stronger $2(0^-)$ $v = -8$ PA resonance $\nu_a = 12557.60$ cm^{-1}. This line decays to a wider spread of vibrational levels, giving more complete coverage of the vibrational lines of the $d\ ^3\Pi$ states, but also making our analysis more difficult, due to the increased congestion of the spectra and frequent overlap between individual lines.

To explore the deeply-bound levels of the $d\,^3\Pi$ states, we used a depletion spectroscopy technique. In these measurements, we used the 150 mW ECDL tuned to the $2(0^-)$ $v = -5$ PA resonance at $\nu_a = 12575.05$ cm^{-1} [56]. Spontaneous decay of this state populates the $a\,^3\Sigma^+$ $v'' = 13$ state. We tune the PDL laser frequency to the (3) $^3\Pi_0$ $v' = 6 \leftarrow a\,^3\Sigma^+$ $v'' = 13$ one-color resonantly-enhanced two-photon ionization (REMPI) transition at 17736.6 cm^{-1} [56]. We then tune the frequency of the Ti:Sapphire laser into resonance with bound-to-bound transitions from the $a\,^3\Sigma^+$ $v'' = 13$ state to ro-vibrational levels in the $d\,^3\Pi$ state. Exciting these transitions depletes the population of the $a\,^3\Sigma^+$ $v'' = 13$ state, causing the REMPI signal to decrease.

5.2 RE2PI Measurements

We show an example of a RE2PI spectrum in Fig. 5.1. Transitions observed in this spectrum are $d\,^3\Pi_\Omega$ $v' \leftarrow a\,^3\Sigma^+$ $v'' = 11$. We have marked the transitions to the $\Omega = 2$ progression with black solid lines, $\Omega = 1$ with blue dashed lines, and $\Omega = 0$ with green dot-dashed lines. Ω is the total electronic angular momentum, orbital L + spin S, projected onto the internuclear axis. The numerical label for each peak is the vibrational number v' of the $d\,^3\Pi_\Omega$ state. We have also marked three lines in this spectrum corresponding to transitions to the $D\,^1\Pi$ state with red dotted lines.

From the spectrum of these $d\,^3\Pi$ states, we observe the typical hierarchy of line spacings: the vibrational splitting is large (on the order of 100 cm^{-1} for low vibrational

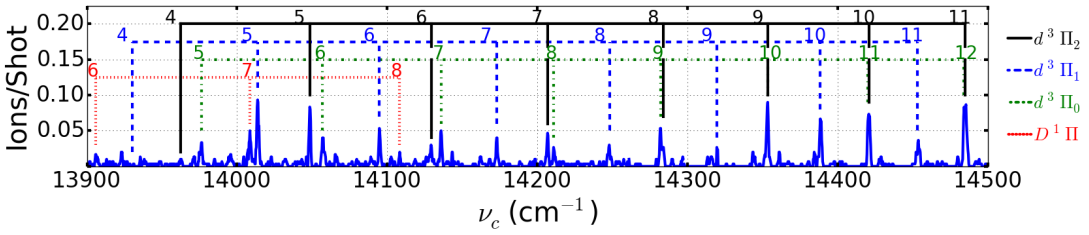

Fig. 5.1. Subsection of the RE2PI spectra. The PA laser is tuned to the $2(0^-)$ $v = -11$ resonance, from which spontaneous decay is primarily to the $a\,^3\Sigma^+$ $v'' = 11$ state. Most of these lines are $d\,^3\Pi_\Omega$ $v' \leftarrow a\,^3\Sigma^+$ $v'' = 11$ transitions, where v' is labeled on individual lines. From top to bottom: black solid lines label transitions to $\Omega = 2$, blue dashed lines label transitions to $\Omega = 1$, green dot-dashed lines label transitions to $\Omega = 0$. Also shown (red dotted lines) are three $D\,^1\Pi$ $v' \leftarrow a\,^3\Sigma^+$ $v'' = 11$ transitions.

quantum number v', and decreasing with increasing v'), and the spin-orbit splitting between different Ω states is smaller (on the order of 30 cm^{-1}). The rotational splitting for low J' (on the order of 0.1 cm^{-1}) is too small to be resolved in these RE2PI spectra since the spectral resolution of the PDL is $\sim$0.5 cm^{-1}.

The appearance of transitions belonging to vibrational levels of the $D\ ^1\Pi$ electronic state in Fig. 5.1 is evidence of mixing between the $D\ ^1\Pi$ and the $d\ ^3\Pi_1$ potentials near an avoided crossing between the two states. The energy of these $D\ ^1\Pi$ states is known from Refs. [51, 54]. State mixing gives these states partial character of each electronic state, which in this case manifests itself through strong transitions from a triplet state (i.e. $a\ ^3\Sigma^+\ v'' = 11$) to singlet states ($D\ ^1\Pi\ v' = 6$, 7, and 8). This state mixing also adds $D^1\Pi$ character to the $d\ ^3\Pi_1$ states, so one should expect the nearby $d\ ^3\Pi_1$ states to appear in the singlet spectra. This expectation is borne out in the spectrum shown in Fig. 5.2. This spectrum is a REMPI scan generated in our system after photoassociating ultracold LiRb molecules through a 2(1) - 4(1) mixed state at $\nu_a = 12574.85$ cm^{-1} [68], which spontaneously decays to vibrational levels of the $X\ ^1\Sigma^+$ ground electronic state. The spectrum in Fig. 5.2 primarily shows transitions to low-lying $D\ ^1\Pi$ vibrational levels from $X\ ^1\Sigma^+\ v'' = 10$. We also observe in this spectrum $d\ ^3\Pi_1\ v' = 4$, 5, and $6 \leftarrow X\ ^1\Sigma^+\ v'' = 10$ transitions. We chose $X\ ^1\Sigma^+\ v'' = 10$ because it is strongly populated by spontaneous decay of the 2(1) - 4(1) PA resonance and transitions to deeply bound $D\ ^1\Pi$ vibrational levels are clearly identified. We can estimate the degree of mixing based on the relative strength of the different REMPI peaks. The $D\ ^1\Pi\ v' = 7 \leftarrow X\ ^1\Sigma^+\ v'' = 10$ transition is twice as strong as the $d\ ^3\Pi_1\ v' = 5 \leftarrow X\ ^1\Sigma^+\ v'' = 10$ transition so there is twice as much singlet character to $D\ ^1\Pi\ v' = 7$ as $d\ ^3\Pi_1\ v' = 5$. Following the same procedure that we have used in the past [68], we can estimate the interaction strength to be about 7 cm^{-1}. Interestingly, this rough estimate is consistent with the following simple perturbative argument. The spin-orbit interaction responsible for the state mixing can be estimated as about one half the spin orbit mixing in atomic rubidium [74], or about 120 cm^{-1}. The Franck - Condon factor (FCF) between $D\ ^1\Pi\ v' = 7$ and $d\ ^3\Pi_1\ v' = 5$, as calculated by LEVEL 8.0 [72] using the PEC from [64], is about 0.08 and thus the strength of interaction between these states should be approximately 10 cm^{-1}. We have applied this perturbative analysis to each of the vibrational levels of the $d\ ^3\Pi_1$ state (not including $v' = 5$), and find that each contains some small component of $D\ ^1\Pi$ perturber state, on

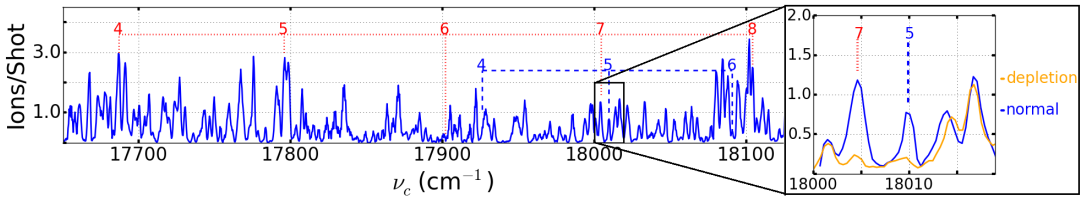

Fig. 5.2. Subsection of REMPI data with the PA laser tuned to the 4(1) $v = -16$ $J = 1$ resonance [68], while scanning the REMPI laser frequency, ν_c. Transitions are labeled as $d\ ^3\Pi_1\ v' \leftarrow X\ ^1\Sigma^+\ v'' = 10$ (blue dashed) and $D\ ^1\Pi\ v' \leftarrow X\ ^1\Sigma^+\ v'' = 10$ (red dotted). The inset shows confirmation of the assignments with depletion spectroscopy. The orange curve in the inset is the REMPI data retaken in the presence of a depletion laser tuned to the $A\ ^1\Sigma^+\ v' = 25\ J' = 1 \leftarrow X\ ^1\Sigma^+\ v'' = 10\ J'' = 0$ [73] transition; the reduction in peak height confirms the assignments. Because the depletion laser reduces the population available for REMPI in both peaks, they must have the same initial state, from which we conclude that we can access triplet REMPI resonances from singlet states.

the order of 10% or smaller. This is too small to be seen in the spectra of Fig. 5.1, but could be sufficient to be useful in a Raman or STIRAP transfer of population to low lying levels of the electronic ground state in the future.

Many of the RE2PI spectra that we collected are less clear than that shown in Fig. 5.1. In particular, the peaks in the RE2PI spectra near the Rb 5S + Li 2P asymptote are strong, but line congestion becomes significant, and clear identification of the lines in this region becomes difficult. These assignments could probably be improved using a spectroscopic technique that is capable of higher spectral resolution, such as photoassociative spectroscopy, but this was beyond the scope of the present work. Assigning peaks in the RE2PI spectra was equally difficult for deeply bound vibrational states (i.e. $v' \leq 4$). In fact we were unable to observe a clear cutoff in our RE2PI data corresponding to $v' = 0$. We attribute this to difficulties with the LDS 750 dye, specifically the large spontaneous emission content in the pulse. To rectify this problem, we turned to a second set of measurements, based upon depletion spectroscopy.

5.3 Finding $d\ ^3\Pi\ v = 0$

We used depletion spectroscopy to identify the lowest two vibrational levels of the $d\ ^3\Pi$ state. We show depletion spectra for $v' = 0$ in Fig. 5.3. To assign these data, care must be taken with selection rules for radiative transitions in molecules. The two that apply here are: $\Delta J = 0,\ \pm 1$ and $- \leftrightarrow +$, that is positive symmetry states (with respect

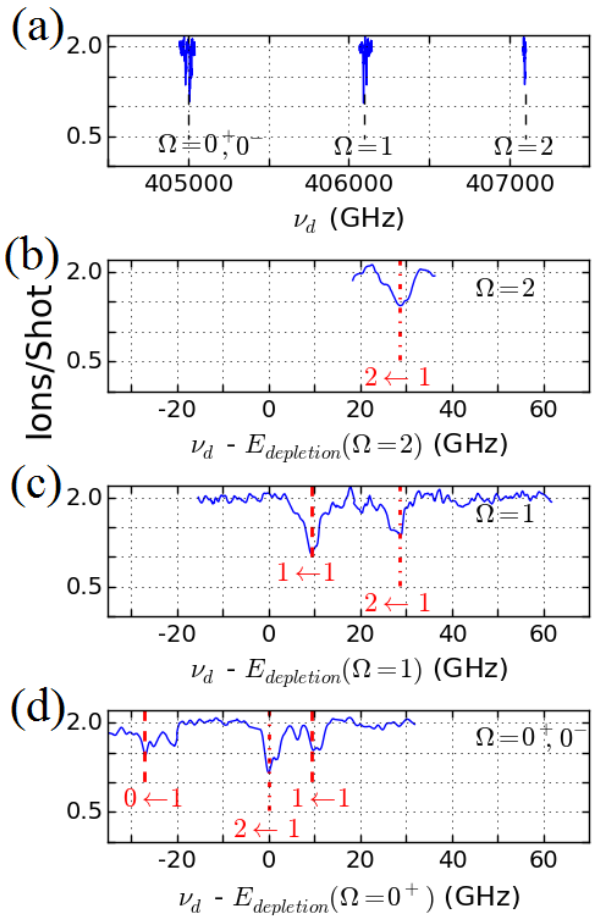

Fig. 5.3. Depletion spectra of an $a\ ^3\Sigma^+\ v'' = 13$ REMPI line using the $d\ ^3\Pi\ v' = 0$ state. The PA laser is locked to the $2(0^-)\ v = -5$ line, the REMPI laser is tuned to the $(3)\ ^3\Pi_0\ v' = 6 \leftarrow v'' = 13$ transition at $\nu_c = 17736.6\ \mathrm{cm}^{-1}$. Panel (a) shows a global view of our depletion data. Panels (b) - (d) show the rotational structure of the depletion lines. All repeatable transitions are labeled $J' \leftarrow J''$. For this $J'' = 1$ ground state, we assign it to the $K'' = 0$, even parity manifold. The abscissa of (b) - (d) is the depletion laser frequency offset by $E_{depletion} = T_{0,\ \Omega} - T_{13}$ where $T_{0,\ \Omega}$ is the rotationless energy of the $d\ ^3\Pi_\Omega\ v' = 0$ state, T_{13} and is the binding energy of the $a\ ^3\Sigma^+\ v'' = 13$ state, assuming $K'' = 0$ is the correct assignment.

	$d\ ^3\Pi_{0^-}$		$d\ ^3\Pi_{0^+}$		$d\ ^3\Pi_1$		$d\ ^3\Pi_2$	
v'	T_v	B_v	T_v	B_v	T_v	B_v	T_v	B_v
0	13507.9	0.148	13508.8		13544.7	0.153	13577.6	
1	13606.8	0.146	13607.6					

Table 5.2.
Experimental assignments for T_v, the rotationless energy, and B_v, the rotational constant, of the vibrational levels of the $d\ ^3\Pi$ state based on our depletion data for $v' = 0$ and 1. All numbers are in cm^{-1}. Uncertainty for all T_v is 0.5 cm^{-1}, and uncertainty in B_v is 0.005 cm^{-1}. Blank entries denote rotational constants or energies that we were not able to measure because of either the tuning range of our Ti:Sapphire laser or because of bound to bound selection rules limited by our PA state.

to coordinate inversion) must transition to negative symmetry states and vise versa. The initial state in this depletion transition is a $^3\Sigma^+$ state, which is a strict Hund's case (b) state. As such, its rotational energy is determined by quantum number K, which designates the total angular momentum of the molecule apart from spin, rather than the total angular momentum (including spin) quantum number J. For this $a^3\Sigma^+$state, the electronic spin is S=1, and levels with $J = K + 1, K$ and $K - 1$, are nearly degenerate for $K \geq 1$. Additionally K determines the symmetry of the state. This is summarized in Fig. 5.4, adapted and modified from Ref. [66].

The logic that leads to our assignments in Fig. 5.3 goes as follows. We start with the depletion data on transitions to $\Omega = 1$ shown in Fig. 4(c), which is extensive enough to show that (1) the spectrum contains only these two peaks; (2) these two peaks are the $J' = 1$ and 2 rotational states of $\Omega = 1$ (we return to this identification later in this paragraph); and (3) there is no peak corresponding to a transition to $J' = 3$. Since we do see transitions to $J' = 1$ and 2, we know that we populate some mix of $J'' = 0$ and 1 belonging to either $K'' = 0$, 1, or 2. The presence of only two peaks suggests that only *one* of these K'' levels is populated. We assign $K'' = 0$, based on (1) the expected dominance of the *s*-wave scattering state, (2) the clear population in even-symmetry ground states through two-photon couplings from the scattering state in other unrelated measurements in our laboratory [67, 68], and (3) the absence of any peaks for $J' > 2$.

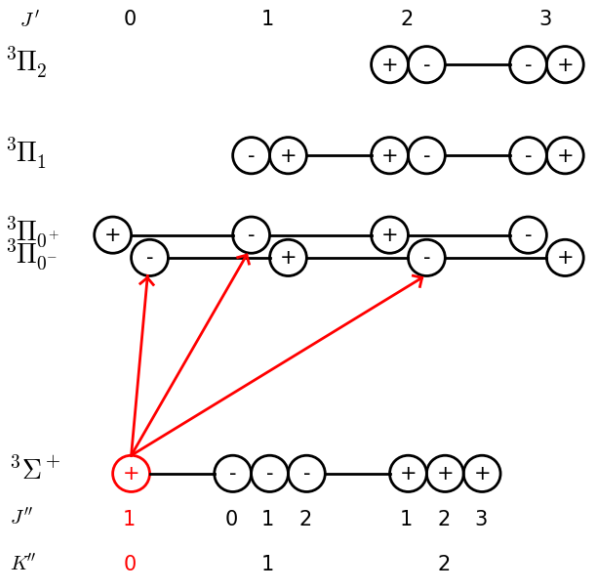

Fig. 5.4. Rotational structure and parity of $^3\Sigma^+$ and $^3\Pi$ vibrational states, the two states in red and green highlight the ground states we populate at the beginning of the depletion process. Transitions from the populated ground states to $^3\Pi_{0^+}$ and $^3\Pi_{0^-}$ are shown by arrows. Transitions to the positive symmetry levels of $^3\Pi_1$ and $^3\Pi_2$ do occur, but are omitted for clarity. The rotational splitting in $^3\Sigma^+$ is determined by $E = B_v K''(K''+1)$ (which makes the J manifold within each K'' state degenerate) and in $^3\Pi$ by $E = B_v[J(J+1) - \Omega^2]$. Adapted and modified from Ref. [66]

The spacing between the two peaks in this spectrum should be $4B_0$, where B_0 is the rotational constant of the $d\ ^3\Pi\ v' = 0$ state, allowing us to determine $B_0 = 4.59$ GHz. This rotational constant agrees with the prediction from LEVEL 8.0 with PECs from Ref. [64], which confirms our assignments of the $d\ ^3\Pi$ state and guides our interpretation of the $\Omega = 0$ data shown in Fig. 5.3(d), in which we see three transitions. The first two are spaced by $6B_0$ (27.5 GHz), implying that these peaks are transitions to the negative symmetry levels of the $\Omega = 0^-$ electronic state, $J' = 0 \leftarrow J'' = 1$ and $J' = 2 \leftarrow J'' = 1$. The absence of a peak for $J' = 1$ is consistent with the selection rule $+ \not\leftrightarrow +$. The remaining transition in $\Omega = 0$ must be the only allowed transition to $\Omega = 0^+$, that is $J' = 1 \leftarrow J'' = 1$. There is only one transition in $\Omega = 2$, which is trivial to identify as $J' = 2 \leftarrow J'' = 1$.

This assignment suggests that the previous assignment of rotational quantum number of the different vibrational levels of the $2(0^-)$ through which we photoassociate the

molecules is incorrect. In Ref. [56,70], we had tentatively identified these states as $J = 1$, which is an even parity state. In those works, however, we could observe only one rotational state, so that rotational assignment was weak. It now appears that odd parity $J = 0$ is a better assignment because we observe an even parity ground state, decay to which can only come from an odd parity PA state. The symmetry of the $J = 2$ rotational state is also odd, but we would expect $J = 2$ to lead to additional rotational structure in the present measurements.

While this interpretation of the depletion data presented here is consistent with other experimental data, it is not consistent with the available theory of the $d\ ^3\Pi$ state. The theory from Ref. [64] predicts $\Omega = 0^+$ should be lower in energy than $\Omega = 0^-$, while our interpretation of the data implies the opposite. One possible resolution to this problem is that we have incorrectly identified the ground state rotational level. If our ground state is $K'' = 1$ instead of $K'' = 0$, this would flip our $\Omega = 0^+,\ 0^-$ ordering. However, this would require that p-wave is the dominant scattering partial wave, a scenario unsupported by Refs. [67, 68] or the best available potential energy curves [54]. It is worth noting that in the $d\ ^3\Pi$ state in RbCs, a close analog, $\Omega = 0^-$ is lower in energy than $\Omega = 0^+$ [13]. Nevertheless, we find the poor agreement with theory unsettling.

We used these data to determine the spin-orbit splitting between the different Ω progressions deep in the $d\ ^3\Pi$ well, and followed these progressions back to the asymptote in our RE2PI data.

5.4 Discussion

We determine the vibrational binding energies and rotational constants of the states seen in depletion spectroscopy, which we tabulate in Table. 5.2. We list in Table 5.3 the assignments and energy of each of the $d\ ^3\Pi$ states that we observe through RE2PI and depletion spectroscopy. We also include in this table the energy difference between adjacent states, which aids in the assignment of the lines.

The theoretical vibrational levels and spin-orbit splittings that we used to guide our work and for comparison of results come from *ab initio* calculations by Korek et al. [64] with aid from LEVEL 8.0 [72]. We found good overall agreement with these *ab initio* results. The spin-orbit splittings for $\Omega = 0$ to $\Omega = 1$, predicted to be 21 cm^{-1}, are

	$d\ ^3\Pi_0$		$d\ ^3\Pi_1$		$d\ ^3\Pi_2$	
v'	T_v (cm^{-1})	ΔE (cm^{-1})	T_v (cm^{-1})	ΔE (cm^{-1})	T_v (cm^{-1})	ΔE (cm^{-1})
0	13508.2	98.8	13545.2	99.1	13578.1	99.3
1	13607.0	94.9	13644.3	95.4	13677.4	92.0
2	13701.9	94.8	13739.7	92.0	13769.4	96.0
3	13796.7	87.3	13831.7	89.6	13865.4	88.1
4	13883.9	83.8	13921.3	83.5	13953.5	86.1
5	13967.7	80.5	14004.8	81.2	14039.6	80.9
6	14048.2	79.0	14086.0	78.1	14120.5	77.5
7	14127.2	74.8	14164.1	75.1	14198.0	75.2
8	14202.0	71.2	14239.2	71.6	14273.2	71.5
9	14273.2	71.5	14310.8	68.7	14344.7	68.0
10	14344.7	66.3	14379.5	64.8	14412.5	64.1
11	14411.0	64.2	14444.3	65.2	14476.6	63.0
12	14475.2	62.1	14509.5	59.4	14539.6	58.8
13	14537.3	59.4	14568.9	56.9	14598.4	55.8
14	14596.7	55.1	14625.8	54.7	14654.2	51.4
15	14651.8	51.4	14680.5	51.4	14705.6	46.2
16	14703.2	47.6	14731.9	44.3	14751.4	43.4
17	14750.8	47.0	14776.2	40.1	14795.2	37.9
18	14797.8	45.9	14816.3	35.5	14833.1	32.5
19	14843.7	25.2	14851.8	24.4	14865.6	23.9
20	14868.9	21.3	14876.2	16.6	14889.5	8.7
21	14890.2	10.7	14892.8	6.9	14898.2	
22	14900.9		14899.7			

Table 5.3.

Experimental assignments for the rotationless energy of the vibrational levels of the $d\ ^3\Pi$ state based on our RE2PI data, aided by our depletion data for $v' = 0$ and 1. Uncertainty for all assignments is 0.5 cm^{-1}. We have referenced the term energies, T_v, to the Rb 5S + Li 2S asymptote.

measured here to be 37 cm^{-1}; for $\Omega = 1$ to $\Omega = 2$, they are predicted to be 38 cm^{-1}, and we found them to be 33 cm^{-1}. For the spin-orbit splitting between the $\Omega = 0^+$ to $\Omega = 0^-$ states, however, we observe -0.9 cm^{-1}, significantly less than the predicted 36 cm^{-1}. Our depletion data is unambiguous in establishing the $\Omega = 0^+$ to $\Omega = 0^-$ splitting, and a small $\Omega = 0^+$ to $\Omega = 0^-$ splitting is consistent with observations of similar states like the (3) $^3\Pi$ state in LiRb [56] and in KRb [75].

We show the vibrational spacing, $\Delta E = E_{v+1} - E_v$ vs v, of the different series in Fig. 5.5. These data are in reasonable agreement with the predicted vibrational splittings although there appears to be a nearly uniform difference of a few cm^{-1}. We found that the depth of the $d\ ^3\Pi$ potential (exp. value) is less than that predicted (th. value). We looked extensively for another vibrational level below our assigned $v' = 0$ level. We covered $\pm$ 10 cm^{-1} around the expected vibrational location with our depletion spectra, but found no indication of a depletion resonance. The calculated FCF for the $d\ ^3\Pi\ v' = 0 \leftarrow a\ ^3\Sigma^+\ v'' = 13$ transition is comparable to the FCF for the $d\ ^3\Pi\ v' = 1 \leftarrow a\ ^3\Sigma^+\ v'' = 13$ transition, which implies that if another vibrational level exists, we would have found it.

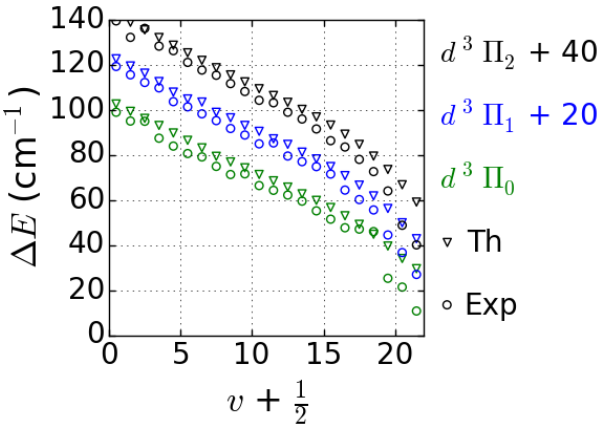

Fig. 5.5. Comparison of our extracted vibrational splitting to predicted vibrational splitting. The circles represent our data, while the triangles are predicted by *ab initio* curves [64]. Green markers label $\Omega = 0$ (compared to *ab initio* $\Omega = 0^+$) spacings. Blue markers are shifted by +20 cm^{-1} and label $\Omega = 1$ spacings. Black markers are shifted by +40 cm^{-1} and label $\Omega = 2$ spacings. We have shifted the $\Omega = 1$ and $\Omega = 2$ progressions (+20 cm^{-1} and +40 cm^{-1}) to make the different progressions more visible.

	$d\ ^3\Pi_0$		$d\ ^3\Pi_1$		$d\ ^3\Pi_2$	
	Exp.	Th.	Exp.	Th.	Exp.	Th.
T_e (cm^{-1})	13459.2 (1.5)	13300.7	13497.5 (2.0)	13359.9	13528.0 (1.4)	13398.2
ω_e (cm^{-1})	101.4 (0.7)	103.6	100.4 (0.9)	102.8	101.7 (0.6)	102.4
x_e (10^{-3})	16.7 (0.8)	13.1	15.0 (1.0)	12.7	15.8 (0.7)	12.5
y_e (10^{-3})	0.068 (0.028)	-0.06	-0.038 (0.033)	-0.10	-0.036 (0.026)	-0.12
B_e (cm^{-1})	0.148 (6)	0.159	0.153 (8)	0.159		0.159

Table 5.4.
Molecular vibrational constants fitted to our data, $T(v) = T_e + \omega_e(v + 1/2) - \omega_e x_e(v+1/2)^2 + \omega_e y_e(v+1/2)^3$ where $T(v)$ is the rotationless energy of the v^{th} vibrational level. Additionally, $B_v = B_e - \alpha_e(v + 1/2)$, where B_v is the rotational constant of the v^{th} vibrational level. We set the α_e term to 0 because we had so few measurements of B_v and it is usually much smaller than B_v; the uncertainty has been increased to account for this. The uncertainty is given in parentheses. The theory values are from fitting the bound states calculated by LEVEL 8.0 using PECs from Ref. [64]. When fitting the experimental data, we used only the v'=0-19 to increase the accuracy.

Our extracted molecular constants are listed in Tab. 5.4. These provide an easy estimation of the spectral structure of the $d\ ^3\Pi$ states as well as a quick comparison to theoretical predictions. As borne out in Fig. 5.5, there is good agreement between our fitted harmonic constant, ω_e, and the predictions. Additionally, there is good agreement between the rotational constants, B_e, extracted from the depletion spectra and the predictions. However, there is considerably less agreement between our extracted term energy, T_e, and the predictions for reasons discussed previously. Additionally, it is important to note that when we fitted the experimental data to determine T_e, ω_e, x_e and y_e we used only v'=0-19. This increased the accuracy of the fit so that for these vibrational levels our molecular constants reproduce our data with a standard deviation of 2 cm^{-1}. We believe most of the deviations are caused by experimental uncertainties on determining the frequencies of the peaks, as well as small perturbations to state locations caused by spin-orbit mixing.

6. SPECTROSCOPY OF THE $C\ ^1\Sigma^+$, STATE AND $A-B$ COMPLEX

Continuing with our plan of mapping out possible diode-laser accessible STIRAP pathways, we study the $A\ ^1\Sigma^+$ and $b\ ^3\Pi_{0^+}$ states in this chapter. However, we will first revisit our RE2PI data on $X\ ^1\Sigma^+\ v''=43$. For a potential energy diagram of this experiment, please consult Fig. 4.1.

6.1 $C\ ^1\Sigma^+$ State Spectroscopy

We make use of the population in the $v''=42$ and 43 levels of the $X\ ^1\Sigma^+$ state, formed by spontaneous decay after the PA step, to record the positions of the $v'=26-45$ vibrational lines of the $C\ ^1\Sigma^+$ state. To detect these molecules we use RE2PI with the LDS 698 dye in the dye laser, which ionizes the molecules through the loosely bound vibrational levels of the $C\ ^1\Sigma^+$ electronic state. Thus we are able to measure the energies of the vibrational levels of the $C\ ^1\Sigma^+$ state relative to $v''=42$ and 43.

As part of our work here, we measured the binding energies of $v''=42$ and $v''=43$ with the highest precision to date. In this project we measured the frequency of the depletion transition $B\ ^1\Pi\ v'=20 \leftarrow X\ ^1\Sigma^+\ v''=43$ to be 12711.71 (0.02) cm^{-1} [4(1) $v=-16$ is the Hund's case (c) labeling of the $B\ ^1\Pi\ v'=20$ state]. In Ref. [68], the binding

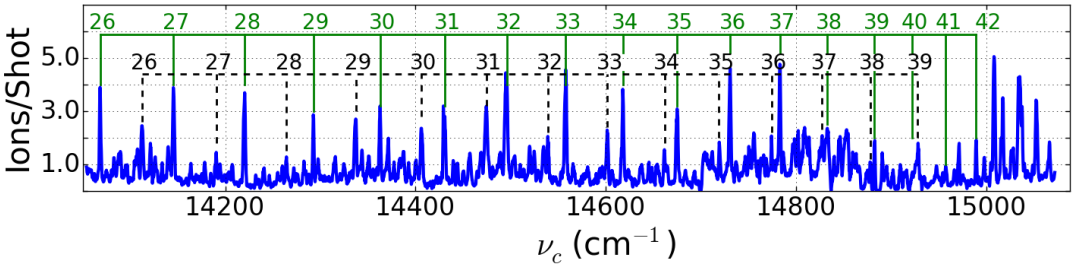

Fig. 6.1. RE2PI spectra from $v''=42$ and 43 to the $C\ ^1\Sigma^+$ electronic state. Green solid lines and numbers label transitions $C\ ^1\Sigma^+\ v' \leftarrow v''=43$; black dashed lines and numbers label transitions $C\ ^1\Sigma^+\ v' \leftarrow v''=42$.

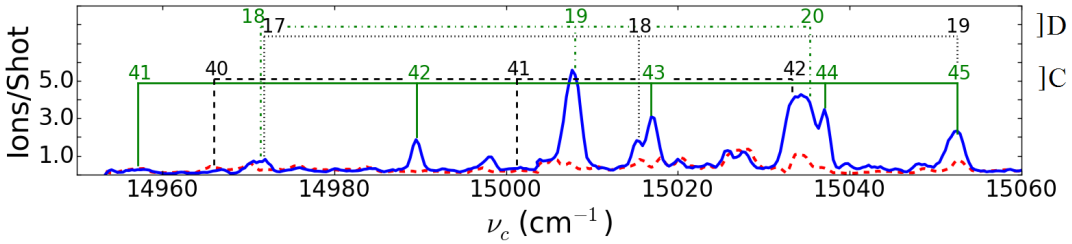

Fig. 6.2. Depletion spectroscopy of RE2PI data on transitions from $v'' = 42$ and 43 to the $C\ ^1\Sigma^+$ and $D\ ^1\Pi$ electronic states. For these data, the blue solid trace is the original data from Fig. 6.1, while the red dashed trace is the RE2PI data retaken in the presence of a depletion laser driving the $B\ ^1\Pi\ v' = 20 \leftarrow v'' = 43$ transition. Reduction of a peak height in the presence of the depletion laser indicates that the initial state is $v'' = 43$. Assignments of these lines are labeled as follows: green, solid lines, $C\ ^1\Sigma^+ \leftarrow v'' = 43$; black, dashed lines, $C\ ^1\Sigma^+ \leftarrow v'' = 42$; black, dotted lines, $D\ ^1\Pi \leftarrow v'' = 42$; green, dot-dashed lines, $D\ ^1\Pi \leftarrow v'' = 43$.

energy of 4(1) $v = -16$ $J = 1$ was measured to be 12574.85 (0.02) cm^{-1}; the difference between these two frequencies gives us the binding energy, $\nu_{43} = -136.86$ (0.02) cm^{-1}. This is in good agreement with, but of higher precision than, the prior measurements by Ref. [54, 55] which measured a binding energy of $\nu_{43} = -137$ (4) cm^{-1}. Additionally using our RE2PI spectra in Fig. 6.1, we extracted the energy difference between $v'' = 42$ and $v'' = 43$ to be 44.1 (0.1) cm^{-1}, which compares favorably to the more accurate energy difference from Ref. [54, 55], 44.04 cm^{-1}.

We show the RE2PI spectrum of $v' = 26$ - 42 of the $C\ ^1\Sigma^+$ state in Fig. 6.1. Two progressions dominate, one from $v'' = 42$ and the other from $v'' = 43$. They are spaced by 44.1 cm^{-1}, precisely the energy difference between $v'' = 42$ and 43 [55]. We have marked these series in Fig. 6.1 with black dashed lines and green solid lines, respectively. The integers indicate our assignments of the intermediate RE2PI state, which is a vibrational level v' of the $C\ ^1\Sigma^+$ state. The weak, unlabeled RE2PI lines in this spectrum originate from $v'' = 38 - 41$, which are also populated by the PA resonance we used. These qualitative features are consistent with the calculation of the FCF for the spontaneous decay from the PA state to $X\ ^1\Sigma^+$, which yields values for $v'' = 43$ and 42 (0.35 and 0.13, respectively) much greater than for any other vibrational level [68]. For frequencies significantly below the Rb 5S + Li 2P asymptote, the line density of the spectrum in

Fig. 6.1 is very low allowing us to measure the energies of $v' = 26 - 40$ twice, thus resulting in $0.5/\sqrt{2} = 0.3$ cm^{-1} precision of the mean.

As the $v'' = 43$ series converges on the Rb 5S + Li 2P asymptote, line congestion increases. This occurs near $\nu_c = \nu_{D_1} + |\nu_{43}| \simeq 15050$ cm^{-1}, where $\nu_{D_1} = 14904$ cm^{-1} is the frequency of the atomic Li D_1 line. To assign these peaks we used depletion spectroscopy to identify sets of RE2PI peaks that share a common initial state, as shown in Fig. 6.2. For these data, the blue solid trace is the original data from Fig. 6.1, while the red dashed trace is the RE2PI data retaken in the presence of a depletion laser driving the $B\ ^1\Pi\ v' = 20 \leftarrow v'' = 43$ transition. The peaks originating from $v'' = 43$ (marked by the green solid and green dot-dashed lines in Fig. 6.2) largely vanish upon introduction of the depletion laser. Careful inspection of Fig. 6.2 shows that all the strong peaks disappear after we introduce the depletion laser; this is consistent with the picture told by FCFs, that is there is three times more population in $v'' = 43$ than in $v'' = 42$. The peak for the $C\ ^1\Sigma^+\ v' = 45 \leftarrow v'' = 43$ is tentative, since the energy of this peak is above the asymptote. Still, we note that the peak is strongly depleted by the depletion laser, the spacing is about right for this progression, and the long range-potential for the $C\ ^1\Sigma^+$ PEC is expected to be repulsive [64], that is $C_6 > 0$, which could lead to a quasi-bound state above the asymptote. The $D\ ^1\Pi$ potential from Ref. [58] provides a good guide in this region, with an average uncertainty of 2.5 cm^{-1}, which allows us to identify candidate lines for transitions to the $C\ ^1\Sigma^+$ state. The unassigned lines in Fig. 6.2 most likely result from transitions $D\ ^1\Pi\ v' = 18 - 20 \leftarrow v'' = 38 - 41$; these initial states are weakly populated by the PA resonance, and the calculated FCFs for these lines are strong.

For $v' < 13$, we used the R590 dye in the pulsed dye laser, and excited from the $v'' = 2$ or 3 level of the ground state. Otherwise, the measurements were similar to those described above. The density of lines in these spectra was great enough to require depletion spectroscopy to make line assignments with confidence. Table 6.1 contains a summary of our observed energies of the $v' = 7,\ 9,\ 12,\ 13$ and $26 - 45$ vibrational levels of the $C\ ^1\Sigma^+$ state.

There have been no previous direct observations of the $C\ ^1\Sigma^+\ v'$ states. In Ref. [58], the authors observed perturbations to the rotational lines of the $B\ ^1\Pi \leftarrow X\ ^1\Sigma^+$ spectrum, from which they extracted the binding energies of $C\ ^1\Sigma^+\ v' \simeq 0 - 13$, and calculated

v'	T_v (cm^{-1})	ΔE (cm^{-1})	v'	T_v (cm^{-1})	ΔE (cm^{-1})
7	12131.2		33	14420.6	60.0
9	12344.2		34	14480.6	57.3
12	12655.8	102.4	35	14537.9	55.5
13	12758.2		36	14593.4	52.6
			37	14646.0	50.0
26	13931.3	77.6	38	14696.0	49.9
27	14008.9	74.4	39	14745.9	44.9
28	14083.2	72.5	40	14784.9	38.9
29	14155.7	69.5	41	14820.1	32.0
30	14225.3	68.3	42	14852.1	27.8
31	14293.6	64.8	43	14879.9	20.2
32	14358.4	62.3	44	14900.1	15.4
			45	14915.5	

Table 6.1.
Measured vibrational energies of the $C\ ^1\Sigma^+$ electronic state. The uncertainty in T_v is 0.5 cm^{-1} for $v' = 7-13$ and $40-45$ and is 0.3 cm^{-1} for $v' = 26-40$. The vibrational numbering was chosen to smoothly connect to the deeply bound vibrational levels measured in Ref. [58]. Energies are referenced to the Rb 5S + Li 2S atomic asymptote.

a $C\ ^1\Sigma^+$ PEC. We see good agreement with the PEC of Ref. [58] for $v' < 13$. We fitted the $C\ ^1\Sigma^+$ $v' = 7-40$ line positions listed in Table 6.1 to

$$\begin{aligned} T(v) &= T_e + \omega_e(v+1/2) \\ &\quad -\omega_e x_e(v+1/2)^2 + \omega_e y_e(v+1/2)^3, \end{aligned} \tag{6.1}$$

and extracted both the term energy T_e and the vibrational constants, and made a smooth connection across the gap from $v' = 13-26$, which lead to the vibrational numbering we report. The energies of states $v' = 41-45$ do not fit Eq. (6.1) well and were omitted from the fit. We present the term energy and molecular constants in Table 6.2.

Recalling from our list of unknowns and goals at the start of Chapter 3, we notice that this is the first observation of any weakly bound $X\ ^1\Sigma^+$ v'' levels with REMPI.

Further, this observation demonstrates why earlier efforts failed: FCFs. The FCFs for the $C\ ^1\Sigma^+ \leftarrow X\ ^1\Sigma^+$ transition get large starting around $v'' = 45$ and for other states that could be accessed by the R590 dye, like (4) $^1\Sigma^+$, the FCFs are orders of magnitude worse.

6.2 $A\ ^1\Sigma^+$ - $b\ ^3\Pi_{0^+}$ Spectroscopy

In this section, we discuss a set of measurements in which we use depletion spectra to identify new excited states. This is in contrast to the previous section where we used depletion spectra only to identify common initial states. In total we deplete two REMPI transitions exciting deeply bound $X\ ^1\Sigma^+$ ground states to the $A\,^1\Sigma^+$ $v' = 0 - 29$ and the $b\,^3\Pi_{0^+}$ $v' = 8 - 18$ levels. For $A\,^1\Sigma^+$ $v' = 19 - 29$ states, we used $v'' = 10$ as the initial state for depletion, and tuned the REMPI laser to the $D\ ^1\Pi$ $v' = 4 \leftarrow v'' = 10$ transition. For $A\,^1\Sigma^+$ $v' = 0 - 18$ and $b\,^3\Pi_{0^+}$ $v' = 8 - 18$ states, we used $v'' = 2$ as the initial state, and tuned the REMPI laser to the $B\ ^1\Pi$ $v' = 14 \leftarrow v'' = 2$ transition. We were unable to

	$C\ ^1\Sigma^+$		
	Exp.	Exp. [58]	Th. [64]
ω_e (cm^{-1})	115.4 (0.9)	113.8 (0.2)	113.4
$x_e \times 10^3$	3.1 (0.4)		2.3
$y_e \times 10^6$	-78 (5)		-87
T_e (cm^{-1})	11288 (13)	11302 (4)	11237.4

Table 6.2.
Molecular constants fitted to our data, compared to fits of other experiments [58] or to theoretical predictions from *ab initio* calculations from Refs. [76] and [64]. The state energies are given by Eq. (6.1). For fitting $C\ ^1\Sigma^+$ we omitted $v' = 41 - 45$ because the energies of these states fall outside the range over which Eq. (6.1) is valid. When fitting $b\ ^3\Pi_{0^+}$, the vibrational numbering is uncertain since we have not observed $v' < 8$. We chose vibrational numbering to force a well depth between the two *ab initio* predictions. Additionally, we omitted $v' = 10$, 12, 14 and 16 from the fit because these levels are strongly perturbed, as shown in Fig. 6.3(b). For these data, a value of y_e is not significant and not included in the table.

search for $v' < 8$ of the $b^3\Pi_{0^+}$, which fall outside the tuning range of our Ti:Sapphire laser. The $A^1\Sigma^+$ and $b^3\Pi_{0^+}$ series are readily distinguishable since the $A^1\Sigma^+$ lines are extremely power broadened. (For example, the linewidth of $A\ ^1\Sigma^+\ v' = 2 \leftarrow v'' = 2$ transition was well in excess of 30 GHz for a depletion laser power of $\sim$ 100 mW.) In fact, their width greatly facilitated their search, with guidance from the *ab initio* calculations of Ref. [64]. Such broad linewidths of the peaks allowed us to increment the depletion laser frequency in 10 GHz steps when searching for resonances. Then, we made low intensity measurements of the line positions to remove any line shifts caused by saturation effects. We tabulate the energies of the $A\ ^1\Sigma^+\ v'\ J' = 1$ states in Table 6.3, and the energies of the $b^3\Pi_{0^+}\ v'\ J' = 1$ states in Table 6.4.

The population distribution of the initial states limits excited states accessible with the depletion laser. Since the ground state molecules are mostly in the $J'' = 0$ rotational state [68], selection rules allow optical transitions to $J' = 1$ rotational states. Transitions from $J'' = 2 \rightarrow J'$ =1 or 3 are barely detectable above the shot noise level, so we are unable to determine the rotational constants of the excited state. Additionally we are limited by the spin of our molecules starting in the $X\ ^1\Sigma^+$ state. For transitions to $b\ ^3\Pi_\Omega$, where $\Omega = 0^+$, 0^-, 1, and 2, only $\Omega = 0^+$ peaks appear in the spectra, borrowing strength from the nearby $A\ ^1\Sigma^+$ vibrational levels. Ω is the projection of the total electronic angular momentum (orbital plus spin) onto the internuclear axis. Transitions to $\Omega = 0^-$ or 2 are not allowed. Transitions to $\Omega = 1$ are possible due to second-order spin-orbit mixing with mixed $A\ ^1\Sigma^+ - b\ ^3\Pi_{0^+}$ states, but they are too weak to observe.

In Fig. 6.3, we show the experimental and theoretical [64] energy spacing between the vibrational lines of (a) the $A\ ^1\Sigma^+$ series and (b) the $b\ ^3\Pi_{0^+}$ series. In this figure, red triangles are the experimental data, blue circles are the theoretical data, vertical black dashed lines guide the eye between the two datasets and dashed red lines are the prediction from the molecular constants presented in Table 6.6. In order to determine these points, we first converted the potential energy curves of Ref. [64] from adiabatic to diabatic, and then used LEVEL 8.0 [72] to calculate the positions of the $J' = 1$ eigenstate of the different vibrational levels. The vibrational line spacings of the $A\ ^1\Sigma^+$ state that we observe show a smooth, gradual decrease for high vibrational states ($v' > 20$), as expected. For lower vibrational numbers, however, there are large shifts in several of the lines, and moderate shifts in others. For example, the energy of $v' = 2$ line is shifted

up by ∼10 cm^{-1} above the general trend; in Fig. 6.3(a) this appears as $T_{v'=2} - T_{v'=1}$ is too large by nearly 10 cm^{-1} while $T_{v'=3} - T_{v'=2}$ is too small by 10 cm^{-1}. Shifts of nearby vibrational lines, $v' = 10$ and 12, of the $b\ ^3\Pi_{0^+}$ state in the opposite direction suggest strong mixing between the $A\ ^1\Sigma^+$ and $b^3\Pi_{0^+}$ state through spin-orbit interactions. These perturbations recur over a rather large range of levels due to near coincidence between three times the vibrational spacing of the $A\ ^1\Sigma^+$ state with two times the vibrational spacing of the $b\ ^3\Pi_{0^+}$ state. We will discuss these perturbations in more detail in the next section. If we remove the most strongly perturbed vibrational states, the predicted vibrational spacings from the *ab initio* calculations are in good agreement with the remaining observed spacings. This is similar to our experience with other states

v'	$T_v + 2\ B_v$ (cm^{-1})	ΔE (cm^{-1})	v'	$T_v + 2\ B_v$ (cm^{-1})	ΔE (cm^{-1})
0	5808.10	122.52	15	7492.70	108.41
1	5930.62	127.55	16	7601.10	104.31
2	6058.17	104.47	17	7705.41	107.04
3	6162.64	117.18	18	7812.45	105.84
4	6279.82	106.67	19	7918.29	104.34
5	6386.50	118.75	20	8022.63	104.44
6	6505.25	111.78	21	8127.07	103.83
7	6617.02	110.61	22	8230.90	103.14
8	6727.63	111.01	23	8334.04	102.90
9	6838.64	110.88	24	8436.95	102.84
10	6949.52	106.71	25	8539.78	100.67
11	7056.23	111.41	26	8640.45	101.80
12	7167.64	110.58	27	8742.26	101.80
13	7278.21	104.49	28	8844.06	97.97
14	7382.65	110.04	29	8942.03	

Table 6.3.
Experimental assignments for the location of $A\ ^1\Sigma^+$ v' $J' = 1$ based on our depletion data. The uncertainty for all assignments is 0.02 cm^{-1}. Energies are referenced to the Rb 5S + Li 2S atomic asymptote.

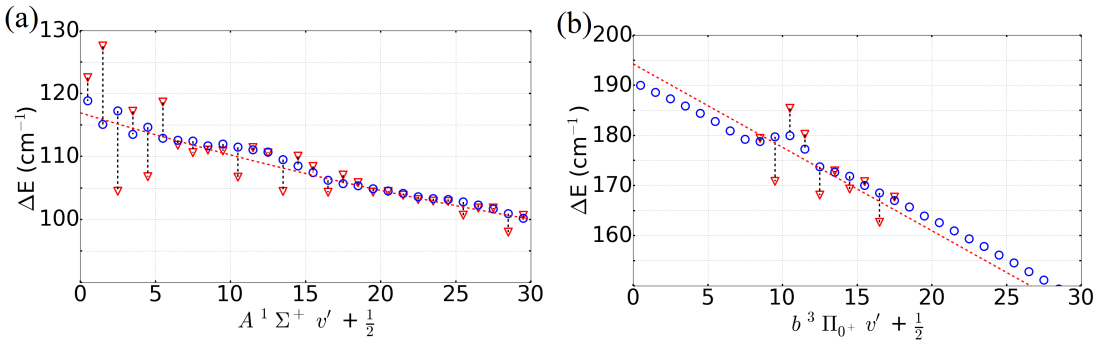

Fig. 6.3. Comparison of theoretical vibrational spacings (blue circles) to our measurements (red triangles) for (a) $A\ ^1\Sigma^+$ and (b) $b\ ^3\Pi_{0^+}$. Black dashed vertical lines connect datasets to guide the eye. The dashed red line is the fit using Eq. (6.1) and the molecular constants shown in Table 6.6. Large deviations in experiment from the theory are driven by perturbations. The unevenness of the theory predictions in the $v' = 0-4$ region for $A\ ^1\Sigma^+$ and $v' = 7-12$ region for $b\ ^3\Pi_{0^+}$ is an artifact caused by imperfect conversion from adiabatic to diabatic PECs. Finally, we note that (b) suggests that our extracted constants, ω_e and x_e, for the $b\ ^3\Pi_{0^+}$ state are too large. Our data for this state is limited, and it appears that if both were smaller, the fit would better match the theory (blue circles).

in previous studies, such as the $d\ ^3\Pi$ state [60], in which we found good general agreement between measured and calculated energy spacings between vibrational levels, but not with the well depth. This disagreement manifests itself through two fewer vibrational levels

v'	$T_v + 2\ B_v$ (cm^{-1})	ΔE (cm^{-1})	v'	$T_v + 2\ B_v$ (cm^{-1})	ΔE (cm^{-1})
8	5682.01	179.41	14	6738.87	169.28
9	5861.42	170.83	15	6908.16	170.78
10	6032.25	185.39	16	7078.94	162.65
11	6217.65	180.22	17	7241.59	167.68
12	6397.87	168.08	18	7409.27	
13	6565.95	172.92			

Table 6.4.
Experimental assignments for the location of $b\ ^3\Pi_{0^+}$ v' $J' = 1$ based on our depletion data. Uncertainty for assignments is 0.02 cm^{-1}, vibrational designation is approximate. Energies are referenced to the Rb 5S + Li 2S atomic asymptote.

$A\ ^1\Sigma^+\ v'$	$b\ ^3\Pi_{0^+}\ v'$	$\hbar\delta$ (cm^{-1})	$(E_+ - E_-)$ (cm^{-1})	$V_{\rm int}$ (cm^{-1})	FCF	$\frac{V_{\rm int}}{FCF}$
2	10	7.7	25.8	12.3	0.06	205
5	12	0.7	11.3	5.6	0.03	187

Table 6.5.
Parameters of the mixed states. δ is the unshifted (bare) energy difference of the states, while $E_+ - E_-$ is the energy difference between the perturbed states. $V_{\rm int}$/FCF as determined through this analysis is in reasonable agreement with $A_{Rb}/2 = 125$ cm^{-1}, where A_{Rb} is the spin-orbit interaction strength in atomic rubidium.

than predicted for the $A\ ^1\Sigma^+\ v'$ series. In Table 6.6, we present a direct comparison of the derived molecular constants from theory and our data, confirming our earlier assertion of excellent agreement.

In this section, we analyze state mixing between several vibrational levels of the $A\ ^1\Sigma^+$ and the $b\ ^3\Pi_{0^+}$ states. The two largest perturbations seen in Fig. 6.3(a) are due to mixing

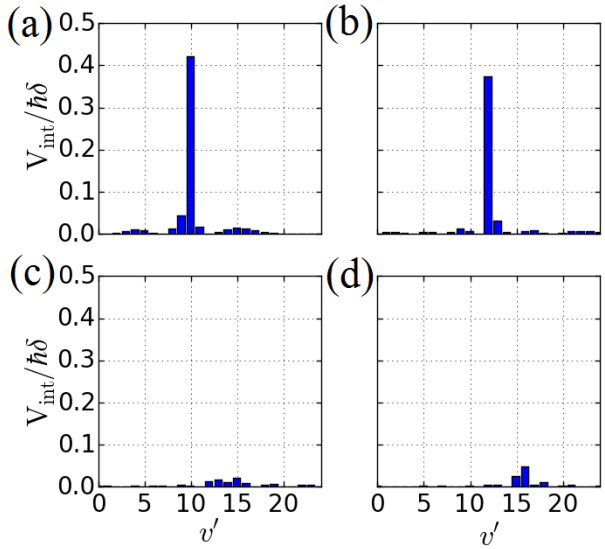

Fig. 6.4. Calculated $V_{\rm int} = A_{Rb}|\langle\Psi_{b\ ^3\Pi}|\Psi_{A\ ^1\Sigma^+}\rangle|^2/2$, divided by the state energy difference, for $A\ ^1\Sigma^+$ (a) $v' = 2$, (b) $v' = 5$, (c) $v' = 8$ and (d) $v' = 11$ interacting with the vibrational levels of the $b\ ^3\Pi_{0^+}$ state. The PECs are from Ref. [64], and we calculated the vibrational wavefunctions and FCFs using LEVEL 8.0 [72]. $A_{Rb} = 250$ cm^{-1} is the atomic rubidium spin-orbit constant.

between the $A\ ^1\Sigma^+\ v' = 2$ level with $b\ ^3\Pi_{0^+}\ v' = 10$, and between the $A\ ^1\Sigma^+\ v' = 5$ level with $b\ ^3\Pi_{0^+}\ v' = 12$. The mixing between states is proportional to [66]

$$\frac{|\langle \Psi_{b\ ^3\Pi} | H_{\mathrm{SO}} | \Psi_{A\ ^1\Sigma^+} \rangle|^2}{\hbar\delta}, \tag{6.2}$$

where H_{SO} is the Hamiltonian for the spin-orbit interaction, and $\hbar\delta$ is the energy difference between the unperturbed states. The vibrational factor of the wavefunctions $|\Psi\rangle$ in this expression implies that strong state mixing requires a large Franck Condon overlap between two states, while the energy denominator requires a small energy difference. In Fig. 6.4, we show a rough estimate for the interaction strength caused by the spin-orbit effect divided by the state energy difference between the $A\ ^1\Sigma^+\ v' = 2$, 5, 8 and 11 states with the various vibrational levels v' of the $b\ ^3\Pi_{0^+}$ state. We estimate the interaction strength with [74] $V_{\mathrm{int}} = A_{Rb}|\langle \Psi_{b\ ^3\Pi} | \Psi_{A\ ^1\Sigma^+} \rangle|^2/2$ where A_{Rb} is the spin-orbit interaction in atomic rubidium, 250 cm^{-1}; we have found that this approximation roughly holds in the past [60]. For $A\ ^1\Sigma^+\ v' = 2$ and 5, mixing with one state is much stronger than any of the rest, justifying a two-state mixing model. The $A\ ^1\Sigma^+\ v' = 8$ state is hardly perturbed because it has a very small Franck Condon overlap with $b\ ^3\Pi_{0^+}\ v' = 14$ despite having nearly identical energies. This is consistent with the story told by Fig. 6.3, as neither $A\ ^1\Sigma^+\ v' = 8$ nor $b\ ^3\Pi_{0^+}\ v' = 14$ appear significantly perturbed. Finally, Fig. 6.3(b) shows that $b\ ^3\Pi_{0^+}\ v' = 16$ is slightly perturbed, by $A\ ^1\Sigma^+\ v' = 10$ and 11, which matches the small interaction strength shown in Fig. 6.4(d).

For the $A\ ^1\Sigma^+\ v' = 2$ and 5, which we approximate as a simple two-state mixing model, we calculated the admixture coefficients. Using the treatment of mixed states in Ref. [66], we write the mixed states as

$$|\Psi_-\rangle = c|\Psi_{A\ ^1\Sigma^+}\rangle - d|\Psi_{b\ ^3\Pi}\rangle \tag{6.3}$$

and

$$|\Psi_+\rangle = d|\Psi_{A\ ^1\Sigma^+}\rangle + c|\Psi_{b\ ^3\Pi}\rangle, \tag{6.4}$$

where $|\Psi_{A\ ^1\Sigma^+}\rangle$ and $|\Psi_{b\ ^3\Pi}\rangle$ are the bare states. The energies of states $|\Psi_-\rangle$ and $|\Psi_+\rangle$ are E_- and E_+, respectively. As we have done in the past [68], we can use the expected energy and observed energy of mixed states to estimate their mixing; we use the molecular

constants of Table 6.6 to predict where the unperturbed state should lie. After we have a prediction for the unperturbed state location we can solve for the admixture coefficients

$$c^2 = \frac{1}{2}\left[1 - \frac{\hbar\delta}{E_+ - E_-}\right] \tag{6.5}$$

and

$$d^2 = \frac{1}{2}\left[1 + \frac{\hbar\delta}{E_+ - E_-}\right]. \tag{6.6}$$

Additionally, we calculate the interaction strength, $V_{\rm int}$, using $V_{\rm int} = \frac{1}{2}\sqrt{(E_+ - E_-)^2 - (\hbar\delta)^2}$ from Ref. [68]. All of the relevant parameters for the strongest mixed $A\ ^1\Sigma^+ - b\ ^3\Pi_{0^+}$ states that we observe and the derived admixture coefficients and interaction strengths are presented in Table 6.5. For both of these states, $V_{\rm int}$/FCF is within a factor of two of $A_{Rb}/2$, showing approximate agreement with the model of Ref. [74].

	$A\ ^1\Sigma^+$		$b\ ^3\Pi_{0^+}$		
	Exp.	Th. [64]	Exp.	Th. [64]	Th. [76]
ω_e (cm^{-1})	117.3 (0.6)	117.9	195.1 (1.0)	190.6	188.3
$x_e \times 10^3$	3.1 (0.4)	3.3	4.3 (0.2)	2.9	3.4
$y_e \times 10^6$	15 (9)	23		-18.4	-29.7
T_e (cm^{-1})	5756.6 (2.2)	5537.7	4083 (7)	3962.3	4180.4

Table 6.6.
Molecular constants fitted to our data, compared to fits of other experiments [58] or to theoretical predictions from *ab initio* calculations from Refs. [76] and [64]. The state energies are given by Eq. (6.1). For fitting $C\ ^1\Sigma^+$ we omitted $v' = 41 - 45$ because the energies of these states fall outside the range over which Eq. (6.1) is valid. When fitting $b\ ^3\Pi_{0^+}$, the vibrational numbering is uncertain since we have not observed $v' < 8$. We chose vibrational numbering to force a well depth between the two *ab initio* predictions. Additionally, we omitted $v' = 10$, 12, 14 and 16 from the fit because these levels are strongly perturbed, as shown in Fig. 6.3(b). For these data, a value of y_e is not significant and not included in the table.

6.3 Spectroscopy Conclusion

When we started doing extra spectroscopy on LiRb molecules, we had three goals. First, we needed a better measurement on the ground state well depth which our PA work provided. Second, we wanted to detect weakly bound singlet molecules made via PA and spontaneous decay with REMPI. We discovered that for some $X\ ^1\Sigma^+$ $v = 42$ and $v = 43$ we could ionize the molecules using the $C\ ^1\Sigma^+$ state as the intermediate state. Unfortunately, this intermediate state will not work for more loosely bound initial states. And finally, we wanted to find suitable intermediate states for a JILA style STIRAP population transfer from weakly bound triplet states to the ground state. Our spectroscopy reveals that states near $d\ ^3\Pi_1$ $v = 4$ or $A\ ^1\Sigma^+$ $v = 5$ would work for STIRAP. Additionally, Ref. [77], suggests a second STIRAP strategy that caught our eye. They transfered population to the ground state, but instead started from a weakly bound singlet state populated by PA. We expect that we could transfer population from $X\ ^1\Sigma^+$ $v = 43$ to $v = 0$ through $C\ ^1\Sigma^+$ $v = 23$. Additionally, we were excited to discover that the colors are nearly the same for a transfer through $C\ ^1\Sigma^+$ $v = 23$ and $d\ ^3\Pi_1$ $v = 4$ suggesting that maybe the same set of lasers could work. We will start here in Chapter 7.

7. OPTICAL PHASE LOCKED LOOPS

This chapter details work on phase stabilizing ECDLs; our ultimate application is STIRAP in the dual species MOT to produce large numbers of ground state LiRb molecules. As demonstrated by Ref. [77], STIRAP to transfer population from weakly bound singlet states populated by PA to the ro-vibronic ground state is possible, even in a dual species MOT. Our plan was to use one of the $C\ ^1\Sigma^+$ vibrational levels as the intermediate state ($|e\rangle$) (which has the benefit that some of the same lasers can drive more traditional STIRAP through $d\ ^3\Pi$ - $D\ ^1\Pi$ mixed states) to transfer population from $X\ ^1\Sigma^+\ v = 43$

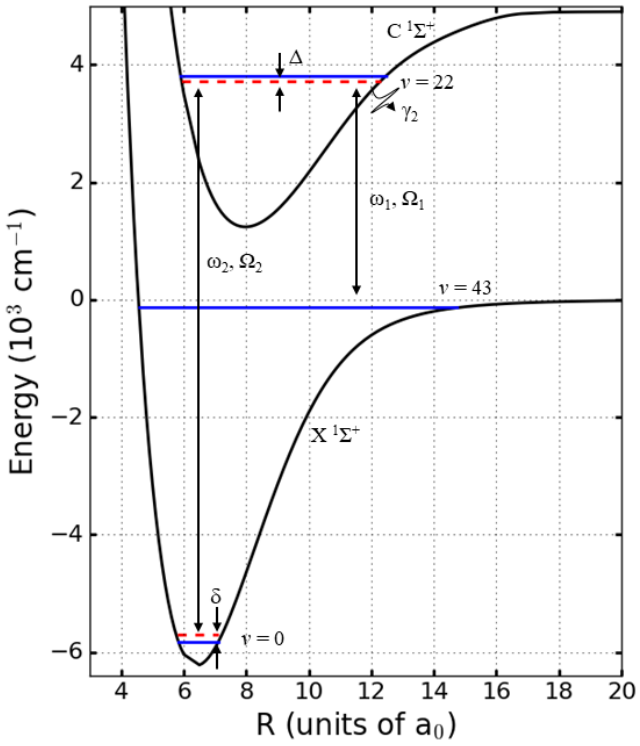

Fig. 7.1. Energy level diagram for STIRAP transfer from $X\ ^1\Sigma^+\ v = 43$ to $X\ ^1\Sigma^+\ v = 0$ through $C\ ^1\Sigma^+\ v = 22$. The 'up' laser has frequency ω_1 and Rabi frequency Ω_1 while the 'down' laser has frequency ω_2 and Rabi frequency Ω_2. The lasers are chosen so that $\omega_2 - \omega_1 = \Delta E_{43\text{ to }0} + \delta$, with a mutual detuning from the intermediate state of Δ. The excited, intermediate state will rapidly decay with rate γ_2.

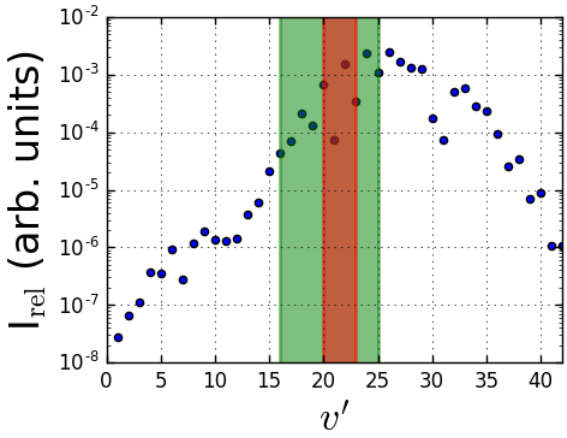

Fig. 7.2. Calculated STIRAP strengths from $v'' = 43$ to $v'' = 0$ through $C\ ^1\Sigma^+\ v'$ as a function of the vibrational level v'. We estimate the STIRAP strength as $I_{\text{rel}} = \sqrt{FCF_{\text{down}} FCF_{\text{up}}}$ in the absence of any information on the transition dipole moments. The wider, shaded green region represents the states accessible with commercially available green diode lasers while the enclosed, shaded red region represents the states accessible with 730 nm diode lasers (the green laser also covers this range). From this $C\ ^1\Sigma^+\ v' = 22$ stands out as the best available intermediate state using these lasers, while being the 3$^{\text{rd}}$ best intermediate state overall

($|i\rangle$), populated by spontaneous decay after photoassociation, to $X\ ^1\Sigma^+\ v = 0$ ($|f\rangle$) as shown in Fig. 7.1. We chose the intermediate state for STIRAP based on our REMPI data and calculated FCFs. Transition dipole moments in molecules are hard to directly access (and require a bit of work to calculate), but seeing the REMPI transitions $C\ ^1\Sigma^+\ v' = 26 \leftarrow X\ ^1\Sigma^+\ v'' = 43$ and $C\ ^1\Sigma^+\ v' = 12 \leftarrow X\ ^1\Sigma^+\ v'' = 2$, inform us that the transition dipole moments for $C\ ^1\Sigma^+\ v' = 22 \leftarrow X\ ^1\Sigma^+\ v'' = 43$ and $C\ ^1\Sigma^+\ v' = 22 \leftarrow X\ ^1\Sigma^+\ v'' = 0$ will also be strong. We picked $C\ ^1\Sigma^+\ v = 22$ via the FCFs, as shown in Fig. 7.2.

The proposed STIRAP implementation will require two lasers, one at 730 nm with frequency ω_2 and Rabi frequency Ω_2 and another at 520 nm with frequency ω_1 and Rabi frequency Ω_1. The difference between the two laser frequencies will need to exactly match the energy difference between the initial and final states, with a small mutual detuning, Δ, from the intermediate state. Δ needs to be large relative to the decay rate from the intermediate state, γ_2, as to not accidentally populate it. The detuning from the

two-photon resonance, δ, needs to be small for this experiment to work. It is fairly easy to set up a three state Hamiltonian to model this system,

$$H = \begin{bmatrix} -i\gamma_1/2 & \Omega_1(t)/2 & 0 \\ \Omega_1(t)/2 & \Delta - i\gamma_2/2 & \Omega_2(t)/2 \\ 0 & \Omega_2(t)/2 & \delta - i\gamma_3/2 \end{bmatrix} \tag{7.1}$$

which can be solved numerically, as shown in Fig. 7.3. Here, we pick relatively modest values for the Rabi frequencies at 2π(10MHz), estimated $\gamma_2 = 2\pi$(10MHz), set $\Delta = 2\pi$(50MHz), and γ_1, γ_3 are insignificantly small. In panel **(b)** of Fig.7.3, we show the counter-intuitive pulse sequence that is typical of STIRAP, along with normal pulse times of around 20 μs. The state occupation for $|i\rangle$, $|e\rangle$, and $|f\rangle$ is shown as a function of time in panel **(a)** of Fig. 7.3, with $\delta = \gamma_2/100$. Finally, panel **(c)** of Fig. 7.3, shows the transfer efficiency as a function of δ. What is clear is that δ needs to be very small for an efficient transfer, and the efficiency drops below 90 % as δ becomes larger than 100 kHz. This imposes two harsh conditions on the two STIRAP lasers. First, the frequency of the each laser needs to be controllable to better than 100 kHz. And second, the phase coherence between the two lasers needs to be a lot better than 100 kHz. Additionally, the frequency difference between the two STIRAP lasers provides a third condition, as our phase stabilization needs to bridge the 5700 cm^{-1} energy difference between the two $X\ ^1\Sigma^+$ states.

Our plan to phase stabilize the two STIRAP lasers was to lock them to a Menlo frequency comb, shared with Dr. Weiner next door. Locking the ECDLs to the frequency comb solves all three problems in theory. As shown in Fig. 7.4, the mode-locked comb laser produces a series of femtosecond pulses which looks like an array of teeth in the frequency domain. The teeth of a frequency comb are at $f = nf_r + f_{ceo}$, where f_r is the repetition rate of the comb, f_{ceo} is the carrier offset phase, and n is a large integer. Both f_r and f_{ceo} are radio frequency signals, with common commercial combs having repetition rates between 100 and 250 MHz. Additionally, both f_r and f_{ceo} are stabilized to an atomic clock in the Menlo frequency comb, implying that each individual tooth shares a similar 10^{-12} fractional instability. Phase locking our ECDLs to the frequency comb passes the phase stability of the comb onto the ECDLs. Additionally, the offset frequency between the ECDL and comb tooth provides a robust method for tuning the

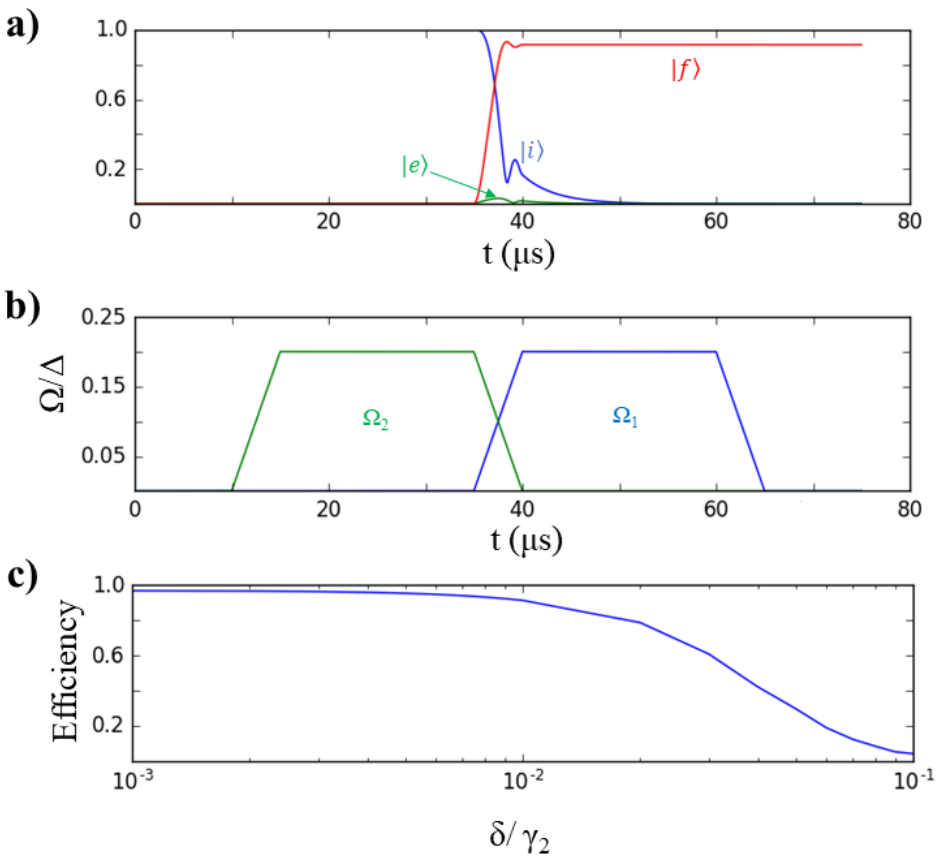

Fig. 7.3. Simulation of Eq. (7.1). **(a)** State occupation of initial state $|i\rangle$, excited state $|e\rangle$ and final state $|f\rangle$ as a function of time. **(b)** STIRAP counter-intuitive laser pulse sequence used in the simulation. **(c)** Efficiency of transfer as a function of δ.

frequency of the ECDLs with nearly 1 Hz level precision. Thus the frequency comb meets our first two STIRAP conditions, laser tunability and phase stability.

To meet our third criteria, that is spanning at least 5700 cm^{-1}, we will turn to super-continuum generation. Super-continuum generation occurs when frequency comb light pumps a highly-non-linear fiber in which internal non-linear processes generate light at nearly every possible sum or difference frequency. The result is an output that spans 500 - 1100 nm and shares the comb structure and stability. This more than spans the energy difference between our states, but at a steep cost. Because the spectrum of the laser is widened by a factor of 25, the power per tooth of the laser drops by a similar amount. This makes signal-to-noise a nightmare for our ECDL - comb beat-notes as we are left trying to dig out a signal formed with a fraction of a nW in the frequency comb tooth.

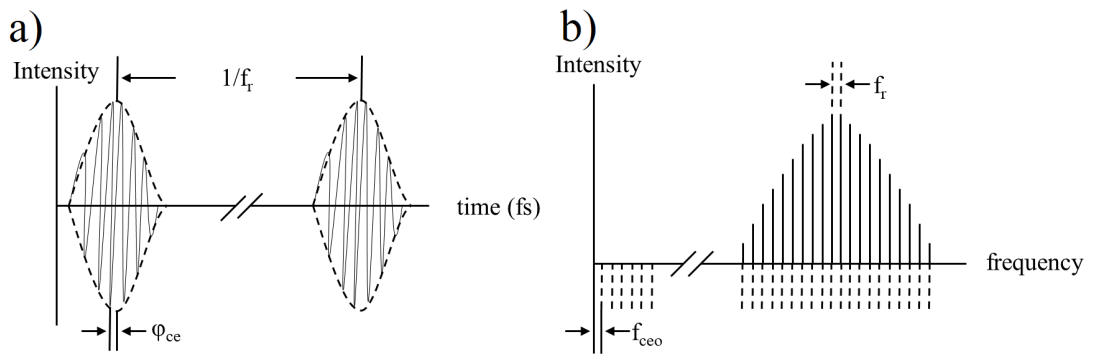

Fig. 7.4. Femtosecond laser pulse. **(a)** Time domain. **(b)** Frequency domain.

Reference	Phase Detector Type	Lasers
Prevedelli *et. al.* (1995)	Digital, homemade counters	ECDL to comb
Cacciapuoti *et. al.* (2005)	Mixed, based on PLC	2 ECDLs
Ni (2008)	Analog mixer, no details	ECDL to comb
Appel *et. al.* (2009)	Digital, ADF4107 internal counters	2 ECDLs
Xu *et. al.* (2012)	Digital, MAX9382 w/ FPGA	2 ECDLs

Our first step in phase locking the exotic colored ECDLs to the frequency comb was to compare previous implementations of optical phase locked loops using one of our 780 nm trapping lasers and find a design that would work at very low signal-to-noise ratios.

7.1 Optical phased locked loop history

Construction of optical phase locked loops with extended cavity diode lasers have been an active field of research basically since the invention of the grating tuned, extended-cavity-diode-laser (ECDL) [78]. Past examples of optical-phase-locked-loops (OPLLs) from the literature deal mostly with systems [49, 79] where the OPLL is constructed between two CW lasers and there are no signal-to-noise ratio (SNR) concerns (although wide frequency operation of the loop can present its own set of problems). One example in the literature similar to our scenario, where the OPLL was formed between a CW laser and a frequency comb, is found in Ref. [80]. However, Ref. [80] used a comb without super-continuum generation leading to a relatively high SNR. In this chapter, we demonstrate OPLL operation between a frequency comb after super-continuum generation and a CW

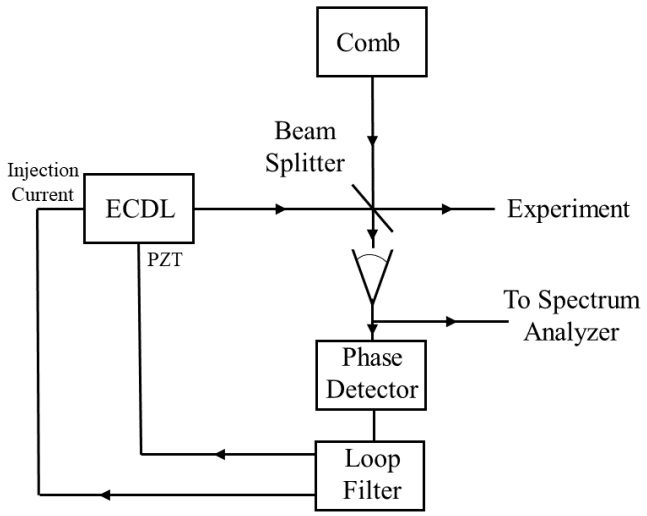

Fig. 7.5. High level block diagram of our OPLL.

ECDL down to an estimated 200 pW per tooth and illustrate the important differences between digital phase detectors and analog phase detectors.

Shown in Fig. 7.5, is a high level block diagram of our experiment. We have two lasers, an ECDL and a frequency comb, combined and sent to a photodetector. This forms the beat-note that we will use to stabilize the ECDL to the comb. Following the photodetector we sample the beat-note with a spectrum analyzer, while sending the majority of the power to the phase detector. The phase detector lives on its own printed-circuit-board (PCB), as does the loop filter it feeds. The loop filter takes in the error signal provided by the phase detector, provides some filtering and then sends two DC coupled outputs to the ECDL; one output feeds the laser injection current and the other controls a PZT to modulate the cavity length.

7.2 Noise considerations

Sources of noise must be carefully considered to extract very low amplitude signals. In any optical-electrical system, the two dominant noise sources are Johnson-Nyquist noise and shot noise. The Johnson-Nyquist noise comes from thermal noise in resistors and its mean-square current noise is

$$\bar{i_n}^2 = (4k_BT/R)B, \tag{7.2}$$

where k_B is Boltzmann's constant, T is the temperature of the resistor, R is the resistance of the resistor and B is the bandwidth of the electrical system. Shot noise is from quantum fluctuations driven by the discreteness of electrons, and its mean-square current noise is

$$\bar{i_n}^2 = 2|e|\eta(I_{\mathrm{CW}} + I_{\mathrm{comb}})B, \tag{7.3}$$

where e is the charge of the electron, η is the photo-sensitivity of the photodiode, I_{CW} is the CW laser intensity incident on the photodiode, and I_{comb} is the comb laser intensity. Meanwhile, the signal current in the photodiode is

$$i = \eta(I_{\mathrm{comb}} + I_{CW} + 2\sqrt{I_{\mathrm{CW}} I_{\mathrm{tooth}}}\cos[\omega t]), \tag{7.4}$$

where I_{tooth} is the power in the comb tooth forming the beat-note, and $2\sqrt{I_{\mathrm{CW}} I_{\mathrm{tooth}}}\cos[\omega t]$ is the beat-note term. From examining our equations, several things become immediately apparent. First, we need to filter out as many comb teeth as possible; the extra comb teeth will add to shot noise, but not contribute to the signal level. Second, we want to minimize the circuit bandwidth. However, this is at odds with detecting the beat-note. To detect the beat-note we need at least $f_r/2$ bandwidth for our photodiode system. Third, by increasing the power in the CW laser, we eventually reach the regime where our signal-to-noise ratio is fixed, as shot noise dominates and our power signal-to-noise ratio is $2\eta I_{tooth}/(|e|B)$. Unfortunately, to reach this regime requires at lot of CW laser power. At 1 mW of CW laser power shot noise and Johnson-Nyquist noise (for a 50 Ω system) are equal, meaning we would like around 10 mW of CW power. This is not practical for most ECDL lasers, and as such we use a transimpedance amplified photodiode. The transimpedance photodiode uses a big resistor, making the Johnson-Nyquist noise small, without sacrificing bandwidth, because of the op-amp.

There are a few ways to optimize the beat-note signal as well. The beat-note detected is

$$\int d^2r \vec{E}_{\mathrm{tooth}}(r) e^{i(\omega_{\mathrm{tooth}} t - \vec{k}_{\mathrm{tooth}}\cdot\vec{r})} \cdot \vec{E}^*_{\mathrm{CW}}(r) e^{-i(\omega_{\mathrm{CW}} t - \vec{k}_{\mathrm{CW}}\cdot\vec{r})} \tag{7.5}$$

where $\int d^2r$ is an integration over the photodiode surface, $E_{\mathrm{CW}}(r)$ is the spatial profile of the CW laser, ω_{CW} is the frequency of the CW laser and k_{CW} is the propagation vector of the CW laser (quantities with the $_{\mathrm{tooth}}$ subscripts are the corresponding quantities of the tooth of the comb laser). This formula warns of three problems. First, both lasers need to match polarization. Second, both lasers must propagate in the same direction as

well as possible. Finally, the spatial profiles of the two lasers need to be matched as well as possible. Careful experiment design will optimize the beat-note signal by optimizing all three quantities.

7.3 Method Details

Our experiment studies locking an ECDL to a frequency comb. For the ECDL, we use a homebuilt cavity following the design of Ref. [50]. It uses a 780 nm, 80 mW diode (QPhotonics QLD-780-80s). Optical feedback is provided by a 1800 groves/mm grating (Thorlabs GH13-18V) and the injection current is controlled by a homebuilt implementation of the Libbrecht-Hall design, detailed in Ref. [47]. The laser is sent through a 35 dB optical isolator before being combined with the frequency comb source on an optical beam splitter. The frequency comb is a commercially available Menlo systems FC1500-250-WG laser, which has a 250 MHz repetition rate and produces 130 mW of power after super-continuum generation spanning 510 - 1000 nm. We chose to conduct this study at 780 nm because the non-linear super-continuum generating fiber is pumped by a 780 nm source. As such, the comb has more power near 780 nm allowing us to demonstrate OPLL performance across many orders of signal magnitude.

Fig. 7.6 shows the optical table setup for our OPLL. We combine our ECDL with the frequency comb on a non-polarizing 90-10 beam splitter (like Thorlabs BSF10-B beam sampler), sending 10% of the laser power (or less) and 90% of the comb power through a polarizer followed by a short length of fiber. The output of the fiber is focused onto a transimpedance amplified photodiode. Before combining the two beams we match their polarizations with a pair of $\lambda/2$ waveplates and filter out most of the comb power with a 10 nm optical bandwidth interference filter (like Thorlabs FBH780-10). We run the combined laser beams through a short section of fiber to simultaneously match the direction of the laser beams and the size/focusing. Even with modest fiber coupling around 20% efficiency, we found the fiber to improve SNR compared to the free space approach. We believe the fiber helps because diode mode profiles are rarely circular and often exhibit significant astigmatism; both effects reduce the mode and k-vector overlap between the two beams on the photodiode. The fiber is not critical for high SNR systems, like with two CW lasers, but often will help with SNR and is an easy

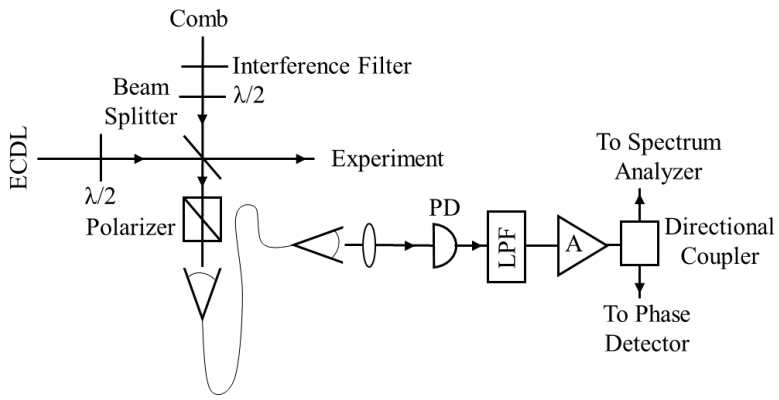

Fig. 7.6. Optical table setup to maximize beat-note signal amplitude. Zero-order half-wave plates match the polarizations of both lasers to a common polarizer. They are combined with a beam sampler, sending 90% of the comb power and 10% of laser power to a fiber coupler. After a short length of fiber matches laser propagation and beam profile, the output is focused onto a fast transimpedance amplified photodiode. After photodiode, a low-pass filter removes the comb self-beat and beat-notes with higher order comb teeth. We pick off 1% of the signal in a directional coupler for analysis and then apply a variable gain before sending to the phase detector.

algorithm to guarantee co-propagation (note: fiber needs to be angle cut on both ends to reduce Fabry-Perot effects in the transmitted beam). Finally, we detect the beat-note on a transimpedance amplified photodiode (Thorlabs PDA10A) which feeds a 50 Ω system. In the 50 Ω system, we have a low-pass filter at 105 MHz (Minicircuits ZX75LP-105-S+) followed by a 20 dB directional coupler and RF amplifiers. The two phase detectors require slightly different gains in the RF amplifiers: the analog detector needs 10 dB of gain, while the digital detector needs 30 dB of gain (provided by Minicircuits ZKL-2+ amplifiers and discrete attenuators).

7.4 Phase Detectors

Most of the available literature on optical phase locking [49, 79–81] relies on digital phase detectors for OPLLs (and ironically, recent advances in digital circuits have rendered most of these references totally obsolete). We feel that the best implementation of a digital OPLL is given in Ref. [49], that uses the ADF4XXX family of digital phase locked loop chips. These chips are all pin compatible allowing the same circuit board to

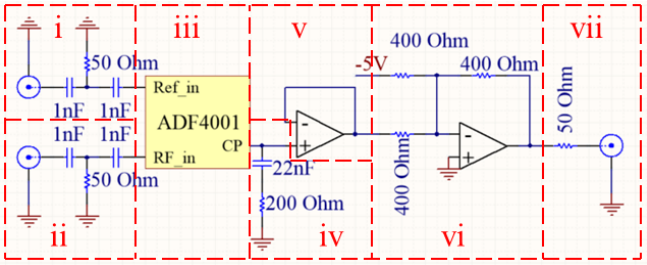

Fig. 7.7. Simplified digital phase detector schematic. **i** Reference RF oscillator input, impedance matching and DC bias isolation. **ii** Beat-note edge launch connector input, impedance matching for 50 Ω RF amplifiers and DC bias isolation. **iii** Digital phase detector, programmed by a PIC24 micro-controller, omitted for clarity. **iv** Charge pump filter, turns current output from chip into a voltage for op-amps. Filter integrates below $f_c = 36$ kHz and provides a gain of one above f_c. **v** Op-amp buffer to prevent stage loading effects. **vi** Amplification and level shifting. **vii** Output impedance matching and edge launch connector.

work across a wide range of frequencies. Fundamentally, the digital phase detector turns the analog beat-note into a digital signal (with the same frequency) and then counts the rate of rising edges, compared to some digital reference signal. If the frequencies are far apart, it functions as a frequency detector and will saturate its output at one of its rails. When the frequencies are close, it tries to force simultaneous rising edges. One of the big advantages of a digital phase detector is that it is very easy to frequency divide a digital signal with some simple logic components. The different chips in the ADF4XXX family feature different front end division stages, allowing the same core circuitry to work between 1MHz and 10 GHz.

We used the ADF4001 chip which does not have the first division stage and functions between a few MHz and 250 MHz. Our implementation is shown in Fig. 7.7. Although the simplicity and robustness of this phase detector has to be praised, we offer the reader a few words of caution. First, it is absolutely critical to run the analog and digital sections of the ADF4XXX chip off different supplies and to carefully isolate the analog and digital grounds on the PCB. Second, the charge pump output needs to be integrated by an RC filter with a time constant set to ≈ 30 kHz. The charge pump can be thought of as an ideal current source that turns on when the beat-signal and the reference signal are out of phase. A passive filter is required to turn the current pulses into voltages for processing in the loop filter. We found any additional filtering will break this phase

detector, resulting in either oscillation or terrible phase noise performance. The choice of $1/(2\pi RC) \approx 30$ kHz is a bit arbitrary but works well (and does not limit the total loop bandwidth to 30 kHz). Third, there is an internal division stage for both the beat-note input and reference input to the ADF4001 chip. We set the chip to divide both signals down to $f_{\text{compare}} = 25$ MHz. It is very important for $f_{\text{compare}} >> f_{\text{3dB}}$, where f_{3dB} is the bandwidth of the whole electronic system (or nothing works). We found that the phase detector works better for higher f_{compare} and recommend the highest f_{compare} possible. Additionally, it is important to have filtering in the loop filter to attenuate signals at f_{compare} to reduce noise caused by the charge pump firing.

In many ways, digital phase detectors are great tools. They are fairly easy to get working, work across a huge frequency range and hold the phase lock almost indefinitely (ours was limited by polarization drifts in the fiber delivering the frequency comb to our lab which is not polarization maintaining). However, they require an input signal with a large SNR to function and an even larger SNR to work well. This can be easily understood. Because the digital circuit examines the beatnote frequency without first down-shifting, the noise sources are integrated over the full circuit bandwidth, between 1 MHz and 105 MHz. For strong signals this is not a problem, but the integrated noise can easily overwhelm weak signals.

There is almost no literature available on analog phase detectors in OPLLs. Perhaps because on the simplest level, an analog phase detector is a mixer followed by a low-

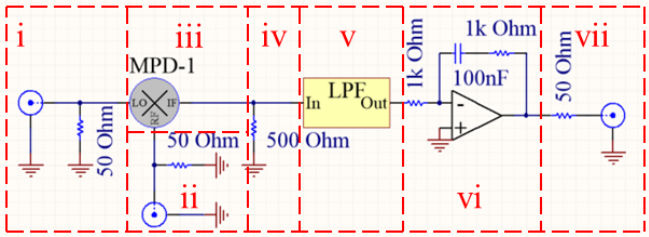

Fig. 7.8. Simplified analog phase detector schematic. **i** Reference oscillator edge launch input and impedance match. **ii** Beat-note edge launch input and impedance match. **iii** Analog phase detector from Minicircuits. **iv** DC current return for phase detector. **v** Low-pass filter to remove f_{lo}, $2f_{lo}$ and extra noise. **vi** Op-amp integrator to turn phase detector output into an error signal. Below $f_c = 1.6$ kHz, it integrates and above f_c it provides a gain of one. **vii** Output impedance matching and edge launch connector.

pass filter, but treating it as a simple system is a recipe for poor performance at best. The function of an analog phase detector is best understood with some math. The beat-note signal will look like $\sin[\omega_{\rm bn}t + \delta\phi(t)]$ and the reference signal will look like $\sin[\omega_{\rm ref}t]$, where $\omega_{\rm bn}$ and $\omega_{\rm ref}$ are the two frequencies and $\delta\phi(t)$ is the time varying phase difference between them. Mixing the two signals results in an output signal of the form $\sin[(\omega_{\rm bn} - \omega_{\rm ref})t + \delta\phi(t)] + \sin[(\omega_{\rm bn} + \omega_{\rm ref})t + \delta\phi(t)]$, and the second term is filtered out electronically. When $(\omega_{\rm bn} - \omega_{\rm ref})$ is small, the output of the mixer is proportional to $\sin[\delta\phi(t)] \approx \delta\phi(t)$, provided the phase difference is also small. Thus, the analog phase locked loop will try to minimize $\delta\phi(t)$ which occurs when $\omega_{\rm bn} = \omega_{\rm ref}$ and $\delta\phi(t) = 0$ (the other stable point for the analog loop is when $\omega_{\rm bn}$ and $\omega_{\rm ref}$ are very different and the low-pass filter following the mixer filters out everything).

Fig. 7.8 shows our implementation of an analog phase detector. We use a MPD-1 chip from Minicircuits, which is a more specialized mixer, designed to be used as a phase detector. Ultimately this means it is designed to have a very low offset voltage (well below 1 mV), is very quiet (less than 1 nV/$\sqrt{Hz}$) and has a high output impedance of 500 Ω. On its output, we have a 500 Ω resistor to ground which provides a path to ground for its output current; an RC filter tuned to $\omega_{\rm ref}$ to absorb residual power at $\omega_{\rm ref}$ and $2\omega_{\rm ref}$; and an op-amp integrator with a transfer function that levels off to a gain of 1 at $\approx$ 1 kHz. The RC corner of the integrator has been optimized for long lock times and we have observed operation in excess of an hour (again limited by polarization drifts in the fiber delivering the frequency comb). Additionally, care must be taken to prevent RF pickup of the reference. We found that edge launch coax connectors paired with a matched 50 Ω transmission line on the PC board were necessary to limit reference oscillator feed-through. The advantage offered by the analog phase detector is that bandwidth over which the noise is integrated is much less than the digital phase detectors. Ours integrates the noise in its $\approx$ 700 kHz loop bandwidth, resulting in two orders of magnitude less noise than the digital phase detector.

We should stop here and mention the phase range of the phase detectors. Other authors have championed digital phase detectors because they can work across a wider range of phase errors (we implemented a $N2\pi = 6\pi$ phase detector, where N is the digital division of the beat-note), while analog phase detectors only work between $-\pi/2$ and $\pi/2$ (after which the sign of $\sin[\delta\phi(t)]$ reverses). This sounds like a big advantage for

the digital detectors on paper, but we have not found this to be an important distinction in practice. Both phase detectors require tuning to get into lock and then once in lock, the digital phase detector is only marginally more stable. The digital detector could be made more stable by increasing N, but this carries other consequences and we found it results in worse phase noise performance.

7.5 Loop Filter

The circuit for our loop filter is given in Chapter 2, along with an explanation of its function. In this chapter, we will discuss how to use it with the phase detectors.

Our steps to tune the loop filter, and achieve locking performance for the first time are as follows. First, we would zero out both current and PZT gains, turn off the PZT integrator and maximize the beat signal, something like 35 dB of signal-to-noise is usually necessary (in a 1 MHz spectrum analyzer bandwidth). Next, while observing the beatnote on a spectrum analyzer, we would increase the current gain until it significantly perturbed the beat-note as the laser is swept through the lock point. It would either avoid the lock point or jump into lock for a short time. The digital phase detector is simpler at this point, because by simply flipping the sign of the current feedback (if it avoids the lock) is enough to get locking behavior; meanwhile the sign does not matter for the analog phase detector, but it will always avoid the lock. Often to get the analog detector into lock, we had to drop the signal level; recall that for the analog phase detector, the error signal is proportional to $\sin[\delta\phi(t)]$, so for large phase errors, the sign of the error signal reverses. At this point, increasing the current gain too much will cause the sideband peaks, visible in Fig. 7.9 (b), to increase in magnitude. For the digital detector, increasing the gain will eventually cause oscillation, while for the analog detector, it will simply bounce out of lock. We operated a hair above this minimum gain-to-lock point. To tune the PZT gain, PZT sign, and integrator switch we follow a similar procedure; the PZT feedback is not necessary for locking, but it does help achieve long lock times. Finally, we note that both phase detectors were quite sensitive to the DC output level of the phase detector. For the digital detector, it could be tuned from oscillation to narrow-band locking by tuning the bias voltage (all while in lock) and the analog detector had similar problems on a smaller scale. We suspect that this issue is caused by a mismatching between the

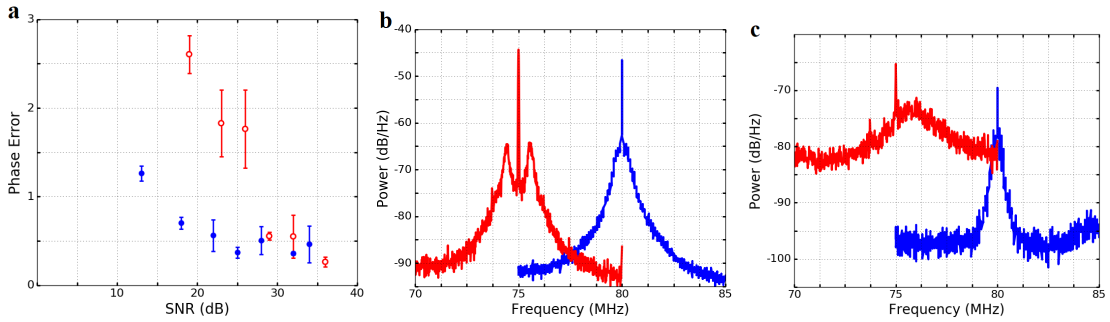

Fig. 7.9. Comparison of analog and digital phase detector performance. **a** Phase error as measured by Eq. (7.6) for the analog phase detector, plotted in blue, and the digital phase detector, plotted in red, as a function of the signal-to-noise ratio, measured in a 1 MHz bandwidth. The signal level was kept fairly constant to avoid dropping out of the working range of the phase detectors (except for the analog phase detector below 20 dB SNR). **b** Raw data as measured by spectrum analyzer for the best performance phase error for the analog detector, blue and centered at 80 MHz, and digital detector, red and centered at 75 MHz. Spectrum analyzer bandwidth was set to 30 kHz for these measurements. **c** Raw data as measured by spectrum analyzer for the analog detector at 18 dB SNR, blue and centered at 80 MHz, and digital detector at 19 dB SNR, red and centered at 75 MHz. Spectrum analyzer bandwidth was set to 30 kHz for these measurements.

relative tuning of the two paths and the relative feedback levels, but carefully matching them results in oscillation (i.e. 1 V of DC offset results in a 1 GHz change in frequency for the PZT, and a 10 GHz change in frequency for the current, but 10 times more PZT feedback than current feedback results in oscillation). We found that nearly identical settings for the loop filter worked for both phase detectors, and the only difference was that the analog phase detector worked better with the PZT integrator turned off, while the digital phase detector benefited from it being on.

7.6 Loop Performance

Our comparison between the performance of the two phase detectors is shown in Fig. 7.9. In these measurements, we fixed the signal level of the beat-note and varied the noise level. Our rationale for this approach is that there is a range of absolute signal levels for which the digital detector works, the chip manufacturer specifies the signal needs to be between -10 and 0 dBm (we have found it works better with more signal

than specified and commonly send it +10 dBm). Our method for varying the noise level was to misalign one of the two lasers until we reached the desired signal-to-noise level, and then use discrete RF attenuators and amplifiers to return to the fixed signal level.

To measure the performance at a given signal-to-noise ratio, we measure the locked beat-note with a spectrum analyzer and then calculate the phase noise according to

$$\text{Phase Error} = -\ln\left(\frac{P_{\text{carrier}}}{\int_{-\infty}^{\infty} P(\nu)d\nu}\right), \tag{7.6}$$

where P_{carrier} is the power at the beat-note carrier frequency, $\int_{-\infty}^{\infty} P(\nu)d\nu$ measures the total power, and $P(\nu)$ the power spectrum as a function of frequency. In our measurements, the carrier power is approximated by the data point at f_{carrier}, and a few points on either side are discarded (because we used a spectrum analyzer bandwidth of 30 kHz which is much greater than the carrier bandwidth, which could not be resolved even in a 1 Hz bandwidth). As is common, we report phase error for a 1 Hz bandwidth by dividing the spectrum analyzer reading (outside of the carrier peak) by the spectrum analyzer bandwidth, 30 kHz. To determine the signal-to-noise ratio, we measured the amplitude of the beat-note in lock and compared it to the noise power density, both in a 1 MHz bandwidth. The error-bars in Fig. 7.9 (a) are statistical, from repeating the measurements, and show one standard deviation of the mean.

Although the individual data points in Fig. 7.9(a) bounce around some, the trend for both detectors is quite clear. The digital detector works great, even outperforming the analog detector, for large signal-to-noise ratios and then catastrophically fails somewhere around 28 dB of signal-to-noise. Meanwhile, the analog detector works fine for signal-to-noise ratios greater than 20 dB and then slowly degrades after that with our measurements likely understating its performance. The limit for the analog detector is two-fold: the local-oscillator feeds through to the laser at a small level and is comparable to the beat signal below our lowest signal-to-noise ratio measurements. Additionally, increasing the gain in RF amplifiers eventually leads to oscillation. Because of the oscillation problem, we were unable to keep the signal level fixed for the last three steps downward in signal-to-noise for the analog phase detector dataset. Though the locking performance was weak at 10 dB (our last functioning data point is 13 dB), we speculate that through careful redesign of our circuit board (and with a wizarding degree in RF

electronics), both issues could be fixed, and the analog detector could function at 10 dB signal-to-noise with an acceptable phase error.

To demonstrate the power of the analog phase detector to dig out small signals, we calculated the minimum power in the comb tooth required for lock functioning. Our application is a stimulated-population transfer, which commonly requires coherence on a 10 μs timescale. To estimate the phase coherence time between the two lasers, we use the average cycle slip time [82], which is

$$t_s = \frac{\pi^2 \rho I_0^2(\rho)}{2B}, \tag{7.7}$$

where $\rho = 1/\text{Phase Error}$, and I_0 is the modified Bessel function of the first kind. For our goal of a cycle slip time greater than 10 μs, we find that 18 dB signal-to-noise ratio is the minimum for the analog detector and 29 dB signal-to-noise is the minimum for the digital detector. The carrier power for the median 18 dB data point is -64.5 dBm as measured by the spectrum analyzer. Because the spectrum analyzer only sees 1% of the power, this implies the transimpedance amplifier outputs -44.5 dBm of signal, or about 280 nA of photodiode current. The photodiode current is $i = 2\eta\sqrt{I_{\text{tooth}} I_{CW}}$ and thus for about 1 mW of CW laser power, we estimate that the comb laser power in the tooth we were using before the 10 nm filter in Fig. 7.6 to be about 200 pW. For the digital phase detector, we estimate 4500 pW is the minimum functioning comb tooth power, as a comparison.

7.7 STIRAP Conclusion

At this point it is useful to stop and review the status of the LiRb experiment. Our goal was to use the data in Chapter 6 to choose a pathway to transfer population in $X\ ^1\Sigma^+\ v'' = 43$ to $X\ ^1\Sigma^+\ v'' = 0$. However, despite our success with the 780 nm ECDL, we never got the 520 nm ECDL to lock to the frequency comb. Our best signal-to-noise ratio for the 520 nm beat note is about 20 dB, which this chapter shows is marginal at best. Further, the 520 nm ECDL had a free running linewidth of about 5 MHz, compared to 600 kHz for the 780 nm ECDL we used in this chapter. I suspect this is a symptom of whatever issue stopped it from locking.

Instead, I recommend a different path forward for the reader. First, consult Chapter 9 on how to produce weakly bound triplet molecules in an optical dipole trap. Then use $A\ ^1\Sigma^+\ v = 5$ or $b\ ^3\Pi\ v = 12$ from Chapter 6 for the STIRAP transfer to $X\ ^1\Sigma^+\ v'' = 0$. The logic is as follows. The wavelengths for this transfer are around 810 nm and 1563 nm, both of which are established diode wavelengths, so finding good diodes should not be a problem (whereas 520 nm is an emerging laser diode wavelength). To stabilize the lasers, double the 1563 nm laser and lock both to the comb (we even have a 1550 nm doubling crystal and a 1550 nm fiber amp in the lab for frequency doubling the 1563 nm laser). The frequency comb will have lots of power at 781 nm and 810 nm as both are close to 780 nm (for readers in other labs, I recommend using a high finesse cavity for laser stabilization like Ref. [30] instead of a frequency comb). Hopefully, higher frequency comb power, combined with better diodes will lead to success.

8. FITTING

Armed with piles of spectroscopic data from Chapter 4 through Chapter 6, we turn our energy to inverting the experimental data into potential energy curves (PECs). PECs are commonly reported in the literature as they are compact and offer additional utility in the form of FCFs. In this chapter, I detail a joint effort with Jesús Pérez-Ríos, to bring machine learning techniques to AMO physics and use genetic algorithms to derive potentials that reproduce the experimental data.

8.1 Introduction

The cornerstone of modern chemistry is the study of molecular interactions and how these lead to all chemical reactions governing the evolution of the universe. However, the available experimental tools, such as spectroscopy and scattering observables, do not generate direct measurements of these interactions, and therefore mapping techniques that translate collisional and spectroscopic data into the underlying interactions are necessary for the chemistry and physics community. First studied in the 1930's, molecular spectral line broadening revealed the long range interactions between the molecules [83–85]. From there, better techniques have resulted in more accurate data. Modern spectroscopic techniques, such as Fourier-transform spectroscopy [86], photoassociation of ultracold atoms [87], and measurement of Feshbach resonances [88], have led to the most accurate atom-atom interaction potentials to date. In the same vein, thanks to the development of molecular beam technology, similar techniques transform scattering information of atom-molecule and molecule-molecule collisions into realistic atom-molecule and molecule-molecule potential energy surfaces [89–95].

Several fitting or inversion techniques to transform vibrational, rotational and hyperfine spectroscopic data into molecular interactions have been developed; semi-classical techniques lead to the celebrated LeRoy-Bernstein formula [96] and the RKR method

(Rydberg, Klein and Rees) [97]. For more accurate results, the inverted perturbation approach (IPA) [98,99] modifies the RKR result by solving the Schrödinger equation and adjusting the potential to better reproduce the experimental data. Many of the older techniques, share something in common: the potential can be found if a functional form is assumed. A functional form limits the search space of the optimization routine and prevents it converging to a true solution if nature escapes description by a simple analytic function. However, more modern techniques such as some variants of the IPA method [54] and machine learning techniques, and in particular genetic algorithms (GA), use non-functional based methods and the machine learning techniques present an alternative to standard fitting procedures with higher accuracy and a more general mathematically fundamental basis.

In the past 15 years, genetic algorithms have slowly crept into chemistry and physics. There are a few fields were the genetic strategy makes a lot of sense. For example, genetic algorithms have been successfully solving atomic or molecular cluster problems for years [100]. Researchers have tried out genetic algorithms in protein folding [101] and assigning absorption spectra [102, 103]. We are not even the first team to use genetic algorithms to fit diatomic potentials. Ref. [104] is the first example we know about, although their algorithm struggled to reproduce the data to better than 1 cm^{-1}. Ref. [105], advanced the technique and was able to reproduce NaLi bound states with better than 0.5 cm^{-1} accuracy using an extended-Rydberg potential [106]. And finally, Ref. [107] was able to directly fit experimental data for RbCs with an updated version of the algorithm from Ref. [105].

Our goal is to develop a real-valued genetic algorithm to directly fit point-wise potentials to experimental data. We explicitly chose a point-wise representation for most of our potentials because it frees us from the confines of potentials describable by analytic functions. Additionally, genetic algorithms tend not to be the most efficient algorithms in terms of number of function calls. We will be using a Numerov solver to calculate bound states in the potentials, and although it runs quickly at 10 ms per call, this adds up fast. Inefficient genetic algorithms can easily take 10^6 function calls to converge which would take nearly 3 hours to converge. While this would be acceptable as a final run time, it is nowhere near acceptable when developing a method and there are likely things not working quite right. Much of our work will be on reducing the number of functions calls

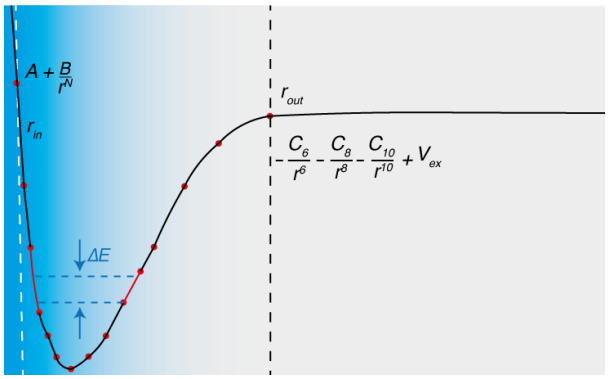

Fig. 8.1. Graphical potential representation corresponding to Eq. 8.1. For $r < r_{\text{in}}$ we use extrapolate inward with an inverse power law. This short range region has almost no impact on the observables (*i.e.* bound state locations). In the middle, between r_{in} and r_{out}, we use a point-wise representation, between which we interpolate with cubic splines. For $r > r_{\text{out}}$, we use a C_6 potential to most accurately capture the physics. The section highlighted in red illustrates that the local slope of the potential determines ΔE, the difference in binding energy of adjacent vibrational states.

the genetic algorithm takes via tricks, careful algorithm design and tedious optimization of algorithm parameters. Our final algorithm takes around 5×10^4 function calls which results in much more reasonable 8 minute run times.

8.2 Potential Representation

We use a potential representation pioneered by Tiemann and coworkers [108], shown graphically in Fig. 8.1. In it, we represent the potential as

$$V(r) = \begin{cases} A + \frac{B}{r^N} & r < r_{\text{in}} \\ \text{point} - \text{wise} & r_{\text{in}} < r < r_{\text{out}} \\ -\frac{C_6}{r^6} - \frac{C_8}{r^8} - \frac{C_{10}}{r^{10}} + V_{\text{ex}} & r_{\text{out}} < r \end{cases} . \tag{8.1}$$

Inside the point-wise region, we interpolate between the points with cubic splines. We directly include the C_6 coefficient in our fit while A, B, N and C_8 are fitted for a smooth connection between the different regions.

We chose this potential representation for a few reasons. First, we like potentials that do not rely on a functional form. Although as humans, we all like nice compact functions,

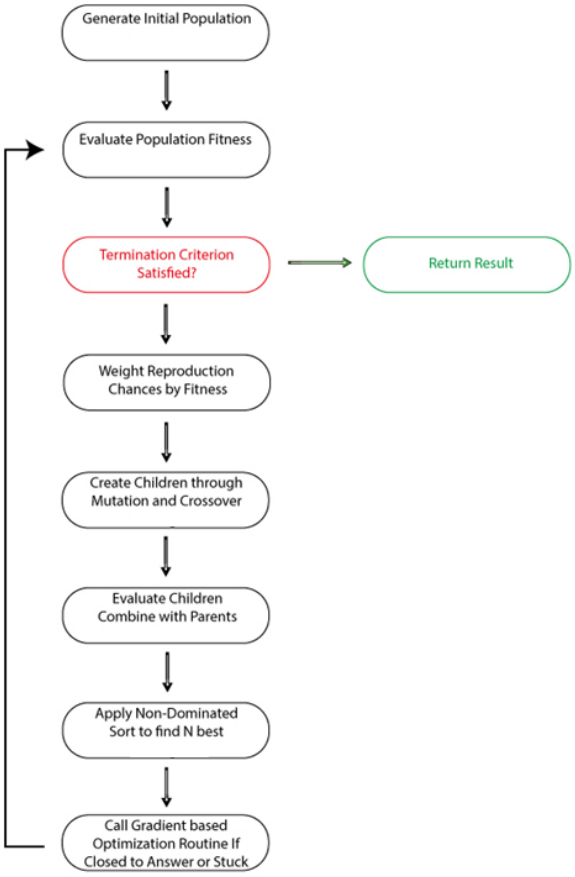

Fig. 8.2. Flow chart illustrating the main loop of the genetic algorithm.

Nature does not share our view and normally real systems escape easy description with functions. Diatomic potential energy curves are no different and using a point-wise potential, between which we interpolate with cubic splines allows us to represent a much larger space than any function-based potential could. Second, the long range form of this potential does a very good job of capturing the physics. As indicated by the success of the LeRoy-Bernstein formula [96], which uses C_6 to predict bound states, the C_6 coefficient almost captures the entirety of the long range physics and directly fitting C_6 is desirable.

8.3 Genetic Algorithm

A flow chart for our algorithm is shown in Fig. 8.2 and each step will be discussed in the following sections. Our first step is to create an initial population to span the possible

solution space as best as possible. Here, we turn to a basic function-based potential. We use a Morse potential [109] which represents the potential as

$$V(r) = D_e[e^{-2\frac{r-r_e}{\Delta r}} - 2e^{-\frac{r-r_e}{\Delta r}}], \tag{8.2}$$

to generate a spread of potentials around the 'true' potential at the beginning of our fitting routine. The three parameters in the Morse potential, D_e which is the potential dissociation energy, r_e which is the equilibrium internuclear separation, and Δr which sets the width of the potential, are commonly reported in literature. We use this function-based potential because the point-wise potentials are unstable to large perturbations to their points (*i.e* they pick up extra minima and crash our Numerov solver), whereas the function-based potential will always be solvable under perturbations to its parameters. In an attempt to span the possible solution space, we generate N Morse potentials with each of the three parameters multiplied by $0.9 + 0.2x$, where x is a uniformly distributed random variable between zero and one, and N is the number of genes in the population. We evaluate our random Morse potentials along the non-uniform r-space grid which all the genes in the population share. These N Morse potentials turned into point-wise potentials form the first generation in our algorithm.

8.3.1 Fitness Evaluation

To evaluate the fitness of each of the N genes in the populations, we calculate the bound states and rotational constants of the gene's potential using a Numerov solver [110] based on Ref. [72] (after discarding any potentials that have too many minima). The simplest way to compare the calculated constants to experiment is via

$$\bar{\chi}^2 = \frac{1}{N_v}\sum_v \frac{(E_{v,\text{ exp.}} - E_{v,\text{ pot.}})^2}{\sigma^2_{E,\text{ exp.}}} + \frac{1}{N_v}\sum_v \frac{(B_{v,\text{ exp.}} - B_{v,\text{ pot.}})^2}{\sigma^2_{B_v,\text{ exp.}}}, \tag{8.3}$$

where N_v is the total number of vibrational states with experimental data, $E_{v,\text{ exp.}}$ is the experimental binding energy of the v^{th} vibrational level, $E_{v,\text{ pot.}}$ is the corresponding calculated binding energy, and $\sigma_{E,\text{ exp.}}$ is the experimental uncertainty of the v^{th} vibrational level. The second term in Eq. 8.3 compares experimental and calculated rotational constants following the same logic as for vibrational binding energies.

The approach of Eq. 8.3 has several problems that we will explain here and illustrate later. First, the energies of the vibrational bound states and their corresponding

rotational constants depend on different parts of the potential. For example, the 0^{th} vibrational level has a binding energy of approximately $D_e + \frac{1}{2}\omega_e$, where ω_e measures the curvature of the bottom of the potential well and D_e simply measures its depth. For comparison, the rotational constant, $B_v \propto \frac{1}{\mu \bar{r}^2}$ [66], looks at the reduced mass μ while $\bar{r}^2$ measures the average internuclear separation of this state. Second, there is no guarantee that the sum over the vibrational binding energy terms, resulting in

$$\bar{\chi}^2_{\text{vibration}} = \frac{1}{N_v} \sum_v \frac{(E_{v,\text{ exp.}} - E_{v,\text{ pot.}})^2}{\sigma^2_{E,\text{ exp.}}}, \tag{8.4}$$

is even remotely close in magnitude to the sum over the rotation terms, resulting in

$$\bar{\chi}^2_{\text{rotation}} = \frac{1}{N_v} \sum_v \frac{1}{N_v} \sum_v \frac{(B_{v,\text{ exp.}} - B_{v,\text{ pot.}})^2}{\sigma^2_{B_v,\text{ exp.}}}. \tag{8.5}$$

Any time $\bar{\chi}^2_{\text{vibration}}$ is several orders of magnitude different from $\bar{\chi}^2_{\text{rotation}}$, the fitting routine can accidentally trap itself. Finally, there is a hidden problem in that $E_{v,\text{ pot.}}$ depends on both getting a correct value for $E_{v-1,\text{ pot.}}$ and the local slope. This sets a series of sharp cliffs in the solution space where the fitting routine can correctly match the binding energies for a subset of the vibrational levels but not the levels below them. For example, the algorithm can correctly match $v = 5$ - 20 while having incorrect values for $v = 0$ - 4. In this scenario fixing $v = 0$ - 4 requires messing up $v = 5$ - 20 which can often be prohibitively expensive for the fitting algorithm. It is a bit unusual to not compare to $E(v, J)$ directly, but we do it this way to separate rotational information from vibrational information, whereas comparing to $E(v, J)$ convolves the two making the problem harder.

The problems with using Eq. 8.3 as the fitness function can be solved with a little bit of trickery. For example, we will compare the calculated vibrational binding energies to the experimental data via

$$\bar{\chi}^2_{\text{vibration}} = \frac{1}{N_v} \sum_v 0.1 \frac{(E_{v,\text{ exp.}} - E_{v,\text{ pot.}})^2}{\sigma^2_{E,\text{ exp.}}} + 0.9 \frac{[(E_{v,\text{ exp.}} - E_{v-1,\text{ exp.}}) - (E_{v,\text{ pot.}} - E_{v-1,\text{ pot.}})]^2}{\sigma^2_{E,\text{ exp.}}}. \tag{8.6}$$

On the surface Eq. 8.6 looks functionally identical to the first term in Eq. 8.3, as any potential that matches the difference in binding energies between neighboring states will also correctly match their absolute binding energies. However, when the potential is partially correct, the difference in binding energies only depends on the local slope of the

potential. Returning to our scenario from above, now the fitting routine can modify the points around $v = 0$ - 4 which will push around $v = 5$ - 20, but this time the cost is small. Although $v = 5$ - 20 will bounce around energetically as the fitting routine works on improving the binding energy of $v = 0$ - 4, they will do so as a group and the difference between their binding energies will be fairly constant. We add in a 10 % contribution to our $\bar{\chi}^2_{\text{vibration}}$ calculation that pays attention to the absolute binding energy of the vibrational states to prevent drifts from accumulating in deep potential wells.

To solve the problems with Eq. 8.3 that result from mismatches between the rotational information and vibrational information, we can consider $\bar{\chi}^2{}_{\text{vibration}}$ and $\bar{\chi}^2_{\text{rotation}}$ independently and on equal footing. For the time being, when we calculate $\bar{\chi}^2$, we will do so as the two-vector

$$\langle \bar{\chi}^2_{\text{vibration}},\ \bar{\chi}^2_{\text{rotation}} \rangle. \tag{8.7}$$

Additionally, our calculation of $\bar{\chi}^2_{rotation}$ will mirror the calculation of $\bar{\chi}^2_{\text{vibration}}$:

$$\bar{\chi}^2_{\text{rotation}} = \frac{1}{N_v} \sum_v 0.1 \frac{(B_{v,\ \text{exp.}} - B_{v,\ \text{pot.}})^2}{\sigma^2_{B,\ \text{exp.}}} + 0.9 \frac{[(B_{v,\ \text{exp.}} - B_{v-1,\ \text{exp.}}) - (B_{v,\ \text{pot.}} - B_{v-1,\ \text{pot.}})]^2}{\sigma^2_{B_v,\ \text{exp.}}}. \tag{8.8}$$

8.3.2 Weighting

There are two parts to selection in our genetic algorithm. The first, which we will talk about in this section is that the different genes in the population get a weighted chance to be picked for reproduction based on their fitness relative to other members of the population. We calculate the weight for each gene as

$$w_i = \frac{\sum_j \left(\frac{\vec{n}_j}{\bar{\chi}^2_{i,j}} \right)^{\frac{1}{x}}}{\sum_{i,j} \left(\frac{\vec{n}_j}{\bar{\chi}^2_{i,j}} \right)^{\frac{1}{x}}}, \tag{8.9}$$

where $x = 2$, i indexes the gene in the population, j indexes the two-vector $\bar{\chi}^2$ from Eq. 8.7, $\vec{n}$ is a two-vector holding the median value of $\bar{\chi}^2$ for the population, and the sum on the bottom normalizes the weights so their sum is one. The goal here is to speed up convergence by creating more children from successful genes. We choose to use the median value of $\bar{\chi}^2_j$ for $\vec{n}_j$ because $\bar{\chi}^2_j$ can easily vary across several orders of magnitude

making the arithmetic mean inaccurate. Additionally, we take the x-th root of $\frac{\vec{n}_j}{\bar{\chi}^2_{i,j}}$ in an attempt to reduce the effect of extreme solutions which will have a very large $\bar{\chi}^2_{\text{vibration}}$ and a very small $\bar{\chi}^2_{\text{rotation}}$ (or vice-versa).

8.3.3 Adaptive Recombination Methods

Adaptive recombination methods are essential to real-valued genetic algorithms. The original genetic algorithms were binary coded, which means that they represent their genes as a long string of 0s and 1s internally [111]. This creates a very natural mutation operator that randomly flips bits with some probability and an equally natural crossover operator that exchanges information above and below a cut point in the string. Defining a good mutation operator and crossover operator for real-valued algorithms is much harder. A natural mutation operator adds a normally distributed, zero-mean random variable to each entry in its gene with some probability. As the algorithm descends to a solution it will need to perturb each entry in its gene less and less, which can be done by simultaneously decreasing the variance of the random variable. However, this leads to problem specific and inefficient solutions. Adaptive methods decrease the perturbation applied to the gene as the algorithm descends to a solution by a variety of widely applicable heuristics. All of these heuristics somehow depend on the euclidean distance between genes in the population decreasing as the algorithm descends. We evaluated three adaptive recombination methods from the literature, before constructing our own tailored to our problem.

For our test problem we will be using a modified version of our full problem, solving for a high accuracy lithium-rubidium (LiRb) $X\ ^1\Sigma^+$ potential. The full details of this problem are found in section 8.4, and we will only note how we modified it here. To reduce the complexity of this problem for quick testing, we increased the uncertainties we input to the solver and then limited the solver to only ten thousand calls of its Numerov solver (it is possible to have more $\bar{\chi}^2$ calls because the $\bar{\chi}^2$ function will not call the Numerov solver if the potential has too many minima). Specifically, we dropped the uncertainty of the vibrational binding energies from 0.02 cm^{-1} to 0.2 cm^{-1} and we removed the calculation of rotational coefficient errors. Removing the calculation of rotational errors allows us to test the solver capabilities without having to deal with the

complexity of a multi-objective problem, detailed in section 8.3.5. Additionally, the error bars in this section result from repeating each group of settings ten times, to account for the stochastic nature of genetic algorithms. Finally, we will be testing each parameter of the algorithm while holding the others constant (the implicit assumption in this approach is that the mutual correlation between the parameters is small).

Differential Evolution

One of the most successful adaptive recombination methods for real-valued genetic algorithms is called Differential Evolution (DE) [112]. Differential evolution works as follows.

1) For each gene in the population, labeled $\vec{x}_i$, select 3 other genes at random from the population (we weight this by Eq. 8.9 which is unusual, but helps with convergence). These will be M dimensional vectors, where M is one plus the number of points in the point-wise potential (+1 for C_6), labeled $\vec{x}_1$, $\vec{x}_2$, and $\vec{x}_3$.

2) Create a new vector $\vec{u}$ according to

$$\vec{u} = \vec{x}_1 + F(\vec{x}_2 - \vec{x}_3), \tag{8.10}$$

where F is a global parameter.

3) Recombine the new vector, $\vec{u}$, with $\vec{x}_i$ according to

$$\vec{v}_j = \begin{cases} \vec{u}_j & \text{If } a < CR \\ \vec{x}_{i,j} & \text{If } a > CR \end{cases}, \tag{8.11}$$

where CR is the second global parameter, a is a uniformly distributed random variable between zero and one (generated for each j) and the index j runs between zero and M.

4) If $\vec{v}$ scores better than $\vec{x}_i$, $\vec{v}$ is added to the next generation, otherwise $\vec{x}_i$ is added.

Shown in Fig. 8.3, is our work to optimize the different parameters for the test problem. From panel **(a)** we see that either a large or a small crossover rate (CR) work best. This corresponds to swapping only a small number of genes between $\vec{u}$ and $\vec{x}_i$. Second from panel **(b)**, it looks like larger F is better, although this is deceiving. In reality, the higher F runs 'cheated' and created a large number of solutions that had extra minima which were not evaluated by the Numerov solver. The result is that $F = 0.7$ had nearly

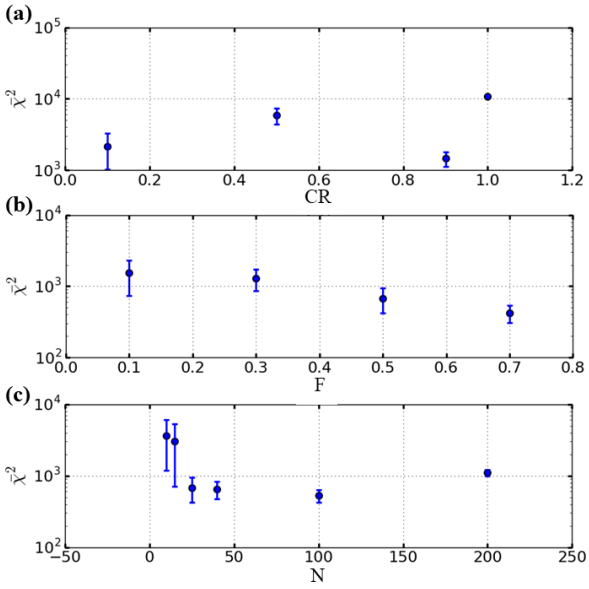

Fig. 8.3. Optimization of Differential Evolution. All subplots have a log scale on the y-axis. **(a)** Optimization of CR. The other two parameters were set to $F = 0.5$ and $N = 25$. **(b)** Optimization of F while holding $CR = 0.1$ and $N = 25$. **(c)** Optimization of N. We fixed $F = 0.5$ and $CR = 0.1$.

twice the number of generations as $F = 0.1$ which helps explain its better success. This pattern continued for as large as we were willing to make F. However, our ultimate goal is a program that runs quickly, and although the Numerov solver is the slowest piece, eventually the raw number of generations for large F values added up resulting in much longer solver run times than for smaller F values. As a compromise we will be using $F = 0.5$ to compare to the other recombination methods. Finally in panel **(c)**, we see that increasing N, the number of genes in the population, helps until around $N = 100$. Additionally, increasing N makes the different runs more consistent, reducing the standard error of the mean. We concluded that $CR = 0.1$, $F = 0.5$, $N = 100$ were the optimal settings for differential evolution for fitting point-wise potentials to experimental data.

Simulated-Binary Crossover

The second recombination operator we investigated is simulated-binary crossover (sbx). Simulated-binary crossover works on a weighted average of the two parent genes

and was originally developed by Ref. [113]. It appears in this chapter because simulated-binary crossover was found to be very successful on a similar problem in Refs. [105, 107, 114]. However, it also needs an independent mutation operator. Ref. [105] suggests using a normal random variable which runs back into all the issues we were trying to avoid. We hybridized the simulated-binary crossover with steps 1 and 2 of the differential evolution algorithm for an adaptive mutation operation.

Our version of simulated binary crossover works as follows.

1) For each gene in the population, labeled $\vec{x}_i$, select 3 other genes at random from the population, labeled $\vec{x}_1$, $\vec{x}_2$, and $\vec{x}_3$.

2) Create a new vector $\vec{u}$ according to Eq. 8.11.

3) Perform simulated-binary crossover between $\vec{u}$ and $\vec{x}_i$.

a) Calculate a random variable $\mu \in [0,\ 1]$.

b) Calculate

$$\beta = \begin{cases} (2\mu)^{\frac{1}{\eta+1}} & \text{if } \mu \leq 0.5 \\ [\frac{1}{2}(1-\mu)]^{\frac{1}{\eta+1}} & \text{if } \mu > 0.5 \end{cases}, \tag{8.12}$$

where η is a global parameter.

c) Calculate the children vectors

$$\vec{v}_1 = \frac{1}{2}[(1+\beta)\vec{u} + (1-\beta)\vec{x}_i] \tag{8.13}$$

$$\vec{v}_2 = \frac{1}{2}[(1-\beta)\vec{u} + (1+\beta)\vec{x}_i], \tag{8.14}$$

where $\vec{v}_1$ and $\vec{v}_2$ are the resultant children and $\vec{u}$ are $\vec{x}_i$ the parent vectors.

4) Randomly pick one of $\vec{v}_1$ and $\vec{v}_2$, called $\vec{v}$. If $\vec{v}$ scores better than $\vec{x}_i$, $\vec{v}$ is added to the next generation, otherwise $\vec{x}_i$ is added.

Fig. 8.4 shows our work on optimizing simulated-binary crossover for our test problem. Again, we have three parameters to optimize, η, F, and N. We started with η, which Ref. [105] recommends to set at 3. Our understanding of how simulated-binary crossover works, is that it is a weighted average of the two parents and η controls how close the children will be to the parents. Larger η results in β closer to one and $\vec{v}_1$ becomes approximately $\vec{u}$ while $\vec{v}_2$ starts to approximate the other parent $\vec{x}_i$. As seen in Fig. 8.4 panel **(a)**, the value of η doesn't effect things much, with larger values doing ever so slightly better. However, Fig. 8.4 panels **(b)** and **(c)** show that the other two parameters

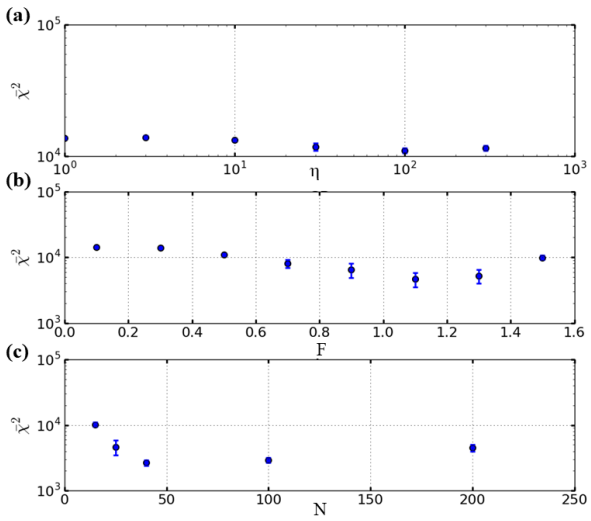

Fig. 8.4. Optimization of simulated-binary crossover. All subplots have a log scale on the y-axis. **(a)** Optimization of η. We set $F = 0.5$ and $N = 25$. For this plot the x-axis also uses a log scale. **(b)** Optimization of F with $\eta = 100$ and $N = 25$. **(c)** Optimization of N with $\eta = 100$ and $F = 1.1$.

F and N are much more important. We found that $F = 1.1$ and $N = 40$ worked best by a large margin, which we will be using, along with $\eta = 100$ to compare to the other recombination operators.

In light of how well of how well simulated-binary crossover works in Ref. [105], which is solving a similar problem, and how poorly it works in our example, a valid question is why. Ref. [115] suggests a possible explanation. Simulated-binary crossover preferentially searches along the coordinate axes which is terribly suited for our problem. Because we use a point-wise potential with cubic spline interpolation, moving individual points, like simulated-binary crossover is likely to do, without also moving the neighboring points is just not very effective. This type of operation is likely to result in extra minima and non-physical potential with many changes in the sign of the first derivative.

Parent-Centric Crossover

Parent-centric crossover (pcx) is the third operator we tried, from Ref. [116]. In many ways, parent-centric crossover is an update to simulated-binary crossover and was even developed by the same research team. We investigated its performance on our test prob-

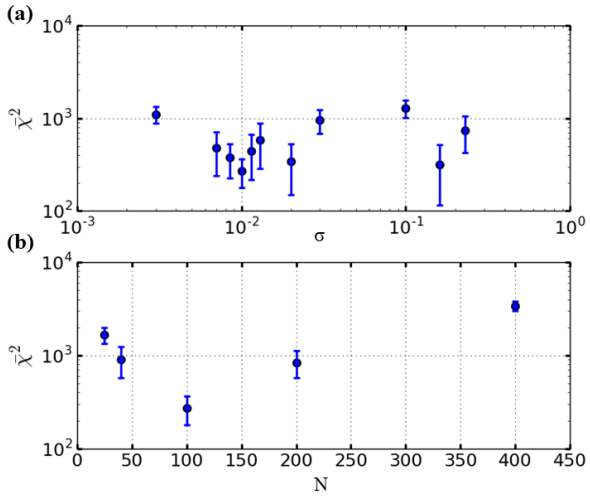

Fig. 8.5. Optimization of the PCX operator. All subplots have a log scale on their y-axis and we set two of the parent-centric crossover parameters, $\mu = 3$ and $\lambda = 2$, to values recommended by Ref. [116] and did not try to optimize them. **(a)** Search for an optimal σ with $N = 100$. **(b)** Optimization of N with $\sigma = 0.01$.

lem because it does not require an external mutation operator and claims to outperform differential evolution. It also carries the rare distinction of being an evolutionary algorithm that can outperform gradient based search methods on unimodal problems (*i.e.* no local minima) [116]. Parent-centric crossover works as follows.

1) Pick μ parents, with vectors $\vec{x}_i$, from the population of N genes. μ is a fixed global parameter and is set to 3 as recommended by Ref. [116].

2) Compute the mean vector $\vec{g}$ from the $\vec{x}_i$ parent vectors. For each of λ children, select one of the parents denoted $\vec{x}_p$ and compute $\vec{d}_p = \vec{x}_p - \vec{g}$. Ref. [116] recommends setting $\lambda = 2$. Additionally, calculate the perpendicular distance D_i to the line $\vec{d}_p$ for each of the other parents and compute the average $\bar{D}$.

3) Create each child by

$$\vec{v} = \vec{x}_p + w_0 \vec{d}_p + \sum_{i=1}^{\mu-1} w_i \bar{D} \vec{e}_i, \tag{8.15}$$

where $\vec{e}_i$ span the subspace perpendicular to $\vec{d}_p$, and w_i are normally distributed, zero-mean random variables with variance σ^2.

4) The best μ of the children and the parents are returned to the population for the next generation.

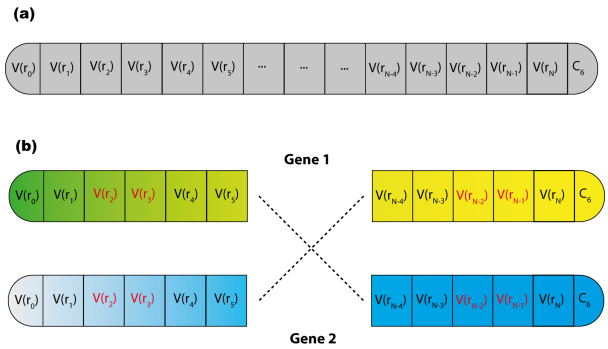

Fig. 8.6. Graphical one point crossover. **(a)** Encoding of potential onto a gene. **(b)** Illustration of one point crossover, where the genes exchange information on inner and outer walls of the potential. Entries in red correspond to highlighted section of the potential in Fig. 8.1.

Because there is an overhead cost associated with each new generation (mostly from sorting the population according to fitness) we modified parent-centric crossover to create N children every generation, by picking N/λ groups of parents. Fig. 8.5 shows our work on optimizing parent-centric crossover. We left $\mu = 3$ and $\lambda = 2$ upon recommendation of Ref. [116] and focused on optimizing N and σ. Like Ref. [116], we found that $N = 100$ works best (which also gives us confidence in μ and λ being close to optimum). However, we had to do quite a bit of searching to find a value for σ that works well. Ultimately, we decided that $\sigma = 0.01$ was the best value.

We should also take a minute and talk about the performance of parent-centric crossover. Genetic algorithms are inherently stochastic, and all of our recombination methods have a spread of results for any given settings of their global parameters across the ten trials we did, but parent-centric crossover had the widest spread by quite a margin. When parent-centric crossover worked, it was the only recombination method to reach the termination threshold for our test problem. However, it also had (comparatively) spectacular failures where it would get stuck on a local minima quickly and never recover. This pattern re-emerges in later sections.

One Point Crossover

After working with the different crossover operators, we liked the relative simplicity of differential evolution, but we were not impressed with its performance. However, we had

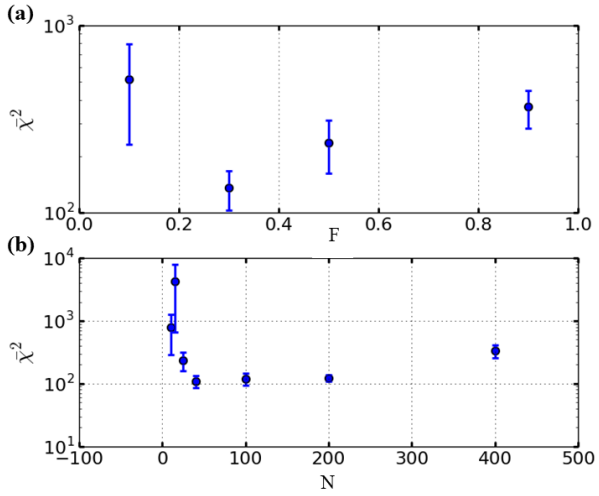

Fig. 8.7. Optimization of one point crossover. All subplots have a log scale on their y-axis. **(a)** Optimization of F with $N = 25$. **(b)** Optimization of N, with $F = 0.5$.

a theory that its crossover operator was the problem, not the mutation operator. Because we use a point-wise potential and interpolate between the points with cubic splines for most of the potential, adjacent points are strongly correlated. The differential evolution crossover operator will break up these correlations because it exchanges points at random. Instead we propose a modified version of differential evolution for our problem that we call one point crossover and works as follows.

1) Select 4 genes at random from the population, labeled $\vec{x}_1$, $\vec{x}_2$, $\vec{x}_3$, and $\vec{x}_4$.

2) Create a new vector $\vec{u}$ according to Eq. 8.10.

3) Recombine the new vector, $\vec{u}$, with $\vec{x}_4$ according to

$$\vec{v}_j = \begin{cases} \vec{u}_j & \text{If } j < P \\ \vec{x}_{4,j} & \text{If } j > P \end{cases}, \tag{8.16}$$

where P is a uniformly distributed random variable between 1 and M - 1, and j indexes the vectors from zero to M.

4) If $\vec{v}$ scores better than $\vec{x}_4$, $\vec{v}$ is added to the next generation, otherwise $\vec{x}_4$ is added.

Our one point crossover operator has two global parameters to optimize, N and F. Fig. 8.7 shows our work to optimize one point crossover, from which we conclude that $N = 100$ and $F = 0.4$ are about optimum.

$\bar{\chi}^2$ Method	DE	SBX	One Pt.	PCX
Eq. 8.3	1070 (310)	4600 (600)	130 (25)	480 (280)
Eq. 8.6	420 (120)	2660 (270)	80 (13)	270 (90)

Table 8.1.
Performance of the different recombination operators on the test problem. The average $\bar{\chi}^2$ error is reported, with the standard error of the mean in parentheses. For this test, the second term in Eq. 8.3 was ignored. The error of the mean is from repeating each test problem ten times to account for the stochastic nature of genetic algorithms.

Table 8.1 shows the performance of the different recombination operators with optimum settings of their individual parameters. First, it is clear that all the algorithms perform better when using Eq. 8.6 to calculate $\bar{\chi}^2$ opposed to Eq. 8.3 (recall, for this test, we neglected the rotational terms in Eq. 8.3). To do our best to make this a fair comparison when using Eq. 8.3, we let the solver descend while using Eq. 8.3 to calculate $\bar{\chi}^2$, but after the algorithm reached its ten thousand Numerov call limit, we recalculated $\bar{\chi}^2$ with Eq. 8.6. Eq. 8.6 and Eq. 8.3 will give different numbers of $\bar{\chi}^2$ for the same potential, but these differences are largest when the potential is inaccurate and become small when the potential is close to converged. Second, Table 8.1 demonstrates that one point crossover performs quite well on the test problem with parent-centric crossover coming in second place. As mentioned earlier, we think parent-centric crossover is worth a second look as about half the time it did fantastic.

8.3.4 Local Optimization

As is common with evolutionary algorithms, we hybridize our algorithm with a local, gradient based solver [105, 117]. Although genetic algorithms are good at handling problems with lots of local minima, they are slow and take a huge number of function calls to descend to the bottom of the global minima. Conversely, gradient based solvers are very efficient at descending inside a local area, but are terrible at finding global minima, provided the solution landscape has a critical mass of local minima. In a perfect world, the genetic algorithm will find the global minima, and then hand-off the problem to the gradient solver which will quickly descend to the bottom of the global minima. A more

common scenario is for the genetic algorithm to hand-off the problem to the gradient solver which will hit a local minimum and then it is up to the genetic algorithm to 'jump' out of the local minima and continue in its search for the global minimum. Still, hybridizing genetic algorithms with local gradient based solvers can be hugely beneficial.

In our algorithm, we call a limited-memory Broyden-Fletcher-Goldfarb-Shanno bounded solver (L-BFGS-B) [118], which is a quasi-Newton method that is designed to work well with a large number of variables, under one of two conditions. First, we will call the gradient based solver if the genetic solver is stuck, which we consider to be 20 generations without any improvement. Second, when the solver is close to converging, which we consider to be when $\bar{\chi}^2 < 10\ \bar{\chi}^2_{\text{target}}$, we will call the gradient based solver. When we were testing the performance of the different recombination operators in section 8.3.3, this feature was disabled.

8.3.5 Multi-objective genetic algorithms

As mentioned in section 8.3.1, there are a several pitfalls involved in comparing vibrational and rotational information. There we mentioned that our solution will be to consider vibrational errors and rotational errors independently of each and on equal footing by storing $\bar{\chi}^2$ as a two-vector illustrated in Eq. 8.7. Of course, optimizing a two-vector presents its own set of unique challenges. In the literature, this is considered a multi-objective problem, and lucky for us, multi-objective genetic algorithms have been an active area of research [119–121].

To understand how multi-objective optimization algorithms work, we will need to introduce a few concepts. First, there is domination and one vector $\vec{u}$ is said to dominate another vector $\vec{v}$ if

$$\vec{u}_i < \vec{v}_i \ \forall\ i, \tag{8.17}$$

where i indexes the vectors. Second, multi-objective algorithms seek to derive a so called pareto-optimum front, shown in Fig. 8.8. A pareto front is a set of vectors in which no vector dominates another vector.

As can be seen in Fig. 8.8, this enables the algorithm to make the trade-off where it makes one coordinate much worse in exchange for slightly improving the other coordinate. Ultimately, we don't care about spanning an optimal front, but it is the trade off property

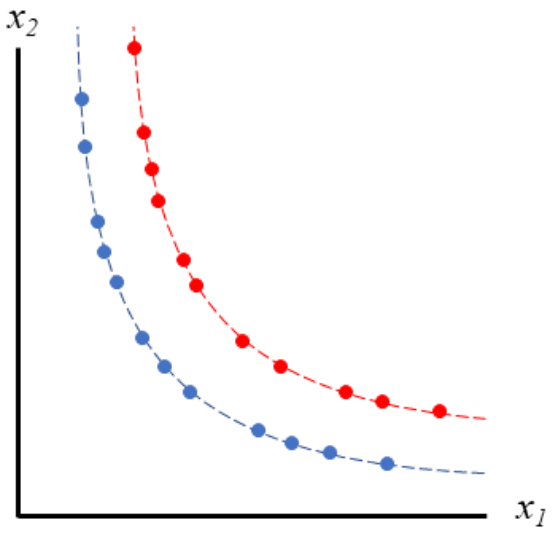

Fig. 8.8. Pareto-fronts for a sets of two-vectors, where x_1 and x_2 are the two objectives the algorithm is trying to minimize. No two vectors in the set of red or blue points are such that one dominates the other, although for each red point, there is at least one blue point that dominates it.

we are after. If we look at the straight sum of $\bar{\chi}^2_{\text{vibration}} + \bar{\chi}^2_{\text{rotation}}$, this trade-off looks really bad, but the multi-object algorithm acknowledges that sometimes this trade off is beneficial in the long run. Functionally what happens is that early in the algorithm descent, it will improve $\bar{\chi}^2_{\text{rotation}}$ at a huge cost in $\bar{\chi}^2_{\text{vibration}}$. This move is prohibited by looking at the sum, but allowed by the multi-objective algorithm. As the algorithm continues its descent, it will improve $\bar{\chi}^2_{\text{vibration}}$ at very little cost to $\bar{\chi}^2_{\text{rotation}}$. Then, looking at the descent path of the two strategies, a straight sum versus the multi-objective algorithm, the sum method will get stuck eventually with a somewhat optimal $\bar{\chi}^2_{\text{vibration}}$ but a terrible $\bar{\chi}^2_{\text{rotation}}$ and no method for making the necessary sacrifices to $\bar{\chi}^2_{\text{vibration}}$. From a physics perspective, the binding energies can be mostly matched by distorting the potential while sitting at the wrong equilibrium inter-nuclear separation, r_e and this will happen with the straight sum method fairly often.

For the multi-objective algorithm, selection takes a different form. For the recombination methods we explored, most would compare the fitness of the children to one or multiple parents and then keep the best of these. For a multi-objective algorithm, the goal is to sort the solutions into different pareto fronts and then keep the best fronts. To maintain elitism (which is a fancy way of saying that you always keep the best solutions),

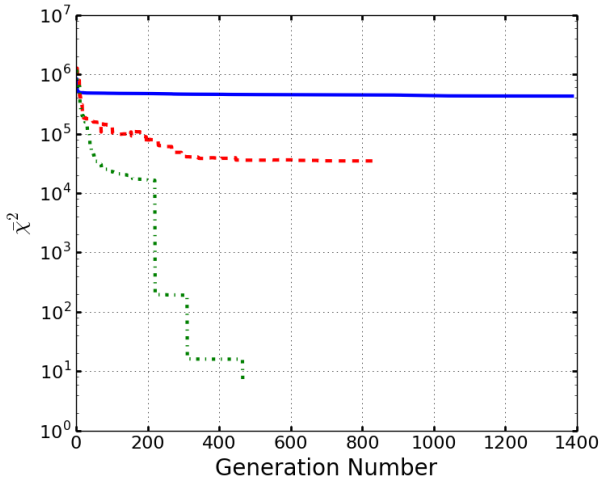

Fig. 8.9. Convergence of the genetic algorithm for LiRb $X\ ^1\Sigma^+$ potential problem working with the one point crossover operator. Solid blue trace uses a single-objective algorithm calculating $\bar{\chi}^2$ = Eq. 8.6 + Eq. 8.8. Dashed red trace uses a multi-objective algorithm calculating $\bar{\chi}^2$ with Eq. 8.3. Dash-dotted green trace uses a multi-objective algorithm calculating $\bar{\chi}^2$ with Eq. 8.6 and Eq. 8.8. The sharp drops in the green trace correspond to calls to the gradient based solver.

the parents and children are usually combined before sorting. We will be using the fast non-dominated sorting algorithm from NSGA-II [119] to sort into pareto-fronts and the improved crowding sort algorithm from Ref. [122] to decide how to break ties when only a fraction of a front gets to be added to the next generation.

As a simple demonstration of the power of the multi-objective approach, we present Fig. 8.9. In Fig. 8.9, we plot the descent of the genetic algorithm using the optimized one point crossover method as a function of generation number (which is a loose approximation of number of Numerov calls). The three different traces compare how the algorithm performs when using the multi-objective implementation (with two different $\bar{\chi}^2$ calculation methods) to the single-objective implementation. Without any doubt, Fig. 8.9, shows that the multi-objective implementations outperform the single-objective implementation.

v	$E_{\text{exp.}}$ (cm^{-1})	$E_{\text{pot.}}$ (cm^{-1})	B_v Exp. (cm^{-1})	B_v Pot. (cm^{-1})
0	-5830.84 (0.02)	-5830.84	0.2158 (3e-05)	0.2159
1	-5637.86 (0.02)	-5637.86	0.2140 (3e-05)	0.2141
2	-5447.13 (0.02)	-5447.14	0.2130 (3e-05)	0.2129
3	-5258.67 (0.02)	-5258.67	0.2110 (3e-05)	0.2110
4	-5072.49 (0.02)	-5072.49	0.2094 (3e-05)	0.2093
5	-4888.61 (0.02)	-4888.60	0.2077 (3e-05)	0.2079
6	-4707.05 (0.02)	-4707.10	0.2064 (3e-05)	0.2064
7	-4527.84 (0.02)	-4527.83	0.2049 (3e-05)	0.2047
8	-4351.00 (0.02)	-4350.97	0.2031 (3e-05)	0.2031
9	-4176.56 (0.02)	-4176.53	0.2013 (3e-05)	0.2013
10	-4004.54 (0.02)	-4004.55	0.1994 (3e-05)	0.1996
11	-3834.99 (0.02)	-3835.01	0.1977 (3e-05)	0.1978
12	-3667.94 (0.02)	-3667.96	0.1959 (3e-05)	0.1959
13	-3503.42 (0.02)	-3503.43	0.1940 (3e-05)	0.1940
14	-3341.47 (0.02)	-3341.48	0.1921 (3e-05)	0.1920
15	-3182.15 (0.02)	-3182.14	0.1903 (3e-05)	0.1901
16	-3025.50 (0.02)	-3025.48	0.1880 (3e-05)	0.1881
17	-2871.57 (0.02)	-2871.55	0.1860 (3e-05)	0.1860
18	-2720.41 (0.02)	-2720.41	0.1840 (3e-05)	0.1840
19	-2572.10 (0.02)	-2572.11	0.1817 (3e-05)	0.1819
20	-2426.69 (0.02)	-2426.67	0.1797 (3e-05)	0.1797
21	-2284.25 (0.02)	-2284.22	0.1772 (3e-05)	0.1774
22	-2144.86 (0.02)	-2144.88	0.1748 (3e-05)	0.1749
23	-2008.61 (0.02)	-2008.69	0.1724 (3e-05)	0.1725
24	-1875.58 (0.02)	-1875.64	0.1701 (3e-05)	0.1699
25	-1745.87 (0.02)	-1745.83	0.1674 (3e-05)	0.1672

Table 8.2.
Bound states and errors in the first half of the LiRb $X\ ^1\Sigma^+$ potential. Blank entries denote states for which there is no experimental data.

v	$E_{\text{exp.}}$ (cm^{-1})	$E_{\text{pot.}}$ (cm^{-1})	B_v Exp. (cm^{-1})	B_v Pot. (cm^{-1})
26	-1619.57 (0.02)	-1619.52	0.1643 (3e-05)	0.1643
27	-1496.80 (0.02)	-1496.83	0.1613 (3e-05)	0.1613
28	-1377.68 (0.02)	-1377.72	0.1585 (3e-05)	0.1584
29	-1262.33 (0.02)	-1262.27	0.1553 (3e-05)	0.1552
30	-1150.88 (0.02)	-1150.86	0.1518 (3e-05)	0.1519
31	-1043.49 (0.02)	-1043.49	0.1485 (3e-05)	0.1485
32	-940.30 (0.02)	-940.27	0.1447 (3e-05)	0.1449
33	-841.48 (0.02)	-841.48	0.1409 (3e-05)	0.1410
34	-747.21 (0.02)	-747.25	0.1368 (3e-05)	0.1369
35	-657.67 (0.02)	-657.71	0.1328 (3e-05)	0.1326
36	-573.07 (0.02)	-573.02	0.1280 (3e-05)	0.1280
37	-493.60 (0.02)	-493.57	0.1229 (3e-05)	0.1229
38	-419.48 (0.02)	-419.56	0.1176 (3e-05)	0.1176
39	-350.94 (0.02)	-351.00	0.1124 (3e-05)	0.1122
40	-288.20 (0.02)	-288.16	0.1061 (3e-05)	0.1058
41	-231.49 (0.02)	-231.45	0.0996 (0.005)	0.0999
42	-181.02 (0.02)	-181.00	0.0930 (0.005)	0.0920
43	-136.98 (0.02)	-136.97	0.0854 (0.005)	0.0861
44	-99.51 (0.02)	-99.5	0.0777 (0.005)	0.0741
45		-76.94		0.0557
46		-63.18		0.0460
47		-48.97		0.0530
48		-32.19		0.0517
49		-15.24		0.0503
50	-1.82 (0.02)	-1.81		0.0274
51	-0.41 (0.02)	-0.39	0.0133 (0.01)	0.0159

Table 8.3.
Bound states and errors in the second half of the LiRb $X\ ^1\Sigma^+$ potential. Blank entries denote states for which there is no experimental data.

8.4 Lithium-rubidium $X\ ^1\Sigma^+$ potential

Throughout this chapter, we have been fitting the $X\ ^1\Sigma^+$ potential of LiRb to test our genetic algorithm. Table 8.2 and Table 8.3 provide a full list of the bound states of this potential along with the rotational constants and the expected experimental error. We chose this molecule/potential pair for two reasons. First, both Jesús and I have worked on LiRb spectroscopy and have familiarity with the details of the experimental data. Second, there is high precision experimental data available making it a good testing ground. This potential was first studied by Refs. [54, 55] with Fourier transform spectroscopy and laser induced fluorescence in a thermal sample. These studies measured the rotational constants and relative binding energies of $v = 0$ to 45 with high precision, but were unable to determine the well depth accurately. Ref. [68] was able to fix the well depth of this potential which provides the absolute uncertainty in the binding energies of states in this potential. Additionally, Ref. [67] performed two-color photoassociation in LiRb and was able to measure the binding energies of $v = 50$ and 51. A sample potential derived by our algorithm that reproduces the experimental data is listed in Table. 8.5.

To derive the potential presented in Table 8.5, we used the one point crossover method that seemed to be the best according to Table. 8.1. However, recall that we had mentioned

		One Pt.		PCX		Hybrid	
	$\bar{\chi}^2$	Converge	Numerov	Converge	Numerov	Converge	Numerov
	Method	Rate	Calls	Rate	Calls	Rate	Calls
S-Obj.	Eqs. 8.6 & 8.8	0/10		2/10	76 (6)	5/10	39 (8)
M-Obj.	Eq. 8.3	5/10	64 (12)	0/10		9/10	52 (5)
M-Obj.	Eqs. 8.6 & 8.8	9/10	65 (7)	6/10	32 (3)	10/10	48 (9)

Table 8.4.
Performance of the different recombination operators on solving for a full LiRb $X\ ^1\Sigma^+$ potential. S-Obj. stands for single-objective formulation and M-Obj. stands for multi-objective formulation. Numerov calls are all in thousands of functions calls, rounded to nearest thousand. Error is the standard error of the mean from the 10 repetitions of each setup. Blank entries for Numerov calls occur when the solver never converged.

r (Å)	E (cm^{-1})	r (Å)	E (cm^{-1})	r (Å)	E (cm^{-1})
2.48	270.5397	4.1	-4922.9598	5.8	-1084.5637
2.52	-544.3594	4.2	-4658.2617	5.9	-966.4383
2.58	-1257.7633	4.3	-4384.1144	6.0	-861.4090
2.62	-1754.1211	4.4	-4105.4199	6.1	-765.4188
2.74	-3031.2257	4.5	-3825.9972	6.2	-681.6994
2.82	-3730.9864	4.6	-3549.3351	6.3	-603.2336
2.9	-4311.4380	4.7	-3278.2943	6.4	-539.1264
3.1	-5320.3889	4.8	-3015.1001	6.5	-478.3379
3.2	-5627.2147	4.9	-2761.7635	6.7	-378.4213
3.3	-5815.1641	5.0	-2518.7458	6.9	-300.0248
3.4	-5914.1939	5.1	-2289.6694	7.1	-237.5067
3.5	-5922.9711	5.2	-2074.6983	7.3	-193.5237
3.6	-5865.6330	5.3	-1872.3884	7.7	-119.4375
3.7	-5755.1548	5.4	-1687.4591	8.1	-94.9608
3.8	-5592.8416	5.5	-1515.6367	8.7	-74.7338
3.9	-5395.1269	5.6	-1358.2086	9.5	-64.8157
4.0	-5170.9475	5.7	-1214.9095	10.3	-11.9104
				10.7	-3.4758
		C_6	11484745.0		

Table 8.5.
Points for LiRb $X\ ^1\Sigma^+$ potential derived by the genetic algorithm. This is the same potential used in Table 8.2 and Table 8.3.

that the parent-centric crossover operator, while sporadic, was at times impressive, and we thought worthy of one last look. Table 8.4 lists how the one point crossover operator and the parent-centric crossover operator, along with a hybrid crossover operator (to be detailed in a second) perform on the full LiRb $X\ ^1\Sigma^+$ potential problem. Perhaps surprisingly, the parent-centric crossover operator converged to a final answer faster than the one point crossover operator, but the cost paid is it only did it about half the time when using the multi-objective approach with the specialized $\bar{\chi}^2$ calculation method.

Upon close inspection the real problem is that the parent-centric crossover operator hates the local gradient based solver (and that both are prone to getting stuck in local minima). After returning for the gradient based solver call, parent-centric crossover just stops functioning all together. Sometimes from here the gradient based solver can pull it into the final solution, other times it can't.

This leads us to propose our hybrid algorithm: it starts with the parent-centric crossover until the first gradient based solver call. Here it switches to the one point crossover, which has no problem recovering after the gradient solver. Despite the added complexity, the hybrid crossover solver is faster than the one point solver and is more consistent that either individual solver. Additionally, the hybrid solver has enough power to reach a solution consistently even when using the simple $\bar{\chi}^2$ calculation method in Eq. 8.3 and can occasionally find a solution when not using the multi-objective formulation.

Additionally, based on Table 8.4, we conclude that the one point crossover operator paired with the $\bar{\chi}^2$ calculation method in Eq. 8.6 and Eq. 8.8 and the multi-objective formulation is a gross over-engineering. Parent-centric crossover retains much of its functionality when working without either the modified $\bar{\chi}^2$ method or the multi-objective formulation while one point crossover does not. Note that the failure of the parent-centric crossover operator when using Eq. 8.3 and the multi-objective formulation has more to do with the failures of the gradient based solver, than parent-centric crossover. This suggests that there is some synergy at play between the combination of one point crossover, the modified $\bar{\chi}^2$ method and the multi-objective formulation that enables the combination to work much better together than any of the three alone. In all likely-hood this synergy is driven by some problem specific detail, likely our decision to use a point-wise potential to represent the molecular interaction, and will not work for other classes of problems (*i.e.* solving potentials that don't use a point-wise representation). Conversely, we expect that parent-centric crossover is a powerful, general operator. Better hybridizing parent-centric crossover with the gradient solver will likely result in it far outperforming the one point crossover (or even the hybrid crossover strategy) and is something we are working on.

8.5 Genetic Algorithm Conclusion

We have demonstrated that genetic algorithms can directly fit diatomic point-wise potentials to high-accuracy experimental data. On its own, this is a bit of an accomplishment. Directly fitting these point-wise potential are likely one of the hardest computational optimization problems around. Not only is the solution landscape filled with local minima, but the individual parameters (the different points) are very highly correlated and even small perturbations can quickly result in extra minima in the potential which crash the Numerov solver.

Although our algorithm works well for the test problem we worked on, there are many open questions that can form the basis for the next couple of studies. On the technical side of the computation, we noticed that the parent-centric crossover operator can outperform all its competitors, nearly by an order of magnitude, but it is sporadic in doing so. It seems worth looking to see if it can be stabilized at little cost in run time and better hybridized with the local gradient based solver. Additionally, the evolutionary algorithm techniques we used are all 15 years old, and in the meantime, newer methods like Mean-Variance Mapping Optimization (MVMO) [117] and adaptive differential evolution [123] have risen displacing the older genetic algorithms. Certainly it is worth looking into the newer evolutionary methods to see if they can perform well on our problem as well.

On the physics side of this project, there are two open questions. First, we studied exactly one potential here, and we want to know if this method can be applied to other systems. Certainly the answer is yes, but we would also like to test our fitting method on notoriously difficult problems like potentials with multiple minima [124]. Second, we were fitting the vibrational binding energies and rotational constants directly, instead of fitting to the term energies $E(v, J)$. We did this to separate rotational information, which is sensitive to the equilibrium inter-nuclear separation of the states, from vibrational information, which is sensitive to the local slope of the potential and the potential depth. Centrifugal distortion coefficients enter nowhere in this equation, but these coefficients are very important for predicting rotational states with $J > 10$, like would be observed in a thermal sample. Thus an open question is can we directly fit $E(v, J)$. It is not obvious that this will be possible with our technique. We have seen that when we considered fitting as a single-objective problem, which convolves rotation and vibration

information, our current algorithm struggled. Part of the problem is that at the start of the fitting routine, the vibrational errors are several orders of magnitude larger than the rotational errors. It is possible that fitting $E(v, J)$ will partially solve this problem because, for thermal states, the $J(J + 1)$ pre-factor for the rotational information will be quite large and could bring rotational information and vibrational information onto a more level playing field.

Finally, we would like to see how our algorithm compares to the semi-quantum approaches to fitting potentials to experimental data. These methods like the RKR and the inverted perturbation approach use problem specific knowledge (based on the molecular Hamiltonian and classical quantization of energy levels) and are well established techniques in the field. Because the semi-quantum techniques can use problem specific information, we expect that they will be faster than the genetic based techniques. But if our genetic based technique can produce a similar quality potential while not running that much slower (*i.e.* only one order of magnitude slower), we would consider that a huge success. In conclusion, we expect genetic based fitting methods to be a very productive avenue of research in the near future.

9. FUTURE WORK

In this chapter, I will layout immediate improvements to the LiRb experiment machine and a few future experiments. Finally, I will lay out two experiments in this chapter, one in LiRb and one in a Rb BEC. Both experiments require loading two species into a dipole trap and cooling them close to the degeneracy point. Both experiments also require a pair of coherent Raman lasers red detuned from the Rb D_1 line.

9.1 Experiment Improvements

There are three immediate improvements that can be made to the LiRb experiment to make it more user-friendly. The biggest improvement would be to replace the Zeeman slower. The slower, as designed by Sourav Dutta, consists of coils of wire with copper tubing wrapped around them, and the cooling water flows through the copper tubing. These get extraordinarily hot after continuous operation for an hour and limit operation to 45 minute duty cycles with 20 minute breaks in between. A better form for slower coils is to use hollow copper refrigerator tubing. The current flows in the copper and the cooling water in the center. This design will require a higher current source, but will result in continuous experiment operation. However to make this change would require a total disassembly of the vacuum system and should not be done until vacuum is broken for other reasons. I also recommend moving to a dual species slower setup as detailed in Ref. [125], if vacuum is ever broken. The dual species slower geometry helps enable a far better vacuum pressure in the main chamber which would be helpful for future BEC type experiments.

Of the smaller projects, the first is to improve the Li heat pipe used for frequency locking the Li trapping laser. Currently we have a heat pipe loaded with a few grams of Li metal, heated to around 400 C and kept at a modest vacuum of 10 mTorr. However, the Li supply has to be replaced every month or so and getting the heat pipe to the right temperature is time consuming. For around a thousand dollars, we could get a custom

built Li vapor cell from Precision Glass Blowing in Colorado. The cell will need to be heated like the heat pipe, but it will never need to have more Li added and once the correct temperature is found, it will not require day to day adjustment like the heat pipe currently does. However, care will need to be taken to ensure that Li vapor does not condense on the optical faces of the vapor cell.

The second project is to replace the Tiger laser, which forms the Rb cooling light with a tapered amplifier. The advantage here is that most of our data is limited by the Tiger laser currently. The laser will spontaneously unlock, usually every 30 minutes or so. This can be improved by periodically replacing its PZT but that also requires a large re-alignment each time. The tapered amplifier will provide the high power of the Tiger laser along with the stability of the low power seed laser. For example, we use a tapered amplifier for the Li trapping light, and it is never a problem. The custom option is to build our own seed laser at 780 nm and build our own tapered amplifier. Information for building the seed laser can be found in Ref. [48] and information on building the tapered amplifier can be found in the appendix to Ref. [126]. The more expensive, but easier option is to let a company like Toptica build both for us (and they can even provide an internal Rb reference).

The final project is to enclose the MOT lasers in plexiglass. A plexiglass enclosure helps with the passive stability of the lasers and also helps keep the optics clean. The goal would be to enclose the lasers and all the optics along the way to fibers; although a bit time consuming, this project would pay dividends in the long run, reducing the need for periodic re-alignment and cleaning.

9.2 Continuum STIRAP

The goal of the first project is to demonstrate an all optical route to ground state bi-alkali molecules. The idea is from Ref. [67]; instead of forming molecules in the dipole trap with magneto-association which will require giant magnetic fields and heavy modifications to the vacuum system, instead use STIRAP to transfer population from the scattering state to the least bound vibrational state. Because LiRb has a very large PA rate coefficient [127], an optical transfer like this will be unusually efficient and Ref. [67] predicts around 5 % efficiency. While not great, this is competitive with many imple-

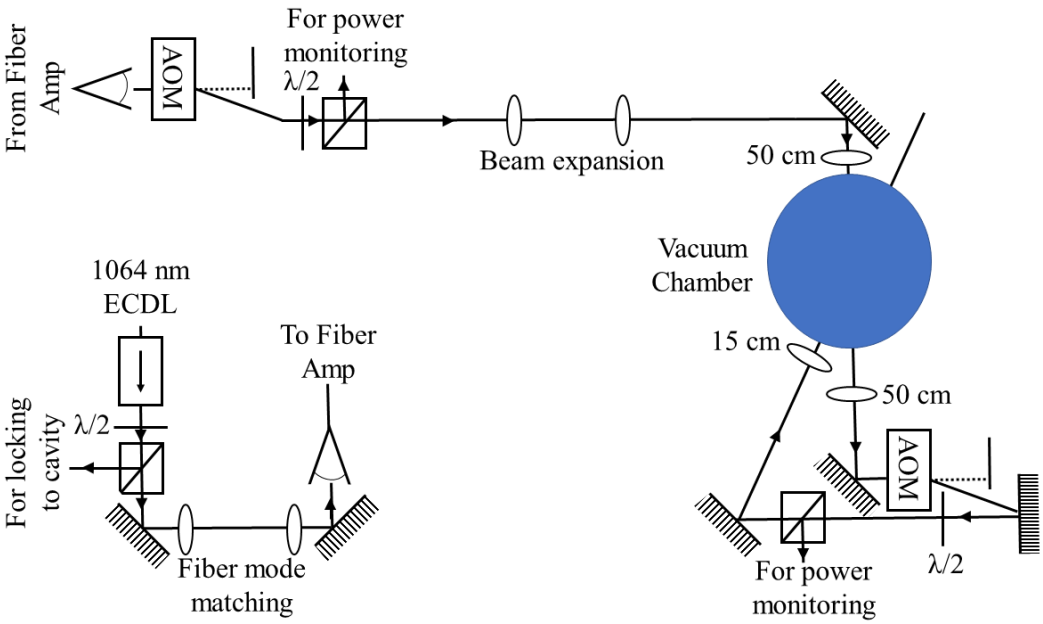

Fig. 9.1. Table diagram for the 1064 nm dipole trap. A 1064 nm ECDL is locked to a cavity to get approximately 1 kHz linewidth. This seeds the fiber amplifier. After the amplifier, an AO directs most of the laser power into the first-order. A pick off is setup to monitor and, in tandem with the AO, finely control the laser power. Lenses focus the beam to about a 150 μm spot size in the middle of the MOTs. The beam is recycled for a second pass. Again, an AO controls the power and it is focused to about a 25 μm spot size. The two beams cross at approximately 15° forming a dimple trap.

mentations of magneto-association, and could be improved upon with similar methods to magneto-association. The least bound vibrational state is chosen for this work to keep the frequency difference between the Raman lasers small. I suspect that the same experiment could be made to work with the $2(1) - 4(1)$ state. However, the $2(1) - 4(1)$ experiment would require a difference between the lasers of 1000's of GHz opposed to the 4.66 GHz difference proposed. (An exciting future project could be a direct transfer from the scattering state to $X\ ^1\Sigma^+\ v = 0$ through the $2(1) - 4(1)$ state.)

To make this transfer happen, two big things need to be done and I will provide as much information as possible at this point in time. First, the atoms need to be transferred to an optical dipole trap and cooled; second, the lasers for the STIRAP transfer need to be assembled and phase locked. In our lab, we have a 1064 nm fiber amplifier from NuFern along with two 1064 nm AOMs. A seed laser for the fiber amplifier would need

to be constructed and stabilized to an optical cavity. The NuFern fiber amplifier needs 50 mW into its fiber. I recommend following the dipole trap design of Ref. [126], using a wide beam and narrow beam, as shown in Fig. 9.1. The output of the fiber amplifier should be sent through an AOM and the first-order beam used as the wide focus beam. After passing through the vacuum chamber once, the beam can be shifted in a second AOM and recycled for use as the narrow beam. The AOM control circuit presented in this thesis can be used to control the AOMs and evaporatively cool the atom. To align the dipole trap beam, I recommend following our general laser alignment plan, and co-propagate it with the Ti:Sapphire output which can be tuned to destroy the MOT, thus guaranteeing proper alignment.

Loading the dipole trap is a bit trickier. Ref. [126] illustrates a timing sequence for loading ^{87}Rb (I recommend using ^{87}Rb for this experiment, by the way). The first goal should be to get a ^{87}Rb BEC before working on loading Li into the dipole trap. To detect atoms in the dipole trap, absorption imaging can be used. For this, pick off a small amount of light from the Rb cooling laser and shift it into resonance with an AOM. Align this light through the MOT and onto a CCD camera; again Ref. [126] offers a good primer.

After the ^{87}Rb BEC is working, work can being on loading Li into the dipole trap. I would recommend a sequential loading sequence like Ref. [125], using a gray molasses on the Li D_2 line. An example of a gray molasses in ^{23}Na can be found in Ref. [128]. From here, the same evaporative cooling sequence can be followed, and interrupted just before the Li BEC would start to form. Getting to this point is a lot of work, but here the science can happen.

For STIRAP, two phase-locked lasers will be needed, around 795 nm. Two ECDLs will work fine, and the first should be locked to a cavity, the second can be locked to the first with a 4.66 GHz offset [67], as shown in Fig. 9.2. The phase lock can be made to happen with the digital phase detector from Chapter 7. Tune the cavity-locked laser about 50 MHz below the $2(0^-)$ $v = -5$ PA resonance, and then use two more AOMs to pulse the lasers and STIRAP should happen, transferring directly into the least bound triplet state in an all optical method. Clean the trap of leftover Li and Rb atoms, and then reverse STIRAP and image to detect.

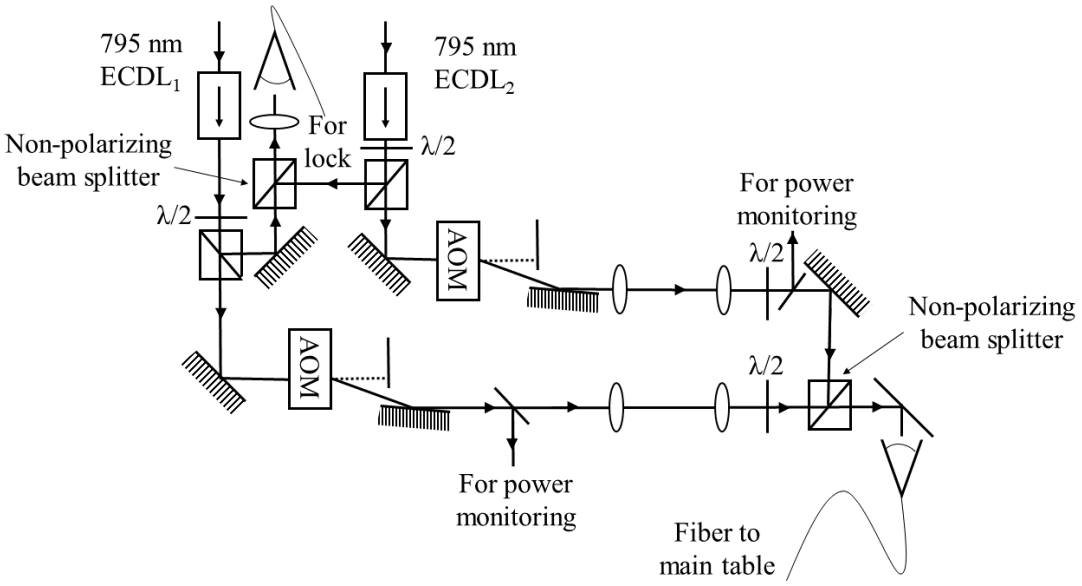

Fig. 9.2. Table diagram for 795 nm lasers setup. A small amount of power is picked off from both lasers and sent through a fiber to lock, one laser to a cavity and the second laser to the first at some offset frequency using a digital OPLL. Afterwards, AOs control the power and timing. Ultimately, the lasers are combined and sent to the experiment through a polarization maintaining fiber.

9.3 Unitary Rb BEC

The final experiment is to demonstrate semi-long-lived all optical control over the atomic scattering length and to produce dynamic unitarity BECs. The original unitarity BEC experiment [129] was a fast ramp from zero interaction to infinite interactions using a magnetic Feshbach resonance. This is accomplished with a ^{85}Rb BEC using a Feshbach resonance around 160 G and it involved sweep from 169 G (0 interactions) to 160 G (infinite interactions) in around 10 μs.

Our twist on the experiment is to instead use a pair of Raman lasers to accomplish the rapid change in the scattering length, inspired by Ref. [130]. A potential energy diagram for this experiment is given in Fig. 9.3. A Feshbach resonance works by tuning the least bound molecular state through the scattering state with the Zeeman effect. Starting with the least bound state tuned near the scattering state, our Raman lasers will dress the least bound molecular state with a second bound, ground molecular state, while being far detuned from the excited state. This is a form of Autler-Townes dressing

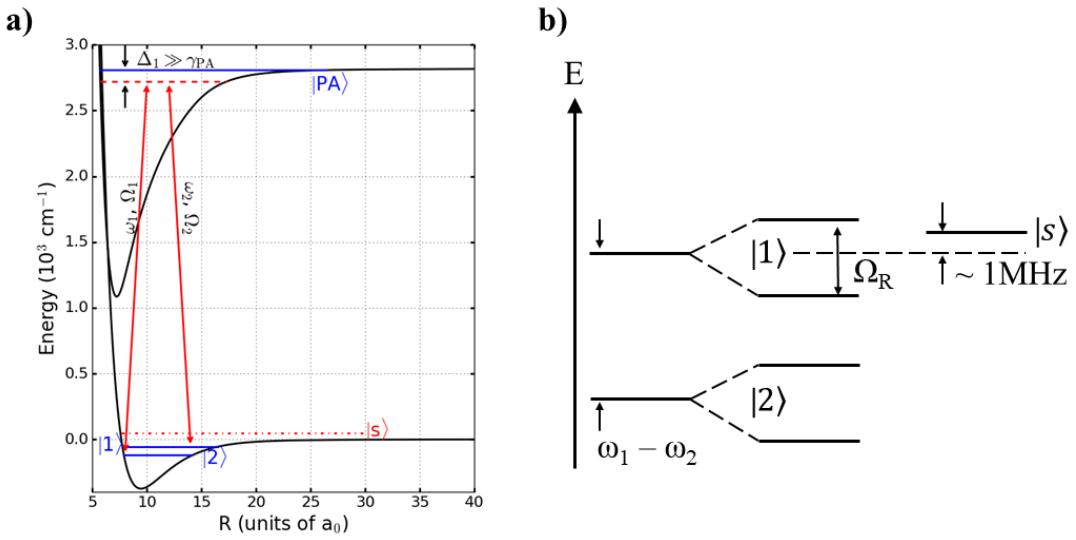

Fig. 9.3. **(a)** Potential energy diagram for a Raman ramp to unitarity in Rb_2. A pair of 795 nm ECDLs, with frequencies ω_1 and ω_2 and Rabi frequencies Ω_1, and Ω_2, couple the two least bound molecular state through an intermediate state. By carefully controlling the laser power, we can increase or decrease the coupling. The detuning from the intermediate state, Δ, will be chosen to be large compared to the lifetime of the excited state, γ_{PA}. **(b)** Dressed state picture in Rb_2. The state coupling Autler-Townes dresses the bare states. By increasing the Autler-Townes splitting, the least bound state can be carried into resonance with the scattering state. This mimics a magnetic Feshbach resonance.

and will push the least bound state up in energy as the laser power is increased. Thus we accomplish a similar effect, tuning the molecular state into resonance with the scattering state, but by an optical means. This also differs from previous implementations of Raman coupling between scattering states and bound molecular states like in Ref. [131]. There, the scattering state itself is coupled to a bound state, and because the scattering to bound transition is so weak, it requires being basically on-resonance with the excited state, whereas our implementation only requires addressing two bound states allowing a much greater detuning from the excited state. This makes all the difference: previously Ref. [131] was limited by PA to the excited state, which is a strong atom loss mechanism, making the technique nearly useless. The advantage of the optical ramp to unitarity (beyond being optical and faster), also lies in its positional dependence. Because Gaussian beams have a non-uniform profile, we can exploit this and make some parts of the

BEC unitary while other will be non-interacting leading to interesting dynamics between different populations in the BEC.

The best method for producing a ^{85}Rb BEC is to sympathetically cool ^{85}Rb with ^{87}Rb, while the ^{85}Rb self-scattering length is tuned to zero around 169 G. There are two options for forming a ^{85}Rb and a ^{87}Rb MOT. The most obvious is to use the Tiger for the ^{85}Rb MOT and its replacement for the ^{87}Rb MOT. The downside to this approach is obvious. Alternately, if we buy the Tiger replacement from Toptica, it should be able to produce both MOTs, sequentially. Toptica's tapered amplifier systems have mode-hop free tuning of 30 GHz which is more than enough to span the 3 GHz difference between the ^{85}Rb and ^{87}Rb cooling transitions. The Toptica laser can be locked to one of the repump laser with a digital OPLL which should allow a rapid change of the offset frequency between the two lasers, as shown in Fig. 9.4.

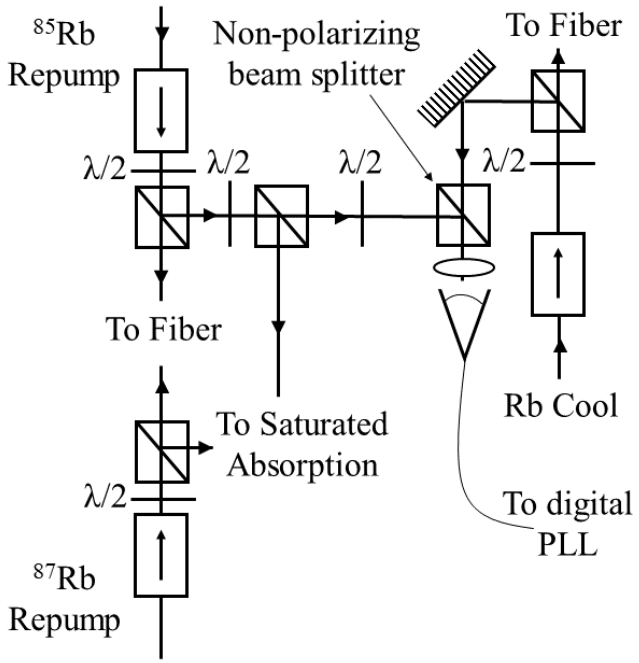

Fig. 9.4. Table diagram for tunable Rb transfer lock. Homebuilt ECDLs form repump lasers and are locked to saturated absorption resonances. A beat-note is formed between one repump laser and the cooling laser. The cooling laser is phase locked to the repump laser with a digital OPLL. The digital OPLL can be used to tune the cooling laser between the ^{85}Rb and ^{87}Rb cooling transitions in a fast, controllable manner.

To generate the 169 G bias Magnetic field, the MOT coils can be changed from an anti-Helmhotz configuration to a Helmhotz configuration. A circuit for rapidly changing the MOT coil current drives can be found in Ref. [37]. Two-photon PA spectroscopy will need to be carried out on ^{85}Rb following the lead of Ref. [67] to find a suitable ground state pair for this experiment. For more information on PA in BECs, consult Ref. [69].

APPENDICES

A. NOTATION AND LABELING

The discussion of diatomic molecules in this section is borrowed from Ref. [66]. To a reasonable approximation, the diatomic Hamiltonian is $H = H_{el} + H_v + H_r$. At this point the Born-Oppenheimer approximation has already been made and the electrons see the stationary nuclear potential in H_{el} that is a function of $\mathbf{R}$, the internuclear separation. Fig. 3.4 shows the low-lying electronic potential energy curves for LiRb. A reasonable guess for solving H is to assume a wavefunction form $|\Psi\rangle = |\Psi_{el}\rangle|\Psi_N\rangle$ and $|\Psi_N\rangle = \frac{1}{r}|\Psi_v\rangle|\Psi_r\rangle$ where the v subscript refers to vibration along the internuclear axis and the r subscript refers to rotation about the internuclear axis. This solution looks like:

$$H|\Psi\rangle = (E_{el} + E_v + E_r)|\Psi\rangle. \tag{A.1}$$

Often this energy E will be written in wavenumber units called term values as $T = T_e + G + F_v$ and $T_e \gg G \gg F_v$.

It is standard to assume that the vibration and rotation are uncoupled. The vibration is modeled as an an-harmonic oscillator:

$$G = \omega_e(v + \frac{1}{2}) - \omega_e x_e(v + \frac{1}{2})^2 + \omega_e y_e(v + \frac{1}{2})^3 + ... \tag{A.2}$$

with ω_e, x_e and y_e constants of the electronic state. The rotation is modeled as a symmetric top:

$$F_v = B_v J(J+1) + (A - B_v)\Lambda^2 - D_v J^2(J+1)^2 + ... \tag{A.3}$$

with B_v and D_v constants of the vibrational level (and $B_v \gg D_v$) and A a constant of the electronic state (usually $A\Lambda^2$ is included in T_e).

In atoms the coupling of different angular momenta is fairly simple, in diatomic molecules an exact solution is not possible (not that it is always possible in relativistic atoms). However, good approximations can be made and the common approximations are the different Hund's coupling cases. For this work the relevant Hund's cases are (a), (b) and (c), with (a) and (c) covering most of our work. Table A.1 shows the analogy between atomic quantum numbers and diatomic quantum numbers. The assumption in

Atomic Quantum Numbers	Molecular Quantum Numbers
L - Orbital angular momentum	L - difficult to define
M_L - Projection of L onto a lab axis	M_L - projection of L onto internuclear axis $\Lambda = \|M_L\|$, M_L=L, L-1, L-2 ... -L
S - electron spin	S - sum of electron spin
M_S - Projection of S onto a lab axis	Σ - projection of S onto internuclear axis
$\vec{J} = \vec{L} + \vec{S}$	$\Omega = \|\Lambda + \Sigma\|$

Table A.1.
Analogy between atom and molecular quantum numbers

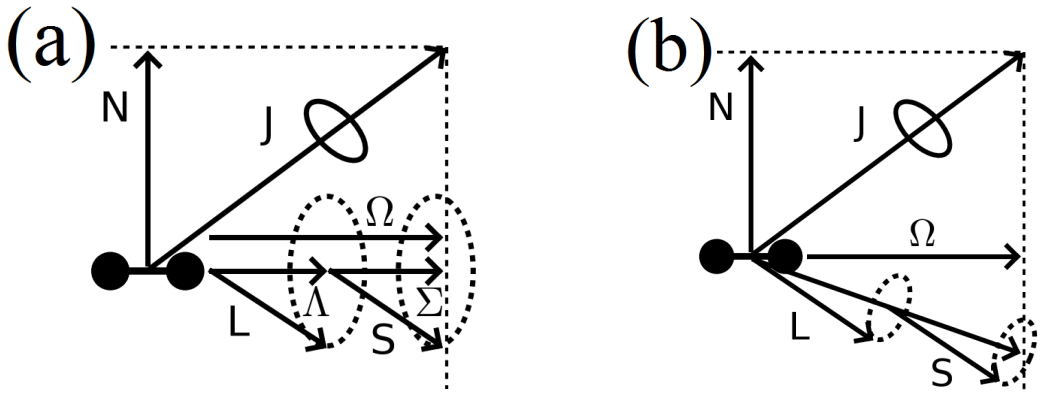

Fig. A.1. Vector coupling of different angular momenta in diatomic molecules. **(a)** Shows coupling in Hund's (a). **(b)** Shows coupling in Hund's (c). Figure borrowed from Ref. [66].

Hund's (a) is that the coupling of the nuclear rotation with the electronic motion is weak, while the electronic motion is strongly coupled to the internuclear axis. This is shown in a vector diagram in Fig. A.1 (a). N is the angular momentum from the nuclear rotation, L is the electronic angular momentum, Λ is the projection of L onto the internuclear axis, S is the total electronic spin, Σ is the projection of S onto the internuclear axis, $\Omega = \Lambda + \Sigma$ and finally $J = \Omega + N$. The good quantum numbers are Λ, S, Σ, Ω and J. The rotational energy is $F_v \simeq B_v[J(J+1) - \Omega^2]$, $J = \Omega,\ \Omega+1,\ \Omega+2, \ldots$

Hund's (b) is a subset of Hund's (a) with $\Lambda = 0$ and $S \neq 0$. In this case Ω cannot be defined and instead we define $K = \Lambda + N$ which is the total angular momentum not from spin. Then we define $J = K + S$. The good quantum numbers are Λ, S, K, and J.

The rotational energy is $F_v \simeq B_v[K(K+1)]$, $K = \Lambda,\ \Lambda+1,\ \Lambda+2, \ldots$ For our work, Hund's (b) comes up when we work out of the lowest triplet state, $a\ ^3\Sigma^+$.

Hund's (c) occurs when the spin-orbit coupling is stronger than the coupling to the internuclear axis. In this case Λ and Σ cannot be defined and instead L and S combine to form a resultant J_a with projection onto the internuclear axis Ω. And we define $J = \Omega + N$. The good quantum numbers are J_a, Ω and J. The rotational energy is the same as in Hund's case (a). This is shown in vector from in Fig. A.1 (b) and this scenario comes up in our loosely bound PA states near atomic asymptotes.

Labeling molecular states is itself complicated. Let's use $a\ ^3\Sigma^+\ v = 11,\ K = 1,\ J = 0^-$ as an example. Here we have labeled the state in Hund's (b) coupling: a labels this as the first $^3\Sigma^+$ state, ^{3} identifies that this is a triplet state ($a\ la$ S=1), Σ^+ identifies this as an $\Lambda = 0$ state ($\Lambda = 1$ is a Π state, and $\Lambda = 2$ is a Δ state) and the $^+$ identifies this as a state with even symmetry upon inversion across any plane containing the two nuclei, v=11 identifies this as the 12^{th} most tightly bound state and $J = 0^-$ identifies the

Hund's case (a) or (b)	Hund's case (c)
$X\ ^1\Sigma^+$	$1(0^+)$
$a\ ^3\Sigma^+$	$1(0^-)$
	$1(1)$
$A\ ^1\Sigma^+$	$2(0^+)$
$c\ ^3\Sigma^+$	$2(0^-)$
	$2(1)$
$b\ ^3\Pi$	$3(0^+)$
	$3(0^-)$
	$3(1)$
	$1(2)$
$B\ ^1\Pi$	$4(1)$

Table A.2.
Correspondence between Hund's case's (a) and (c) in LiRb. We use Hund's case (c) labeling for our PA states and Hund's case (a) for bound to bound transitions.

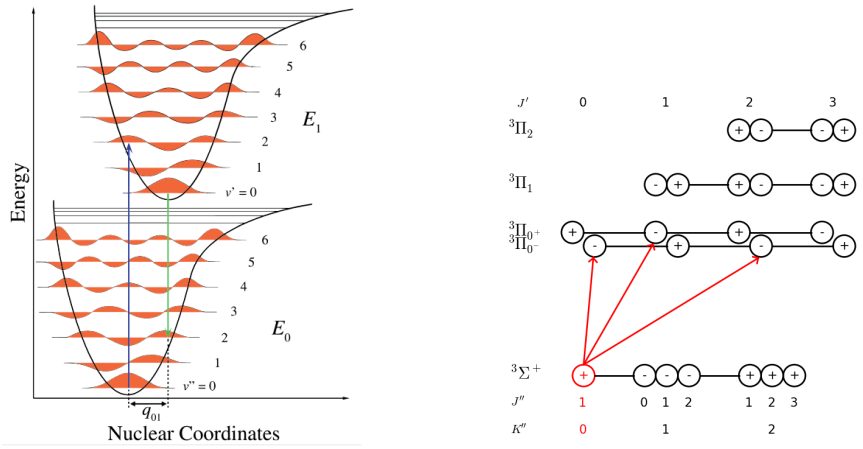

Fig. A.2. **(a)** Schematic representation of overlap between ground and excited state vibrational levels. The degree of overlap, which in turn determines the strength of the transition, is given by the Franck-Condon factor. Figure adapted from Ref [132]. **(b)** Rotational structure and parity of different electronic states in diatomic molecules, adapted from Ref. [66].

Selection rules for radiative transitions in diatomic molecules		
$\Delta J = 0,\ \pm 1$ and $J = 0 \nrightarrow J = 0$		
$+ \leftrightarrow -$, $+ \nleftrightarrow +$, and $- \nleftrightarrow -$ or for $\Delta J = 0,\ e \leftrightarrow f$ and for $\Delta J = \pm 1,\ e \leftrightarrow e$ and $f \leftrightarrow f$		
Hund's (a) only	Hund's (b) only	Hund's (c) only
$\Delta\Lambda = 0,\ \pm 1$ (i.e. $\Sigma - \Sigma$, $\Sigma - \Pi$ but no $\Sigma - \Delta$)		$\Delta\Omega = 0,\ \pm 1$
$\Sigma^+ \leftrightarrow \Sigma^+$, $\Sigma^- \leftrightarrow \Sigma^-$, $\Sigma^+ \nleftrightarrow \Sigma^-$		$0^+ \leftrightarrow 0+$, $0^- \leftrightarrow 0^-$, $0^+ \nleftrightarrow 0^-$
$\Delta S = 0$		
$\Delta\Sigma = 0$ (i.e. $^3\Pi_0 - ^3\Pi_0$, but no $^3\Pi_0 - ^3\Pi_1$)	$\Delta K = 0,\ \pm 1$, $\Delta K = 0$ is forbidden for $\Sigma - \Sigma$	
$\Delta\Omega = 0,\ \pm 1$, if $\Sigma - \Sigma$, $\Delta J = 0$ is forbidden		

Table A.3.
Selection rules for radiative transitions in diatomic molecules, rules compiled from Ref. [66].

rotational quantum number as zero with overall - symmetry when rotated π about the internuclear axis. In Hund's (c) labeling this state would be $1(0^-)$ $v = -4$ $J = 0^-$. This labeling works as follows: $1(0^-)$ means that this is the first state with $\Omega = 0^-$ and $v = -4$ means this is the fourth bound state counting from the asymptote. Table A.2 lists the correspondence between the Hund's a) and c) labeling for the low-lying electronic series in LiRb.

Selection rules for radiative transitions in diatomic molecules are also more complicated than those in atomic systems. There are no selection rules for different vibrational states, instead the probability of different vibrational transitions are governed by Franck-Condon factors (FCF) illustrated in Fig. A.2(a). A FCF is the nuclear wavefunction overlap between the two different vibrational levels, $|\langle\Psi_{v_i}|\Psi_{v_f}\rangle|^2$. Classically (and usually a good guide for identifying strong transitions) there is a large probability for the wavefunction to be at its turning points and slow moving while there. Because of this vertical transitions from inner-inner, inner-outer or outer-outer turning points are strong. For example, in Fig. A.2(a), $v_i = 0 \rightarrow v_f = 2$ would be strong while $v_i = 0 \rightarrow v_f = 6$ would be weaker.

While there are no selection rules for vibrational quantum numbers, there are selection rules for other molecular quantum numbers. These are summarized in Table A.3. As it should be expected, these vary with the different Hund's cases and it is worth starting with the two selection rules that are true across all Hund's cases.

1) $\Delta J = 0,\ \pm 1$ and $J = 0 \nrightarrow J = 0$. This is analogous to the selection rule for total angular momentum F in atomic systems.

2) $+ \leftrightarrow -$, $+ \nleftrightarrow +$, and $- \nleftrightarrow -$ or for $\Delta J = 0,\ e \leftrightarrow f$ and for $\Delta J = \pm 1,\ e \leftrightarrow e$ and $f \leftrightarrow f$.

The second selection rule requires a little more knowledge to understand. Here $+$ and $-$ refer to the total parity of the wavefunction while e and f refer to the parity of the rotational wavefunction. For dipole allowed transitions, the wavefunction parity has to change just like in atomic systems. Rigorously the definitions for $+$ and $-$ are as follows: in general the wavefunction for a molecule can be written as

$$\Psi_e = c\Psi_e^+ + d\Psi_e^- \text{ with } \Psi_e^+ = \chi e^{i\Lambda\phi_i} + \bar{\chi}e^{-i\Lambda\phi_i} \text{ and } \Psi_e^- = \chi e^{i\Lambda\phi_i} - \bar{\chi}e^{-i\Lambda\phi_i}. \qquad \text{(A.4)}$$

Under the mapping $\phi_i \mapsto -\phi_i$ it can be seen that $\Psi_e^+ \mapsto \Psi_e^+$ while $\Psi_e^- \mapsto -\Psi_e^-$. The definitions of e/f parity are: levels with parity $+(-1)^J$ are e parity and levels with parity $-(-1)^J$ are f parity [133]. Both are widely used in the literature. Fig. A.2(b) shows the parity and rotational structure of common Hund's case (a) and (b) vibrational states.

Finally because there are multiple LiRb isotopes, we care about the isotope shift for molecules. The isotope shift shows up as a slight modification to the vibrational spring constant and the moment of inertia. Specifically if the two isotopes have reduced masses μ and μ^i then we can define

$$\rho = \sqrt{\frac{\mu}{\mu^i}} = \frac{v_{osc}^i}{v_{osc}}. \tag{A.5}$$

Now the vibrational energy of the second isotope will be

$$G^i = \rho\omega_e(v+\frac{1}{2}) - \rho^2\omega_e x_e(v+\frac{1}{2})^2 + \rho^3\omega_e y_e(v+\frac{1}{2})^3 + ... \tag{A.6}$$

and the rotational energy will be

$$F_v = \rho^2 B_v J(J+1) + \rho^2(A-B_v)\Lambda^2 - \rho^4 D_v J^2(J+1)^2 + ... \tag{A.7}$$

There is no shift in T_e, the electronic energy of the state and the potential energy curves do not change.

B. EVAPORATIVE COOLING

Evaporative cooling is not trivial; at one point it was the greatest experimental challenge in realizing a BEC. The techniques for evaporative cooling have gotten better reducing the required trapping time from 100 s to 10 s. This drastically reduces the quality of vacuum system needed and obviously speeds up experiments. A proposed experiment requires evaporative cooling in a crossed beam dipole trap and as such this section exists as a repository for the mathematics describing the process of evaporative cooling, dipole trap loading and absorption imaging.

B.1 Trap loading

If the dipole trap and MOT are in equilibrium we can calculate how many atoms will be loaded into the dipole trap from the MOT. This is done with the Fokker - Planck model and

$$N_T = n_{MOT} V_{trap} \mathcal{F}(\frac{U_0}{k_B T}) \tag{B.1}$$

where n_{MOT} is the density of the MOT, V_{trap} is the volume of the dipole trap and $\mathcal{F}$

$$\mathcal{F}(q) = \frac{q^{\frac{3}{2}}}{2} \int_0^1 g_1(x) e^{q(1-x)} dx; \tag{B.2}$$

where

$$g_1(x) = \beta^{\frac{3}{2}} \sqrt{1-x} \frac{16}{\pi} \int_0^1 u^2 \sqrt{e^{\beta(1-u^2)}} du \text{ and } \beta = -ln(1-x). \tag{B.3}$$

These equations do not account for the finite size of the MOTs and are significantly complicated by our trap geometry with the crossed beams. If we compute N_T for Rb and Li using MOT temperatures and densities stated earlier and for only the wide beam present we arrive at $N_{T,Rb} = 8 \times 10^5$ and $N_{T,Li} = 3 \times 10^4$. This can be improved upon by using transient techniques to cool and compress the MOT; in Ref. [134] they worked in ^{6}Li (so comparison is apt) and found that the cooling and compression technique increase their loading by a factor of 20. We won't realize quite such a high increase because we have to pick a magnetic field gradient somewhere between the Rb and Li maximum, but

I would expect and factor of 10 increase would be reasonable. Important for us, 8×10^5 and 3×10^4 are large enough to be detected by absorption imaging.

B.2 Absorption imaging

Ignoring the imaging optics for a second, absorption imaging measures the optical density, OD, of an atom cloud. To do this takes 3 images, one with atoms and the resonant light, one without atoms but with the resonant light and one with no atoms or light. From these images the optical density of the cloud at pixel i,j can be found

$$OD_{ij} = ln(\frac{CCD_{atoms} - CCD_{background}}{CCD_{no\ atoms} - CCD_{background}}). \tag{B.4}$$

At this point we will assume a Gaussian density distribution for the atoms, $n(x, y, z) = Ne^{-(\frac{x^2}{2\sigma_x^2}+\frac{y^2}{2\sigma_y^2}+\frac{z^2}{2\sigma_z^2})}$ and then extract the atom number by the fit

$$N_{fit} = \frac{A_{pix}}{\sigma_{eg}} \sum_{i,j} OD_{i,j} \tag{B.5}$$

where σ_{eg} is the absorption cross-section of the cycling transition and A_{pix} is the area of each pixel. By extracting the atomic cloud size at different times, the temperature of each degree of freedom can be measured

$$T = \frac{m}{k_B} \frac{\sigma_f^2 - \sigma_i^2}{t_f^2 - t_i^2}. \tag{B.6}$$

B.3 Evaporative Cooling

First we will address the one species case and then we will discuss the binary mixture case. For one species in the dipole trap, the momentum distribution of atoms is

$$f(r, p) = n_0 \lambda_{dB}^3 e^{-\frac{U(r)+p^2/2m}{k_B T}} \Theta(\eta k_B T - U(r) - p^2/2m) \tag{B.7}$$

where $\lambda_{dB} = \sqrt{\frac{2\pi\hbar^2}{mk_BT}}$, n_0 is the peak density, U(r) is the dipole trapping potential, $\Theta(\eta k_B T - U(r) - p^2/2m)$ is the Heaviside function concatenating the momentum distribution because of the finite trap depth, and $\eta = \frac{U}{k_B T}$ is how many times deeper the trap is relative to the atomic thermal energy. It is normal to introduce parameters η and ν defined as $\bar{\omega} \propto U^\nu$ and then keep these fixed through out evaporation [126]. The peak density

$$n_0 = N\bar{\omega}^3 (\frac{m}{2\pi k_B T})^{\frac{3}{2}} \tag{B.8}$$

where N is the total number of the atoms in the trap. At this point the spatial density and energy densities can be derived using Eq B.7

$$n(r) = \frac{1}{(2\pi\hbar)^3}\int f(r,p)d^3p = n_0 e^{-\frac{U(r)}{k_B T}} \; and \tag{B.9}$$

$$e(r) = \frac{1}{(2\pi\hbar)^3}\int (\frac{p^2}{2m} + U(r))f(r,p)d^3p = \frac{3}{2}n_0 k_b T e^{-\frac{U(r)}{k_B T}} + U(r)n(r). \tag{B.10}$$

Now we can write down the differential equations for the energy and atom number

$$\dot{N} = \dot{N}_{ev} + \dot{N}_{\theta} + \dot{N}_{1B} + \dot{N}_{3B} \tag{B.11}$$

$$\dot{E} = \dot{E}_{ev} + \dot{E}_{\theta} + \dot{E}_{1B} + \dot{E}_{3B} + \dot{E}_{ad} \tag{B.12}$$

The terms in this equation are as follows: $\dot{N}_{ev}$ and $\dot{E}_{ev}$ are losses due to evaporation; $\dot{N}_{\theta}$ and $\dot{E}_{\theta}$ are losses due to the changing number of states and this is small for deep traps [126]; $\dot{N}_{1B}$ and $\dot{E}_{1B}$ are losses due to collisions with background gases; finally, $\dot{N}_{3B}$ and $\dot{E}_{3B}$ are losses due to three body collisions which become significant at high densities. These can be found using Eqs B.9, B.10:

$$\dot{N}_{1B} + \dot{N}_{3B} = -\Gamma_{1B}N - \Gamma_{3B}N \tag{B.13}$$

$$\dot{E}_{1B} + \dot{E}_{3B} = -\Gamma_{1B}E - \Gamma_{3B}\frac{2}{3}E. \tag{B.14}$$

Here Γ_{1B} is based on the vacuum system which we have previously measured to be between 0.1 - 0.2 s^{-1} and $\Gamma_{3B} = L_{3B}\frac{n_0^2}{3\sqrt{3}}$ and $L_{3B} = 4.3 \times 10^{-29}$ cm^6/s for ^{87}Rb. Additionally, $\dot{N}_{ev} = -\Gamma_{ev}N$, $\dot{E}_{ev} = -N\Gamma_{ev}(\eta + \frac{\eta-5}{\eta-4})k_B T$ and $\Gamma_{ev} = (\eta-4)e^{-\eta}\Gamma_{el}$ ($\Gamma_{el} = n_0\sigma\bar{v}$ and $\sigma = 8\pi a_s^2$ with $a_s = 98$ a_0 for ^{87}Rb is the scattering cross-section and $\bar{v} = 4\sqrt{\frac{k_B T}{\pi m}}$ is the average relative velocity). Finally, $\dot{E}_{ad} = \nu E\frac{\dot{T}}{T}$ accounts for work done by changing the trap shape. This provides a full set of differential equations to model one species evaporation courtesy of Ref. [126]. The reason for developing this formalism is that efficient evaporative cooling is much more complicated than simply lowering the trap depth by decreasing the power in the trapping beams. As outlined in Ref. [126] different cooling routes are defined by those rather arbitrary looking parameters we picked earlier, η and ν; they found that $\eta = 8.5$ and $\nu = 0.22$ provided the most efficient route for them. These parameters are dependent on the initial conditions and will change when we account for our second species.

B.4 Sympathetic Cooling

When there are two species in a dipole trap in thermal contact, they will exchange energy through collisions and if they start at different temperatures, they will meet at some intermediate temperature as $t \to$ inf. In Eq. B.11 there will be a couple three body interspecies loss terms $\Gamma_{Rb-Rb-Li}$ and $\Gamma_{Rb-Li-Li}$ which haven't been measured and I hope are small (this can be forced by changing the relative densities). Neglecting the new 3 body loss the energy now has an additional factor

$$\dot{E}_{Rb} = \Gamma_{coll}\zeta k_B(T_{Li} - T_{Rb}) = -\dot{E}_{Li} \tag{B.15}$$

where $\zeta = \frac{4m_{Rb}m_{Li}}{(m_{Rb}+m_{Li})^2}$ and

$$\Gamma_{coll} = \sigma\bar{v}_{th}n_{Li}n_{87}(\frac{2\pi k_B T}{m_{Li}\bar{\omega}_{Li}^2 + m_{Rb}\bar{\omega}_{Rb}^2})^{\frac{3}{2}} e^{\frac{m_{Li}\bar{\omega}_{Li}^2 d}{2(m_{Li}\bar{\omega}_{Li}^2 + m_{Rb}\bar{\omega}_{Rb}^2)} - \frac{m_{Li}\bar{\omega}_{Li}^2 d^2}{2k_B T}} \tag{B.16}$$

and again $\sigma = 4\pi a_{Li,Rb}^2$ is the scattering cross-section with $a_{Li,Rb} = 59$ a_0, $\bar{v}_{th} = \frac{8k_B}{\pi}\sqrt{\frac{T_{Li}}{m_{Li}} + \frac{T_{Rb}}{m_{Rb}}}$ and d is an offset between the two clouds. The full model is

$$\dot{N_{Rb}} = \dot{N_{Rbev}} + \dot{N_{Rb1B}} + \dot{N_{Rb3B}} \tag{B.17}$$

$$\dot{N_{Li}} = \dot{N_{Li1B}} + \dot{N_{Li3B}} \tag{B.18}$$

$$\dot{E_{Rb}} = \dot{E_{Rbev}} + \dot{E_{Rb1B}} + \dot{E_{Rb3B}} + \dot{E_{Rbad}} + \Gamma_{coll}\zeta k_B(T_{Li} - T_{Rb}) \tag{B.19}$$

$$\dot{E_{Li}} = \dot{E_{Li1B}} + \dot{E_{Li3B}} + \dot{E_{Liad}} + \Gamma_{coll}\zeta k_B(T_{Rb} - T_{Li}). \tag{B.20}$$

Work is currently in progress to simulate evaporative cooling with this model.

C. CIRCUIT DIAGRAMS

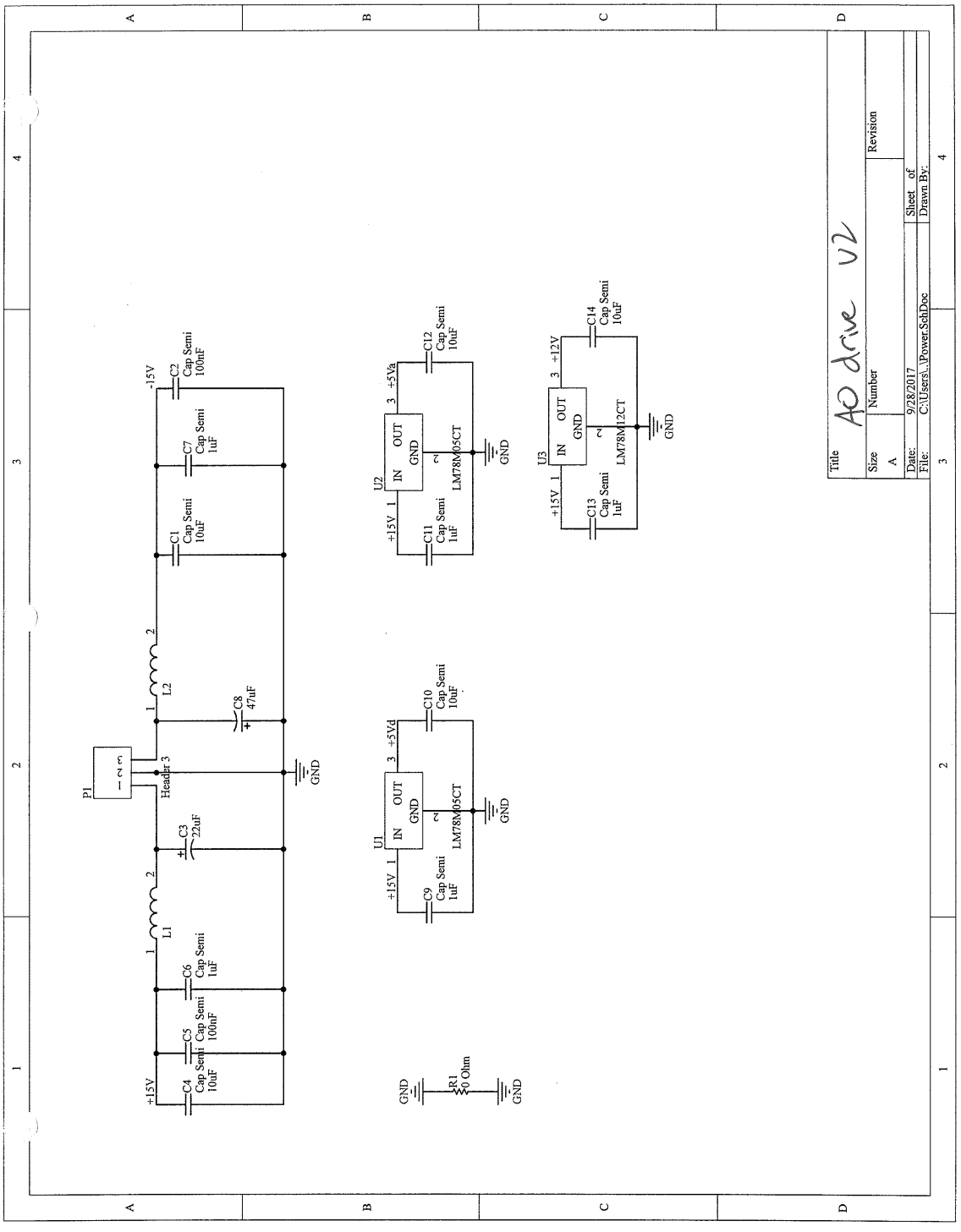
Title
AO drive V2
Size
A
Number
Revision
Date: 9/28/2017
File: C:\Users\..\Power.SchDoc
Sheet of
Drawn By:
P1
Header 3
L1
L2
C1 Cap Semi 10uF
C2 Cap Semi 100nF
C3 22uF
C4 Cap Semi 10uF
C5 Cap Semi 100nF
C6 Cap Semi 1uF
C7 Cap Semi 1uF
C8 47uF
-15V
+15V
GND
U1
U2
U3
IN
OUT
GND
LM78M05CT
LM78M12CT
+15V
+5Vd
+5Va
+12V
C9 Cap Semi 1uF
C10 Cap Semi 10uF
C11 Cap Semi 1uF
C12 Cap Semi 10uF
C13 Cap Semi 1uF
C14 Cap Semi 10uF
R1
50 Ohm

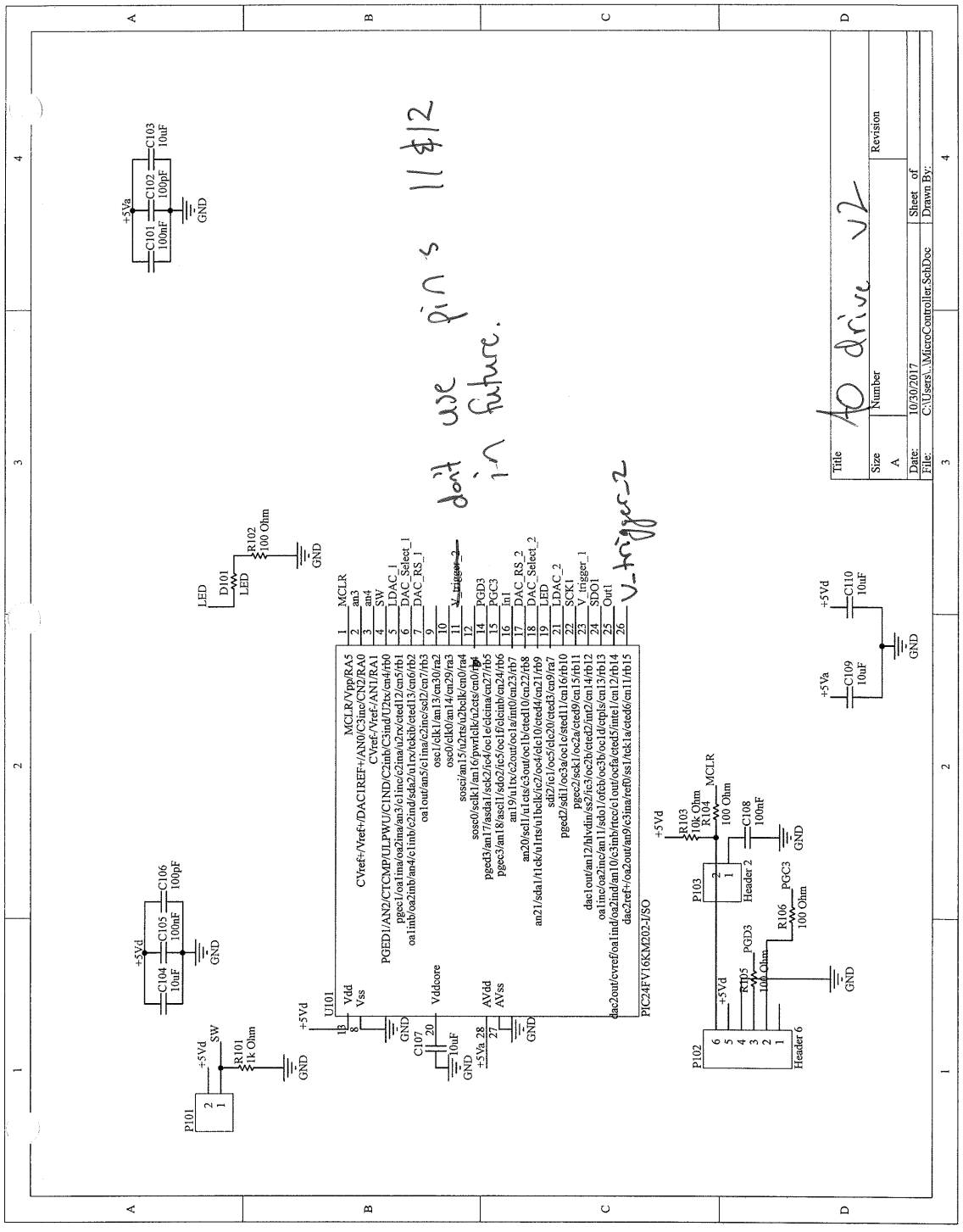
don't use pins 11 & 12 in future.
V_trigger_2
AO drive v2
Title
Size
A
Number
Revision
Date: 10/30/2017
Sheet of
File: C:\Users\..\MicroController.SchDoc
Drawn By:
PIC24FV16KM202-I/SO
MCLR/Vpp/RA5
CVref+/Vref+/DAC1REF+/AN0/C3inc/CN2/RA0
CVref-/Vref-/AN1/RA1
PGED1/AN2/CTCMP/ULPWU/CINID/C2inb/C3ind/U2tx/cn4/rb0
pgec1/oa1ina/oa2ina/an3/c1inc/c2ina/u2rx/cted12/cn5/rb1
oa1inb/oa2inb/an4/c1inb/c2ind/sda2/u1rx/ckib/cted13/cn6/rb2
oa1out/an5/c1ina/c2inc/scl2/cn7/rb3
osci/clkI/an13/cn30/ra2
osco/clko/an14/cn29/ra3
sosci/an15/u2rts/u2bclk/cn0/ra4
sosc0/sclk1/an16/pwrtclk/u2cts/cn0/rb4
pged3/an17/asda1/sck2/ic4/oc1e/clcina/cn27/rb5
pgec3/an18/ascl1/sdo2/ic5/oc1f/clcinb/cn24/rb6
an19/u1tx/c2out/oc1a/int0/cn23/rb7
an20/scl1/u1cts/c3out/oc1b/cted10/cn22/rb8
an21/sda1/t1ck/u1rts/u1bclk/ic2/oc4/clc10/cted4/cn21/rb9
sdi2/ic1/oc5/clc20/cted3/cn9/ra7
pgec2/sck1/oc2a/cted9/cn15/rb11
dac1out/an12/hlvdin/ss2/ic3/oc2b/cted2/int2/cn14/rb12
oa1inc/oa2inc/an11/sdo1/ofcb/oc3b/oc1d/ctpls/cn13/rb13
oa1out/cvref/oa1ind/oa2ind/an10/c3inb/ftcc/c1out/ocfa/cted5/inte1/cn12/rb14
dac2ref+/oa2out/an9/c3ina/refl0/ss1/tck1a/cted6/cn11/rb15
dac2out/cvref-/oa1out/an8/c3inc/refl0/ss1/tck1a/cted6/cn11/rb15
MCLR
an3
an4
SW
LDAC_1
DAC_Select_1
DAC_RS_1
V_trigger_2
PGD3
PGC3
in1
DAC_RS_2
DAC_Select_2
LED
LDAC_2
SCK1
V_trigger_1
SDO1
Out1
U101
LED
D101
R102
100 Ohm
P101
SW
R101
1k Ohm
P102
Header 6
P103
Header 2
R103
10k Ohm
R104
100 Ohm
R105
100 Ohm
R106
100 Ohm
C101
100nF
C102
100pF
C103
10uF
C104
10uF
C105
100nF
C106
100pF
C107
10uF
C108
100nF
C109
10uF
C110
10uF
+5Va
+5Vd
GND
Vdd
Vss
Vddcore
AVdd
AVss

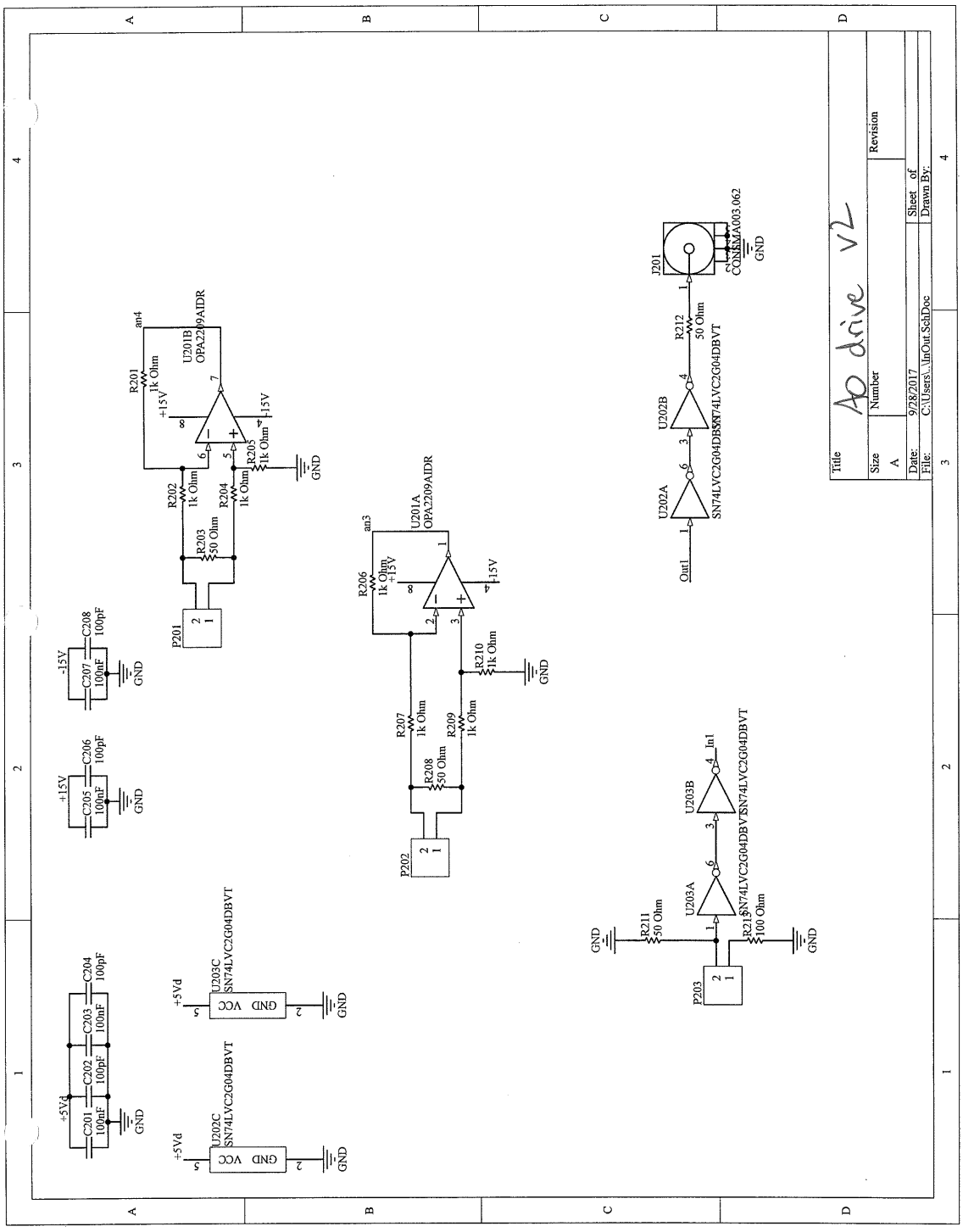
AO drive v2
Title
Size
A
Number
Revision
Date: 9/28/2017
File: C:\Users\...\InOut.SchDoc
Sheet of
Drawn By:
U201A OPA2209AIDR
U201B OPA2209AIDR
U202A SN74LVC2G04DBVT
U202B SN74LVC2G04DBVT
U202C SN74LVC2G04DBVT
U203A SN74LVC2G04DBVT
U203B SN74LVC2G04DBVT
U203C SN74LVC2G04DBVT
P201
P202
P203
J201
CONMMA003.062
R201 1k Ohm
R202 1k Ohm
R203 50 Ohm
R204 1k Ohm
R205 1k Ohm
R206 1k Ohm
R207 1k Ohm
R208 50 Ohm
R209 1k Ohm
R210 1k Ohm
R211 50 Ohm
R212 50 Ohm
R213 100 Ohm
C201 100nF
C202 100pF
C203 100nF
C204 100pF
C205 100nF
C206 100pF
C207 100nF
C208 100pF
+15V
-15V
+5Vd
GND
Out1
In1

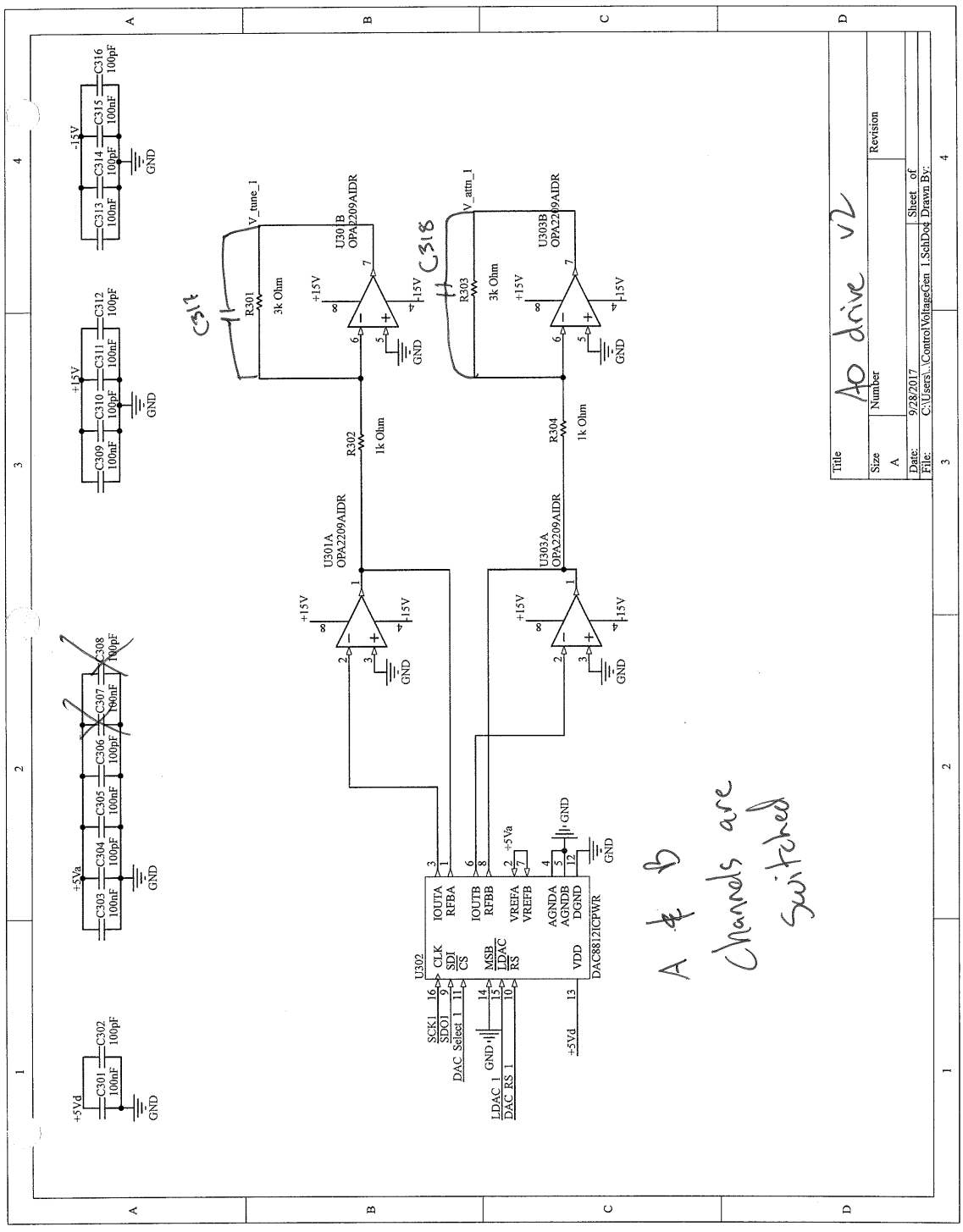
Title
AO drive v2
Size
A
Number
Revision
Date: 9/28/2017
File: C:\Users\...\ControlVoltageGen_1.SchDoc
Sheet of
Drawn By:
V_tune_1
V_attn_1
R301
3k Ohm
R302
1k Ohm
R303
3k Ohm
R304
1k Ohm
U301A OPA2209AIDR
U301B OPA2209AIDR
U303A OPA2209AIDR
U303B OPA2209AIDR
U302
DAC88121CPWR
IOUTA
RFBA
IOUTB
RFBB
VREFA
VREFB
AGNDA
AGNDB
DGND
VDD
CLK
SDI
CS
MSB
LDAC
RS
SCK1
SDO1
DAC_Select_1
LDAC_1
DAC_RS_1
+15V
-15V
+5Va
+5Vd
GND
C301 100nF
C302 100pF
C303 100nF
C304 100pF
C305 100nF
C306 100pF
C307 100nF
C308 100pF
C309 100nF
C310 100pF
C311 100nF
C312 100pF
C313 100nF
C314 100pF
C315 100nF
C316 100pF
C317
C318
A & B
Channels are
switched

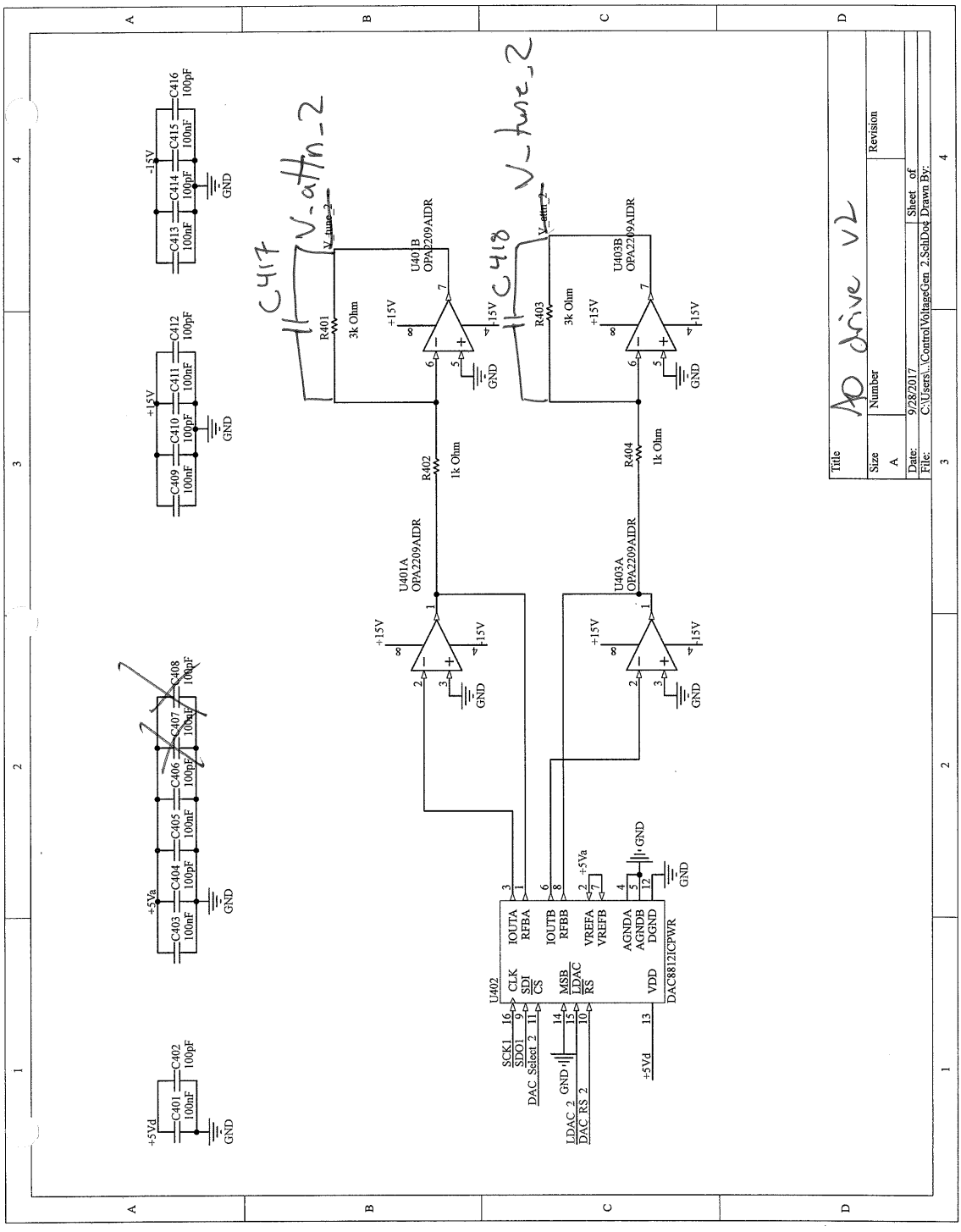
Title
AO drive v2
Size
A
Number
Revision
Date: 9/28/2017
File: C:\Users\...\ControlVoltageGen_2.SchDoc
Sheet of
Drawn By:
C417
V-attn_2
V_tune_2
C418
V_tune_2
V_attn_2
R401
3k Ohm
R402
1k Ohm
R403
3k Ohm
R404
1k Ohm
U40 B
OPA2209AIDR
U401A
OPA2209AIDR
U403B
OPA2209AIDR
U403A
OPA2209AIDR
+15V
-15V
GND
+5Va
+5Vd
C401 100nF
C402 100pF
C403 100nF
C404 100pF
C405 100nF
C406 100pF
C407 100nF
C408 100pF
C409 100nF
C410 100pF
C411 100nF
C412 100pF
C413 100nF
C414 100pF
C415 100nF
C416 100pF
U402
DAC8812ICPWR
SCK1
SDO1
DAC_Select_2
LDAC_2
DAC_RS_2
IOUTA
RFBA
IOUTB
RFBB
VREFA
VREFB
AGNDA
AGNDB
DGND
VDD
CLK
SDI
CS
MSB
LDAC
RS

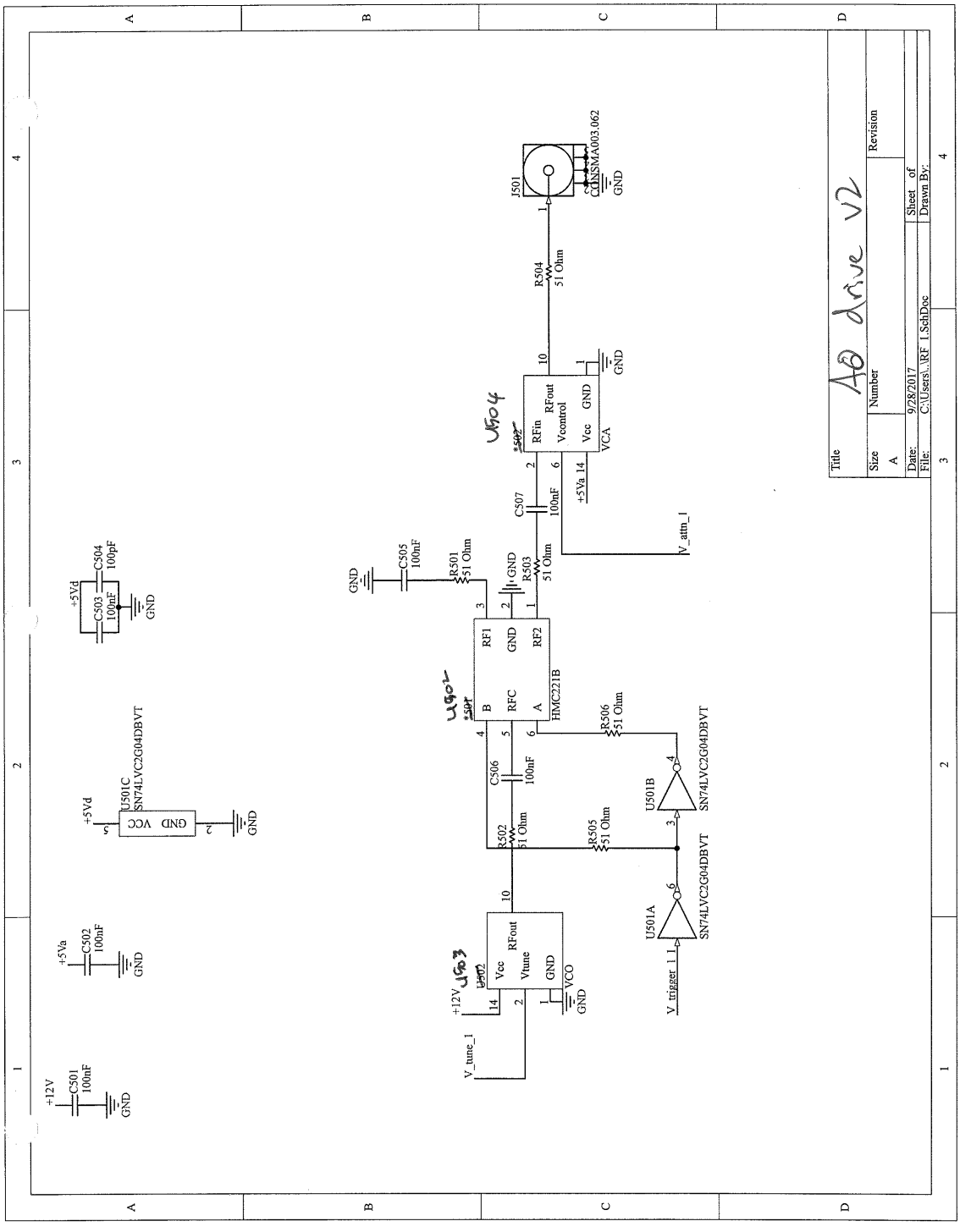
AB drive V2
Title
Size
A
Number
Revision
Date: 9/28/2017
File: C:\Users\...\RF_1.SchDoc
Sheet of
Drawn By:
+12V
C501 100nF
GND
+5Va
C502 100nF
GND
+5Vd
C503 100nF
C504 100pF
GND
U501C SN74LVC2G04DBVT
GND VCC
+5Vd
GND
C505 100nF
GND
R501 51 Ohm
R503 51 Ohm
C507 100nF
+5Va_14
V_attn_1
U504
RFin
Vcontrol
Vcc
RFout
GND
VCA
R504 51 Ohm
J501
CONSMA003.062
GND
U501
RF1
GND
RF2
RFC
B
A
HMC221B
R506 51 Ohm
C506 100nF
R502 51 Ohm
R505 51 Ohm
U501B
SN74LVC2G04DBVT
U501A
SN74LVC2G04DBVT
V_trigger_1_1
U503
Vcc
Vtune
GND
RFout
VCO
+12V
V_tune_1
GND

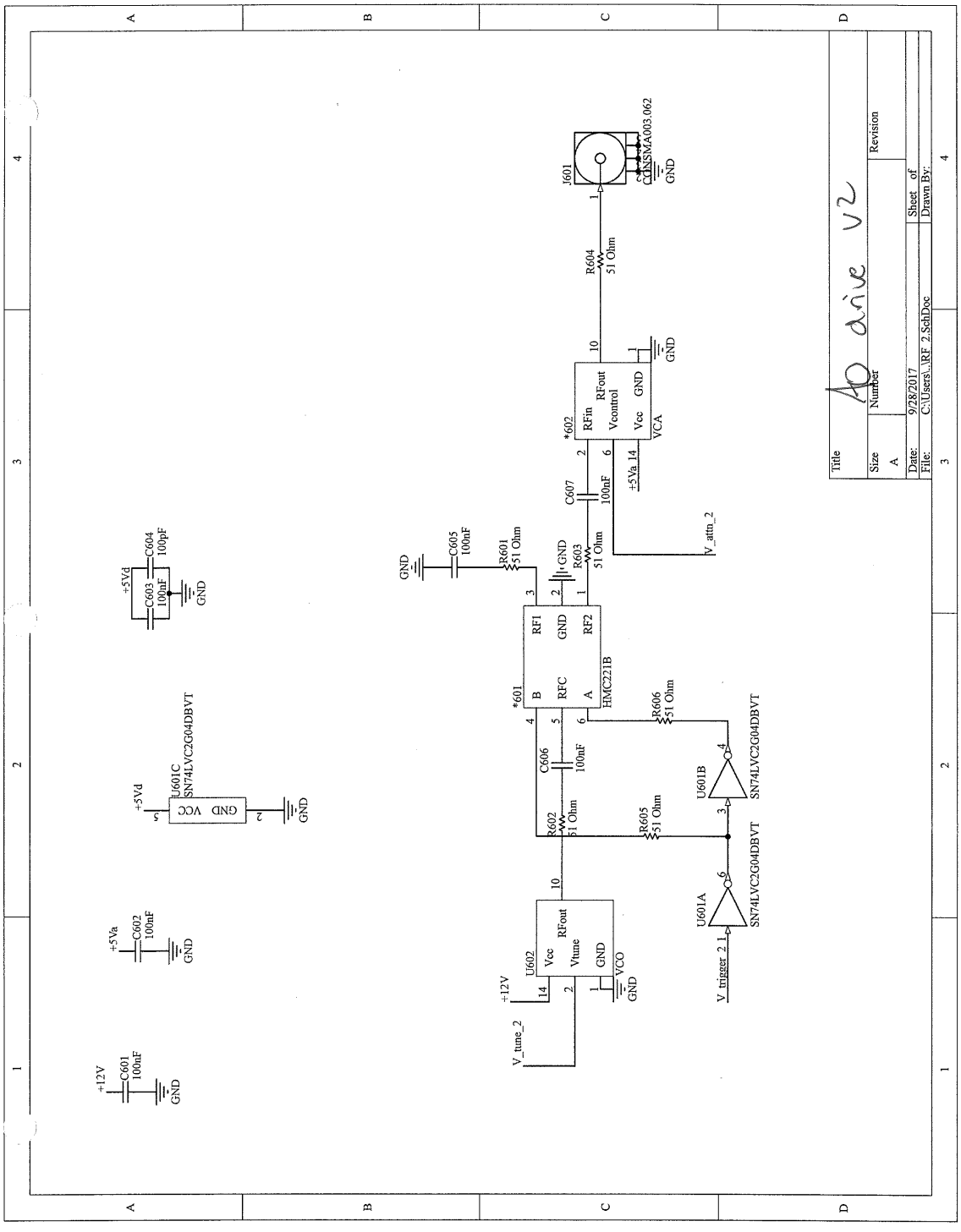
Title
IQ drive V2
Size
A
Number
Revision
Date: 9/28/2017
File: C:\Users\...\RF 2.SchDoc
Sheet of
Drawn By:
J601
CONSMA003.062
GND
R604
51 Ohm
*602
RFin
RFout
Vcontrol
Vcc
GND
VCA
+5Va_14
C607
100nF
R603
51 Ohm
V_attn_2
C605
100nF
R601
51 Ohm
*601
RF1
GND
RF2
RFC
B
A
HMC221B
C606
100nF
R602
51 Ohm
R606
51 Ohm
R605
51 Ohm
U602
Vcc
RFout
Vtune
GND
VCO
+12V
V_tune_2
U601A
U601B
SN74LVC2G04DBVT
V_trigger_2
+5Vd
C603
100nF
C604
100pF
U601C
SN74LVC2G04DBVT
GND VCC
+5Va
C602
100nF
+12V
C601
100nF

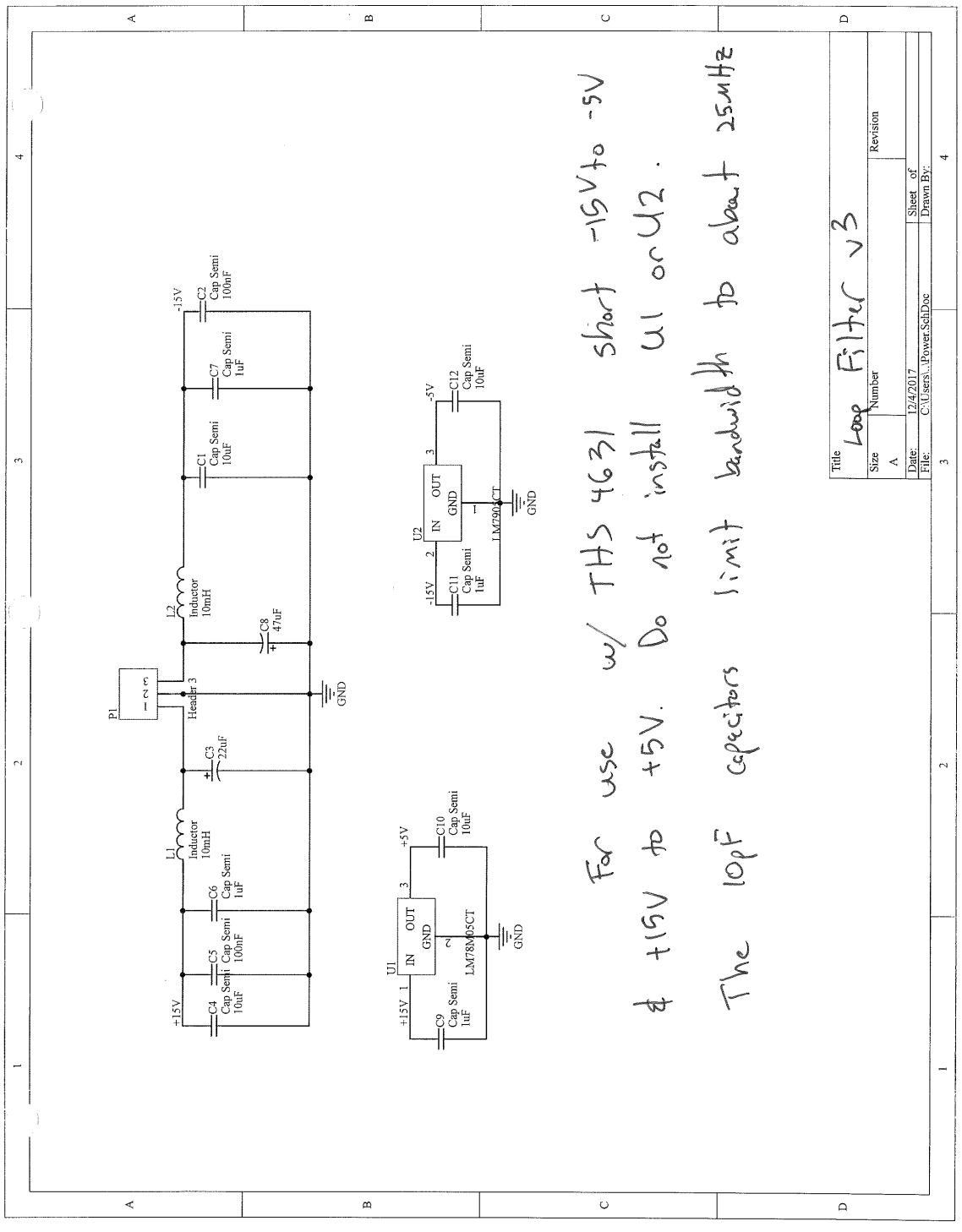
P1
Header 3
L1
Inductor
10mH
L2
Inductor
10mH
C1
Cap Semi
10uF
C2
Cap Semi
100nF
C3
22uF
C4
Cap Semi
10uF
C5
Cap Semi
100nF
C6
Cap Semi
1uF
C7
Cap Semi
1uF
C8
47uF
+15V
-15V
GND
U1
IN
OUT
GND
LM7805CT
C9
Cap Semi
1uF
C10
Cap Semi
10uF
+5V
U2
LM7905CT
C11
Cap Semi
1uF
C12
Cap Semi
10uF
-5V
For use w/ THS 4631 short -15V to -5V
& +15V to +5V. Do not install U1 or U2.
The 10pF capacitors limit bandwidth to about 25mHz
Title
Loop Filter v3
Size
A
Number
Revision
Date: 12/4/2017
Sheet of
File: C:\Users\...\Power.SchDoc
Drawn By:

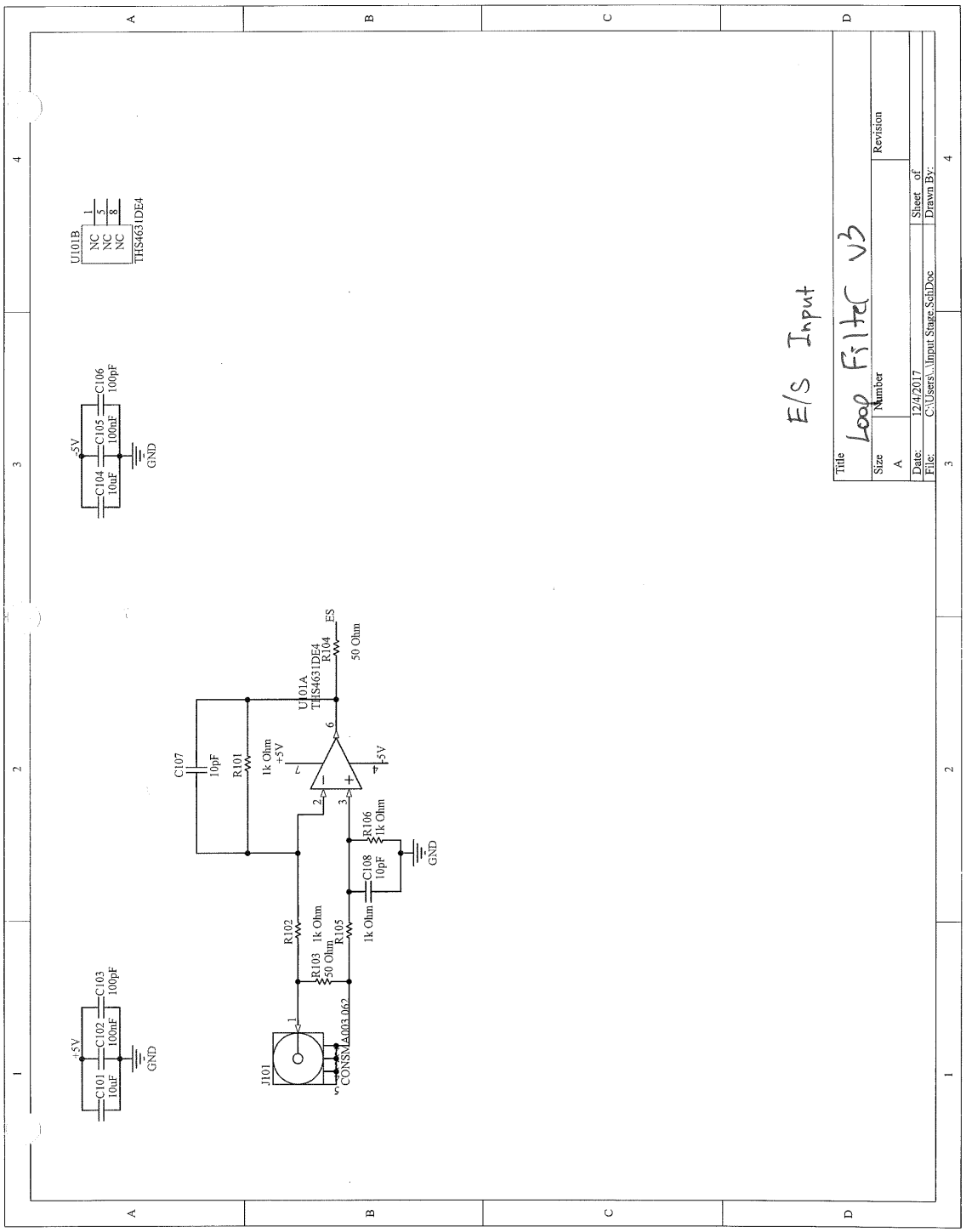
E/S Input
Title
Loop Filter V3
Size
A
Number
Revision
Date: 12/4/2017
Sheet of
File: C:\Users\...\Input Stage.SchDoc
Drawn By:
U101B
NC
NC
NC
THS4631DE4
C104 10uF
C105 100nF
C106 100pF
+5V
GND
C101 10uF
C102 100nF
C103 100pF
C107 10pF
R101 1k Ohm
R102 1k Ohm
R103 50 Ohm
R105 1k Ohm
R106 1k Ohm
C108 10pF
R104 50 Ohm
ES
U101A
THS4631DE4
J101
CONSMA003.062

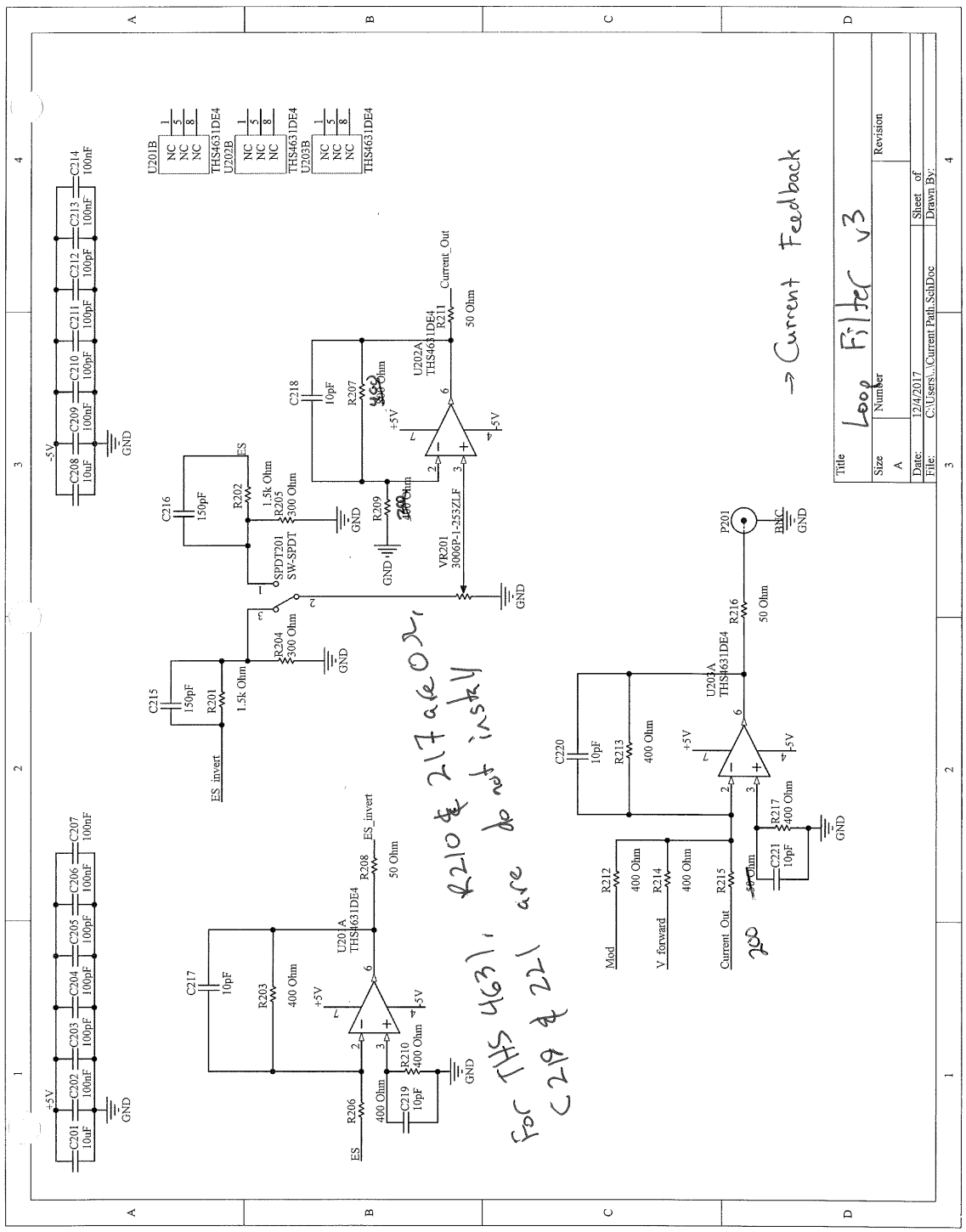
Loop Filter v3
-> Current Feedback
For THS4631, use R210 & 217 as 0Ω, do not install
C219 & 221
ES
ES_invert
Current_Out
Mod
V_forward
SPDT201 SW-SPDT
VR201 3066P-1-253ZLF
THS4631DE4
GND
+5V
-5V

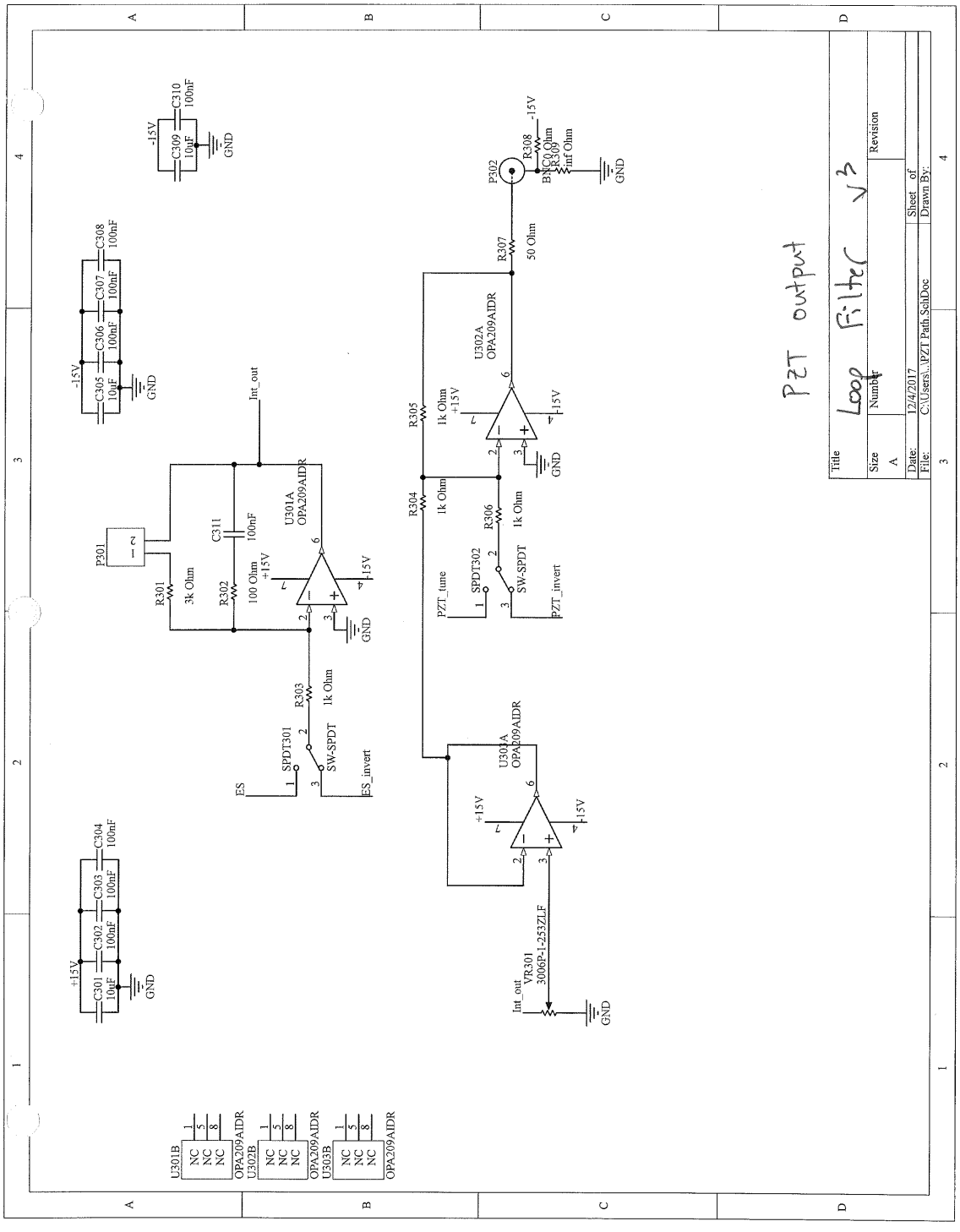
PZT output
Loop Filter v3
Title
Size
A
Number
Revision
Date: 12/4/2017
File: C:\Users\..\PZT Path.SchDoc
Sheet of
Drawn By:
P301
P302
R301 3k Ohm
R302 100 Ohm
R303 1k Ohm
R304 1k Ohm
R305 1k Ohm
R306 1k Ohm
R307 50 Ohm
R308 50 Ohm
C301 10uF
C302 100nF
C303 100nF
C304 100nF
C305 10uF
C306 100nF
C307 100nF
C308 100nF
C309 10uF
C310 100nF
C311 100nF
U301A OPA209AIDR
U301B OPA209AIDR
U302A OPA209AIDR
U302B OPA209AIDR
U303B OPA209AIDR
SPDT301 SW-SPDT
SPDT302 SW-SPDT
VR301 3006P-1-253ZLF
+15V
-15V
GND
Int_out
ES
ES_invert
PZT_tune
PZT_invert

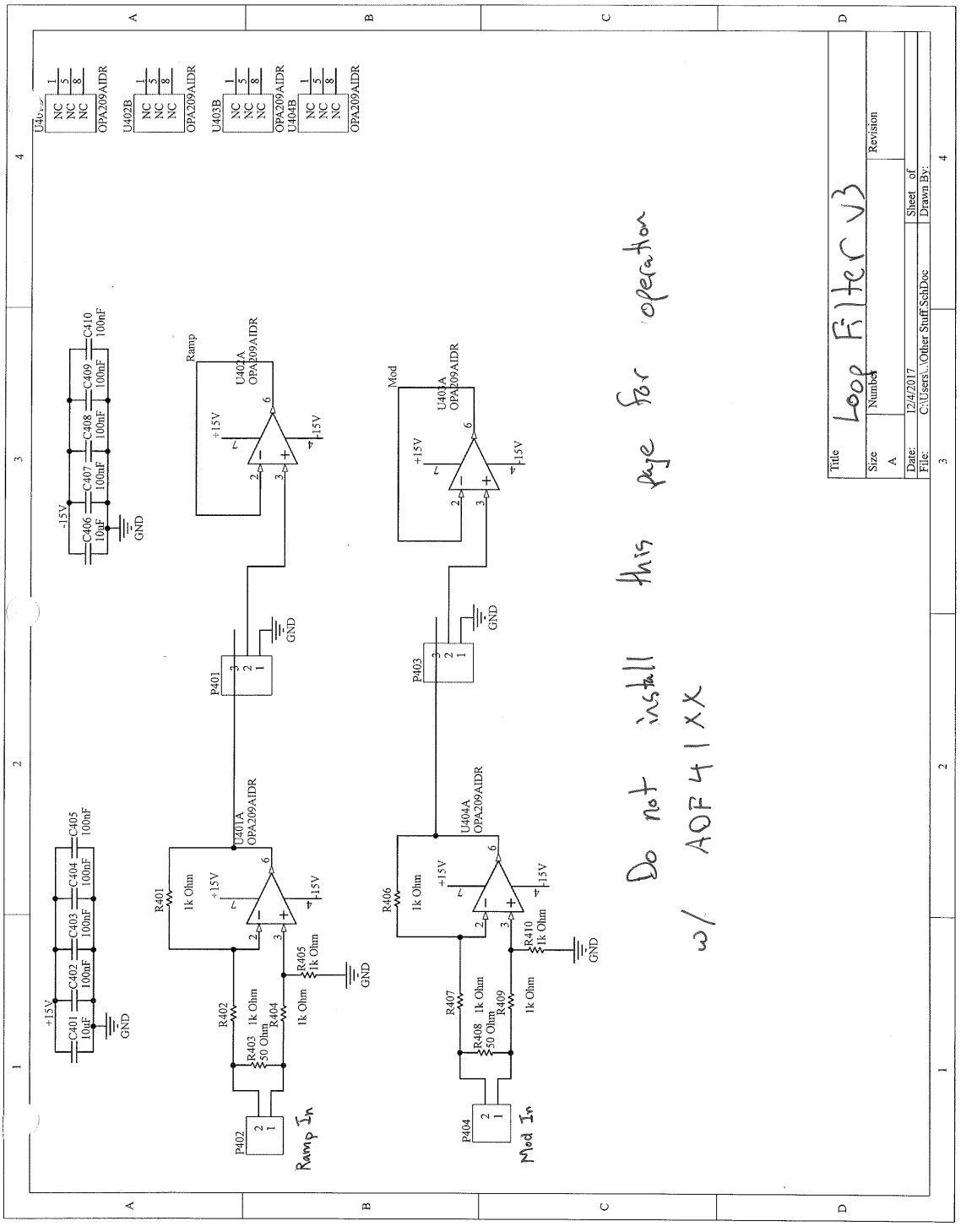
Loop Filter v3
Do not install this page for operation
w/ A0F41XX
Ramp In
Mod In
Ramp
Mod
U401A OPA209AIDR
U402A OPA209AIDR
U403A OPA209AIDR
U404A OPA209AIDR
U402B OPA209AIDR
U403B OPA209AIDR
U404B OPA209AIDR
P401
P402
P403
P404
R401 1k Ohm
R402 1k Ohm
R403 50 Ohm
R404 1k Ohm
R405 1k Ohm
R406 1k Ohm
R407 1k Ohm
R408 50 Ohm
R409 1k Ohm
R410 1k Ohm
C401 10uF
C402 100nF
C403 100nF
C404 100nF
C405 100nF
C406 10uF
C407 100nF
C408 100nF
C409 100nF
C410 100nF
+15V
-15V
GND
Size A
Number
Revision
Date: 12/4/2017
Sheet of
File: C:\Users\...\Other Stuff.SchDoc
Drawn By:

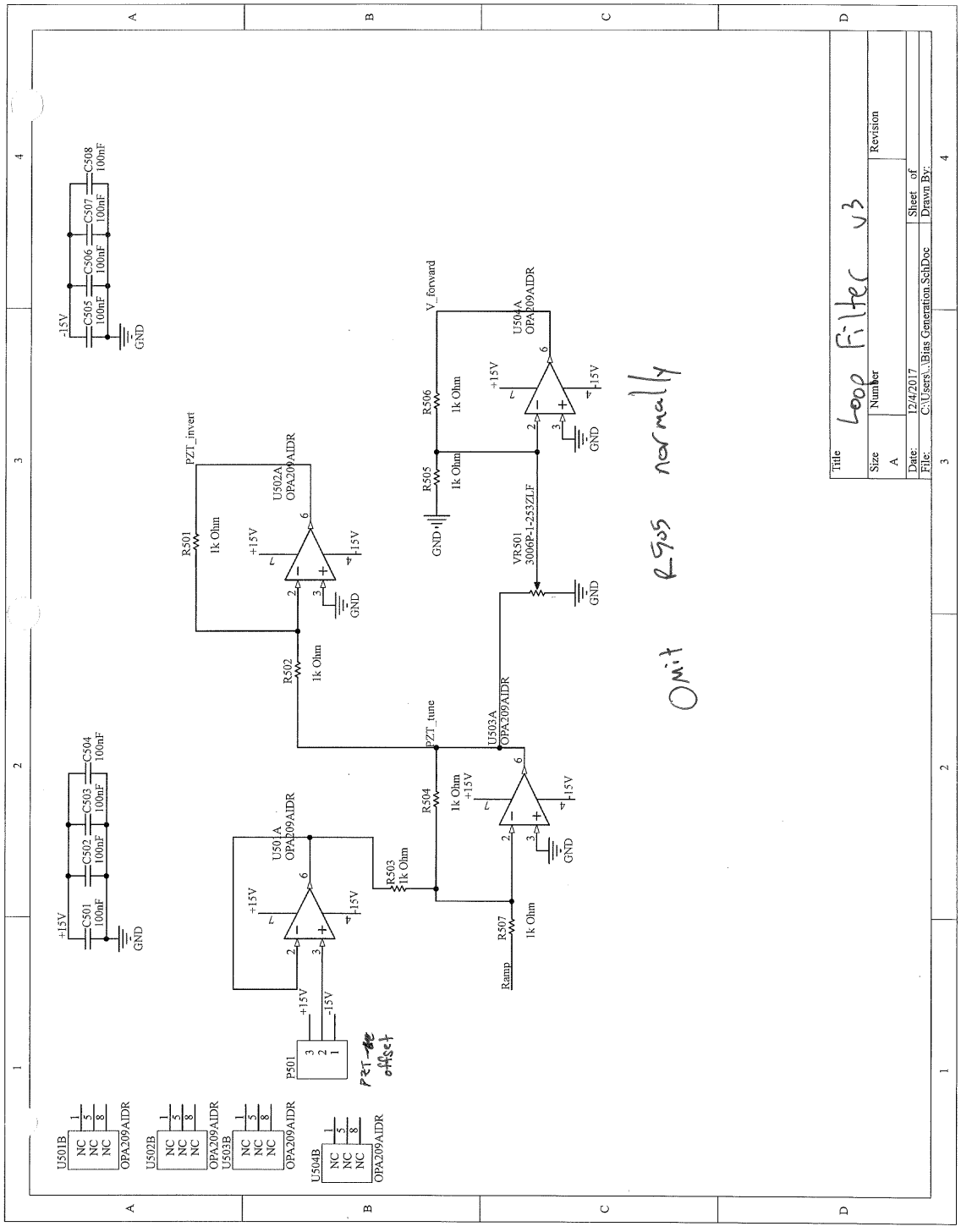
Loop Filter v3
Omit R505 normally
PZT-fine offset
PZT_invert
PZT_tune
V_forward
Ramp
R501 1k Ohm
R502 1k Ohm
R503 1k Ohm
R504 1k Ohm
R505 1k Ohm
R506 1k Ohm
R507 1k Ohm
VR501 3006P-1-253ZLF
U501A OPA209AIDR
U502A OPA209AIDR
U503A OPA209AIDR
U504A OPA209AIDR
U501B OPA209AIDR
U502B OPA209AIDR
U503B OPA209AIDR
U504B OPA209AIDR
C501 100nF
C502 100nF
C503 100nF
C504 100nF
C505 100nF
C506 100nF
C507 100nF
C508 100nF
P501
+15V
-15V
GND
Size A
Number
Revision
Date: 12/4/2017
Sheet of
File: C:\Users\...\Bias Generation.SchDoc
Drawn By:

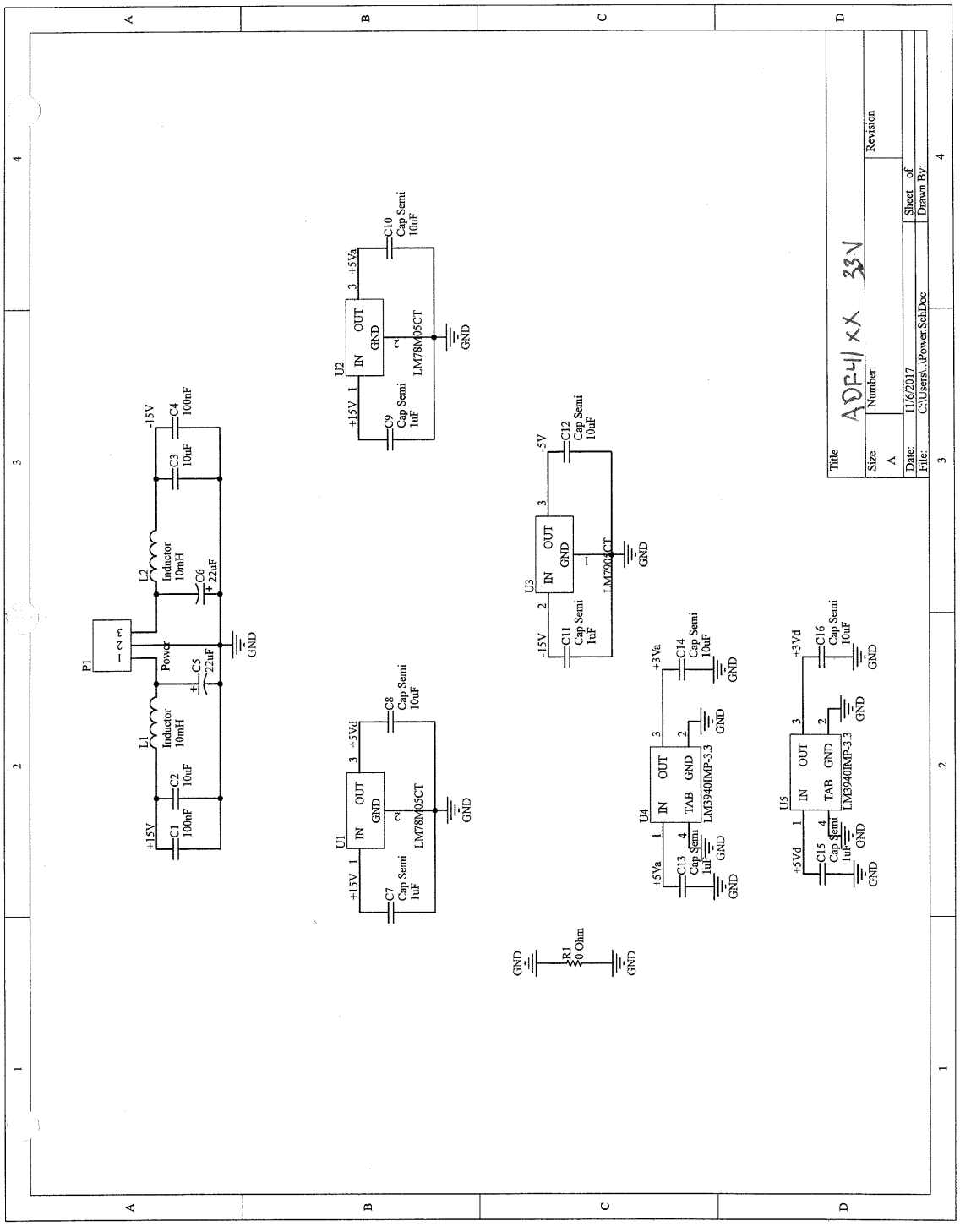
P1
Power
L1
Inductor
10mH
L2
Inductor
10mH
C1
100nF
C2
10uF
C3
10uF
C4
100nF
C5
22uF
C6
22uF
+15V
-15V
GND
U1
LM78M05CT
C7
Cap Semi
1uF
C8
Cap Semi
10uF
+5Vd
U2
LM78M05CT
C9
Cap Semi
1uF
C10
Cap Semi
10uF
+5Va
U3
LM7905CT
C11
Cap Semi
1uF
C12
Cap Semi
10uF
-5V
U4
LM3940IMP-3.3
C13
Cap Semi
1uF
C14
Cap Semi
10uF
+3Va
U5
LM3940IMP-3.3
C15
Cap Semi
1uF
C16
Cap Semi
10uF
+3Vd
R1
0 Ohm
Title
ADF4l xx 33V
Size
A
Number
Revision
Date:
11/6/2017
Sheet of
File:
C:\Users\...\Power.SchDoc
Drawn By:

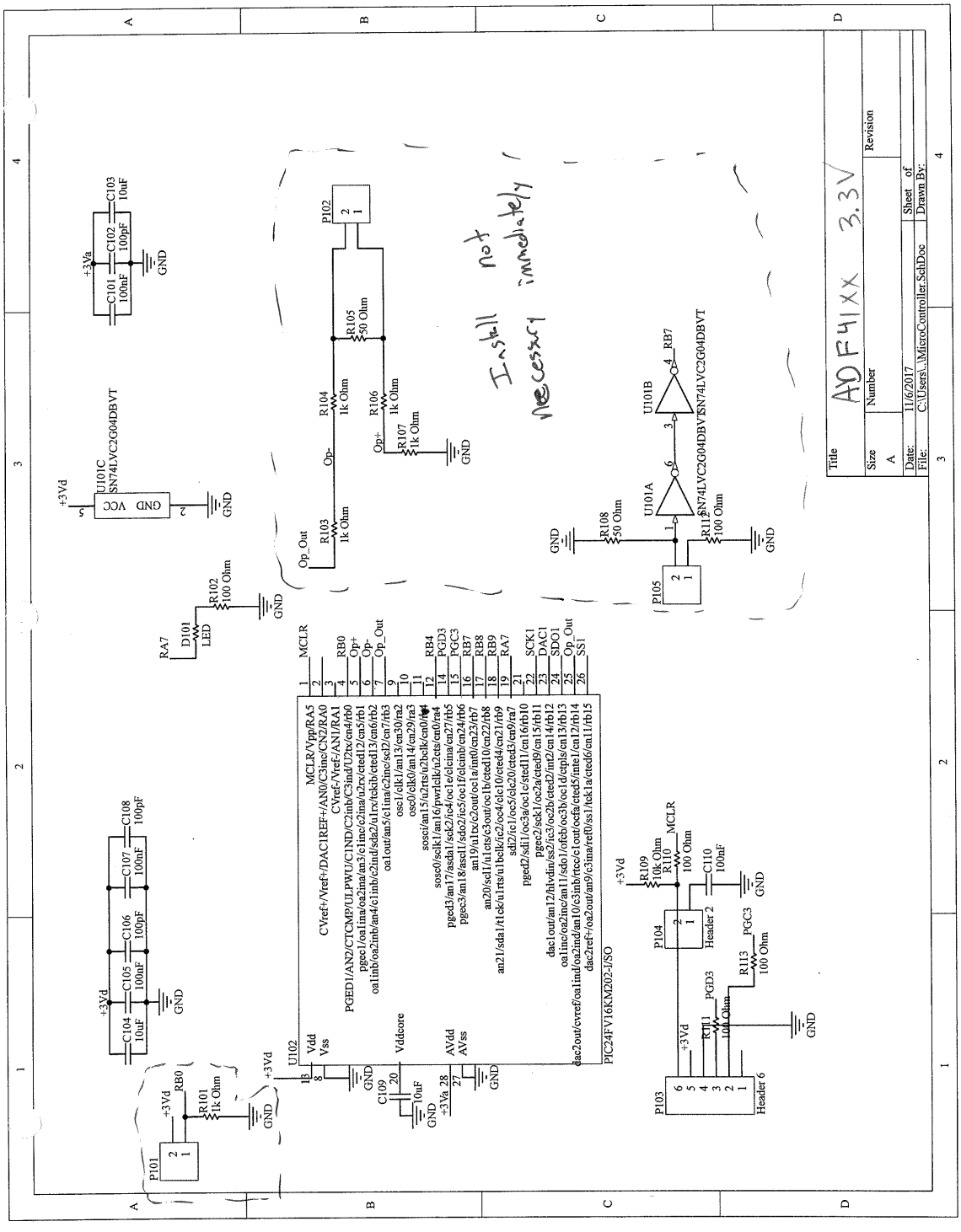
PIC24FV16KM202-I/SO
MCLR/Vpp/RA5
CVref+/Vref+/DAC1REF+/AN0/C3inc/CN2/RA0
CVref-/Vref-/AN1/RA1
PGED1/AN2/CTCMP/ULPWU/C1ND/C2inb/U2rx/can4/rb0
pgec1/oa1ina/oa2ina/an3/c1inc/c2ina/u2rx/cted12/can5/rb1
oa1inb/oa2inb/an4/c1inb/c2ind/sda2/u1rx/tckib/cted13/can6/rb2
oa1out/an5/c1ing/c2inc/scl2/can7/rb3
osc1/clki/an13/can30/ra2
osc0/clko/an14/can29/ra3
sosci/an15/u2rts/u2bclk/can0/ra4
sosco/sclk1/an16/pwrtclk/u2cts/can0/ra4
pged3/an17/asda1/sck2/ric4/oc1e/cleina/ca27/rb5
pgec3/an18/ascl1/sda2/ric5/oc1f/clcinb/can24/rb6
an19/u1tx/c2out/oc1a/int0/cn23/rb7
an20/scl1/u1cts/c3out/oc1b/cted10/cn22/rb8
an21/sda1/tclk/u1rts/u1bclk/ic2/oc4/clc10/cted4/cn21/rb9
sdi2/ic1/ocs5/clc20/cted3/cn9/ra7
pged2/sdi1/oc3a/oc1c/sted11/cn16/rb10
pgec2/sck1/oc2a/cted9/cn15/rb11
dac1out/an12/hlvdin/ss2/ic3/oc2b/cted2/int2/cn14/rb12
oa1inc/oa2inc/an11/sdo1/ofcb/oc3b/oc1d/ctpls/cn13/rb13
oa1ind/oa2ind/an10/c3inb/rtcc/c1out/ocfa/cted5/intel/cn12/rb14
dac2ref+/oa2out/an9/c3ina/refi0/ss1/tdk1a/cted6/cn11/rb15
dac2out/cvref/oa1ind/oa2ind/an10/c3inb/rtcc/c1out/ocfa/cted5/intel/cn12/rb14
MCLR
Vdd
Vss
Vddcore
AVdd
AVss
U102
P101
P102
P103
P104
P105
Header 2
Header 6
R101 1k Ohm
R102 100 Ohm
R103 1k Ohm
R104 1k Ohm
R105 50 Ohm
R106 1k Ohm
R107 1k Ohm
R108 50 Ohm
R109 10k Ohm
R110 100 Ohm
R111 100 Ohm
R113 100 Ohm
C101 100nF
C102 100pF
C103 10uF
C104 10uF
C105 100nF
C106 100pF
C107 100nF
C108 100pF
C109 10uF
C110 100nF
D101 LED
U101A SN74LVC2G04DBVT
U101B SN74LVC2G04DBVT
U101C SN74LVC2G04DBVT
GND
+3Vd
+3Va
RA7
RB0
RB4
RB7
RB8
RB9
PGD3
PGC3
SCK1
SDO1
SS1
DAC1
Op+
Op-
Op_Out
Op_Out
Op+
Op-
Title
AD F41XX 3.3V
Size
A
Number
Revision
Date: 11/6/2017
File: C:\Users\...\MicroController.SchDoc
Sheet of
Drawn By:
Install not necessary immediately

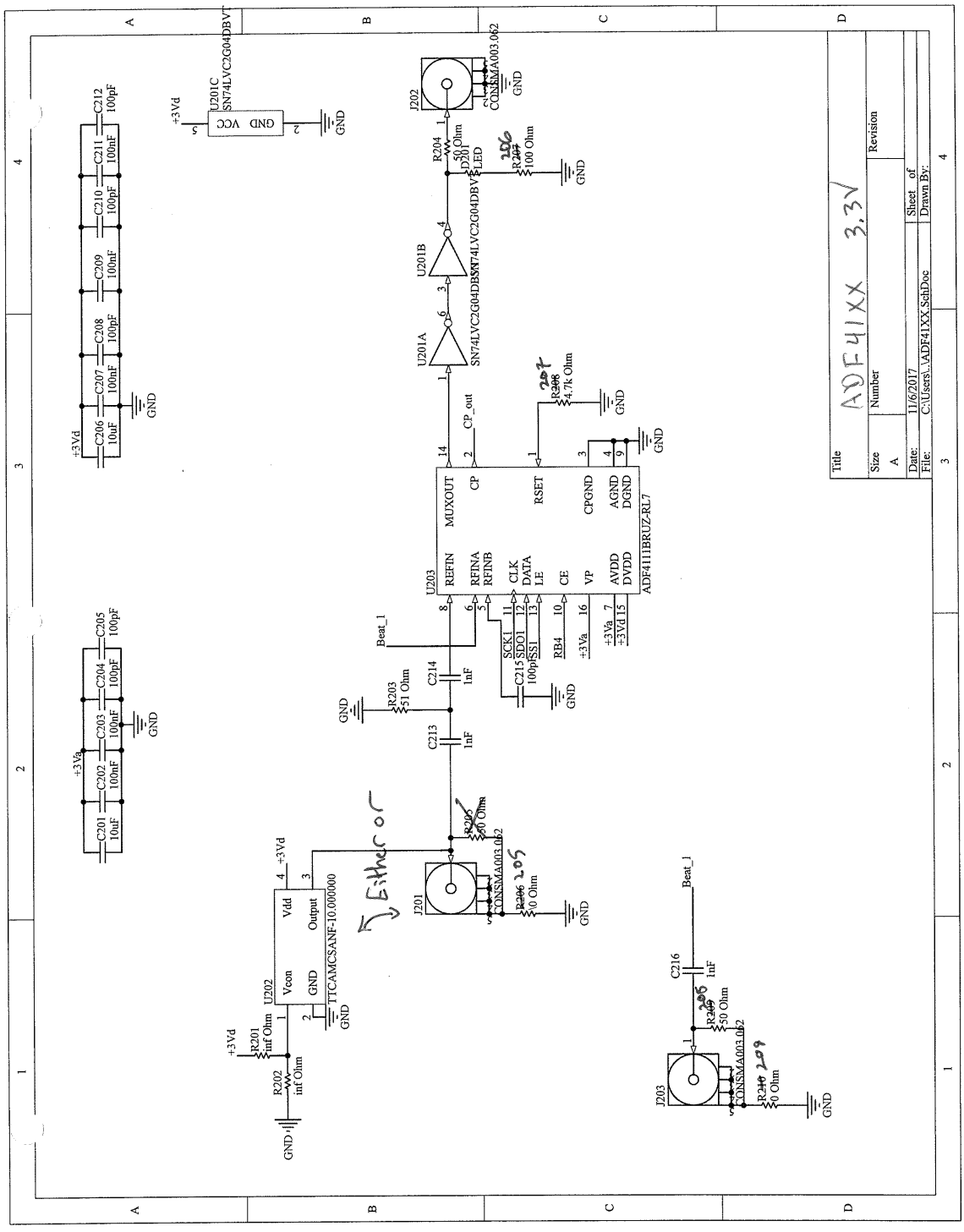
U201C
SN74LVC2G04DBVT
GND VCC
+3Vd
GND
U201A
U201B
SN74LVC2G04DBVT
U203
ADF4111BRUZ-RL7
REFIN
MUXOUT
CP
RSET
CPGND
AGND
DGND
RFINA
RFINB
CLK
DATA
LE
CE
VP
AVDD
DVDD
SCK1
SDO1
SS1
RB4
+3Va
+3Vd
CP_out
Beat_1
U202
TTCAMCSANF-10.000000
Vcon
GND
Vdd
Output
J201
J202
J203
CONSMA003.062
D201
LED
R201 inf Ohm
R202 inf Ohm
R203 51 Ohm
R204 50 Ohm
R205 50 Ohm
R206 10 Ohm
R207 100 Ohm
R208 4.7k Ohm
R209 50 Ohm
R210 0 Ohm
C201 10uF
C202 100nF
C203 100nF
C204 100pF
C205 100pF
C206 10uF
C207 100nF
C208 100pF
C209 100nF
C210 100pF
C211 100nF
C212 100pF
C213 1nF
C214 1nF
C215 100pF
C216 1nF
Either or
ADF41XX 3.3V
Title
Size
A
Number
Revision
Date: 11/6/2017
File: C:\Users\..\ADF41XX.SchDoc
Sheet of
Drawn By:

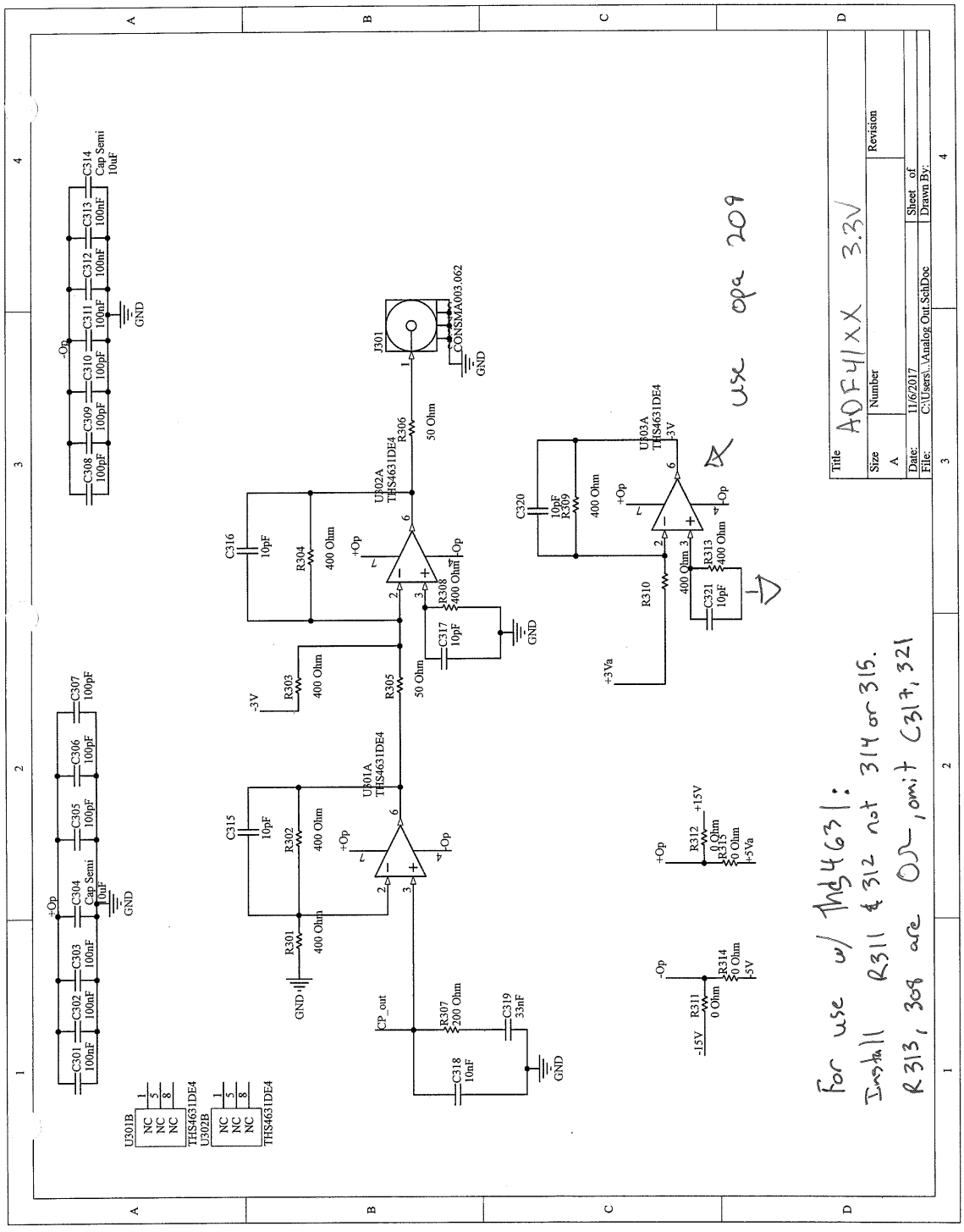
Title AOF4/XX 3.3V
Size A
Number
Revision
Date: 11/6/2017
Sheet of
File: C:\Users\..\Analog Out.SchDoc
Drawn By:
U301A THS4631DE4
U301B THS4631DE4
U302A THS4631DE4
U302B THS4631DE4
U303A THS4631DE4
J301 CONSMA003.062
C301 100nF
C302 100nF
C303 100nF
C304 Cap Semi 10uF
C305 100pF
C306 100pF
C307 100pF
C308 100pF
C309 100pF
C310 100pF
C311 100nF
C312 100nF
C313 100nF
C314 Cap Semi 10uF
C315 10pF
C316 10pF
C317 10pF
C318 10nF
C319 33nF
C320 10pF
C321 10pF
R301 400 Ohm
R302 400 Ohm
R303 400 Ohm
R304 400 Ohm
R305 50 Ohm
R306 50 Ohm
R307 200 Ohm
R308 400 Ohm
R309 400 Ohm
R310 400 Ohm
R311 0 Ohm
R312 0 Ohm
R313 400 Ohm
R314 0 Ohm
R315 0 Ohm
+Op
-Op
GND
-3V
+3Va
-15V
+15V
+5Va
-5V
CP_out
for use w/ THS4631:
Install R311 & 312 not 314 or 315.
R313, 309 are OK, omit C317, 321
use opa 209

How to get PLL to oscillate

1) Set mux out to display serial data out. Play around w/ clock settings (idle high or low & transmit on transition) until chip echo's your data to it.

2) Use N-counter & R-counter output on mux to find out actual divide ratios.

3) Set proper division and 5mA (full gain) for charge pump gain. Play w/ CP sign to get oscillation.

Notes:

How to go from PLL oscilating to locked

1) Go thru loop looking for railing of op-amps. Reduce the gain until they don't rail.

2) Use vco_calc spread sheet to recalculate C_1, C_2 & R_2. Change to close to ideal values. Make sure to use COG caps.

   On ADF 41XX board, C_1 = C314
   C_2 = C315
   R_2 = R307

3) If it now locks but is noisy, try increasing signal into ADF41XX chip. It will get a noisy lock with too little signal.

4) Go back and slowly add in gain in op amps if desired. This will reduce linewidth at the cost of operating range & pull in range.

Notes:

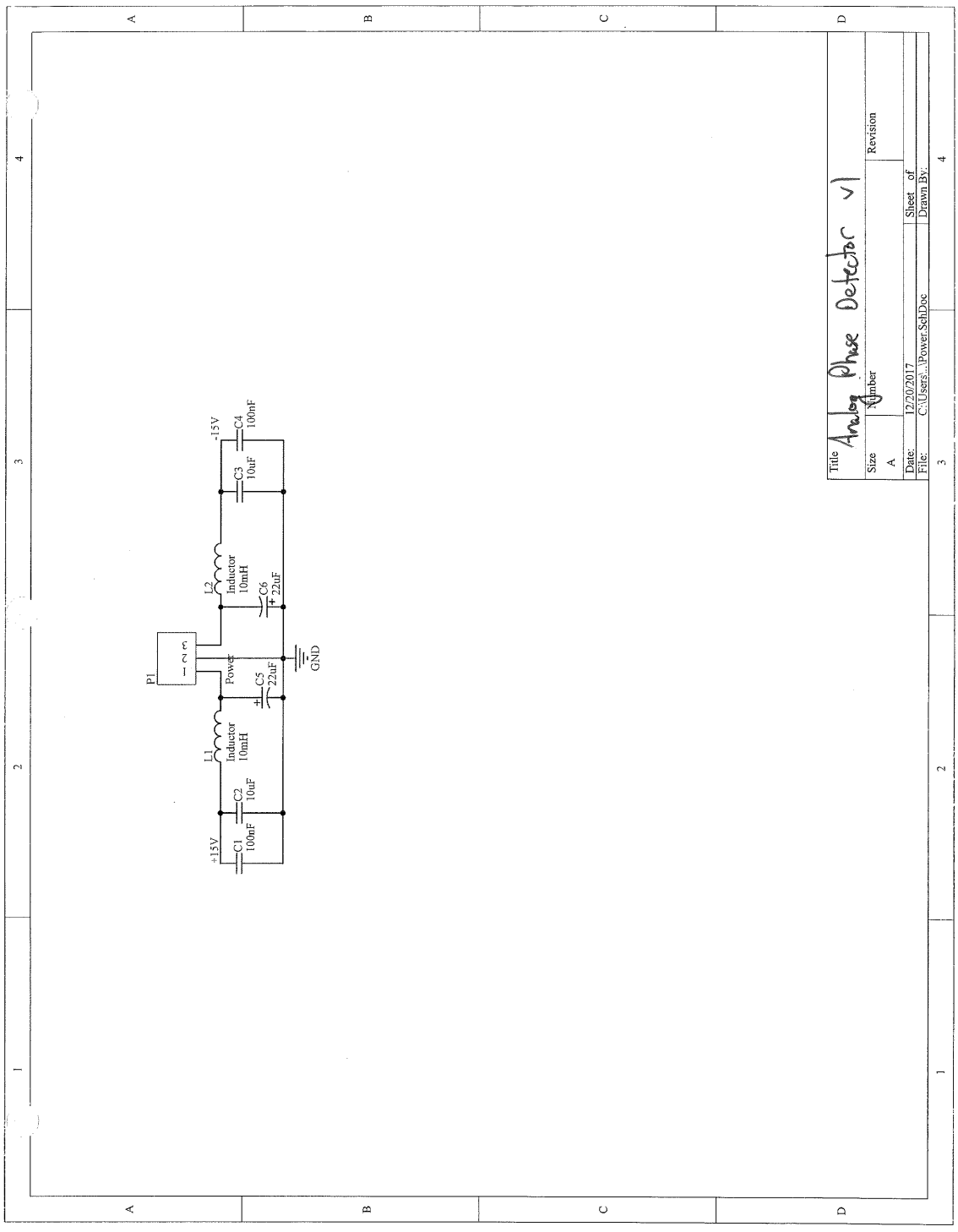
Title
Analog Phase Detector v1
Size
A
Number
Revision
Date:
12/20/2017
Sheet of
File:
C:\Users...\Power.SchDoc
Drawn By:
P1
Power
GND
+15V
-15V
C1
100nF
C2
10uF
C3
10uF
C4
100nF
C5
22uF
C6
22uF
L1
Inductor
10mH
L2
Inductor
10mH

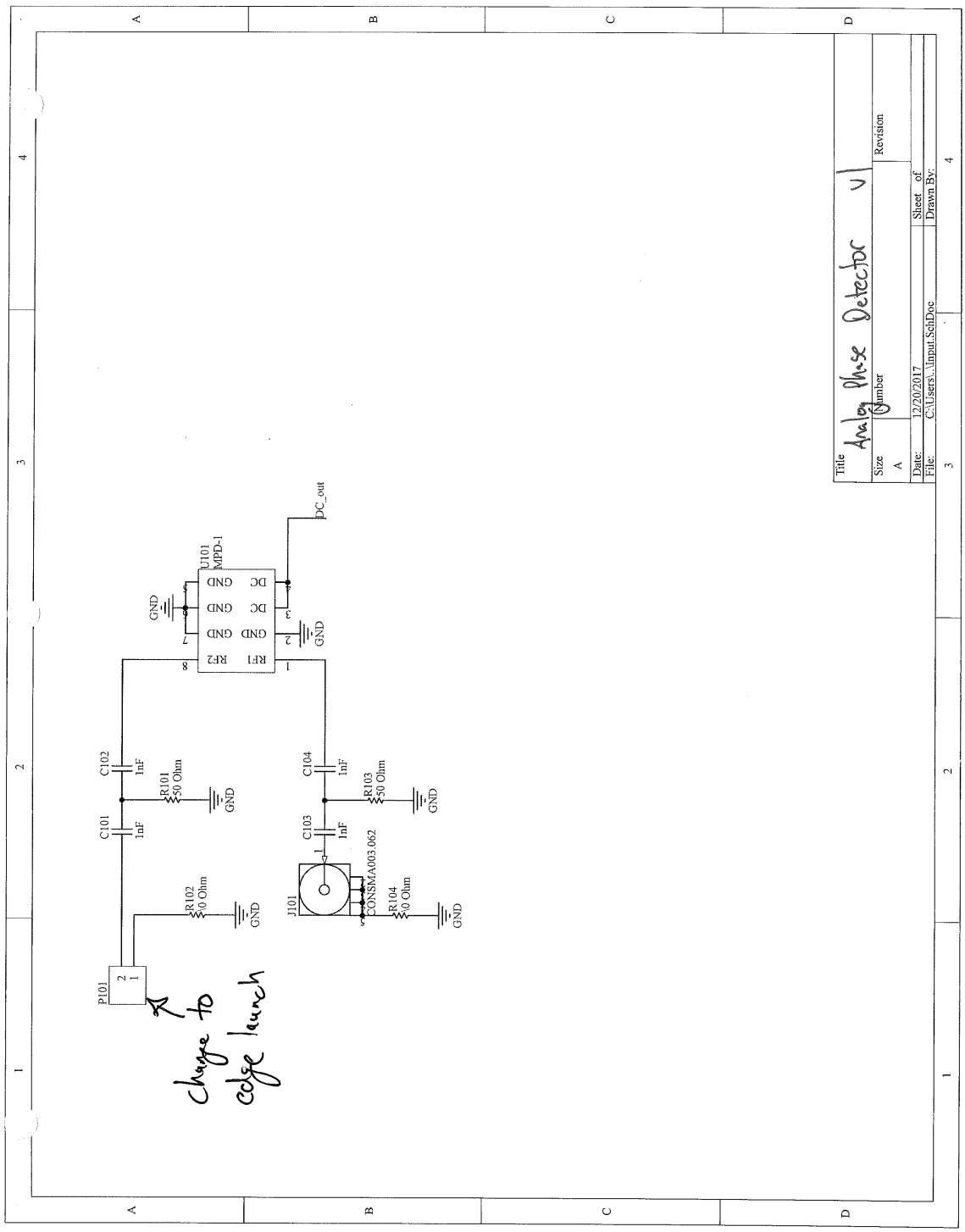
Title
Analog Phase Detector v1
Size
A
Number
Revision
Date: 12/20/2017
Sheet of
File: C:\Users\...\Input.SchDoc
Drawn By:
U101
MPD-1
RF1
RF2
GND
GND
GND
GND
DC
DC
DC_out
C101
1nF
C102
1nF
C103
1nF
C104
1nF
R101
50 Ohm
R102
50 Ohm
R103
50 Ohm
R104
50 Ohm
J101
CONSMA003.062
P101
Charge to edge launch

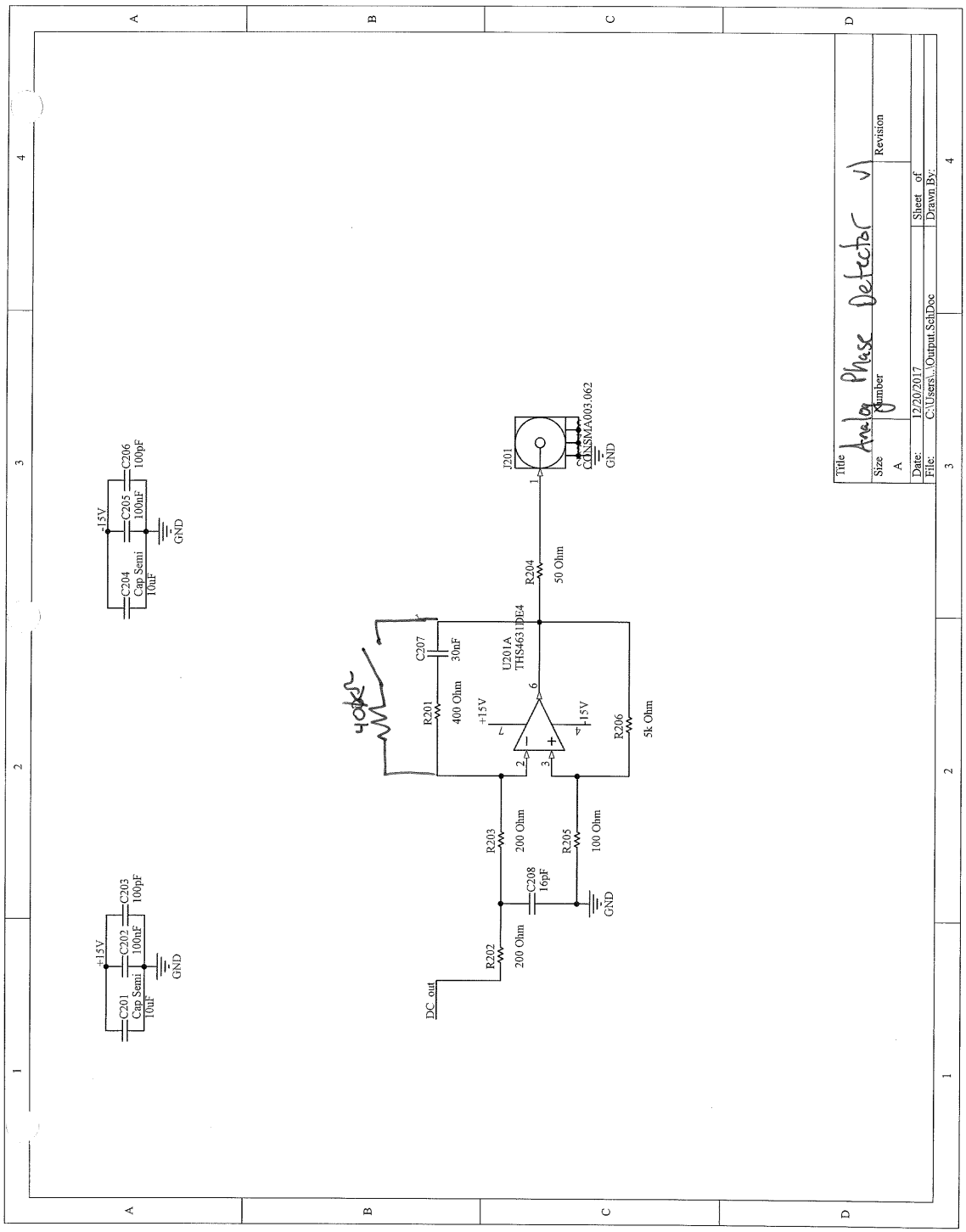
Title
Analog Phase Detector v1
Size
A
Number
Revision
Date: 12/20/2017
Sheet of
File: C:\Users\...\Output.SchDoc
Drawn By:
J201
CONSMA003.062
GND
C207
30nF
R201
400 Ohm
U201A
THS4631IDE4
R204
50 Ohm
+15V
-15V
R206
5k Ohm
R203
200 Ohm
R205
100 Ohm
C208
16pF
R202
200 Ohm
DC_out
C201
Cap Semi
10uF
C202
100nF
C203
100pF
C204
Cap Semi
10uF
C205
100nF
C206
100pF

D. CODE

D.1 Micro-controller code

```
// FBS
#pragma config BWRP = OFF     // Boot Segment Write Protect->Disabled
#pragma config BSS = OFF     // Boot segment Protect->No boot program flash
    segment

// FGS
#pragma config GWRP = OFF     // General Segment Write Protect->General
    segment may be written
#pragma config GCP = OFF     // General Segment Code Protect->No Protection

// FOSCSEL
#pragma config FNOSC = FRCPLL     // Oscillator Select->Fast RC Oscillator
    with Postscaler and PLL Module (FRCDIV+PLL)
#pragma config SOSCSRC = DIG     // SOSC Source Type->Analog Mode for use
    with crystal
#pragma config LPRCSEL = HP     // LPRC Oscillator Power and Accuracy->High
    Power, High Accuracy Mode
#pragma config IESO = ON     // Internal External Switch Over bit->Internal
    External Switchover mode enabled (Two-speed Start-up enabled)

// FOSC
#pragma config POSCMOD = NONE     // Primary Oscillator Configuration bits->
    Primary oscillator disabled
#pragma config OSCIOFNC = CLKO     // CLKO Enable Configuration bit->Port I/
    O enabled (CLKO disabled)
#pragma config POSCFREQ = HS     // Primary Oscillator Frequency Range
    Configuration bits->Primary oscillator/external clock input frequency
    greater than 8MHz
#pragma config SOSCSEL = SOSCHP     // SOSC Power Selection Configuration
    bits->Secondary Oscillator configured for high-power operation
```

```
#pragma config FCKSM = CSDCMD    // Clock Switching and Monitor Selection ->
    Both Clock Switching and Fail-safe Clock Monitor are disabled

// FWDT
#pragma config WDTPS = PS32768    // Watchdog Timer Postscale Select bits
    ->1:32768
#pragma config FWPSA = PR128    // WDT Prescaler bit->WDT prescaler ratio
    of 1:128
#pragma config FWDTEN = OFF    // Watchdog Timer Enable bits->WDT disabled
    in hardware; SWDTEN bit disabled
#pragma config WINDIS = OFF    // Windowed Watchdog Timer Disable bit->
    Standard WDT selected(windowed WDT disabled)

// FPOR
#pragma config BOREN = BOR3    // Brown-out Reset Enable bits->Brown-out
    Reset enabled in hardware, SBOREN bit disabled
#pragma config RETCFG = OFF    // ->Retention regulator is not available
#pragma config PWRTEN = ON    // Power-up Timer Enable bit->PWRT enabled
#pragma config I2C1SEL = PRI    // Alternate I2C1 Pin Mapping bit->Use
    Default SCL1/SDA1 Pins For I2C1
#pragma config BORV = V18    // Brown-out Reset Voltage bits->Brown-out
    Reset set to lowest voltage (1.8V)
#pragma config MCLRE = ON    // MCLR Pin Enable bit->RA5 input pin disabled
    , MCLR pin enabled

// FICD
#pragma config ICS = PGx3    // ICD Pin Placement Select bits->EMUC/EMUD
    share PGC3/PGD3

#include "config_bits.h"

void system_init( void){

    __builtin_write_OSCCONL((uint8_t) (0x0100 & 0x00FF));

    CLKDIV = 0x0000; // No clk division
    TRISB = 0x0081; // Sets RB0, RB7 as inputs
    TRISA = 0x0003; // Sets RA0-1 as input
```

```
    ANSB = 0x0000; // Sets no RB to analog in
    ANSA = 0x0003; // Sets RA0-1 to be analog inputs
    ODCA = 0x0000;
    ODCB = 0x0000;

    LATA = 0;
    LATB = 0;

    CNPD1bits.CN4PDE = 1; // Enables pull down on RB0
    CNPD2bits.CN23PDE = 1; // Enables pull down on RB7

    SPI_init();
    Timer_init();
};

void SPI_init( void) {
    /*
     * Configures for SPI master w/ clk at fosc/8, clk idle low, data tx on
     * transition from idle to active and input data is sampled at middle
     */
    SSP1CON1bits.SSPEN = 1;
    SSP1STAT = 0x0000;
    SSP1STATbits.CKE = 0;
    SSP1CON1 = 0x0031;
};

void Timer_init( void) {
    /*
     * Sets timer to use fosc/2 and turns it on
     */
    T1CONbits.TCKPS = 0b00;
    T1CONbits.TCS = 0;
    T1CONbits.TON = 1;
};
```

```
#include "spi_driver.h"
```

```
2
uint8_t tx_byte(volatile unsigned int * spi_reg, uint8_t byte, volatile
    unsigned int * spi_stat_reg){
4    *spi_reg = byte;
    while ((*spi_stat_reg & 0x01) == 0);
6    return *spi_reg;
};
8
void tx_word(volatile unsigned int * ssi_Reg, uint16_t mask_ssi, volatile
    unsigned int * spi_reg, uint16_t byte, volatile unsigned int *
    spi_stat_reg){
10    uint8_t thro_away;

12    *ssi_Reg &= ~mask_ssi;

14    thro_away=tx_byte(spi_reg, (uint8_t) byte >> 8, spi_stat_reg);
    thro_away=tx_byte(spi_reg, (uint8_t) byte, spi_stat_reg);
16
    *ssi_Reg |= mask_ssi;
18};

20void tx_3Byte(volatile unsigned int * ssi_Reg, uint16_t mask_ssi, volatile
    unsigned int * spi_reg, uint16_t byte1, uint16_t byte2, volatile
    unsigned int * spi_stat_reg){
    uint8_t thro_away;
22    *ssi_Reg &= ~mask_ssi;

24    thro_away=tx_byte(spi_reg, (uint8_t) byte1, spi_stat_reg);
    thro_away=tx_byte(spi_reg, (byte2 >> 8), spi_stat_reg);
26    thro_away=tx_byte(spi_reg, (uint8_t) byte2, spi_stat_reg);

28    *ssi_Reg |= mask_ssi;
};
```

```
/*
2 * File:   main.c
```

```
 * Author: steve_000
 *
 * Created on August 17, 2017, 10:44 AM
 */

#include <stdio.h>
#include <stdlib.h>
#include <xc.h>
#include "config_bits.h"
#include "spi_driver.h"

void delay_ms(uint16_t time);
void blink_LED(volatile unsigned int * ledReg, uint16_t mask);
void write_dac8812_1(uint16_t dac1, uint16_t dac2);
void write_dac8812_2(uint16_t dac1, uint16_t dac2);

/*
 *
 */
int main(void) {
    /* Pin assignments:
     * ra0 = analog in 1
     * ra1 = analog in 2
     * ra2 =
     * ra3 =
     * ra4 = AO_2_On/Off (mistake, can't be an output)
     * ra7 = LED
     *
     * rb0 = switch
     * rb1 = LDAC_1
     * rb2 = DAC_Select_1
     * rb3 = DAC_1_RS
     * rb4 = Digital_Output
     * rb5, rb6 = PGD3, PGC3
     * rb7 = Digital_Input
     * rb8 = DAC_2_RS
     * rb9 = DAC_Select_2
     * rb10 = LDAC_2
```

```
     *
     * rb12 = AO_1_On/Off
     *
     * rb14 = Digital_Output (sometimes, please check physical board)
     * rb15 = AO_2_On/Off (needs to be jumpered)
     */
    system_init();

    LATBbits.LATB12 = 0;
    LATAbits.LATA4 = 0;
    // Turns off AO's while setting up

    LATBbits.LATB1 = 1;
    LATBbits.LATB2 = 1;
    LATBbits.LATB9 = 1;
    LATBbits.LATB10 = 1;
    // Sets active low LDAC and CS to be high

    LATBbits.LATB3 = 1;
    LATBbits.LATB8 = 1;
    // Pulls DAC's out of reset

    write_dac8812_1(0xFFFF, 0x84CC); // for use with Rb MOT
    write_dac8812_2(0xFFFF, 0xD658);
    // a channel for both is attenuation, set to minimum at +15V
    // b channel for both controls VCO freq, set to MHz and MHz

    LATBbits.LATB12 = 1;
    LATBbits.LATB15 = 1;
    // Turns on AO drives

    while(1){
        // Main loop, waits for digital trigger
        // and then turns off AO's for about 10 us

        while(PORTBbits.RB7 == 0);

        LATBbits.LATB12 = 0;
```

```
        LATBbits.LATB15 = 0;

        while(PORTBbits.RB7 == 1);

        TMR1 = 0;
        while (TMR1<160);

        LATBbits.LATB12 = 1;
        LATBbits.LATB15 = 1;

    };

    return 1;
}

void delay_ms(uint16_t time) {
    while (time>0) {
        time--;
        TMR1 = 0;
        while (TMR1<16000);
    };
};

void blink_LED(volatile unsigned int * ledReg, uint16_t mask){
    *ledReg |= mask;
    delay_ms(200);
    *ledReg &= ~mask;
};

void write_dac8812_1(uint16_t dac_a, uint16_t dac_b) {
    /*
     * rb2 = DAC_2_Select
     * rb1 = LDAC2
     */
    tx_3Byte(&LATB, 0x0004, &SSP1BUF, 0x0001, dac_a, &SSP1STAT);
    tx_3Byte(&LATB, 0x0004, &SSP1BUF, 0x0002, dac_b, &SSP1STAT);
    LATBbits.LATB1 = 0;
    TMR1 = 0;
```

```
    while (TMR1<10);
    LATBbits.LATB1 = 1;
};

void write_dac8812_2(uint16_t dac_a, uint16_t dac_b) {
    /*
     * rb9 = DAC_2_Select
     * rb10 = LDAC2
     */
    tx_3Byte(&LATB, 0x0200, &SSP1BUF, 0x0001, dac_a, &SSP1STAT);
    tx_3Byte(&LATB, 0x0200, &SSP1BUF, 0x0002, dac_b, &SSP1STAT);
    LATBbits.LATB10 = 0;
    TMR1 = 0;
    while (TMR1<10);
    LATBbits.LATB10 = 1;
};
```

```
/*
 * File:   main.c
 * Author: steve_000
 *
 * Created on August 17, 2017, 10:44 AM
 */

#include <stdio.h>
#include <stdlib.h>
#include <xc.h>
#include "config_bits.h"
#include "spi_driver.h"

void delay_ms(uint16_t time);
void blink_LED(volatile unsigned int * ledReg, uint16_t mask);
void write_adf4111( void);
void write_adf4113(uint16_t sign);
void write_adf4001( void);
```

```
20 /*
 *
22 */
int main(void) {
24     system_init();

26     /*
       * RB0 is switch input
28     *
       * RB15 is Slave Select
30     * RB8 is Chip Enable (sometimes RB4)
       *
32     * RA7 is LED
       */
34
     LATBbits.LATB15 = 1;
36   LATBbits.LATB4 = 0;
     LATBbits.LATB10=0;
38
     write_adf4113(0x0000);
40
     LATAbits.LATA7=1;
42
     while(1){
44       if (PORTBbits.RB0==0) {
             write_adf4113(0x0000);
46           LATAbits.LATA7=0;
             while(PORTBbits.RB0==0){
48               delay_ms(100);
             };
50       } else {
             write_adf4113(0x0080);
52           LATAbits.LATA7=1;
             while(PORTBbits.RB0==1){
54               delay_ms(100);
             };
56       };
     };
```

```
58
    return 1;
60 }

62 void delay_ms(uint16_t time) {
    while (time>0) {
64      time--;
        TMR1 = 0;
66      while (TMR1<16000);
    };
68 };

70 void blink_LED(volatile unsigned int * ledReg, uint16_t mask){
    *ledReg |= mask;
72  delay_ms(200);
    *ledReg &= ~mask;
74 };

76 void write_adf4111( void) {
    tx_3Byte(&LATB, 0x8000, &SSP1BUF, 0x003D, 0xB822, &SSP1STAT); // Writes
     function latch
78  // last word 0xB812 (or 0xB892) is for lock detect on mux out, 0xB862
    is for serial data output, 0xB8A2 is for N counter, 0xB8C2 is for R
    counter
    tx_3Byte(&LATB, 0x8000, &SSP1BUF, 0x00F0, 0x0140, &SSP1STAT); // Writes
     R counter latch
80  // Writes 80 to R counter
    tx_3Byte(&LATB, 0x8000, &SSP1BUF, 0x0000, 0x8209, &SSP1STAT); // Writes
     A B counter latch
82  // Should write A=2, B=31
    delay_ms(200);
84  LATBbits.LATB8=1; // Turns on RF PLL
};
86

void write_adf4113(uint16_t sign) {
88  LATBbits.LATB8 = 0;  // Turns off RF PLL
    tx_3Byte(&LATB, 0x8000, &SSP1BUF, 0x00BB, (0xB822 | sign), &SSP1STAT);
    // Writes function latch
```

```
90      // Uses 32/33 prescaler
        // last word 0xB812 (or 0xB892) is for lock detect on mux out, 0xB862
        is for serial data output, 0xB8A2 is for N counter, 0xB8C2 is for R
        counter
92      tx_3Byte(&LATB, 0x8000, &SSP1BUF, 0x00F0, 0x0258, &SSP1STAT); // Writes
        R counter latch
        // Writes 150 to R counter
94      tx_3Byte(&LATB, 0x8000, &SSP1BUF, 0x0021, 0x6401, &SSP1STAT); // Writes
        A B counter latch
        // Should write A=0, B=356
96      delay_ms(200);
        LATBbits.LATB4=1; // Turns on RF PLL
98  };

100 void write_adf4001( void) {
        // These are test values for adf4111 (need to change B for adf4001)
102     tx_3Byte(&LATB, 0x8000, &SSP1BUF, 0x003F, 0xB822, &SSP1STAT); // Writes
        function latch
        // last word 0xB812 (or 0xB892) is for lock detect on mux out, 0xB862
        is for serial data output, 0xB8A2 is for N counter
104     tx_3Byte(&LATB, 0x8000, &SSP1BUF, 0x00F0, 0x0008, &SSP1STAT); // Writes
        R counter latch
        tx_3Byte(&LATB, 0x8000, &SSP1BUF, 0x0000, 0x0601, &SSP1STAT); // Writes
        A B counter latch
106     // Last word is 0x5001 locks to 80 MHz, 0x9601 locks to 150 MHz
        // Should write R=2, N=6
108     delay_ms(200);
        LATAbits.LATA4=1; // Turns on RF PLL
110     LATBbits.LATB10=1; // Damaged chip requires use of RB10?
    };
```

```
1   /*
     * File:   main.c
3    * Author: steve_000
     *
5    * Created on August 17, 2017, 10:44 AM
```

```
 */

#include <stdio.h>
#include <stdlib.h>
#include <xc.h>
#include "config_bits.h"
#include "spi_driver.h"

void delay_ms(uint16_t time);
void blink_LED(volatile unsigned int * ledReg, uint16_t mask);
void write_adf4001( void);

/*
 *
 */
int main(void) {
    system_init();
    /*
     *  RB0 is switch
     *  RB1 is analog in 1
     *  RB2 is analog in 2
     *  RB7 is digital in
     *
     *  RA7 is LED
     *  RB14 is Chip Enable
     *  RB15 is chip Select
     */
    LATBbits.LATB15=1;

    write_adf4001();

    LATAbits.LATA7=1;

    while(1);

    return 1;
}

```

```
void delay_ms(uint16_t time) {
    while (time>0) {
        time--;
        TMR1 = 0;
        while (TMR1<16000);
    };
};

void blink_LED(volatile unsigned int * ledReg, uint16_t mask){
    *ledReg |= mask;
    delay_ms(200);
    *ledReg &= ~mask;
};

void write_adf4001( void) {
    // These are test values for adf4001
    tx_3Byte(&LATB, 0x8000, &SSP1BUF, 0x003F, 0xB8A2, &SSP1STAT); // Writes
    function latch
    // last word 0xB812 (or 0xB892) is for lock detect on mux out, 0xB862
    is for serial data output, 0xB8A2 is for N counter
    tx_3Byte(&LATB, 0x8000, &SSP1BUF, 0x00F0, 0x07D0, &SSP1STAT); // Writes
    R counter latch
    tx_3Byte(&LATB, 0x8000, &SSP1BUF, 0x0003, 0x2001, &SSP1STAT); // Writes
    A B counter latch
    // Should write R=500, N=800 enables steps of 100 kHz
    delay_ms(200);
    LATBbits.LATB14=1; // Turns on RF PLL
};
```

```
/*
 * File:   main.c
 * Author: steve_000
 *
 * Created on August 17, 2017, 10:44 AM
 */

```

```
#include <stdio.h>
#include <stdlib.h>
#include <xc.h>
#include "config_bits.h"
#include "spi_driver.h"

void delay_ms(uint16_t time);
void delay_us(uint16_t time);
void blink_LED(volatile unsigned int * ledReg, uint16_t mask);
void write_dac8812_1(uint16_t dac1, uint16_t dac2);
uint16_t read_ADC_fast();
uint16_t read_ADC_slow();

/*
 *
 */
int main(void) {
    /* Pin assignments:
     * ra0 = analog in 1 (Used for Photodiode)
     * ra1 = analog in 2 (Used for POT)
     * ra2 =
     * ra3 =
     * ra4 = (Can't be an output)
     * ra7 = LED (Not installed)
     *
     * rb0 = switch
     * rb1 = LDAC_1
     * rb2 = DAC_Select_1
     * rb3 = DAC_1_RS
     * rb4 = Digital_Output (Not installed)
     * rb5, rb6 = PGD3, PGC3
     * rb7 = Digital_Input (Not installed)
     * rb8 = DAC_2_RS (Not installed)
     * rb9 = DAC_Select_2 (Not installed)
     * rb10 = LDAC_2 (Not installed)
     *
     * rb12 = AO_1_On/Off
     *
```

```
     * rb14 = Digital_Output (Not installed)
     * rb15 = AO_2_On/Off (Not installed)
     */
    system_init();

    uint16_t num;

    LATBbits.LATB12 = 0;
    // Turns off AO's while setting up

    LATBbits.LATB1 = 1;
    LATBbits.LATB2 = 1;
    // Sets active low LDAC and CS to be high

    LATBbits.LATB3 = 1;
    // Pulls DAC's out of reset

    write_dac8812_1(0xFFFF, 0x84CC);
    // a channel is attenuation, set to minimum at +5V
    // b channel controls VCO freq, set to 76 MHz

    LATBbits.LATB12 = 1;
    // Turns on AO drives
    while(1){
        num = read_ADC_fast();
        write_dac8812_1((num<<4), 0x84CC);
    };

    return 1;
}

void delay_ms(uint16_t time) {
    while (time>0) {
        time--;
        TMR1 = 0;
        while (TMR1<16000);
    };
};
```

```
85 void delay_us(uint16_t time) {
       while (time>0) {
87         time--;
           TMR1 = 0;
89         while (TMR1<16);
       };
91 };

93 void blink_LED(volatile unsigned int * ledReg, uint16_t mask){
       *ledReg |= mask;
95     delay_ms(200);
       *ledReg &= ~mask;
97 };

99 void write_dac8812_1(uint16_t dac_a, uint16_t dac_b) {
       /*
101     * rb2 = DAC_1_Select
        * rb1 = LDAC1
103     */
       tx_3Byte(&LATB, 0x0004, &SSP1BUF, 0x0001, dac_a, &SSP1STAT);
105    tx_3Byte(&LATB, 0x0004, &SSP1BUF, 0x0002, dac_b, &SSP1STAT);
       LATBbits.LATB1 = 0;
107    TMR1 = 0;
       while (TMR1<10);
109    LATBbits.LATB1 = 1;
   };
111

   uint16_t read_ADC_fast() {
113    /*
        *
115     */
       AD1CON1bits.SAMP = 1;
117    delay_us(1);
       AD1CON1bits.SAMP = 0;
119    while (AD1CON1bits.DONE==0);
       return ADC1BUF0;
121 };
```

```
123 uint16_t read_ADC_slow() {
    /*
125  *
     */
127 AD1CON1bits.SAMP = 1;
    delay_us(1);
129 AD1CON1bits.SAMP = 0;
    while (AD1CON1bits.DONE==0);
131 return ADC1BUF0;
};
```

E. FEMTOSECOND LASERS INTERACTING WITH ULTRACOLD ATOMS

Using spectroscopic data from previous Chapters, I worked on coherently imaging rotational wavefunctions with a mode-locked Ti:Sapphire laser in this Chapter. A sketch of this experiment is as follows. We currently continuously create LiRb molecules in $X\ ^1\Sigma^+\ v'' = 43$ with PA to 4(1) $v = -16$ and then in the future we will form a superposition between the $J = 0$ and $J = 1$ states with an RF pulse. The energy difference between these states is 5.1 GHz and so a superposition state will evolve with a period of 1/5.1 GHz = 0.2 ns. The repetition rate of the mode-locked Ti:Sapphire laser will be coherent with the energy difference between the states, and thus the femtosecond (fs) pulses, which have a duration much less than 0.2 ns, will consistently interrupt, and hopefully ionize, the molecule at the same point in the state evolution. Finally, by imaging the ionization pattern spatially we should be able to see the full, spatial evolution of the rotational wavefunction with almost arbitrary precision.

E.1 Femtosecond Laser

In order to make this experiment happen we will need a femtosecond laser. Shown in Fig. E.1, is the table setup of a mode-locked Ti:Sapphire laser we borrowed from Dan Leaird and Dr. Andy Wiener. The laser is based on a design from Ref. [135], and it is capable of producing 11 fs pulses with a pulse energy around 1 nJ (or 500 mW average power) between 740 - 900 nm. Unlike our REMPI laser which produces pulses through Q-switching, the femtosecond pulses are produced by mode-locking. Mode-locking occurs when the laser lases across a wide band of transverse modes, all separated by c/cavity length, and the internal quantum effects force phase coherence between the different modes. To get this to happen, cavity dispersion needs to be compensated. Dispersion is $\frac{d\omega}{dk}$ and on some level it is related to slightly different path lengths for the different CW laser modes. For coherence between the different modes to be sustainable,

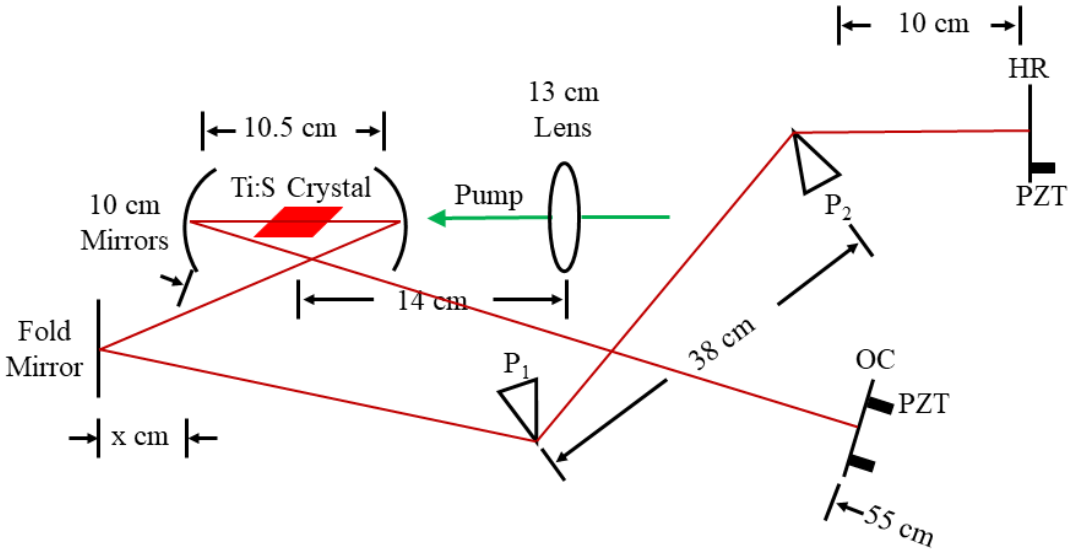

Fig. E.1. Table diagram of femtosecond Ti:Sapphire laser; design is from Ref. [135]. The repetition rate of this laser maybe tuned on a gross scale by changing the distance to the folding mirror, labeled as x. Fine control of the repetition rate is established by mounting the output coupler (OC) on a translation stage and a PZT in the translation stage provides ultra-fine tuning.

they all need exactly the same path length, and/or the dispersion needs to be zero for a wide range of modes. The dispersion usually comes from the variation of index of refraction in the Ti:Sapphire crystal with wavelength, i.e. $\frac{dn}{d\lambda} \neq 0$, and is compensated for either with prisms or specially designed mirrors. As seen in Fig. E.1, our laser uses the older prism method. The laser makes a not-very-good CW Ti:Sapphire initially and then by carefully tuning the prisms it will start mode-locking.

Once mode locking, it produces pulses like shown in Fig. 7.4 (a). Fig. 7.4 presents the time domain picture of a mode-locked laser pulses. It will produce pulses (usually around 100 fs) separated by $1/f_r$, where $f_r = c/\text{cavity length}$ is the repetition rate. This can be easily thought of as an optical carrier wave, carrying a sharp and well defined RF envelope. For low pulse energies, a frequency domain treatment often makes more sense, like shown in Fig. 7.4 (b). Here, the femtosecond pulse can be thought of as a large number of low intensity, phase coherent CW lasers each with narrow linewidth and a frequency $f = Nf_r + f_{\text{ceo}}$, where N is a large integer, and f_{ceo} is the carrier-envelop offset frequency (which by definition $-f_r < f_{\text{ceo}} < f_r$). In this frequency domain picture,

each CW laser has an intensity equal to the laser average intensity divide by M, where M is the number of modes. We can estimate the equivalent CW laser intensities for our laser. It produces about 500 mW, and has a bandwidth around 15 nm. Thus M is around 70,000 which results in an effective power for each CW laser around 10 μW.

E.2 Molecular transition

Shown in Fig. E.2 is the expected three-photon doubly-resonant pathway from the $X\ ^1\Sigma^+\ v'' = 43$ state to the ionization continuum. Our original plan is much like REMPI except with the fs Ti:Sapphire providing the photons connecting the states. At first we estimated the laser intensity for REMPI and the fs Ti:Sapphire lasers in the interaction region. REMPI has a 10 ns pulse, 1mJ/pulse and a 4 mm diameter spot size which corresponds to nearly 10^6 mW/cm^2. The fs laser is 500 mW averaged power, with 100 fs duration pulses every 10 ns, in a 300 μm diameter spot size which corresponds to about 10^8 mW/cm^2. From this perspective, the fs laser looks like it should behave like an extra saturated version of REMPI.

The fs laser repetition rate is around 100 MHz, which is much too fast for time-of-flight to separate out $LiRb^+$ ions from Rb^+ ions. Instead we use an AOM to pick out a handful of femtosecond pulses and send them to the experiment region while rejecting the rest. In the end, we decided on picking out 1 μs worth of femtosecond pulses (around 100 pulses in total) followed by 99 μs of dead time, for an experiment repetition rate around 10 kHz. After the pulse of fs pulses, the $LiRb^+$ or Rb^+ arrive at the MCPs around 20 μs later. The 1 μs on time was chosen because this is the longest time possible, that still allows us to separate $LiRb^+$ ions from Rb^+ ions.

For our first attempt at this experiment, we set the center frequency of the femtosecond laser to around 787 nm, to be close to the first molecular transition, see Fig. E.2 (b), tuned the bandwidth to around 10 nm, which should include the second transition but we saw no evidence of $LiRb^+$ ions.

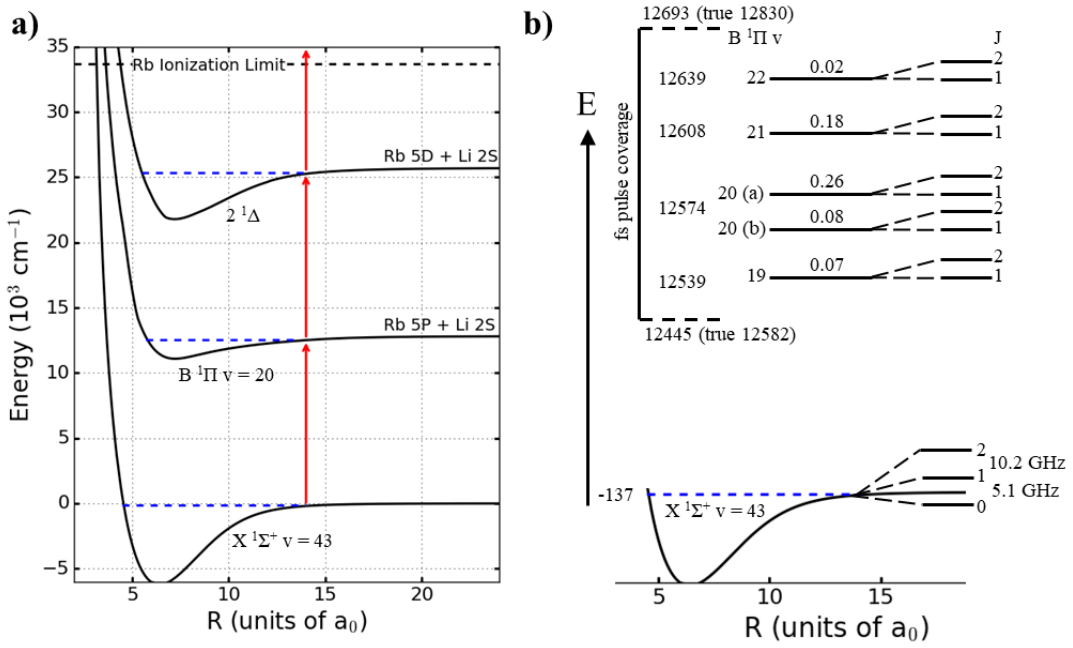

Fig. E.2. Energy level diagram for LiRb showing doubly resonant ionization pathway for $X\ ^1\Sigma^+\ v = 43$ molecules. **(a)** Double photon path. **(b)** Close examination of first transition with smaller splitting from vibration, rotation and hyperfine structure labeled from previous spectroscopy.

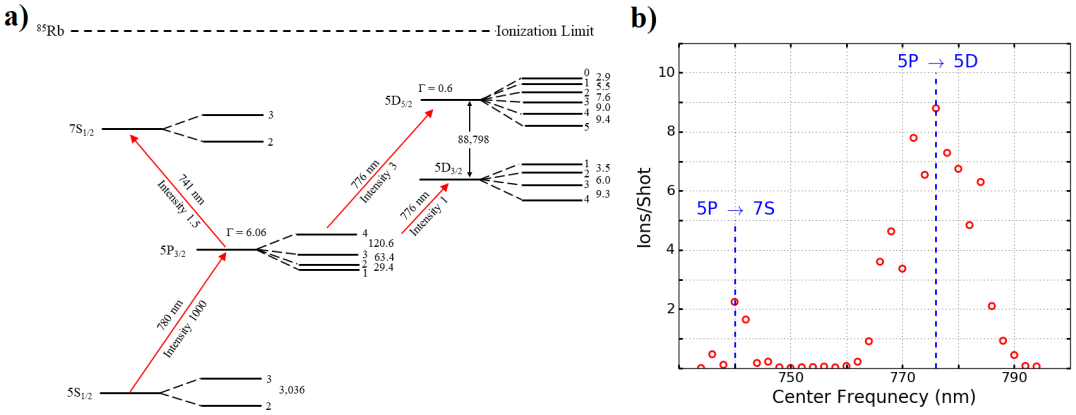

Fig. E.3. **(a)** Energy level diagram for ^{85}Rb showing doubly resonant ionization pathway. Data is from Refs. [136,137] and the NIST data tables on atomic Rb. The integers label the the hyperfine quantum number, while the decimals next to them label the difference in energy between neighboring hyperfine states in MHz. **(b)** Ionization signal as a function of center wavelength of femtosecond laser.

E.3 Atomic transition

We turned to ionizing atomic Rb^+, in our first step in trying to better understand why we saw no $LiRb^+$ ions. Our logic is that the Rb density is around 10^4 higher than the

LiRb molecule density, and there is a three-photon, doubly-resonant ionizing transition at 778 nm; the molecular states are asymptotic to this progression of atomic states. The atomic energy level diagram for this process is shown in Fig. E.3. After playing around with the fs laser a little, we found Rb^+ ions and worked on studying the ionization of atomic Rb in order to understand how the fs laser was interacting with the atoms and molecules.

Our first step was to study the dependence of the center wavelength on the atomic signal. We had seen in REMPI that having light resonant with a molecular or atomic transition is very important and expected a similar result here. It is worth noting that the fs laser has a bandwidth of 15 nm, or nearly 250 cm^{-1}, which is much greater than REMPI's 0.5 cm^{-1} bandwidth, so we expect much wider features. Fig. E.3 (b) shows how the atomic Rb count varies as a function of center wavelength. Clearly there are two strong peaks, one centered between 776 and 780 nm, which could either be the three photon, doubly resonant transition $5S_{1/2} \rightarrow 5P_{3/2} \rightarrow 5D_{5/2}$ or a two photon transition from the $5P_{3/2}$ state, and a second peak around 740 nm which is the transition energy for the $5P_{3/2} \rightarrow 7S_{1/2}$ transition. Our conclusion from this is that the dominant ionization process was the fs laser picking off atoms in the $5P_{3/2}$ state from the MOT, as this is the only way to populate the $5P_{3/2}$ state for the $5P_{3/2} \rightarrow 7S_{1/2}$ transition and in a MOT there are a small number of atoms in the excited state of the cooling transition. As we wanted to study the three photon ionizing transition, this was a problem. Ultimately we used the AOMs in the beam path of the Rb trapping lasers to shutter the Rb trapping lasers in advance of the fs pulse of pulses. The timing diagram is shown in Fig. E.4.

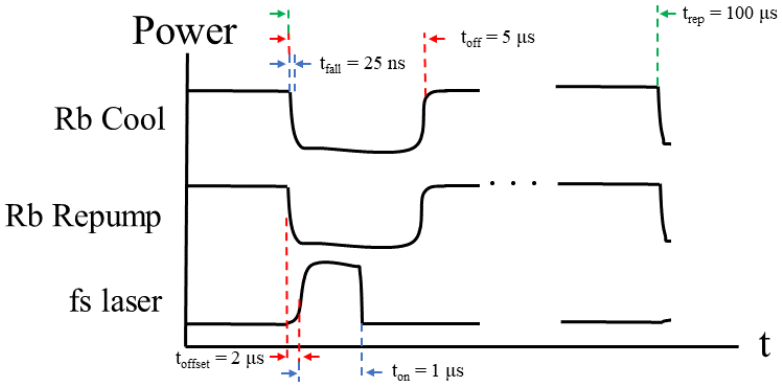

Fig. E.4. Timing of fs experiment.

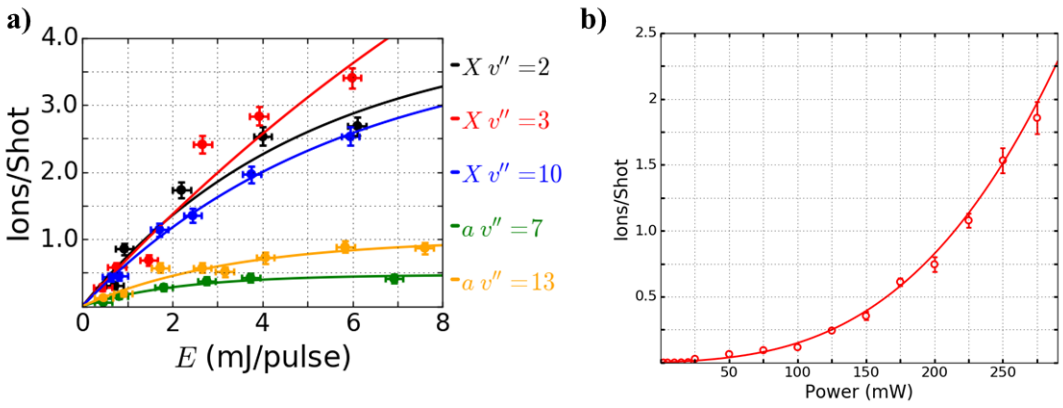

Fig. E.5. Comparison between REMPI and fs laser. **(a)** Molecular ionization signal across many initial vibrational levels as a function of REMPI laser intensity. All fits are to $X(1-e^{-\alpha I})$, where X is the ion count at infinite power, α is a constant, and I is the laser power. **(b)** Atomic ion signal as a function of fs laser intensity. Fit is to $ax+bx^2+cx^3$, where a, b, and c are all constants and x is the measured laser power.

Our second step was to study the power dependence of our ion count at the three-photon transition. We were looking to better understand how to consider the fs pulse interacting with the atoms. Fig. E.5 (b) shows how our Rb^+ ion count varies as we attenuate the laser power, and contrast this with Fig. E.5 (a) which shows how the REMPI ion count varies as we drop the pulse energy of the REMPI laser. The REMPI laser follows a traditional saturated type curve. The first REMPI transition is saturated so more power does not do much and most of the population that makes it to the first excited state get ionized (so adding more power does not help here either). The fs laser is clearly different, despite having a larger intensity. Instead, a cubic polynomial fits the progression well suggesting that none of the three transitions are saturated. Perplexed by this, we consulted our friends in theory. After talking with them, we returned to our presentation of a fs laser in the frequency domain at the start of this chapter (which is put there because of our discovery). The Rb atoms act as a frequency discriminator and only talk to the modes of the fs laser close to the D_2 line. So long as the intensity of these pseudo-CW modes are low, about 1 mW/cm^2, compared to the saturation intensity, 3.8 mW/cm^2, all modes of the fs laser more than a few natural linewidths, 6.06 MHz, away from the D_2 line can be ignored. This effectively drops the pulse intensity by a factor of 10^5, and suddenly the fs laser and REMPI laser pictures look very different.

Data from our second experiment inspired the second round of improvements to the fs laser. First, we changed the focusing of the femtosecond laser. Previously we had around a 300 μm spot size in the MOT region and we switched to a best-form 15 cm lens that results in around a 50 μm spot size. We expected this to produce 36 times more signal, and were not disappointed. Now at full power, we saturate our ion detection so heavily as to make accurate ion counting impossible. Second, we built a plexiglass enclosure around our femtosecond to help isolate it from environment perturbations. We noticed that the ion count would drift between highs, an order of magnitude above what is reported in Fig. E.5 (b), and lows, often two orders of magnitude below the average. The enclosure helped slow down the drifting ion counts and helped keep it mode-locking for longer periods of time. Third, we worked on, but did not finish trying to stabilize the repetition rate and carrier-envelop offset of the laser. Ultimately, we stopped work on stabilizing our laser after determining that even with the stabilization improvements, we would not be able to find molecular signal.

Our second search for molecular signal began with the femtosecond laser in its box, and with the 15 cm lens in place. We co-propagated the PA laser with the femtosecond laser, verified that we still had a strong REMPI signal, and then went looking for a molecular signal. We didn't get very far. Because our Rb^+ signal was so well optimized, it spilled into the $LiRb^+$ time-of-flight window at a level 100 times what we expected the $LiRb^+$ count to be. We investigated two strategies to remove unwanted Rb^+ ions. First, we noticed that Rb^+ ions occured at high rates, even with the fs laser off, in roughly an exponential decay pattern. We suspect that the PA laser was picking off leftover population in the semi-long lived atomic 5D state. We tried to gate the PA laser with an AOM, to no success. We suspect that because of the tight focusing of the CW laser (which co-propagated with the fs laser), that even with the factor of 10^3 attenuation provided by the AOM, the ionization transition was still saturated.

Our second approach was to use a pulse shaper to remove the light resonant with the atomic transitions from the femtosecond pulse. Fig. E.6 shows a pulse shaper table diagram. For additional information on pulse shapers please consult Ref. [138] (or any of Dr. Wiener's students). A pulse shaper works by using a pair of gratings and lenses to Fourier transform a femtosecond pulse spatially. The first grating separates the different pulse colors angularly and the lens following it collimates the beam. At the midpoint

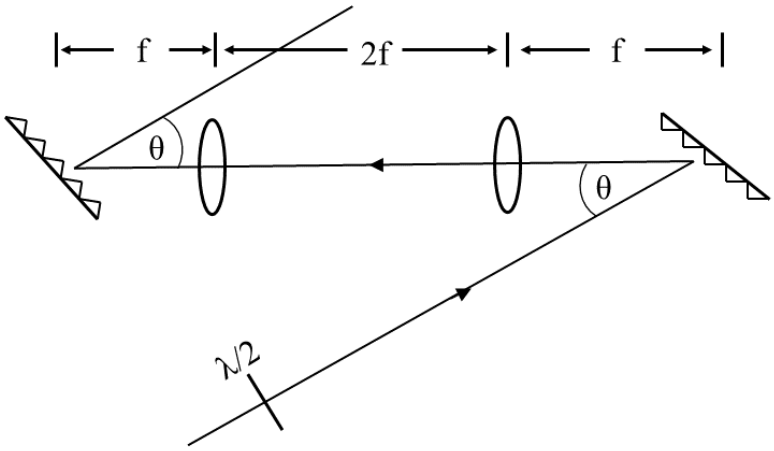

Fig. E.6. Femtosecond pulse shaper, design is from Ref. [138].

between the two lenses lies the Fourier plane, here a spatial light modulator can be placed to phase shift the different colors of the pulse, or in our case we placed a razor blade to form a band-pass filter, and by sliding the razor blade into the pulse, we removed the higher frequency colors. After the Fourier plane, the second lens focuses the different colors onto the grating which reforms the pulse. A pulse shaper requires diffracting off gratings twice which resulted in a loss of 65 % of our power. With the pulse shaper created, we tried to measure molecular signal again. This time, we tuned the razor blade into the pulse until the atomic signal went away, verified we were not blocking the colors we needed but again observed no $LiRb^+$ ion signal.

E.4 fs ionization probability

At this point it is useful to examine the observed ionization probability for atomic Rb and then compare it to the molecular system. In the second generation of this experiment, where we focused the fs laser to a 300 μm spot size, we would observe around 2 ions for each pulse of fs pulses. The Rb MOT is around 2 mm diameter and holds about 3×10^6 atoms. About 1 % of the Rb atoms will be in the fs beam. This implies a cumulative ionization probability for the fs pulses is about 10^{-4}. Assuming things remain linear as we focus to the 50 μm spot size, we expect an atomic ionization probability around 10^{-3}.

For the molecular system, we generate around 10^5 molecules per second, implying that there will be around 50 LiRb molecules available for each pulse of fs pulses. We

usually integrated across 10^4 pulse of pulses and have a dark count around 5. This suggests we should see around 500 $LiRb^+$ ions, if the molecular ionization probability is equivalent to the atomic ionization probability. However, we know that molecular transitions are usually weaker than their atomic counterparts. On the simplest level, this is just caused by FCFs. We calculated the molecular FCFs and they are about 0.2 and 0.15, which suggests that the molecular transition should be around 0.03 times as strong as the atomic transition. Adding this extra factor results in an estimate of 15 $LiRb^+$ ions against a background of 5. If there are any further imperfections in the molecular signal (maybe just a misalignment between the two lasers) it becomes clear why we will not see any signal. Fundamentally, there are too few LiRb molecules and/or the ionization probability is far too small.

E.5 Next steps

Here I propose three possible fixes to our signal problem.

1) Use a dense sample of LiRb molecules. An ideal target would be molecules formed in a dipole trap either after magneto-association or by continuum STIRAP.

2) Use an ECDL laser to provide the second photon and let the photoassociation laser provide the last photon. This guarantees the second and third legs to be strongly driven transitions (currently a problem), while maintaining the pulsed nature of the femtosecond laser.

3) Get a regenerative amplifier for the femtosecond laser. These amplifiers can turn 1 nJ pulses into 1 mJ pulses, which will solve the low signal level problem (and possibly cause other problems).

Of these, I expect number three to be the best solution overall, although it will be costly and labor intensive. Number two is the easiest, and although it may require a bit of luck to get working, it is the one I will discuss further. My recommendation is to first get a two-step depletion system working. The goal is to probe the bound state locations for the second photon in the ionizing pathway and get some understanding of transition strengths. Again there are some unknowns and problems. We have seen that populating these highly excited states and having a CW laser on at the same time results in ionization (at least in the atomic system), and I expect the molecule system will require

turning off the CW lasers a few μs in advance of REMPI laser as to not contaminate the $LiRb^+$ ion arrival window. Additionally, I'm not sure how good the mutual coherence between the two lasers will have to be. The two-photon Rabi frequency is $\frac{\Omega_1\Omega_2}{2\Delta}$, where Ω_1 and Ω_2 are the one-photon Rabi frequencies and Δ is the detuning. I would expect detunings of a few GHz to be optimal, as this avoids too much one-photon depletion while not being so far detuned as to have no signal. You would also need to make sure that the second photon does not one-photon deplete the signal (because they are so close in color, it might hit a nearby resonance). If I were to try this, I would use an ECDL for PA, a second ECDL for the first depletion step and the Ti:Sapphire for the second depletion step. If I don't get signal, locking the two depletion lasers to the Menlo frequency comb would be an early thing to try. Using the results of Chapter 7, this should be possible as the Menlo comb is quite strong around 780 nm.

REFERENCES

REFERENCES

[1] S. Chu, "Laser manipulation of atoms and particles," *Science*, vol. 253, no. 5022, pp. 861–866, 1991.

[2] M. H. Anderson, J. R. Ensher, M. R. Matthews, C. E. Wieman, and E. A. Cornell, "Observation of Bose-Einstein condensation in a dilute atomic vapor," *Science*, vol. 269, no. 5221, pp. 198–201, 1995.

[3] E. S. Shuman, J. F. Barry, and D. DeMille, "Laser cooling of a diatomic molecule," *Nature*, vol. 467, no. 7317, pp. 820–823, 2010.

[4] D. Egorov, W. Campbell, B. Friedrich, S. Maxwell, E. Tsikata, L. van Buuren, and J. Doyle, "Buffer-gas cooling of NH via the beam loaded buffer-gas method," *The European Physical Journal D-Atomic, Molecular, Optical and Plasma Physics*, vol. 31, no. 2, pp. 307–311, 2004.

[5] A. V. Avdeenkov and J. L. Bohn, "Collisional dynamics of ultracold OH molecules in an electrostatic field," *Physical Review A*, vol. 66, no. 5, p. 052718, 2002.

[6] R. Napolitano, J. Weiner, C. J. Williams, and P. S. Julienne, "Line shapes of high resolution photoassociation spectra of optically cooled atoms," *Physical review letters*, vol. 73, no. 10, p. 1352, 1994.

[7] R. Véxiau, N. Bouloufa, M. Aymar, J. G. Danzl, M. J. Mark, H.-C. Naegerl, and O. Dulieu, "Optimal trapping wavelengths of Cs_2 molecules in an optical lattice," *The European Physical Journal D*, vol. 65, no. 1-2, pp. 243–250, 2011.

[8] M. Bellos, D. Rahmlow, R. Carollo, J. Banerjee, O. Dulieu, A. Gerdes, E. Eyler, P. Gould, and W. Stwalley, "Formation of ultracold Rb_2 molecules in the $v = 0$ level of the $a\ ^3\Sigma_u^+$ state via blue-detuned photoassociation to the $1\ ^3\Pi_g$ state," *Physical Chemistry Chemical Physics*, vol. 13, no. 42, pp. 18 880–18 886, 2011.

[9] K.-K. Ni, S. Ospelkaus, M. De Miranda, A. Pe'er, B. Neyenhuis, J. Zirbel, S. Kotochigova, P. Julienne, D. Jin, and J. Ye, "A high phase-space-density gas of polar molecules," *Science*, vol. 322, no. 5899, pp. 231–235, 2008.

[10] J. Banerjee, D. Rahmlow, R. Carollo, M. Bellos, E. E. Eyler, P. L. Gould, and W. C. Stwalley, "Direct photoassociative formation of ultracold KRb molecules in the lowest vibrational levels of the electronic ground state," *Physical Review A*, vol. 86, no. 5, p. 053428, 2012.

[11] J. Deiglmayr, A. Grochola, M. Repp, K. Mörtlbauer, C. Glück, J. Lange, O. Dulieu, R. Wester, and M. Weidemüller, "Formation of ultracold polar molecules in the rovibrational ground state," *Physical review letters*, vol. 101, no. 13, p. 133004, 2008.

[12] J. M. Sage, S. Sainis, T. Bergeman, and D. DeMille, "Optical production of ultracold polar molecules," *Physical review letters*, vol. 94, no. 20, p. 203001, 2005.

[13] C. Gabbanini and O. Dulieu, "Formation of ultracold metastable RbCs molecules by short-range photoassociation," *Physical Chemistry Chemical Physics*, vol. 13, no. 42, pp. 18 905–18 909, 2011.

[14] P. Zabawa, A. Wakim, M. Haruza, and N. Bigelow, "Formation of ultracold $X\ ^1\Sigma^+(v = 0)$ NaCs molecules via coupled photoassociation channels," *Physical Review A*, vol. 84, no. 6, p. 061401, 2011.

[15] C. Trefzger, C. Menotti, and M. Lewenstein, "Pair-supersolid phase in a Bilayer system of dipolar lattice bosons," *Physical review letters*, vol. 103, no. 3, p. 035304, 2009.

[16] P. Rabl and P. Zoller, "Molecular dipolar crystals as high-fidelity quantum memory for hybrid quantum computing," *Physical Review A*, vol. 76, no. 4, p. 042308, 2007.

[17] A. Micheli, G. Pupillo, H. Büchler, and P. Zoller, "Cold polar molecules in two-dimensional traps: Tailoring interactions with external fields for novel quantum phases," *Physical Review A*, vol. 76, no. 4, p. 043604, 2007.

[18] G. Quemener and P. S. Julienne, "Ultracold molecules under control!" *Chemical Reviews*, vol. 112, no. 9, pp. 4949–5011, 2012.

[19] M. Lu, N. Q. Burdick, S. H. Youn, and B. L. Lev, "Strongly dipolar Bose-Einstein condensate of dysprosium," *Physical review letters*, vol. 107, no. 19, p. 190401, 2011.

[20] J. Stuhler, A. Griesmaier, T. Koch, M. Fattori, T. Pfau, S. Giovanazzi, P. Pedri, and L. Santos, "Observation of dipole-dipole interaction in a degenerate quantum gas," *Physical Review Letters*, vol. 95, no. 15, p. 150406, 2005.

[21] A. Griesmaier, J. Werner, S. Hensler, J. Stuhler, and T. Pfau, "Bose-Einstein condensation of chromium," *Physical Review Letters*, vol. 94, no. 16, p. 160401, 2005.

[22] M. Schmitt, M. Wenzel, F. Böttcher, I. Ferrier-Barbut, and T. Pfau, "Self-bound droplets of a dilute magnetic quantum liquid," *Nature*, vol. 539, no. 7628, p. 259, 2016.

[23] D. DeMille, "Quantum computation with trapped polar molecules," *Physical Review Letters*, vol. 88, no. 6, p. 067901, 2002.

[24] B. Yan, S. A. Moses, B. Gadway, J. P. Covey, K. R. Hazzard, A. M. Rey, D. S. Jin, and J. Ye, "Observation of dipolar spin-exchange interactions with lattice-confined polar molecules," *Nature*, vol. 501, no. 7468, pp. 521–525, 2013.

[25] A. Micheli, G. Brennen, and P. Zoller, "A toolbox for lattice-spin models with polar molecules," *Nature Physics*, vol. 2, no. 5, pp. 341–347, 2006.

[26] V. Galitski and I. B. Spielman, "Spin–orbit coupling in quantum gases," *Nature*, vol. 494, no. 7435, p. 49, 2013.

[27] S. A. Moses, J. P. Covey, M. T. Miecnikowski, B. Yan, B. Gadway, J. Ye, and D. S. Jin, "Creation of a low-entropy quantum gas of polar molecules in an optical lattice," *Science*, vol. 350, no. 6261, pp. 659–662, 2015.

[28] T. M. Rvachov, H. Son, A. T. Sommer, S. Ebadi, J. J. Park, M. W. Zwierlein, W. Ketterle, and A. O. Jamison, "Long-lived ultracold molecules with electric and magnetic dipole moments," *Physical review letters*, vol. 119, no. 14, p. 143001, 2017.

[29] M. Guo, B. Zhu, B. Lu, X. Ye, F. Wang, R. Vexiau, N. Bouloufa-Maafa, G. Quéméner, O. Dulieu, and D. Wang, "Creation of an ultracold gas of ground-state dipolar ^{23}Na ^{87}Rb molecules," *Physical review letters*, vol. 116, no. 20, p. 205303, 2016.

[30] J. W. Park, S. A. Will, and M. W. Zwierlein, "Ultracold dipolar gas of Fermionic ^{23}Na ^{40}K molecules in their absolute ground state," *Physical review letters*, vol. 114, no. 20, p. 205302, 2015.

[31] P. K. Molony, P. D. Gregory, Z. Ji, B. Lu, M. P. Köppinger, C. R. Le Sueur, C. L. Blackley, J. M. Hutson, and S. L. Cornish, "Creation of ultracold ^{87}Rb ^{133}Cs molecules in the rovibrational ground state," *Physical review letters*, vol. 113, no. 25, p. 255301, 2014.

[32] M. Aymar and O. Dulieu, "Calculation of accurate permanent dipole moments of the lowest $^{1,3}\Sigma^+$ states of heteronuclear alkali dimers using extended basis sets," *The Journal of chemical physics*, vol. 122, no. 20, p. 204302, 2005.

[33] P. S. Żuchowski and J. M. Hutson, "Reactions of ultracold alkali-metal dimers," *Physical Review A*, vol. 81, no. 6, p. 060703, 2010.

[34] X. Ye, M. Guo, M. L. González-Martínez, G. Quéméner, and D. Wang, "Collisions of ultracold ^{23}Na ^{87}Rb molecules with controlled chemical reactivities," *Science advances*, vol. 4, no. 1, p. eaaq0083, 2018.

[35] J. Barry, D. McCarron, E. Norrgard, M. Steinecker, and D. DeMille, "Magneto-optical trapping of a diatomic molecule," *Nature*, vol. 512, no. 7514, p. 286, 2014.

[36] E. Norrgard, D. McCarron, M. Steinecker, M. Tarbutt, and D. DeMille, "Submillikelvin dipolar molecules in a radio-frequency magneto-optical trap," *Physical review letters*, vol. 116, no. 6, p. 063004, 2016.

[37] D. McCarron, M. Steinecker, Y. Zhu, and D. DeMille, "Magnetically-trapped molecules efficiently loaded from a molecular MOT," *arXiv preprint arXiv:1712.01462*, 2017.

[38] B. Hemmerling, E. Chae, A. Ravi, L. Anderegg, G. K. Drayna, N. R. Hutzler, A. L. Collopy, J. Ye, W. Ketterle, and J. M. Doyle, "Laser slowing of CaF molecules to near the capture velocity of a molecular MOT," *Journal of Physics B: Atomic, Molecular and Optical Physics*, vol. 49, no. 17, p. 174001, 2016.

[39] S. Truppe, H. Williams, M. Hambach, L. Caldwell, N. Fitch, E. Hinds, B. Sauer, and M. Tarbutt, "Molecules cooled below the doppler limit," *Nature Physics*, vol. 13, no. 12, p. 1173, 2017.

[40] T. Chen, W. Bu, and B. Yan, "Radiative deflection of a BaF molecular beam via optical cycling," *Physical Review A*, vol. 96, no. 5, p. 053401, 2017.

[41] M. Yeo, M. T. Hummon, A. L. Collopy, B. Yan, B. Hemmerling, E. Chae, J. M. Doyle, and J. Ye, "Rotational state microwave mixing for laser cooling of complex diatomic molecules," *Physical review letters*, vol. 114, no. 22, p. 223003, 2015.

[42] C. Marzok, B. Deh, C. Zimmermann, P. W. Courteille, E. Tiemann, Y. Vanne, and A. Saenz, "Feshbach resonances in an ultracold ^{7}Li and ^{87}Rb mixture," *Physical Review A*, vol. 79, no. 1, p. 012717, 2009.

[43] C. Marzok, B. Deh, P. W. Courteille, and C. Zimmermann, "Ultracold thermalization of ^{7}Li and ^{87}Rb," *Physical Review A*, vol. 76, no. 5, p. 052704, 2007.

[44] A. Altaaf, "Spectroscopy of ultracold LiRb molecules using ionization detection," Ph.D. dissertation, Purdue University, 2014.

[45] D. A. Steck, "Rubidium 85 D line data (2008)," *URL http://steck. us/alkalidata/rubidium85numbers. pdf. Rubidium*, vol. 85.

[46] K. Libbrecht and J. L. Hall, "A low-noise high-speed diode laser current controller," *Review of scientific instruments*, vol. 64, no. 8, pp. 2133–2135, 1993.

[47] C. J. Erickson, M. Van Zijll, G. Doermann, and D. S. Durfee, "An ultrahigh stability, low-noise laser current driver with digital control," *Review of Scientific Instruments*, vol. 79, no. 7, p. 073107, 2008.

[48] E. C. Cook, P. J. Martin, T. L. Brown-Heft, J. C. Garman, and D. A. Steck, "High passive-stability diode-laser design for use in atomic-physics experiments," *Review of Scientific Instruments*, vol. 83, no. 4, p. 043101, 2012.

[49] J. Appel, A. MacRae, and A. Lvovsky, "A versatile digital GHz phase lock for external cavity diode lasers," *Measurement Science and Technology*, vol. 20, no. 5, p. 055302, 2009.

[50] S. Dutta, D. Elliott, and Y. P. Chen, "Mode-hop-free tuning over 135 GHz of external cavity diode lasers without antireflection coating," *Applied Physics B*, vol. 106, no. 3, pp. 629–633, 2012.

[51] J. Lorenz, "Formation of deeply bound LiRb molecules via photoassociation to near asymptotic states," Ph.D. dissertation, Purdue University, 2014.

[52] W. Ketterle, K. B. Davis, M. A. Joffe, A. Martin, and D. E. Pritchard, "High densities of cold atoms in a dark spontaneous-force optical trap," *Physical review letters*, vol. 70, no. 15, p. 2253, 1993.

[53] S. Dutta, "Experimental studies of LiRb: spectroscopy and ultracold molecule formation by photoassociation," Ph.D. dissertation, Purdue University, 2013.

[54] M. Ivanova, A. Stein, A. Pashov, H. Knöckel, and E. Tiemann, "The $X\ ^1\Sigma^+$ state of LiRb studied by Fourier-transform spectroscopy," *The Journal of chemical physics*, vol. 134, no. 2, p. 024321, 2011.

[55] S. Dutta, A. Altaf, D. Elliott, and Y. P. Chen, "Laser spectroscopy of the $X\ ^1\Sigma^+$ and $B\ ^1\Pi$ states of the LiRb molecule," *Chemical Physics Letters*, vol. 511, no. 1, pp. 7–11, 2011.

[56] A. Altaf, S. Dutta, J. Lorenz, J. Pérez-Ríos, Y. P. Chen, and D. Elliott, "Formation of ultracold ^{7}Li^{85}Rb molecules in the lowest triplet electronic state by photoassociation and their detection by ionization spectroscopy," *The Journal of chemical physics*, vol. 142, no. 11, p. 114310, 2015.

[57] D. B. Blasing, I. C. Stevenson, J. Pérez-Ríos, D. S. Elliott, and Y. P. Chen, "Short-range photoassociation of LiRb," *Physical Review A*, vol. 94, no. 6, p. 062504, 2016.

[58] M. Ivanova, A. Stein, A. Pashov, H. Knöckel, and E. Tiemann, "The B $^1\Pi$ and D $^1\Pi$ states of LiRb," *The Journal of chemical physics*, vol. 138, no. 9, p. 094315, 2013.

[59] J. Lorenz, A. Altaf, S. Dutta, Y. P. Chen, and D. Elliott, "Formation of deeply bound ultracold LiRb molecules via photoassociation near the Li 2 $S_{1/2}$ + Rb 5 $P_{3/2}$ asymptote," *Physical Review A*, vol. 90, no. 6, p. 062513, 2014.

[60] I. Stevenson, D. Blasing, A. Altaf, Y. Chen, and D. Elliott, "The d $^3\Pi$ state of LiRb," *The Journal of chemical physics*, vol. 145, no. 22, p. 224301, 2016.

[61] P. Pillet, A. Crubellier, A. Bleton, O. Dulieu, P. Nosbaum, I. Mourachko, and F. Masnou-Seeuws, "Photoassociation in a gas of cold alkali atoms: I. Perturbative quantum approach," *Journal of Physics B: Atomic, Molecular and Optical Physics*, vol. 30, no. 12, p. 2801, 1997.

[62] J. Deiglmayr, A. Grochola, M. Repp, O. Dulieu, R. Wester, and M. Weidemüller, "Permanent dipole moment of LiCs in the ground state," *Physical Review A*, vol. 82, no. 3, p. 032503, 2010.

[63] D. Wang, J.-T. Kim, C. Ashbaugh, E. Eyler, P. Gould, and W. Stwalley, "Rotationally resolved depletion spectroscopy of ultracold KRb molecules," *Physical Review A*, vol. 75, no. 3, p. 032511, 2007.

[64] M. Korek, G. Younes, and S. Al-Shawa, "Theoretical calculation of the electronic structure of the molecule LiRb including the spin–orbit interaction," *Journal of Molecular Structure: THEOCHEM*, vol. 899, no. 1, pp. 25–31, 2009.

[65] C. Bruzewicz, M. Gustavsson, T. Shimasaki, and D. DeMille, "Continuous formation of vibronic ground state RbCs molecules via photoassociation," *New Journal of Physics*, vol. 16, no. 2, p. 023018, 2014.

[66] G. Herzberg, *Molecular Spectra and Molecular Structure, I. Spectra of Diatomic Molecules*, 2nd ed. Krieger, Malabar FL, 1989.

[67] S. Dutta, J. Pérez-Ríos, D. Elliott, and Y. P. Chen, "Two-photon photoassociation spectroscopy of an ultracold heteronuclear molecule," *Physical Review A*, vol. 95, no. 1, p. 013405, 2017.

[68] I. Stevenson, D. Blasing, Y. Chen, and D. Elliott, "Production of ultracold ground-state LiRb molecules by photoassociation through a resonantly coupled state," *Physical Review A*, vol. 94, no. 6, p. 062510, 2016.

[69] D. Blasing, "Photoassociation in ^{87}Rb BECs and in ultracold ^{7}Li-^{85}Rb," Ph.D. dissertation, Purdue University, 2018.

[70] S. Dutta, D. S. Elliott, and Y. P. Chen, "Formation of ultracold LiRb molecules by photoassociation near the Li $(2s\ ^2S_{1/2})$ + Rb $(5p\ ^2P_{1/2})$ asymptote," *EPL (Europhysics Letters)*, vol. 104, no. 6, p. 63001, 2014.

[71] S. Eckel, S. Ashman, and J. Huennekens, "Spin-orbit coupling of the NaK (3) $^3\Pi$ and (3) $^1\Pi$ states: Determination of the coupling constant and observation of quantum interference effects," *Journal of Molecular Spectroscopy*, vol. 242, no. 2, pp. 182–194, 2007.

[72] R. J. Le Roy, "LEVEL: A computer program for solving the radial Schrödinger equation for bound and quasibound levels," *Journal of Quantitative Spectroscopy and Radiative Transfer*, vol. 186, pp. 167–178, 2017.

[73] I. Stevenson, D. Blasing, Y. Chen, and D. Elliott, "C $^1\Sigma^+$, A $^1\Sigma^+$, and b $^3\Pi_{0^+}$ states of LiRb," *Physical Review A*, vol. 94, no. 6, p. 062503, 2016.

[74] J. Ulmanis, J. Deiglmayr, M. Repp, R. Wester, and M. Weidemüller, "Ultracold molecules formed by photoassociation: Heteronuclear dimers, inelastic collisions, and interactions with ultrashort laser pulses," *Chemical Reviews*, vol. 112, no. 9, pp. 4890–4927, 2012.

[75] J. Banerjee, D. Rahmlow, R. Carollo, M. Bellos, E. E. Eyler, P. L. Gould, and W. C. Stwalley, "Spectroscopy of the double minimum (3) $^3\Pi_\Omega$ electronic state of ^{39}K^{85}Rb," *The Journal of Chemical Physics*, vol. 138, no. 16, p. 164302, 2013.

[76] Y. You, C.-L. Yang, Q.-Q. Zhang, M. Wang, X.-G. Ma, and W.-W. Liu, "The ab initio study on the spin-forbidden cooling transitions of LiRb molecule," *Physical Chemistry Chemical Physics*, 2016.

[77] K. Aikawa, D. Akamatsu, M. Hayashi, K. Oasa, J. Kobayashi, P. Naidon, T. Kishimoto, M. Ueda, and S. Inouye, "Coherent transfer of photoassociated molecules into the rovibrational ground state," *Physical review letters*, vol. 105, no. 20, p. 203001, 2010.

[78] G. Santarelli, A. Clairon, S. Lea, and G. Tino, "Heterodyne optical phase-locking of extended-cavity semiconductor lasers at 9 GHz," *Optics communications*, vol. 104, no. 4-6, pp. 339–344, 1994.

[79] L. Cacciapuoti, M. De Angelis, M. Fattori, G. Lamporesi, T. Petelski, M. Prevedelli, J. Stuhler, and G. Tino, "Analog+digital phase and frequency detector for phase locking of diode lasers," *Review of scientific instruments*, vol. 76, no. 5, p. 053111, 2005.

[80] M. Prevedelli, T. Freegarde, and T. Hänsch, "Phase locking of grating-tuned diode lasers," *Applied Physics B Lasers and Optics*, vol. 60, no. 2, p. 3, 1995.

[81] Z. Xu, X. Zhang, K. Huang, and X. Lu, "A digital optical phase-locked loop for diode lasers based on field programmable gate array," *Review of Scientific Instruments*, vol. 83, no. 9, p. 093104, 2012.

[82] F. M. Gardner, *Phaselock techniques*. John Wiley & Sons, 2005.

[83] H. Kuhn, "Pressure shift and boradening of spectral lines," *Phil. Mag.*, vol. 18, 1934.

[84] ——, "Pressure broadening of spectral lines and van der Waals forces. I. influence of argon on the mercury resonace line," *Proc. R. Soc. A*, vol. 158, p. 212, 1937.

[85] ——, "Pressure broadening of spectral lines and van der Waals forces. II. Continous broadening and discrete bands in pure mercury vapor," *Proc. R. Soc. A*, vol. 158, p. 230, 1937.

[86] E. D. Becker and T. Farrar, "Fourier transform spectroscopy," *Science*, vol. 178, no. 4059, pp. 361–368, 1972.

[87] H. Thorsheim, J. Weiner, and P. S. Julienne, "Laser-induced photoassociation of ultracold sodium atoms," *Physical review letters*, vol. 58, no. 23, p. 2420, 1987.

[88] C. Chin, R. Grimm, P. S. Julienne, and E. Tiesinga, "Feshbach resonances in ultracold gases," *Rev. Mod. Phys.*, vol. 82, p. 1225, 2010.

[89] V. Aquilanti, D. Ascenzi, D. Cappelletti, M. de Castro, and F. Pirani, "Scattering of aligned molecules. The potential energy surfaces for the Kr-O_2 and Xe-O_2 systems," *J. Chem. Phys.*, vol. 109, p. 3898, 1998.

[90] V. Aquilanti, D. Ascenzi, M. de Castro Vítores, and F. Pirani, "A quantum mechanical view of molecular alignment and cooling in seeded supersonic expansions," *J. Chem. Phys.*, vol. 111, p. 2620, 1999.

[91] V. Aquilanti, M. Bartolomei, D. Cappelletti, E. Carmona-Novilli, and F. Pirani, "The N_2-N_2 system: an experimental potential energy surface and calculated rotovibrational levels of the molecular nitrogen dimer," *J. Chem. Phys.*, vol. 117, p. 615, 2002.

[92] R. B. Bernstein and R. A. LaBudde, "On the analysis of glory scattering data for the extraction of information on the interatomic potential well," *J. Chem. Phys.*, vol. 58, p. 1109, 1973.

[93] R. B. Bernstein and T. J. P. O'Brien, "Potential-well characteristics from the energy dependence of the glory extrema in total elastic scattering cross sections," *J. Chem. Phys.*, vol. 46, p. 1208, 1967.

[94] D. Cappelletti, V. Aquilanti, E. Cornicchi, M. M. Teixidor, and F. Pirani, "Molecular-beam study of the water-helium system: features of the isotropic component of the itnermolecular interaction and a critical test for the available potential-energy surfaces," *J. Chem. Phys.*, vol. 123, p. 024302, 2005.

[95] E. F. Greene and E. A. Mason, "Physical interpretation of Glory undulations in scattering cross sections," *J. Chem. Phys.*, vol. 57, p. 2065, 1972.

[96] R. J. LeRoy and R. B. Bernstein, "Dissociation energy and long-range potential of diatomic molecules from vibrational spacings of higher levels," *The Journal of Chemical Physics*, vol. 52, no. 8, pp. 3869–3879, 1970.

[97] A. Rees, "The calculation of potential-energy curves from band-spectroscopic data," *Proceedings of the Physical Society*, vol. 59, no. 6, p. 998, 1947.

[98] W. M. Kosman and J. Hinze, "Inverse peturbations analysis: improving the accuracy of potential energy curves," *J. Mol. Spectros.*, vol. 56, p. 93, 1975.

[99] C. R. Vidal and H. Scheingraber, "Determination of diatomic molecular constants using an inverted perturbation approach: application to the $A^1\sigma_u^+$ - $X^1\sigma_g^+$," *J. Mol. Spectros.*, vol. 65, 1977.

[100] D. M. Deaven and K.-M. Ho, "Molecular geometry optimization with a genetic algorithm," *Physical review letters*, vol. 75, no. 2, p. 288, 1995.

[101] G. A. Cox, T. V. Mortimer-Jones, R. P. Taylor, and R. L. Johnston, "Development and optimisation of a novel genetic algorithm for studying model protein folding," *Theoretical Chemistry Accounts*, vol. 112, no. 3, pp. 163–178, 2004.

[102] M. H. Hennessy and A. M. Kelley, "Using real-valued multi-objective genetic algorithms to model molecular absorption spectra and raman excitation profiles in solution," *Physical Chemistry Chemical Physics*, vol. 6, no. 6, pp. 1085–1095, 2004.

[103] W. L. Meerts and M. Schmitt, "A new automated assign and analysing method for high-resolution rotationally resolved spectra using genetic algorithms," *Physica Scripta*, vol. 73, no. 1, p. C47, 2005.

[104] L. F. Roncaratti, R. Gargano, and G. M. e Silva, "A genetic algorithm to build diatomic potentials," *Journal of Molecular Structure: THEOCHEM*, vol. 769, no. 1-3, pp. 47–51, 2006.

[105] J. Marques, F. V. Prudente, F. Pereira, M. M. Almeida, A. Maniero, and C. E. Fellows, "A new genetic algorithm to be used in the direct fit of potential energy curves to ab initio and spectroscopic data," *Journal of Physics B: Atomic, Molecular and Optical Physics*, vol. 41, no. 8, p. 085103, 2008.

[106] P. Huxley and J. N. Murrell, "Ground-state diatomic potentials," *Journal of the Chemical Society, Faraday Transactions 2: Molecular and Chemical Physics*, vol. 79, no. 2, pp. 323–328, 1983.

[107] M. M. Almeida, F. V. Prudente, C. E. Fellows, J. M. Marques, and F. B. Pereira, "Direct fit of spectroscopic data of diatomic molecules by using genetic algorithms: Ii. the ground state of RbCs," *Journal of Physics B: Atomic, Molecular and Optical Physics*, vol. 44, no. 22, p. 225102, 2011.

[108] C. Samuelis, E. Tiesinga, T. Laue, M. Elbs, H. Knöckel, and E. Tiemann, "Cold atomic collisions studied by molecular spectroscopy," *Physical Review A*, vol. 63, no. 1, p. 012710, 2000.

[109] P. M. Morse, "Diatomic molecules according to the wave mechanics. II. Vibrational levels," *Physical Review*, vol. 34, no. 1, p. 57, 1929.

[110] J. Cooley, "An improved eigenvalue corrector formula for solving the Schrödinger equation for central fields," *Mathematics of Computation*, vol. 15, no. 76, pp. 363–374, 1961.

[111] K. A. De Jong, "Analysis of the behavior of a class of genetic adaptive systems," 1975.

[112] R. Storn and K. Price, "Differential evolution–a simple and efficient heuristic for global optimization over continuous spaces," *Journal of global optimization*, vol. 11, no. 4, pp. 341–359, 1997.

[113] K. Deb and R. B. Agrawal, "Simulated binary crossover for continuous search space," *Complex Systems*, vol. 9, no. 3, pp. 1–15, 1994.

[114] R. Rodríguez-Fernández, F. B. Pereira, J. M. Marques, E. Martínez-Núñez, and S. A. Vázquez, "GAFit: a general-purpose, user-friendly program for fitting potential energy surfaces," *Computer Physics Communications*, vol. 217, pp. 89–98, 2017.

[115] P. J. Ballester and J. N. Carter, "An effective real-parameter genetic algorithm with parent centric normal crossover for multimodal optimisation," in *Genetic and Evolutionary Computation Conference*. Springer, 2004, pp. 901–913.

[116] K. Deb, A. Anand, and D. Joshi, "A computationally efficient evolutionary algorithm for real-parameter optimization," *Evolutionary computation*, vol. 10, no. 4, pp. 371–395, 2002.

[117] J. L. Rueda and I. Erlich, "Hybrid Mean-Variance Mapping Optimization for solving the IEEE-CEC 2013 competition problems," in *Evolutionary Computation (CEC), 2013 IEEE Congress on*. IEEE, 2013, pp. 1664–1671.

[118] C. Zhu, R. H. Byrd, P. Lu, and J. Nocedal, "Algorithm 778: L-BFGS-B: Fortran subroutines for large-scale bound-constrained optimization," *ACM Transactions on Mathematical Software (TOMS)*, vol. 23, no. 4, pp. 550–560, 1997.

[119] K. Deb, A. Pratap, S. Agarwal, and T. Meyarivan, "A fast and elitist multiobjective genetic algorithm: NSGA-II," *IEEE transactions on evolutionary computation*, vol. 6, no. 2, pp. 182–197, 2002.

[120] E. Zitzler, M. Laumanns, and L. Thiele, "SPEA2: Improving the strength Pareto evolutionary algorithm," *TIK-report*, vol. 103, 2001.

[121] J. D. Knowles and D. W. Corne, "Approximating the nondominated front using the Pareto archived evolution strategy," *Evolutionary computation*, vol. 8, no. 2, pp. 149–172, 2000.

[122] M. T. Jensen, "Reducing the run-time complexity of multiobjective EAs: The NSGA-II and other algorithms," *IEEE Transactions on Evolutionary Computation*, vol. 7, no. 5, pp. 503–515, 2003.

[123] R. Tanabe and A. S. Fukunaga, "Improving the search performance of SHADE using linear population size reduction," in *Evolutionary Computation (CEC), 2014 IEEE Congress on*. IEEE, 2014, pp. 1658–1665.

[124] A. Pashov, W. Jastrzebski, and P. Kowalczyk, "The Li_2 F $^1\Sigma_g^+$ "shelf" state: Accurate potential energy curve based on the inverted perturbation approach," *The Journal of Chemical Physics*, vol. 113, no. 16, pp. 6624–6628, 2000.

[125] W. Bowden, W. Gunton, M. Semczuk, K. Dare, and K. W. Madison, "An adaptable dual species effusive source and Zeeman slower design demonstrated with Rb and Li," *Review of Scientific Instruments*, vol. 87, no. 4, p. 043111, 2016.

[126] A. Olson, "The dynamics of ultracold atoms in syntheic gauge fields," Ph.D. dissertation, Purdue Universtiy, 2015.

[127] S. Dutta, J. Lorenz, A. Altaf, D. Elliott, and Y. P. Chen, "Photoassociation of ultracold LiRb* molecules: observation of high efficiency and unitarity-limited rate saturation," *Physical Review A*, vol. 89, no. 2, p. 020702, 2014.

[128] Z. Shi, P. Wang, Z. Li, Z. Meng, L. Huang, and J. Zhang, "Sub-doppler laser cooling of ^{23}Na in gray molasses on the D_2 line," *arXiv preprint arXiv:1803.05108*, 2018.

[129] P. Makotyn, C. E. Klauss, D. L. Goldberger, E. Cornell, and D. S. Jin, "Universal dynamics of a degenerate unitary Bose gas," *Nature Physics*, vol. 10, no. 2, p. 116, 2014.

[130] Y. Ding, J. P. D'Incao, and C. H. Greene, "Effective control of cold collisions with radio-frequency fields," *Physical Review A*, vol. 95, no. 2, p. 022709, 2017.

[131] G. Thalhammer, M. Theis, K. Winkler, R. Grimm, and J. H. Denschlag, "Inducing an optical Feshbach resonance via stimulated Raman coupling," *Physical Review A*, vol. 71, no. 3, p. 033403, 2005.

[132] M. M. Somoza, "Depiction of Franck Condon principle in absorption and fluorescence," *URL http://en.wikipedia.org/wiki/File:Franck-Condon-diagram.png*, 2006.

[133] J. Brown, J. Hougen, K.-P. Huber, J. Johns, I. Kopp, H. Lefebvre-Brion, A. Merer, D. Ramsay, J. Rostas, and R. Zare, "The labeling of parity doublet levels in linear molecules," *Journal of Molecular Spectroscopy*, vol. 55, no. 1-3, pp. 500–503, 1975.

[134] K. O'Hara, "Optical trapping and evaporative cooling of Fermionic atoms," Ph.D. dissertation, Duke University, 2000.

[135] M. T. Asaki, C.-P. Huang, D. Garvey, J. Zhou, H. C. Kapteyn, and M. M. Murnane, "Generation of 11-fs pulses from a self-mode-locked Ti: sapphire laser," *Optics letters*, vol. 18, no. 12, pp. 977–979, 1993.

[136] F. Nez, F. Biraben, R. Felder, and Y. Millerioux, "Optical frequency determination of the hyperfine components of the $5S_{\frac{1}{2}}$-$5D_{\frac{3}{2}}$ two-photon transitions in rubidium," *Optics communications*, vol. 102, no. 5-6, pp. 432–438, 1993.

[137] A. J. Olson, E. J. Carlson, and S. K. Mayer, "Two-photon spectroscopy of rubidium using a grating-feedback diode laser," 2006.

[138] A. M. Weiner, "Femtosecond pulse shaping using spatial light modulators," *Review of scientific instruments*, vol. 71, no. 5, pp. 1929–1960, 2000.